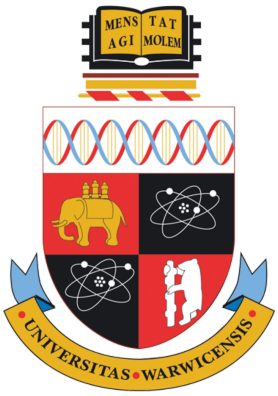

PLASMA HEATING AND KINETIC INSTABILITIES IN THE TERRESTRIAL FORESHOCK

by

DANIEL J. O'CONNELL

A thesis submitted in partial fulfilment of the requirements for the degree of

Doctor of Philosophy in Physics

UNIVERSITY OF WARWICK, DEPARTMENT OF PHYSICS

September 2017

Contents

Acknowledgements

I would like to thank my supervisor Bogdan Hnat for his tireless support throughout my time at Warwick, and my various co-authors; Torbjorn Sundberg, Valery Nakariakov, Dmitrii Kolotkov and George Rowlands. I would like to extend my appreciation to my colleagues at the Centre for Fusion, Space and Astrophysics for countless fruitful discussions and constructive advice. I also thank the *Cluster* team for data provision, without which this work would not have been possible.

Declaration

I declare that this thesis is my own original work except where indicated otherwise, and has not been submitted for a degree at another university. Parts of this thesis have been published by, or in collaboration with, the author in the following peer-reviewed journal articles:

- B. Hnat, D. Y. Kolotkov, D. O'Connell, V. M. Nakariakov and G. Rowlands, Non-linear waves in the terrestrial quasiparallel foreshock, *Physical Review Letters*, 117(23):235102, 2016.

- B. Hnat, D. O'Connell, V. M. Nakariakov and T. Sundberg, Statistically determined dispersion relations of magnetic field fluctuations in the terrestrial foreshock, *The Astrophysical Journal*, 827(2):91, 2016

Abstract

The terrestrial foreshock, the area upstream of, and magnetically connected to, the bow shock is a complex system in which the turbulent, supersonic and superalfvénic solar wind encounters the Earth's magnetosphere. As a result, particle populations stream sunwards against the solar wind flow, creating a kinetic two-stream instability that leads to a variety of linear and nonlinear plasma processes. Foreshock plasma is collisionless, and the instability supports a variety of ultra-low frequency (ULF) modes. A statistical technique, based on categorizing wavenumber-frequency pairs by their associated power, is used to determine the dispersion relations for ULF modes in a number of case studies using magnetic field data from two-point measurements of the *Cluster* mission. Sunward-propagating fast magnetosonic and beam resonant modes are identified, as well as Alfvén modes propagating both sunwards and anti-sunwards. The fast magnetosonic modes are advected towards the Earth by the solar wind, and due to a cubic nonlinearity, steepen into sharply peaked waves. Three examples of these nonlinear wavetrains are compared to solutions of the derivative nonlinear Schrődinger equation, and are found to be in good agreement. The impact of the waves on the form of the pseudopotential, a quantity related to core plasma parameters, is also discussed. Wave-wave interactions are investigated for a case study of Cluster data, with a focus on energy transfer between ULF modes and a band of frequencies centred at 1Hz. Evidence for three-wave processes, formed by quadratic nonlinearities that interact between triads of frequencies that satisfy the frequency ($f_1 + f_2 = f_3$) and wavenumber ($\vec{k}_1 + \vec{k}_2 = \vec{k}_3$) resonance conditions, is presented. Evidence for four wave processes in the same interval is also discussed.

Chapter 1

Introduction

1.1 Thesis Overview

The overall aim of the work is to further the understanding of the linear and nonlinear processes that exist in the terrestrial foreshock; the area upstream of the Earth's bow shock. In the second chapter, well-known spectral techniques are adapted for use with the multi-spacecraft *Cluster II* mission, in conjunction with a statistical method, to derive dispersion relations of ULF modes for two datasets of magnetic field fluctuations. The third chapter focuses on the analysis of non-linear wavetrains, using the ensemble empirical mode decomposition to compare magnetic field measurements containing cubic non-linearities with solutions obtained using the derivative non-linear Schrödinger equation. The fourth chapter involves methods built on higher-order statistical analysis; the bicoherence and wavenumber mismatch; to investigate the role of wave-wave interactions in magnetic field fluctuations, with a focus on coupling between the ULF modes and frequencies close to 1Hz. The introduction offers a general background to relevant plasma physics concepts, and provides a detailed, linearized derivation of relevant plasma modes, as well as a brief tour of terrestrial space plasma physics and the Cluster II satellites.

1.2 Plasma Physics

A plasma may be described as a gaseous admixture of neutral and positively and negatively charged species of particles that is macroscopically charge-neutral (ie, *quasineutral*), or more simply as an ionized gas. The prototypical example is a two species plasma consisting of two particle populations: ions and free electrons. Since the constituent particles all hold charge, plasmas will interact strongly with magnetic fields. A plasma is therefore characterized by the usual descriptors for gasses (such as the temperature and pressure), with the addition of terms used to reflect the response of the plasma to electromagnetic

fields and effects resulting from interactions between the charged particles themselves. In classical gases, interactions between electrically neutral particles are short-range. Forces between particles are initially attractive (the Van der Waals force, for example, is proportional to r^{-7}, where r is the distance between particles [1]), and then immediately repulsive before particles contact. In contrast, charged particles are affected by the much longer-ranged Coulomb force (as r^{-2} [2]) and therefore do not behave exactly as would be expected by the laws that govern classical gases. A plasma is also electrically conducting; an externally applied magnetic field applied to a plasma may induce currents that reciprocally alter the magnetic field itself. The study of electrically conducting fluids (termed *magnetohydrodynamics (MHD)* in 1942 by Hannes Alfvén [3]) whilst not a complete theory of plasma dynamics, is still a very useful one, and a natural starting point for the study of plasmas.

1.2.1 Gyromotion

Firstly, let us consider the dynamics of single particles in a plasma. The introduction of an electromagnetic field to a charged particle produces a classical *Lorentz force*. This Lorentz force will act on every particle of the plasma. The equation of motion for a typical particle of mass m_s and charge q_s, moving at a velocity $\vec{v}$ in the presence of electric, $\vec{E}$, and magnetic, $\vec{B}$, fields is given by the *Lorentz equation* [4]:

$$m_s \frac{d\vec{v}}{dt} = q_s\left(\vec{E} + \vec{v} \times \vec{B}\right) \tag{1.1}$$

where s represents the species of the plasma. For a static, one-dimensional externally applied magnetic field, we may decompose the particle's velocity into its components parallel and perpendicular to the magnetic field, $\vec{v} = \vec{v}_\perp + \vec{v}_\parallel$ to show that

$$\frac{d\vec{v}_\parallel}{dt} = 0 \tag{1.2}$$

$$\frac{d\vec{v}_\perp}{dt} = \frac{q_s}{m_s}(\vec{v}_\perp \times \vec{B}) \tag{1.3}$$

from which we may conclude that a charged particle gyrates around a magnetic field line in the perpendicular plane only, at the *cyclotron frequency*

$$\omega_{cs} = \frac{|q_s|B}{m_s} \tag{1.4}$$

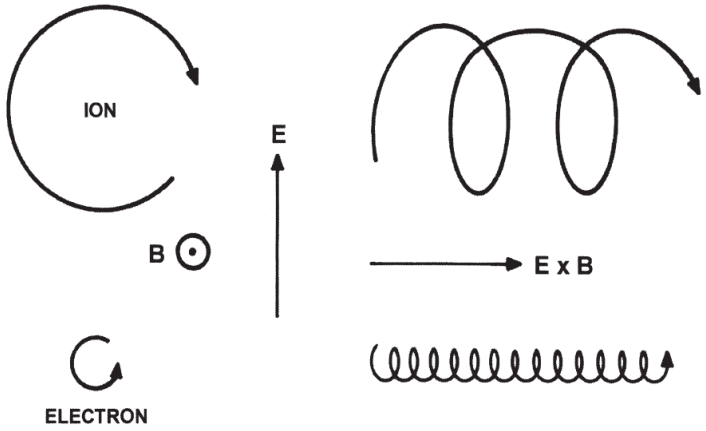

Figure 1.1: Cycloidal motion of ions and electrons in orthogonal electric and magnetic field. The $\vec{E} \times \vec{B}$ drift direction is shown. (From [5])

and moves at a constant velocity in the parallel direction, see figure (1.1). Since the handedness of the gyration (1.4) is charge-dependent, electrons and ions will gyrate with opposite polarities. The distance from the field line at which the particle gyrates is known as the *Larmor radius*

$$r_L = \frac{m_s v_\perp}{q_s B} \tag{1.5}$$

and is larger for electrons than for ions.

1.2.2 Drifts

A plasma particle gyrates around a magnetic field line according to equation (1.4), around the *guiding centre*. The particle's overall motion can be treated as the superposition of a relatively fast circular motion around the guiding centre and any additional, relatively slow, motion of this point called a *drift* [6]. Modelling this drift as the result of some force, $F_\perp$, acting perpendicular to the magnetic field on a gyrating particle, the equation of motion can be derived from the Lorentz force [7][8]:

$$m_s \frac{d\vec{v}}{dt} = F_\perp + |q_s| \vec{v} \times \vec{B} \tag{1.6}$$

Taking the velocity as the superposition of the velocity around the guiding centre and the drift velocity $\vec{v} = \vec{v}_{gc} + \vec{v}_d$, and substituting into (1.1) gives:

$$m_s \frac{d\vec{v}_d}{dt} = F_\perp + q_s \vec{v}_d \times \vec{B} \tag{1.7}$$

for the drift velocity, and reduces to equations (1.2) and (1.3) for the velocity around the guiding centre. Assuming that the drift velocity is time-independent, the cross product of the expression with $\vec{B}$ gives:

$$\vec{v}_d - \frac{\vec{v}_d \cdot \vec{B}}{B^2} = \frac{F_\perp \times \vec{B}}{q_s B^2} \tag{1.8}$$

For a purely perpendicular drift velocity, we have:

$$v_\perp = \frac{F_\perp \times \vec{B}}{q_s B^2} \tag{1.9}$$

This expression shows that in general, any perpendicular force exerted on a plasma particle will create a drift perpendicular to both the magnetic field and the applied force. For example, an electric field applied perpendicular to a magnetic field will produce a Coulomb force, $\vec{F} = q_s \vec{E}$, that will cause a particle to drift such that:

$$v_\perp = \frac{\vec{E} \times \vec{B}}{B^2} \tag{1.10}$$

This drift is known as the $\vec{E} \times \vec{B}$ drift, and is shown in figure (1.4).

1.2.3 The Distribution Function

The collective motion of the plasma particles is described in an analogous way to that of a gas, with the use of the *distribution function*, such that the number of particles per unit volume with velocities in the range $\vec{v} \to \vec{v} + \vec{d}v$ and $\vec{r} \to \vec{r} + \vec{d}r$ is [9]:

$$dn = f(\vec{r}, \vec{v}, t) d^3\vec{v} d^3\vec{r} \tag{1.11}$$

The distribution function describes a point in the 6-dimensional *phase space* of $\vec{r}$ and $\vec{v}$ at time t. Taking the Maxwell-Boltzmann form of $f(\vec{r}, \vec{v}, t)$ we find the plasma number density for a species s in thermal and electrostatic equilibrium is given by the *Boltzmann relation* [10].

$$n_s(\phi_2) = n_s(\phi_1) e^{\frac{-q_s(\phi_2 - \phi_1)}{k_B T_s}} \tag{1.12}$$

where n_s and T_s are the species number density and temperature respectively, ϕ_1 and ϕ_2 represent the local electrostatic potential at two nearby locations, and k_B is the Boltzmann constant. Since a plasma is a combination of charged populations, the plasma's total charge density is [4]:

$$\sigma = \sum_s q_s n_s \tag{1.13}$$

and the current density vector created by the movement of these charges is given by [4]:

$$\vec{J} = \sum_s n_s q_s \vec{v}_s \tag{1.14}$$

The thermal motion of a plasma can be described by the kinetic pressure tensor. The simplest form is attained by assuming this tensor to be reducible to a scalar isotropic pressure, p_s that depends on the species' temperature: [11]

$$p_s = n_s k_B T_s \tag{1.15}$$

Our basic two-species electron-ion plasma, for example, will be in thermodynamic equilibrium when T_e and T_i, the electron and ion temperatures, are equal.

1.2.4 Maxwell's Equations

The collective plasma behaviour responds to externally applied electromagnetic fields. These fields are governed by the set of *Maxwell's equations* [5] [12]

$$\vec{\nabla} \cdot \vec{E} = \frac{\sigma}{\epsilon_0} \tag{1.16}$$

$$\vec{\nabla} \times \vec{E} = -\frac{\partial \vec{B}}{\partial t} \tag{1.17}$$

$$\vec{\nabla} \cdot \vec{B} = 0 \tag{1.18}$$

$$\vec{\nabla} \times \vec{B} = \mu_0 \left(\vec{J} + \epsilon_0 \frac{\partial \vec{E}}{\partial t} \right) \tag{1.19}$$

where ϵ_0 and μ_0 are the vacuum permittivity and permeability, respectively. The electromagnetic field exerts influence on each charged particle of the plasma, but the charged particles themselves also produce electromagnetic fields. We are thus left with a consistency problem whereby particles that produce fields are also in turn influenced by fields, and move in a fluid-like manner. Maxwell's equations and the Lorentz force law are therefore an intractable description of the plasma and more information is necessary.

1.2.5 The Vlasov Equation

The plasma density can be modified by two phenomena; sources (or sinks) of particles and inter-particle collisions. The plasma is assumed to be a closed system and the systems studied in later chapters are of densities sparse enough to be considered completely *collisionless*, and hence collisions will be neglected. In a collisionless plasma, perturbed particles in a neighbourhood of position A will move along a continuous curve of phase space to position B. The total number of particles in this small element will therefore remain constant subject to a *continuity equation* [11][12]

$$\frac{\partial f(\vec{r},\vec{v},t)}{\partial t} + \vec{\nabla}_{\vec{r},\vec{v}} \cdot [f(\vec{r},\vec{v},t)(\dot{\vec{r}},\dot{\vec{v}})] = 0 \tag{1.20}$$

where

$$\vec{\nabla}_{\vec{r},\vec{v}} = \left[\frac{\partial}{\partial x}, \frac{\partial}{\partial y}, \frac{\partial}{\partial z}, \frac{\partial}{\partial v_x}, \frac{\partial}{\partial v_y}, \frac{\partial}{\partial v_z}\right] \tag{1.21}$$

is a 6-dimensional divergence operator, and

$$\left(\dot{\vec{r}},\dot{\vec{v}}\right) = \left(\dot{x},\dot{y},\dot{z},\dot{v_x},\dot{v_y},\dot{v_z}\right) \tag{1.22}$$

is the "velocity" of a point in the phase space [13]. Substituting the Lorentz force law (1.1) for $\dot{\vec{v}}$ we may rewrite (1.20) to derive the *Vlasov equation*: [12]

$$\frac{\partial f(\vec{r},\vec{v},t)}{\partial t} + \vec{v}\cdot\vec{\nabla}_{\vec{r}} f(\vec{r},\vec{v},t) + \frac{q}{m}\left(\vec{E}+\vec{v}\times\vec{B}\right)\cdot\vec{\nabla}_{\vec{v}} f(\vec{r},\vec{v},t) = 0 \tag{1.23}$$

Or, more succinctly:

$$\frac{\mathrm{d}f(\vec{r},\vec{v},t)}{\mathrm{d}t} = \frac{\partial f(\vec{r},\vec{v},t)}{\partial t} + \frac{\mathrm{d}\vec{r}}{\mathrm{d}t}\cdot\vec{\nabla}_{\vec{r}} f(\vec{r},\vec{v},t) + \frac{\mathrm{d}\vec{v}}{\mathrm{d}t}\cdot\vec{\nabla}_{\vec{v}} f(\vec{r},\vec{v},t) = 0 \tag{1.24}$$

where the left-hand-side is the total time derivative, or *convective derivative*, of the distribution function. The Vlasov equation thus evaluates the variation of the distribution function due to both the change of a particle's position in the phase space, and to the time variation of the distribution function itself. Each species of the plasma requires a separate solution. We may take moments of (1.24). Firstly, by integrating over velocity space and using (1.11), we derive the *particle continuity equation:* [11]

$$\frac{\partial n_s}{\partial t} + \vec{\nabla} \cdot n_s \vec{v}_s = 0 \tag{1.25}$$

which describes particle number conservation. Secondly, by multiplying (1.24) by $m_s \vec{v}_s$, the integration yields the relation for *momentum conservation*:

$$n_s m_s \frac{\partial \vec{v}_s}{\partial t} = q n_s \left(\vec{E} + \vec{v}_s \times \vec{B} \right) - \vec{\nabla} p_s \tag{1.26}$$

These forms of the continuity and momentum equations unaltered by the effects of collisions. The moments of the Vlasov equation are closed using the equation of state (1.15).

1.2.6 Alfvén's Theorem

Some effects of the plasma can be modelled independently of the smaller particle-scale dynamics. To illustrate this, consider a surface, $\vec{s}$, of plasma. The magnetic flux through this surface is:

$$\Phi = \int_s \vec{B} \cdot \vec{d}s \tag{1.27}$$

If the plasma has a bulk velocity $\vec{u}$, and the surface moves with the plasma, then:

$$\frac{d\vec{s}}{dt} = \vec{u} \times dl \tag{1.28}$$

Where dl is an element of the perimeter, l, of the surface $\vec{s}$, and ds is an infinitesimal of $\vec{s}$. Hence:

$$\frac{d\Phi}{dt} = \int_s \frac{\partial \vec{B}}{\partial t} \cdot \vec{d}s + \int_l \vec{B} \cdot (\vec{u} \times dl) \tag{1.29}$$

And by Stokes's theorem:

$$\int_l \vec{B} \cdot (\vec{u} \times d\,l) = -\int_s \vec{\nabla} \times \left(\vec{B} \times \vec{u}\right) \cdot \vec{d}s \tag{1.30}$$

Using Faraday's law, equation (1.17):

$$\frac{d\Phi}{d\,t} = -\int_s \vec{\nabla} \times \left(\vec{E} + \vec{u} \times \vec{B}\right) \cdot \vec{d}s \tag{1.31}$$

We now consider Ohm's law

$$\vec{J} = \sigma \vec{E}' \tag{1.32}$$

where σ is the electrical conductivity; the reciprocal of η, the resistivity; and $\vec{E}'$ is the electric field experienced by the plasma fluid element *in its rest frame*. When the plasma moves with respect to the external field, we see from equation (1.1), that:

$$\vec{E}' = \vec{E} + \vec{u} \times \vec{B} \tag{1.33}$$

and so we may rewrite Ohm's law:

$$\frac{J}{\sigma} = \vec{E} + \vec{u} \times \vec{B} \tag{1.34}$$

A highly conductive plasma will therefore satisfy $\vec{E} + \vec{u} \times \vec{B} = 0$, and we can see from the combination of equations (1.34) and (1.31) that the magnetic flux within a fluid element is conserved. The flux is therefore confined to the fluid element and must move as the element does. It is usually remarked that the flux is "frozen in" to the plasma. In the case of perfect conductivity, $\sigma \to \infty$ and:

$$\vec{E} = -\vec{u} \times \vec{B} \tag{1.35}$$

Combining this result with equation (1.17), we find:

$$\frac{\partial \vec{B}}{\partial t} = \vec{\nabla} \times \left(\vec{u} \times \vec{B}\right) \tag{1.36}$$

which is the *induction equation*. A time-dependent surface, $\vec{s}$, of a highly conducting

plasma will therefore move to conserve magnetic flux. This movement forms a volume enclosed by flux lines known as a *flux tube*, shown in figure (1.2). Let $\vec{s}_1$ denote the surface at t, $\vec{s}_2$ the surface at $t+dt$, and $\vec{s}_3$ the surface that encloses the flux tube volume, shown in figure (1.2). The magnetic fluxes through surfaces $\vec{s}_{1,2,3}$ are denoted as $\Phi_{1,2,3}$ respectively. Since the magnetic field does not diverge, due to equation (1.16), we have:

$$-\Phi_1 + \Phi_2 + \Phi_3 = 0 \tag{1.37}$$

where the negative sign of the first term arises from the fact that outward flux opposes the inward-pointing normal of s_1. Denote by Φ the flux through the surface perimeter $l(t)$, as in figure (1.2). Then:

$$\frac{d\Phi}{dt} = \lim_{t\to 0} \frac{\Phi_2(t+\Delta t) - \Phi_1(t)}{\Delta t} \tag{1.38}$$

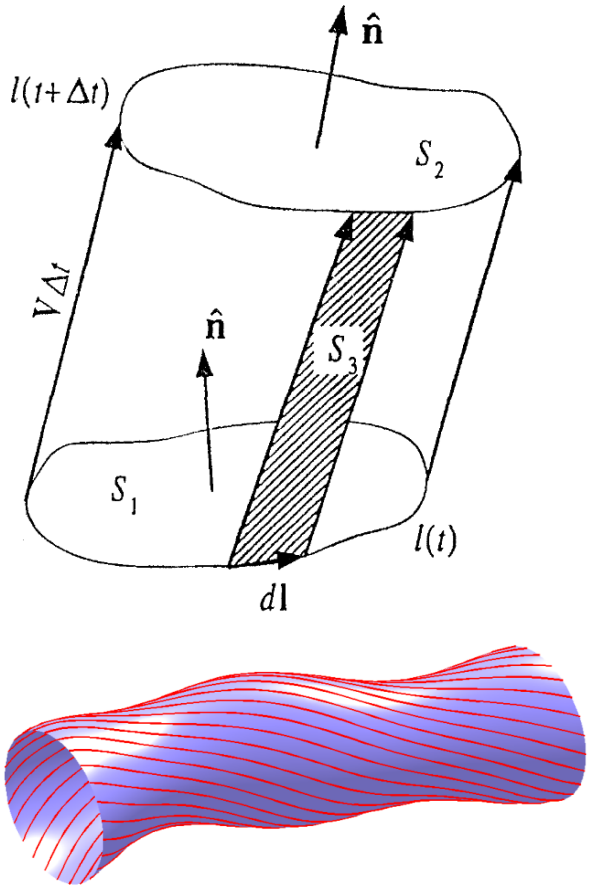

Figure 1.2: Above: flux tube schematic showing the time evolution of a plasma element surface. Below: depiction of a flux tube volume with twisted flux lines shown in red.

Substituting (1.27) into (1.37), and eliminating Φ_2 from (1.38), we find:

$$\frac{d\Phi}{dt} = \int_{s_1} \left[\frac{d\vec{B}}{dt} - \nabla \times \left(\vec{u} \times \vec{B} \right) \right] \tag{1.39}$$

By the induction equation, (1.36), we find $\frac{d\Phi}{dt} = 0$, and the flux is conserved. The effect of this is that the plasma within a flux tube will remain in that flux tube as the plasma moves. Plasma elements on a field line will also remain on that field line, as the plasma and the field lines move.

1.3 Plasma Waves

Plasmas can be described on different spatial scales. The most common of these is the Debye length, λ_D given by:

$$\lambda_D^2 = \frac{\epsilon_0 k_B T_e}{n_e q_e^2} \tag{1.40}$$

where the ion motion has been neglected as compared to the electron. The Deybe length is a measure of a charge carrier's net electrostatic effect in solution, and to what extent its electrostatic effect persists in the plasma. On temporal scales, plasmas are capable of supporting a large amount of wave modes, the most commonly referenced is the plasma oscillation.

1.3.1 Plasma Oscillation

In a collisionless plasma, waves will naturally emerge as the principal mechanism through which energy transfer takes place in the plasma. The simplest wave is the *plasma oscillation*. Since a plasma is quasineutral, the charges are distributed uniformly on particles scales. In the absence of any external electromagnetic fields, a one-dimensional perturbation of charged particles (eg an electron population) along some axis z will result in a charge separation, creating an electric field E_z that produces a Coulomb restoring force. This force will then act to pull the particles back to the equilibrium position such that

$$m_s \ddot{z} = -q_s E_z \tag{1.41}$$

This expression may be integrated using Gauss' theorem;

$$\oint_S \vec{E} \cdot \vec{dS} = Q/\epsilon_0 \tag{1.42}$$

with

$$Q = Ln_s q_s z \tag{1.43}$$

representing the charge of a plane of area of charge separation z, and characteristic plasma length scale L, to show that:

$$E_z = \frac{n_s q_s z}{\epsilon_0} \tag{1.44}$$

Then,

$$\ddot{z} = -\omega_{ps}^2 z \tag{1.45}$$

And the perturbation oscillates at the *plasma frequency:*

$$\omega_{ps} = \sqrt{\frac{n_s q_s^2}{m_s \epsilon_0}} \tag{1.46}$$

The most basic plasma oscillations are produced by perturbations of ions and electrons, with the electron plasma frequency 2-3 orders of magnitude greater than the ion.

1.3.2 The Dispersion Relation

In the general case, the propagation of a wave in a plasma can be described as a perturbation of the descriptive variables so far considered and the electromagnetic fields. The *plane wave* form of waves propagating in the positive z direction is [11]:

$$A(z,t) = A_0 e^{-i(kz-\omega t)} \tag{1.47}$$

Here, A_0 is the wave amplitude, k is the wavenumber, and ω is the angular frequency. A plane wave thus represents a wave with wavefronts of infinite parallel planes, with the normal vector of each plane pointing always in the direction of propagation of the wave. When the wave number is real, the wave travels unattenuated with phase and group ve-

locities:

$$v_\phi = \frac{\omega}{k} \tag{1.48}$$

$$v_g = \frac{\mathrm{d}\omega}{\mathrm{d}k} \tag{1.49}$$

and k can be calculated from the wavelength, λ:

$$k = \frac{2\pi}{\lambda} \tag{1.50}$$

It can be shown that the plane wave is a solution to the Maxwell equations, (1.16-1.19). Taking the curl of (1.17) we eliminate the magnetic field dependence and derive [11]

$$\vec{\nabla} \times \vec{\nabla} \times \vec{E} + \frac{1}{c^2}\frac{\partial^2 \vec{E}}{\partial t^2} + \mu_0 \frac{\partial \vec{J}}{\partial t} = 0 \tag{1.51}$$

where $c^2 = \frac{1}{\epsilon_0 \mu_0}$ is the square of the speed of light. In the absence of sources of charge, $\vec{J} = 0$, and (1.16) becomes $\vec{\nabla} \cdot \vec{E} = 0$, which may be combined with the vector identity

$$\vec{\nabla}\left(\vec{\nabla} \cdot \vec{E}\right) = \left(\vec{\nabla} \times \vec{\nabla} \times \vec{E}\right) + \vec{\nabla}^2 \vec{E} \tag{1.52}$$

to show that the relation (1.51) reduces to the wave equation:

$$\vec{\nabla}^2 \vec{E} - \frac{1}{c^2}\frac{\partial^2 \vec{E}}{\partial t^2} = 0 \tag{1.53}$$

A similar argument can be made for the magnetic field vector $\vec{B}$. For a wave travelling in a plasma we are not afforded this $\vec{J} = 0$ simplification and so more detail is necessary. By inspection of (1.47), and assuming that the wave varies sinusoidally in $\vec{E}$ and $\vec{B}$, we may permit the use of the linear operators

$$\frac{\partial}{\partial t} = i\omega \tag{1.54}$$

$$\vec{\nabla} = -i\vec{k} \tag{1.55}$$

and can introduce these operators into (1.51) along with the current vector, (1.14) to get [11]

$$\left(\frac{k^2c^2}{\omega^2}-1\right)E_x=\frac{1}{i\omega\epsilon_0}\sum_s \bar{n}_s q_s \vec{v}_{sx} \tag{1.56}$$

$$\left(\frac{k^2c^2}{\omega^2}-1\right)E_y=\frac{1}{i\omega\epsilon_0}\sum_s \bar{n}_s q_s \vec{v}_{sy} \tag{1.57}$$

$$-E_z=\frac{1}{i\omega\epsilon_0}\sum_s \bar{n}_s q_s \vec{v}_{sz} \tag{1.58}$$

with $\bar{n}_s$ representing the average density of the species s, unperturbed by the wave. This average density is taken from the current vector and is the result of assuming a constant average current. For the average density to remain constant, only waves of small amplitude can be considered. If we further assume that the perturbations caused by the wave are adiabatic, then we may use (1.15) to write

$$\vec{\nabla}p_s=k_B T_s \vec{\nabla}n_s=m_s\bar{V}_s^2\vec{\nabla}n_s \tag{1.59}$$

where the average thermal motion of the species, $\bar{V}_s$, is given by the modal velocity of the Maxwell-Boltzmann distribution:

$$V_s=\sqrt{\frac{2k_B T_s}{m_s}} \tag{1.60}$$

Substituting the equations (1.54) and (1.55) into the continuity equation, (1.25), we rewrite (1.59) as

$$\vec{\nabla}p_s=-\frac{1}{\omega}ik\bar{n}_s m_s \bar{V}_s^2 v_{sz}\vec{k} \tag{1.61}$$

and in doing so, eliminate the density fluctuations due to the wave. We now replace the pressure gradient of the momentum equation, (1.26), with the above and, with reference to (1.54) and (1.55), rewrite the components of the momentum equation as: [11]

$$i\omega\bar{n}_s m_s v_{sx}=\bar{n}_s q_s\left(E_x+v_{sy}B_z-v_{sz}B_y\right) \tag{1.62}$$

$$i\omega\bar{n}_s m_s v_{sy}=\bar{n}_s q_s\left(E_y+v_{sz}B_x-v_{sx}B_z\right) \tag{1.63}$$

$$i\omega\bar{n}_s m_s v_{sz}=\bar{n}_s q_s\left(E_z+v_{sx}B_y-v_{sy}B_x\right)+\frac{ik^2}{\omega}\bar{n}_s m_s \bar{V}_s^2 v_{sz} \tag{1.64}$$

By eliminating the current density and wave magnetic field vectors from the Maxwell equa-

tions, we have created a number of equations, containing an equal number of unknown variables, that completely describe the wave. This set comprises the momentum equations (1.62-1.64) and wave equations (1.56-1.58). For the simplest case of an electron-ion plasma, the set consists of nine equations and nine unknown variables; these are the three components of each of the vectors $\vec{E}$, $\vec{v}_e$ and $\vec{v}_i$. For a solution to exist, the determinant of this set of equations must be equal to zero. We convert these equations to matrix form in table (1.1). In the first column, the equation containing the variables of each row is listed. The top row shows the variables contained in the equations listed in the first column. If a solution to this set of equations exists, it will be unchanged by multiplying each element in a select row or column by the same factor. Such a transformation is effected by the multipliers shown in the last row and column of table (1.1); each row is multiplied by the factor in the last column, and each column by the factor in the last row. Whilst this does not change the determinant, it does change the relevant variables that correspond to each column. A transformed matrix containing the new relevant variables is shown in table (1.2), and it can be seen that the effect of the transformation is to recast the matrix in terms of the physically relevant cyclotron and plasma frequencies. For mathematical convenience, the cyclotron frequencies have been split into their components parallel and perpendicular to the magnetic field, defined by:

$$\omega_{cs,\parallel} = \frac{q_s B_\parallel}{m_s} \qquad\qquad \omega_{cs,\perp} = \frac{q_s B_\perp}{m_s} \tag{1.65}$$

Setting the determinant of table (1.2) to zero will provide a relation between the propagation constant k and the angular frequency ω, that we refer to as the *dispersion relation* [11][5]. In Appendix (A) it is shown that the determinant of table (1.2), and therefore the dispersion relation, is a fourth order equation in k^2, the four roots corresponding to four modes of dispersion that are distinct, with each root containing two conjugate solutions that represent the mode's parallel and antiparallel motion along the z axis. The modes differ in the amplitude and polarization of the associated electromagnetic fields and the motions of particles. We may include more modes by introducing more species into the system, and as adding more species will add an equal number of momentum equations, we may follow the same general procedure.

1.3.3 Simplifications

Finding the determinant of table (1.2) is not a trivial calculation. The most straightforward approach is to make simplifications that describe the desired system at appropriate limits before deriving the dispersion relations.

Equations	Variables									
	E_x	v_{ex}	v_{ix}	E_y	v_{ey}	v_{iy}	E_z	v_{ez}	v_{iz}	
(1.56)	$i\left(\frac{k^2c^2}{\omega^2}-1\right)$	$-\frac{n_e q_e}{\epsilon_0\omega}$	$-\frac{n_i q_i}{\epsilon_0\omega}$	0	0	0	0	0	0	i
(1.62)	$n_e q_e$	$-in_e m_e\omega$	0	0	$n_e q_e B_\parallel$	0	0	$-n_e q_e B_\perp$	0	$\frac{1}{n_e q_e}$
(1.62)	$n_i q_i$	0	$-in_i m_i\omega$	0	0	$n_i q_i B_\parallel$	0	0	$-n_i q_i B_\perp$	$\frac{1}{n_i q_i}$
(1.57)	0	0	0	$i\left(\frac{k^2c^2}{\omega^2}-1\right)$	$-\frac{n_e q_e}{\epsilon_0\omega}$	$-\frac{n_i q_i}{\epsilon_0\omega}$	0	0	0	-1
(1.63)	0	$n_e q_e B_\parallel$	0	$n_e q_e$	$-in_e m_e\omega$	0	0	0	0	$\frac{i}{n_e q_e}$
(1.63)	0	0	$-n_i q_i B_\parallel$	$n_i q_i$	0	$-in_i m_i\omega$	0	0	0	$\frac{i}{n_i q_i}$
(1.58)	0	0	0	0	0	0	$-i$	$\frac{n_e q_e}{\epsilon_0\omega}$	$\frac{n_i q_i}{\epsilon_0\omega}$	-1
(1.64)	0	$n_e q_e B_\perp$	0	0	0	0	$n_e q_e$	$-in_e m_e\left(\omega-\frac{k^2V_e^2}{\omega}\right)$	0	$\frac{i}{n_e q_e}$
(1.64)	0	0	$n_i q_i B_\perp$	0	0	0	$n_i q_i$	0	$-in_i m_i\left(\omega-\frac{k^2V_i^2}{\omega}\right)$	$\frac{i}{n_i q_i}$
	1	$\frac{iq_e}{m_e\omega}$	$\frac{iq_i}{m_i\omega}$	$-i$	$\frac{q_e}{m_e\omega}$	$\frac{q_i}{m_i\omega}$	$-i$	$\frac{q_e}{m_e\omega}$	$\frac{q_i}{m_i\omega}$	Multipliers

Table 1.1: The full determinant for the set of equations (1.56-1.58) and (1.62-1.64). The top column represents the unknown variables, and for simplicity the leftmost column represents the equations from which the variables are taken. This matrix is transformed into the more intuitive table (1.2) by multiplying each row and column by the variables listed in the last column and row, respectively.

Equations	Variables								
	E_x	$\frac{v_{ex}m_e\omega}{iq_e}$	$\frac{v_{ix}m_i\omega}{iq_i}$	iE_y	$\frac{v_{ey}m_e\omega}{q_e}$	$\frac{v_{iy}m_i\omega}{q_i}$	iE_z	$\frac{v_{ez}m_e\omega}{q_e}$	$\frac{v_{iz}m_i\omega}{q_i}$
(1.56)	$1-\frac{k^2c^2}{\omega^2}$	$\frac{\omega_{pe}^2}{\omega^2}$	$\frac{\omega_{pi}^2}{\omega^2}$	0	0	0	0	0	0
(1.62)	1	1	0	0	$\frac{\omega_{ce\parallel}}{\omega}$	0	0	$-\frac{\omega_{ce\perp}}{\omega}$	0
(1.62)	1	0	1	0	0	$\frac{\omega_{ci\parallel}}{\omega}$	0	0	$-\frac{\omega_{ci\parallel}}{\omega}$
(1.57)	0	0	0	$1-\frac{k^2c^2}{\omega^2}$	$\frac{\omega_{pe}^2}{\omega^2}$	$\frac{\omega_{pi}^2}{\omega^2}$	0	0	0
(1.63)	0	$\frac{\omega_{ce\parallel}}{\omega}$	0	1	1	0	0	0	0
(1.63)	0	0	$\frac{\omega_{ci\parallel}}{\omega}$	1	0	1	0	0	0
(1.58)	0	0	0	0	0	0	1	$\frac{\omega_{pe}^2}{\omega^2}$	$\frac{\omega_{pi}^2}{\omega}$
(1.64)	0	$-\frac{\omega_{ce\perp}}{\omega}$	0	0	0	0	1	$1-\frac{k^2\bar{V}_e^2}{\omega^2}$	0
(1.64)	0	0	$-\frac{\omega_{ci\perp}}{\omega}$	0	0	0	1	0	$1-\frac{k^2\bar{V}_i^2}{\omega^2}$

Table 1.2: Reduced form of table (1.1) for the set of nine linear homogeneous equations, the determinant of which gives the dispersion relation. The equations from which the variables are taken are listed in the first column. The top row lists the transformed versions of the physical variables taken from the listed equations. The cyclotron resonances have been defined according to equation (1.65).

1.3.3.1 No Magnetic Field, B = 0

In the case where the magnetic field is zero, table (1.2) reduces to the pseudo-diagonal matrix: [11]

Δ_l			0	0	0	0	0	0
			0	0	0	0	0	0
			0	0	0	0	0	0
0	0	0	Δ_l			0	0	0
0	0	0				0	0	0
0	0	0				0	0	0
0	0	0	0	0	0	Δ_L		
0	0	0	0	0	0			
0	0	0	0	0	0			

Hence, the determinant:

$$\Delta_l^2 \Delta_L = 0 \tag{1.66}$$

is a product of three factors, of which the first two are identical. If ω and k are such that $\Delta_l = 0$, we find that there are two solutions; one for which only E_x, v_{ix} and v_{ex} are nonzero; and a similar wave for which only E_y, v_{iy} and v_{ey} are nonzero. Both of these waves are independent of Δ_L, and therefore are transverse. Setting $\Delta_l = 0$ we find that the form of these solutions satisfy

$$\omega^2 = k^2 c^2 + \omega_{pi}^2 + \omega_{pe}^2 \approx k^2 c^2 + \omega_{pe}^2 \tag{1.67}$$

which describes a light wave dispersing through a medium of oscillating electrons and ions. The movement of the ions can usually be ignored as compared to the electrons, due to their greater inertia. We also recover the nondispersive plasma waves first described by equation (1.4).

Alternatively, in the case that $\Delta_L = 0$ we obtain a solution in which the only nonzero variables are E_z, v_{ez} and v_{iz}. This means the wave is polarized parallel to the z-axis, that is; purely longitudinal. The determinant is quadratic in k^2, and there are therefore two longitudinal modes.

1.3.3.2 Longitudinal Waves, $\mathbf{B}_\perp = 0$

Considering initially only waves propagating along the field, with a zero transverse magnetic field, $B_\perp$, the dispersion relation is obtained by setting the determinant of the last three rows and columns of table (1.2), Δ_L, to zero. It is immediately apparent that the longitudinal waves are affected by the thermal motion of the particles. Rather than computing the determinant directly, we first calculate the quantity $\frac{v_{iz}}{v_{ez}}$. Looking to table (1.2), we note that the variables associated with the last two columns contain these variables. For a set of homogeneous linear equations expressed in matrix form, the ratio of any two variables is equivalent to the ratio of the minors associated with the corresponding elements of any row. Applying this rule to the three rows of the reduced determinant, Δ_L, we show: [11]

$$-\frac{m_i v_{iz}}{m_e v_{ez}} = -\frac{k^2 V_e^2 - \omega^2}{k^2 V_i^2 - \omega^2} = \frac{\omega_{pe}^2}{k^2 V_i^2 - \omega^2 + \omega_{pi}^2} = \frac{k^2 V_e^2 - \omega^2 + \omega_{pe}^2}{\omega_{pi}^2} \tag{1.68}$$

Where the negative sign originates from the quotient of the electron and ion charges. This relation can be used to form the dispersion relation, by noting:

$$\left(k^2 V_e^2 - \omega^2 + \omega_{pe}^2\right)\left(k^2 V_i^2 - \omega^2 + \omega_{pi}^2\right) - \omega_{pe}^2 \omega_{pi}^2 = 0 \tag{1.69}$$

Expanding, we find:

$$\left(V_e^2 V_i^2\right) k^4 + \left[\omega_{pe}^2 V_i^2 + \omega_{pi}^2 V_e^2 - \omega^2\left(V_e^2 + V_i^2\right)\right] k^2 + \omega^2\left(\omega^2 - \omega_{pe}^2 - \omega_{pi}^2\right) = 0 \tag{1.70}$$

In the absence of thermal motion $V_e = V_i = 0$, and equation (1.70) reduces to $\omega^2 = \left(\omega_{pe}^2 + \omega_{pi}^2\right)$, which corresponds to longitudinal plasma oscillations when both the ion and electron behaviours are accounted for. The neglect of the thermal velocities is akin to taking the *cold plasma limit* for obvious reasons. The names for the two general roots of equation (1.70) are the *longitudinal electron* and *longitudinal ion* waves [5]. These waves do not depend on the magnetic field and are in fact the two missing modes of the previous section. Rather than computing these roots directly, it is easier to first make simplifications about the plasma environment before solving the equation. For example, in the case of static ions and mobile electrons, we find that equation (1.70) becomes: [11]

$$\omega^2 = \omega_{pe}^2 + V_e^2 k^2 \tag{1.71}$$

which is the dispersion relation for a *Langmuir wave*. Taking $V_e^2 = \gamma k_B T_e / m_e$, and

$$\gamma = 1 + \frac{2}{f} \tag{1.72}$$

where f is the amount of degrees of freedom of the system. Since longitudinal plane waves are compressional in one dimension only, $f = 1$, and $\gamma = 3$. Substituting into (1.71):

$$\omega^2 = \omega_{pe}^2 + \left(\frac{3k_B T_e}{m_e}\right) k^2 \tag{1.73}$$

This relation is the *Bohm-Gross* dispersion relation for the longitudinal electron wave [5]. At high frequencies, $\omega >> \omega_{pe}$, it becomes an *electron acoustic wave*[5]:

$$\omega = kV_e \tag{1.74}$$

But we may also modify equation (1.70) for high frequencies. From equation (1.46) we have:

$$\omega_{pe}^2 V_i^2 = \frac{T_i}{T_e} \omega_{pi}^2 V_e^2 \tag{1.75}$$

Taking the high frequency limit such that $\omega^2 >> \omega_{pi}^2 \left(1 + \frac{T_i}{T_e}\right)$, we derive from equation (1.70), with inclusion of both ion and electron motion;

$$V_e^2 V_i^2 k^4 - \omega^2 \left(V_e^2 + V_i^2\right) k^2 + \omega^2 \left(\omega^2 - \omega_{pe}^2 - \omega_{pi}^2\right) = 0 \tag{1.76}$$

Furthermore, we may take $V_e^2 \omega^2 >> V_i^2 (\omega_{pe}^2 + \omega_{pi}^2)$, which is a condition equivalent to $\omega^2 >> \omega_{pi}^2 \left(\frac{T_i}{T_e}\right)\left(1 + \frac{m_e}{m_i}\right)$, and satisfies $\omega^2 >> \omega_{pi}^2 \left(1 + \frac{T_i}{T_e}\right)$. Doing so, and adding the term $V_i \left(\omega_{pe}^2 + \omega_{pi}^2\right) k^2$ to the left hand side of (1.76), we rearrange to the approximate form:

$$\left(V_i^2 k^2 - \omega^2\right)\left(V_e^2 k^2 - \omega + \omega_{pe}^2 + \omega_{pi}^2\right) = 0 \tag{1.77}$$

From this, we may determine the longitudinal *ion plasma wave* dispersion relation for the high frequency limit:

$$\omega = V_i k \tag{1.78}$$

and that of the electron plasma wave:

$$\omega^2 = \omega_{pe}^2 + \omega_{pi}^2 + V_e^2 k^2 \tag{1.79}$$

At low frequencies, such that $\omega^2 << \omega_{pi}^2 \left(1 + \frac{T_i}{T_e}\right)$, equation (1.70) becomes:

$$V_e^2 V_i^2 k^4 + V_e^2 \omega_{pi}^2 \left(1 + \frac{Ti}{T_e}\right) k^2 - \omega^2 \omega_{pe}^2 = 0 \tag{1.80}$$

Multiplying by $\frac{-\omega^2}{(\omega_{pe}^2 k^4)}$, assuming $k \neq 0$, we rewrite as:

$$\left(\frac{\omega^4}{k^4}\right) - V_e^2 \left(\frac{\omega_{pi}^2}{\omega_{pe}^2}\right)\left(1 + \frac{T_i}{T_e}\right)\left(\frac{\omega^2}{k^2}\right) - V_e^2 V_i^2 \left(\frac{\omega^2}{\omega_{pe}^2}\right) = 0 \tag{1.81}$$

We are considering low frequencies, and as long as $\frac{\omega}{k}$ is not much greater than V_i, we may ignore the last term of equation (1.81) as compared to the second. Hence, in the low frequency limit, equation (1.81) becomes:

$$\frac{\omega^2}{k^2} = V_e^2 \left(\frac{\omega_{pi}^2}{\omega_{pe}^2}\right)\left(1 + \frac{T_i}{T_e}\right) \tag{1.82}$$

Or

$$\omega^2 = V_c^2 k^2 \tag{1.83}$$

where

$$V_c^2 = V_i^2 + V_e^2 \approx \frac{\gamma k_B T_e}{m_i} \tag{1.84}$$

is the *plasma* or *ion sound speed*. The remaining root of equation (1.80) gives an evanescent solution at low frequencies. The longitudinal waves which travel at a phase velocity of V_e and V_i represent acoustic oscillations due to the electrons and ions respectively. At lower frequencies, the wave travels at the sound speed, V_c and is usually referred to as the *ion acoustic wave* [5]. These waves are shown in figure (1.3).

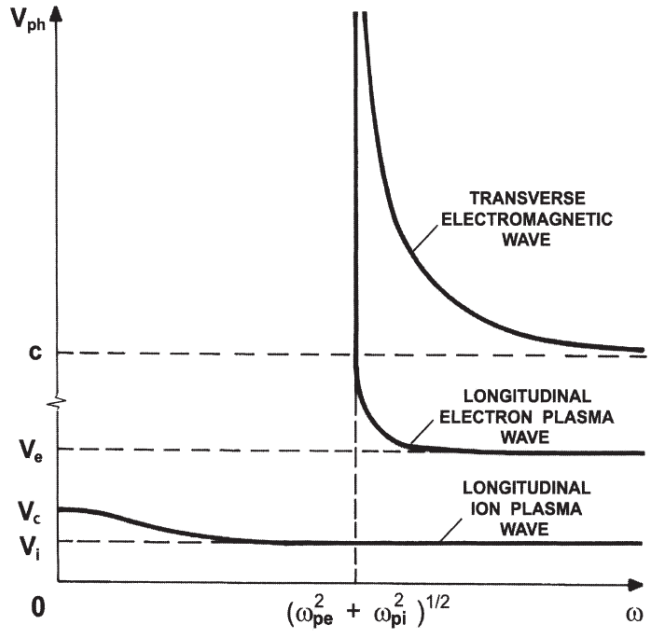

Figure 1.3: Phase velocity dependence on frequency for waves in an isotropic warm plasma. (From [5])

1.3.3.3 Transverse Waves, $\mathbf{B}_\perp = \mathbf{0}$

We now turn our attention now to the transverse modes, limiting our treatment again to waves propagating exclusively along the field, with zero transverse field. We may determine these transverse modes by computing the determinant for the first six rows and columns of table (1.2), as the remaining rows and columns describe motion along the axis of travel; the z axis. Table (1.2) becomes:

Δ_l			0	0	0	0	0	0
			0	$\frac{-\omega_{ce\parallel}}{\omega}$	0	0	0	0
			0	0	$\frac{\omega_{ci\parallel}}{\omega}$	0	0	0
0	0	0	Δ_l			0	0	0
0	$\frac{-\omega_{ce\parallel}}{\omega}$	0				0	0	0
0	0	$\frac{\omega_{ci\parallel}}{\omega}$				0	0	0
0	0	0	0	0	0	Δ_L		
0	0	0	0	0	0			
0	0	0	0	0	0			

Its is immediately obvious that the longitudinal waves are unaltered by the presence of a longitudinal field, justifying our earlier ansantz. The magnetic field has introduced a coupling between the two transverse waves found in section (1.3.3.1). The result is two distinct

waves which both have E_x, v_{ix}, v_{ex} and E_y, v_{iy}, v_{ey} components [11]. It can be seen directly that thermal motion plays no role in the properties of these transverse waves. The expansion of the determinant is, as with the longitudinal modes, not strictly necessary. For the present discussion it will suffice to eliminate the components of $\vec{v}_e$ and $\vec{v}_i$ from equations (1.56), (1.57), (1.62) and(1.63). Taking $E_z = v_{iz} = v_{ez} = 0$, we obtain:

$$v_{ex}\left(\omega_{ce\|} - \omega^2\right) = \frac{q_e}{m_e}\left(i\omega E_x - \omega_{ce\|} E_y\right) \tag{1.85}$$

$$v_{ey}\left(\omega_{ce\|} - \omega^2\right) = \frac{q_e}{m_e}\left(i\omega E_y - \omega_{ce\|} E_x\right) \tag{1.86}$$

$$v_{ix}\left(\omega_{ci\|} - \omega^2\right) = \frac{q_i}{m_i}\left(i\omega E_x - \omega_{ce\|} E_y\right) \tag{1.87}$$

$$v_{iy}\left(\omega_{ci\|} - \omega^2\right) = \frac{q_i}{m_i}\left(i\omega E_y - \omega_{ce\|} E_x\right) \tag{1.88}$$

Eliminating the components of velocity from the above expressions and equations (1.56) (1.57), we may determine the ratio:

$$\frac{E_y}{E_x} = -\frac{\frac{\omega_{pe}^2\omega_{ce\|}}{\omega^2-\omega_{ce\|}^2} - \frac{\omega_{pi}^2\omega_{ci\|}}{\omega^2-\omega_{ci\|}^2}}{i\omega\left[\frac{k^2c^2}{\omega^2} - 1 + \frac{\omega_{pe}^2}{\omega^2-\omega_{ce\|}^2} + \frac{\omega_{pi}^2}{\omega^2-\omega_{ci\|}^2}\right]} = \frac{i\omega\left[\frac{k^2c^2}{\omega^2} - 1 + \frac{\omega_{pe}^2}{\omega^2-\omega_{ce\|}^2} + \frac{\omega_{pi}^2}{\omega^2-\omega_{ci\|}^2}\right]}{\frac{\omega_{pe}\omega_{ce\|}}{\omega^2-\omega_{ce\|}^2} - \frac{\omega_{pi}\omega_{ci\|}}{\omega^2-\omega_{ci\|}^2}} \tag{1.89}$$

From which we obtain the compatibility condition:

$$\omega\left(\frac{k^2c^2}{\omega^2} - 1 + \frac{\omega_{pe}^2}{\omega^2-\omega_{ce\|}^2} + \frac{\omega_{pi}^2}{\omega^2-\omega_{ci\|}^2}\right) = \pm\left(\frac{\omega_{pe}^2\omega_{ce\|}}{\omega^2-\omega_{ce\|}^2} - \frac{\omega_{pi}^2\omega_{ci\|}}{\omega^2-\omega_{ci\|}^2}\right) \tag{1.90}$$

Equation (1.90) is the dispersion relation for transverse waves. The two solutions of (1.90) are:

$$\frac{k^2c^2}{\omega^2} = 1 + \left[\frac{\omega_{pe}^2 + \omega_{pi}^2}{\left(\omega + \omega_{ce\|}\right)\left(\omega - \omega_{ci\|}\right)}\right] \tag{1.91}$$

$$\frac{k^2c^2}{\omega^2} = 1 + \left[\frac{\omega_{pe}^2 + \omega_{pi}^2}{\left(\omega - \omega_{ce\|}\right)\left(\omega + \omega_{ci\|}\right)}\right] \tag{1.92}$$

It is common usage to refer to these solutions as the *ion cyclotron* and the *electron cyclotron* modes, respectively [5]. Electron cyclotron waves are produced naturally in light-

ning, and disperse as they propagate through the atmosphere; the higher frequencies propagating faster than the lower. This results in a distinctive glissando sound when detected, earning them the nickname *whistlers*. Substituting the above solutions into equation (1.90), we obtain:

$$\frac{E_y}{E_x} = +i \quad \text{for the ion cyclotron wave} \tag{1.93}$$

$$\frac{E_y}{E_x} = -i \quad \text{for the electron cyclotron wave} \tag{1.94}$$

The time dependence of $\vec{E}$ is of the form $\exp(-i\omega t)$. If we take $E_x \propto \cos(\omega t)$, then for the electron cyclotron wave, $E_y \propto \sin(\omega t)$, and for the ion cyclotron, $E_y \propto -\sin(\omega t)$. An observer looking at the outgoing wave (along the positive z-direction) will see a clockwise rotation of $\vec{E}_\perp$ for the electron cyclotron wave, and a counterclockwise rotation for the ion cyclotron. Thus, the two waves are circularly polarized in opposite handedness. The electric vector of the ion and electron waves rotate in the same sense as the ion and electron gyromotions, respectively. These waves are therefore strongly perturbed by particle motion at the cyclotron frequencies, equation (1.4), where the wavevector and index of refraction approach infinity. This phenomenon is known as *resonance*, and is shown in figure 1.4 [5]. By taking the limit $\omega \to 0$ in equations 1.92 and 1.91, we find the limit on the index of refraction for parallel propagation:

$$n^2 = 1 + \left[\frac{\omega_{pe}^2 + \omega_{pi}^2}{\left(\omega_{ce\parallel}\right)\left(\omega_{ci\parallel}\right)} \right] = 1 + \frac{\epsilon_0 \sum_s n_s m_s}{B^2} \tag{1.95}$$

Hence, there should be some similar limit on the phase velocity. That velocity is defined:

$$v = \frac{c}{n} = \frac{c}{\sqrt{1 + \frac{\epsilon_0 \sum_s n_s m_s}{B^2}}} = \frac{v_A}{\sqrt{1 + \frac{v_A^2}{c^2}}} \tag{1.96}$$

Let this limit be v_A, the *Alfvén velocity*, defined:

$$v_A = \sqrt{\frac{c^2}{n^2}} = \frac{B}{\sqrt{\mu_0 \rho}} \tag{1.97}$$

where $\rho = \sum_s n_s m_s$. The electron contribution is often neglected. A wave travelling at this Alfvén speed will obey

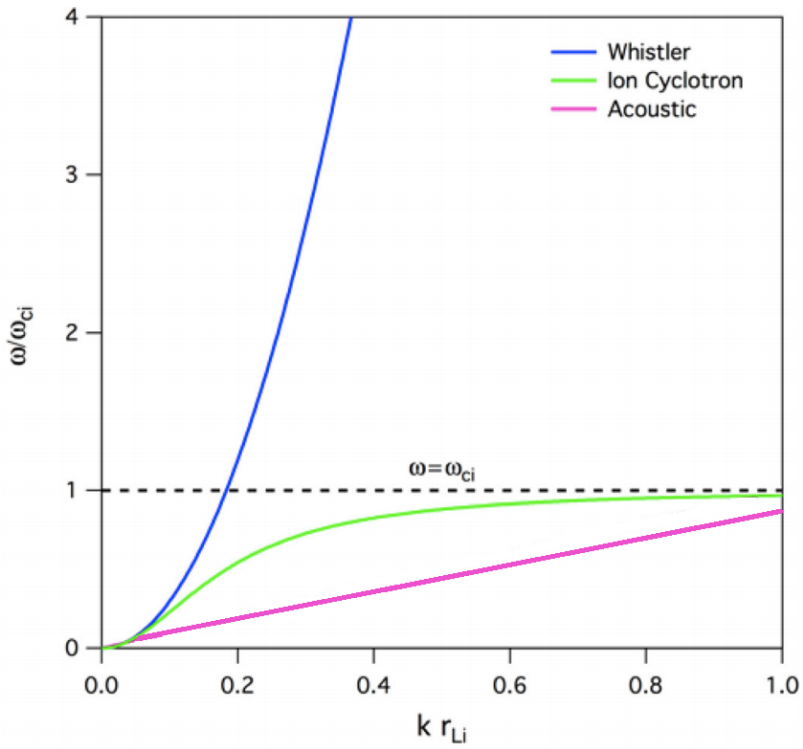

Figure 1.4: Parallel propagation dispersion relation for a two-fluid plasma model. The ion cyclotron mode, green, resonates at the ion cyclotron frequency. Similarly, the whistler mode, blue, has an asymptote at the electron cyclotron frequency (not pictured). 'Whistler' refers to the right-hand cicrcularly polarized wave described in equation (1.92). The acoustic wave is that described by equation 1.83 and does not resonate at $\omega = \omega_{ci}$. Here, r_{Li} is the Larmor radius. (From [14])

$$\omega = k v_A \tag{1.98}$$

and physically represents a particle oscillation in response to a restoring force caused by an effective tension of the magnetic field lines. This wave and waves similar to it will be addressed in more detail in section(1.3.4.1).

1.3.4 The General Dispersion Relation

In the previous two sections, we limited the treatment to waves propagating parallel to the magnetic field lines. We now derive the general dispersion relation for an arbitrary field direction. The process of deriving these modes involves finding the general determinant of table 1.2 and taking appropriate limits and simplifications afterwards. This calculation is complex and, for the sake of brevity, is performed fully in appendix (B) with only the

general argument reproduced in this section. The general dispersion relation is discussed for the sake of the magnetohydrodynamic waves. Whilst these waves can be calculated in simpler fashions; by the differentiation of the equation of momentum for a fluid element of the plasma, for example; it is more consistent to stay in keeping with the discussion thus far, and derive these waves using table (1.2) [11].

1.3.4.1 Magnetohydrodynamic Waves

We are now in a position to solve for the general dispersion relation by taking the full determinant of table (1.2). The procedure is outlined in appendix (B); the general argument involves expanding table (1.2) with respect to the powers of $\omega_{ci\perp}$ and $\omega_{ce\perp}$. Applying the computation rules for determinants, we may write the general dispersion relation in the form:

$$\Delta_T \Delta_L + B + C + D + E = 0 \tag{1.99}$$

where

$$\Delta_T = \Delta_l^2 + \frac{\omega_{ce\parallel}^2 \omega_{ci\parallel}^2}{\omega^4}(y-1)^2 - \frac{\omega_{ce\parallel}^2}{\omega^2}\left(y-1+\frac{\omega_{pi}^2}{\omega^2}\right)^2 - \frac{\omega_{ci\parallel}^2}{\omega^2}\left(y-1+\frac{\omega_{pe}^2}{\omega^2}\right)^2 + \frac{2\omega_{ci\parallel}\omega_{ce\parallel}\omega_{pe}^2\omega_{pi}^2}{\omega^6} \tag{1.100}$$

$$\Delta_L = \left(1-\frac{y}{\epsilon_e}\right)\left(1-\frac{y}{\epsilon_i}\right) - x\left(1-\frac{y}{\epsilon_s}\right) \tag{1.101}$$

$$B = \frac{\omega_{ce\perp}^2}{\omega^2}\left(\frac{y}{\epsilon_i} - 1 + \frac{\omega_{pi}^2}{\omega^2}\right)\left[\Delta_1\left(y-1+\frac{\omega_{pi}^2}{\omega^2}\right) - \frac{\omega_{ci\parallel}^2}{\omega^2}(y-1)\left(y-1+\frac{\omega_{pe}^2}{\omega^2}\right)\right] \tag{1.102}$$

$$C = \frac{\omega_{ci\perp}^2}{\omega^2}\left(\frac{y}{\epsilon_e} - 1 + \frac{\omega_{pe}^2}{\omega^2}\right)\left[\Delta_1\left(y-1+\frac{\omega_{pe}^2}{\omega^2}\right) - \frac{\omega_{ce\parallel}^2}{\omega^2}(y-1)\left(y-1+\frac{\omega_{pi}^2}{\omega^2}\right)\right] \tag{1.103}$$

$$D = \frac{2\,\omega_{ci\perp}\omega_{ce\perp}\omega_{pe}^2\omega_{pi}^2}{\omega^6}\left[-\Delta_1 + (y-1)\frac{\omega_{ci\parallel}\omega_{ce\parallel}}{\omega^2}\right] \tag{1.104}$$

$$E = \frac{\omega_{ci\perp}^2\omega_{ce\perp}^2}{\omega}(y-1)\Delta_1 \tag{1.105}$$

$$\Delta_1 = y - 1 + x \tag{1.106}$$

$$y = \frac{k^2 c^2}{\omega^2} \qquad x = \frac{\omega_{pe}^2 + \omega_{pi}^2}{\omega^2} \tag{1.107}$$

$$\epsilon_{i,e,s} = \frac{c^2}{V_{i,e,s}^2} \tag{1.108}$$

and Δ_l is as defined in section (1.3.3.1). We now define $u = y - 1$ to rewrite the above expressions in powers of $\frac{1}{\omega}$, that is, as a polynomial in x. The solution of equation (1.99) is discussed in appendix (B) and will not be reproduced here. The three low-frequency ($(\omega << \omega_{ce})$) solutions correspond to waves with dispersion relations [11]:

$$\left(k^2 c^2/\omega^2\right)_2 = \epsilon_A (1+s) \tag{1.109}$$

$$\left(k^2 c^2/\omega^2\right)_{1,3} = \frac{1}{2}\left\{(\epsilon_A + \epsilon_s - 1)(1+s) + 1 \pm \left[(\epsilon_A + \epsilon_s - 1)^2 - 4(\epsilon_A - 1)(\epsilon_s - 1)(1+s)\right]^{\frac{1}{2}}\right\} \tag{1.110}$$

where

$$\epsilon_A = \frac{c^2}{V_A^2} = (1 + A) = 1 + \frac{\omega_{pe}^2 + \omega_{pi}^2}{\omega_{ci}\omega_{ce}} \tag{1.111}$$

$$s = \tan^2\theta \tag{1.112}$$

and the + of equation (1.110) corresponds to $\left(k^2 c^2/\omega^2\right)_1$, the − to $\left(k^2 c^2/\omega^2\right)_3$, and θ is the angle between the magnetic field and the direction of propagation. The velocities are then:

$$V_2^2 = V_A^2 \cos^2\theta \tag{1.113}$$

$$\begin{aligned} V_1^2, V_3^2 &= \frac{1}{2}\left[V_A^2 + V_s^2 - \epsilon_0 \mu_0 V_A^2 V_s^2 \sin^2\theta\right] \\ &\pm \frac{1}{2}\left[\left\{\left[V_A^2 + V_s^2 - \epsilon_0\mu_0 V_A^2 V_s^2\left(1 + \cos^2\right)\right]^2 - 4V_A^2 V_s^2\left(1 - \frac{V_A^2}{c^2}\right)\left(1 - \frac{V_s^2}{c^2}\right)\cos^2\theta\right\}\right] \end{aligned} \tag{1.114}$$

Where the + sign now corresponds to V_3, and the − to V_1. Hence;

$$V_1 \leq V_2 \leq V_3 \tag{1.115}$$

We can distinguish $\left(k^2c^2/\omega^2\right)_2$ from the others by its speed, V_2, which is intermediate between the other two solutions, independent of ϵ_s, and hence is independent of the thermal motion of the medium. This is the *shear Alfvén wave*, the general form of the transverse wave from section (1.3.3.2), equation (1.98). It propagates with lowest impedance along the field line, which is how it was derived earlier. This wave is independent of the plasma pressure and temperature, and is purely a perturbation of the magnetic field. It will therefore satisfy the linearized MHD Ohm's law, equation (1.34): $\vec{E} + \vec{u} \times \vec{B} = 0$. We already know that the shear Alfvén wave is a transverse wave, and therefore has some transverse component only to its velocity perturbation , $\vec{u} = \left(u_x, u_y, 0\right)$. Hence, for a field along the z axis, Ohm's law gives us [11]:

$$E_x = -u_y B_z \quad E_y = u_x B_z \quad E_z = 0 \tag{1.116}$$

Thus, this wave is linearly polarized. We may use the momentum equations, (1.62)-(1.64) to show:

$$u_x = 0 \quad u_y = -\frac{E_x}{B_z} \quad u_z = 0 \tag{1.117}$$

Taking the velocity divergence:

$$\vec{\nabla} \cdot \vec{u} = i\vec{k} \cdot \vec{u} = ik u_x \sin\theta = 0 \tag{1.118}$$

and hence there is zero-divergence of the flow. Physically then, the shear Alfvén wave represents a torsional wave created by the resistance of the magnetic field itself since the dispersion is independent of the plasma pressure. The wave resembles a perturbation of the field line travelling in the direction of the field, depicted in figure (1.5).

The other two solutions, $\left(k^2c^2/\omega^2\right)_1$ and $\left(k^2c^2/\omega^2\right)_3$, are the two *magnetoacoustic* or *magnetosonic waves*. These waves are associated with non-zero perturbations in the plasma density and pressure. The wave $\left(k^2c^2/\omega^2\right)_1$ represents the slow magnetoacoustic mode, as it travels at a lower velocity than that of $\left(k^2c^2/\omega^2\right)_3$; the fast wave. In the low temperature limit, $V_s \to 0$, the slow wave ceases to exist. The fast wave will tend to the dispersion relation:

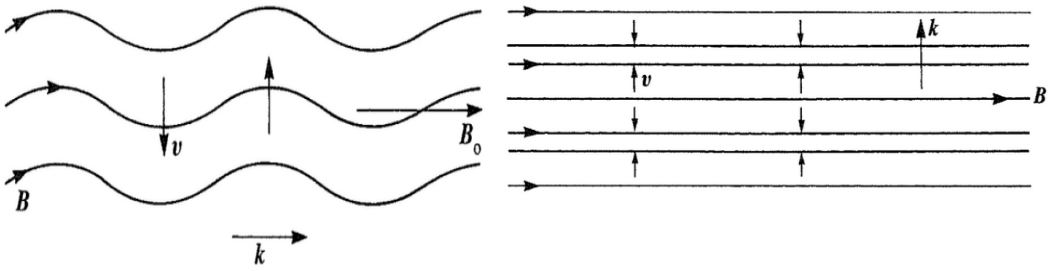

Figure 1.5: Left, the shear Alfvén mode, expressed as a torsional perturbation of $\vec{B}$, propagating along the field line. Right, the compressional Alfvén mode, a perturbation of the magnetic flux density perpendicular to the field direction. (From [15])

$$\omega = kV_A \tag{1.119}$$

which is the dispersion relation for the *compressional Alfvén wave*, and can be compared to equation (1.98) and (1.113). The difference with equation (1.119) however, is that it is arbitrarily oriented with respect to the magnetic field. In this limit, the dispersion is independent of the plasma temperature, and so the perturbations in pressure and density are due entirely to the magnetic field. In a similar way to the shear wave, we can show for equation (1.119):

$$u_x = \frac{E_y}{B_z} \quad u_y = 0 \quad u_z = 0 \tag{1.120}$$

The flow divergence, equation (1.118), is therefore non-zero. Equation (1.120) holds for both the ions and electrons, and so this wave is associated with a bulk motion of the entire fluid mass along the x axis; perpendicular to the magnetic field. This wave is a propagation of a fluid element orthogonal to the magnetic field, and is therefore a perturbation in the magnetic flux density. This coupling of the fluid element and the magnetic flux density is congruent with our treatment of Alfvén's theorem, in section (1.2.6), and is shown in figure (1.5).

1.3.5 Instabilities

Any net forces that exist in a plasma otherwise at equilibrium will grow, oscillate, or be damped out. An *instability* is an infinitesimal perturbation that produces a force that grows or oscillates, ie; that has a positive *growth rate*. Instabilities can be classified as macroinstabilities; those instabilities that are driven by inhomogeneity in coordinate space,

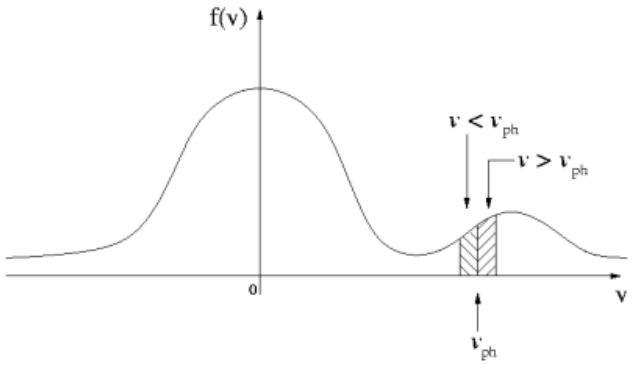

Figure 1.6: The Maxwellian distribution function, showing the difference in distribution density between two points either side of a phase velocity, v_{ph}. The "bump" on the "tail" of the Maxwellian, which can lead to instabilities of positive growth rate, is also shown

and microinstabilities; driven by a velocity-space anisotropy in the plasma. Macroinstabilities are describable with fluid and kinetic approximations. Microinstabilities are not derivable from the standard MHD equations and may occur from non-Maxwellian velocity distributions [16]. Instabilities can also be classified according to their free energy source:

- Rayleigh-Taylor macroinstabilities due to density gradients associated forces other than those of electromagnetism, eg; gravity.
- Gradient driven microinstabilities caused by thermodynamic forces due to gradients in plasmas that are otherwise described by Maxwellian distributions.
- Kinetic microinstabilities caused by deviations from the Maxwellian distribution function.
- Streaming microinstabilities produced by energetic particles interacting with the plasma.

The main mechanism through which kinetic instabilities are suppressed is via *Landau damping*. Landau damping is a wave-particle energy interaction that acts between a wave of phase speed v_{ph} and particles moving in the plasma with velocities close to v_{ph}. According to Jean's theorem, for a collisionless plasma the distribution function is Maxwellian, as shown in figure (1.6). A wave produced by an instability will absorb or transfer energy to local particle populations close to the phase speed of the wave, depending on the velocity of the particles. A positive gradient in the distribution function means there are more particles faster than the phase speed than slower, and the wave will absorb energy from the particles. Inversely, the wave is damped if slower particle populations in the neighbourhood of the phase speed of the wave are more numerous; if the gradient is negative. In the two-stream instability, the Maxwellian distribution is modified by a smaller maximum

Name	Frequencies, center of mass polariztion	Parameter regimes	Other names
Ion/ion right-hand resonant	$\omega_r \ll \Omega_p$, *right-hand*	$v_A \lesssim v_0$ and very small n_b/n_e	'magnetosonic' 'fast MHD' B&T:RFxS
Ion/ion nonresonant	$\omega_r \simeq 0$, varies	$v_A \ll v_0$ or modest n_b/n_e	'firehose' B&T:LFNR
Ion/ion left-hand resonant	$\omega_r \ll \Omega_p$, *left-hand*	Warm or hot beam and $v_A \lesssim v_0$	'Alfvén'
Ion cyclotron anisotropy	$\omega_r < \Omega_p$, left-hand	$T_{\parallel b} < T_{\perp b}$	B&T:LFxS and LBxS
Electron/ion whistler	$\Omega_p < \omega_r$, right-hand	$v_A \ll v_0$	B&T:RFxH

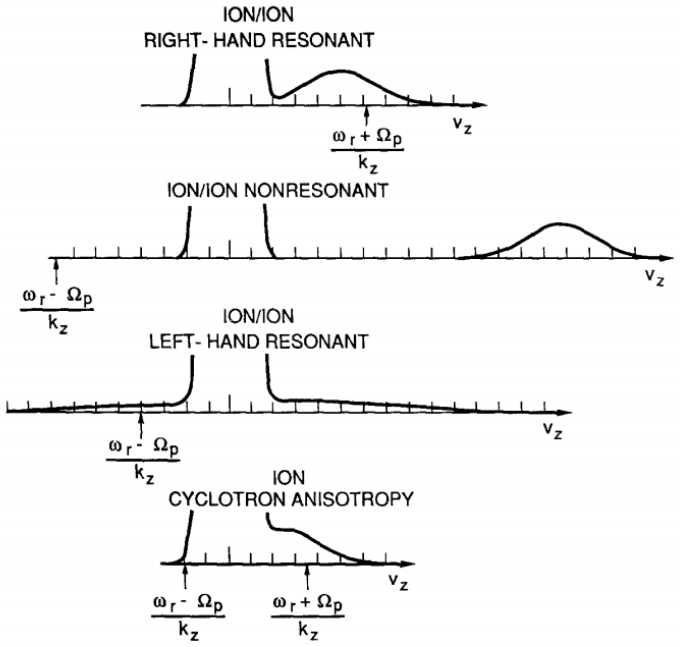

Figure 1.7: Top: table showing five examples of parallel beam instabilities and their associated parameter regimes. Bottom: reduced ion particle distributions associated with four of the instabilities of the top table, and their associated proton cyclotron resonant speeds, showing that the nature of the distribution function determines the quickest growing unstable modes. (From [17])

at some velocity separate from the Maxwellian mode velocity; the so called "bump" on the "tail" of the Maxwellian. Gary [17] derived linear dispersion relations for a variety of plasma parameters for a plasma consisting of a Maxwellian electron population, and two Maxwellian proton distributions; the core and beam protons. Figure (1.7) shows properties of several types of instabilities with maximum growth rates parallel to the magnetic field for some of these parameters. The associated ion distribution functions and the corresponding cyclotron resonant speeds for four of these instabilities are shown in figure (1.7). In these figures, Ω is the gyrofrequency, ω is the plasma frequency, T represents temperature, v_0 the parallel drift velocity and the subscripts b, e and r refer to electrons, the beam, and resonant modes; those modes that satisfy Landau or cyclotron resonance.

1.4 Space Plasma Physics

Space plasmas provide a natural environment in which to study large-scale and high-energy plasma dynamics. Plasmas are abundant in the universe and the solar system, and the subject therefore models phenomena of a diverse range of physical characteristics. Figure (1.8) shows typical values of the usual attributes of different geophysical plasmas. The more specific field of space weather is the study of the changing conditions in the space plasma physics in near-Earth space and the wider solar system [15].

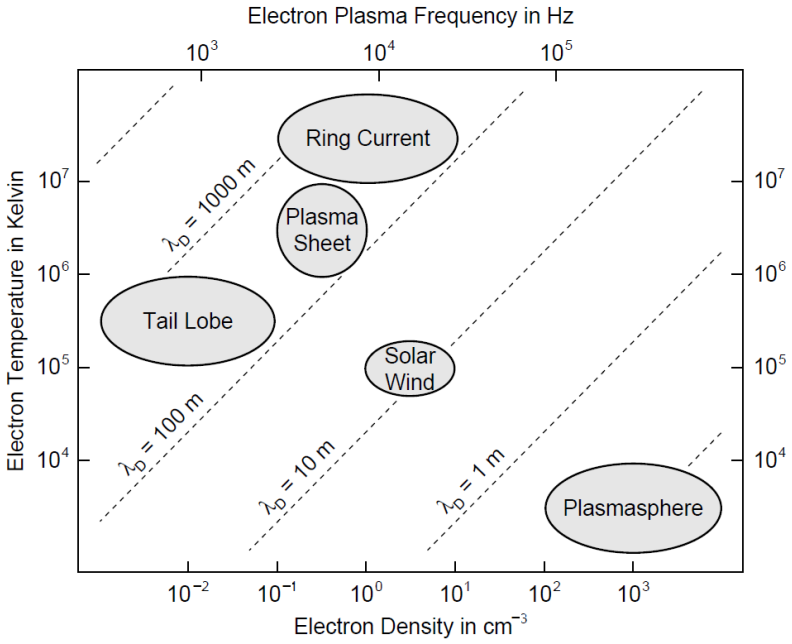

Figure 1.8: Typical geophysical phenomena arranged by plasma parameters. (From [15])

1.4.1 The Solar Wind

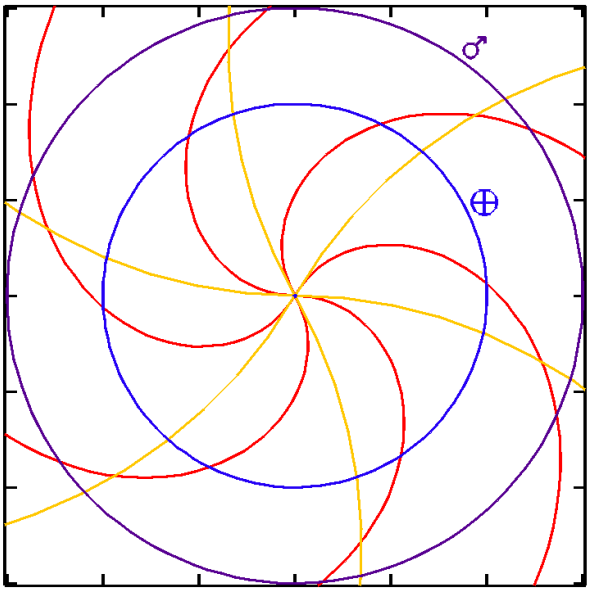

Figure 1.9: The Parker spiral. The Sun is at the centre of the spiral and rotates anticlockwise. The red lines represent a solar wind flow speed of 400 kms^{-1}, and the yellow 2000 kms^{-1}. The orbits of Mercury and Venus are represented with their astrological symbols.

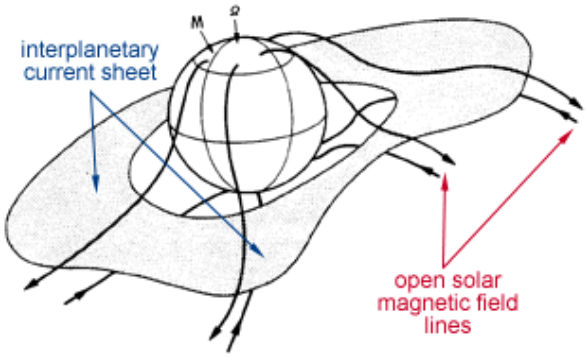

Figure 1.10: The solar magnetic field, the origin of the IMF, and the interplanetary current sheet. The field lines are closed in opposite hemispheres of the Sun. (From [18])

The solar wind is a super-sonic and super-Alfvénic radial stream of plasma continuously ejected by the Sun [15]. Heating in the solar corona causes supersonic expansion, heating electrons and ions to sufficiently large energies that they are able to escape the solar gravitational pull and expand into interplanetary space [20]. The solar wind travels at an average speed of 500kms^{-1}, but measurements at 1AU are generally of two types, slow (300-500 kms^{-1}) and fast (600-800 kms^{-1})[21][22]. The radial expansion of the solar wind

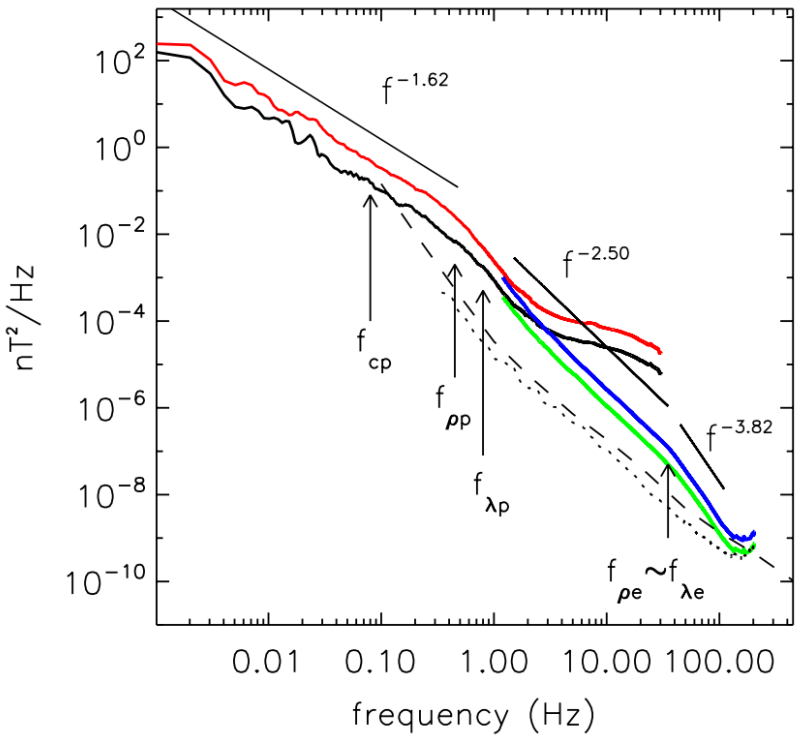

Figure 1.11: Solar wind power spectrum, taken from FGM data on Cluster for parallel (black) and perpendicular (red) and STAFF parallel (green) and perpendicular (blue) data, for 19/03/2006 20:30-23:30, showing power law dependence on scale. The proton gyrofrequency is f_{cp}, and frequencies of the inertial length $\lambda = v_A/\omega_{ci}$ and thermal gyroscale $\rho = V_s/\omega_{ci}$ are also included. (From [19])

means that the density decreases as the square of the distance from the Sun[23][24]. Typical plasma parameters for the solar wind at 1AU are $n \approx 5\text{cm}^{-1}$, $T_e \approx 10^5$K, $T_i \approx 10^4$K. The solar wind plasma is highly conductive, and so carries part of the coronal magnetic field "frozen" into it according to Alfvén's theorem (section 1.2.6). This field is drawn outwards into the solar system and forms the *interplanetary magnetic field*, or IMF. The IMF magnitude at 1 AU varies between (3-15)nT [25]. The radial expansion of the solar wind and the Sun's own rotation cause the IMF to travel in an Archimedean spiral pattern, termed the Parker spiral, often likened to a rotating sprinkler. The overall bulk velocity of the solar wind, however, is directed radially outwards from the Sun, figure (1.9). The polarity of the magnetic field is reversed in the Sun's northern hemisphere relative to the southern, resulting in the formation of large closed loops in the IMF that extend into space, as shown in figure (1.10). This juxtaposition of the IMF polarities creates a thin current sheet, the *interplanetary current sheet*, along the plane of the Sun's equator, which is tilted due to the offset between the Sun's rotational and magnetic axes, and warped due to the quadrupole moment of the Sun's magnetic field [26]. The Earth therefore experiences alternating periods of positive and negative IMF polarity known as *magnetic sectors* [26][15].

The solar wind contains convective structures and exhibits a power law spectra, f^{α}, where α is variable depending on scale [20][27]. At frequencies smaller than the proton cyclotron resonance, $\alpha = -5/3$, and above 1Hz, $\alpha = -5/2$, shown in figure (1.11)[19]. The solar wind also exhibits intermittency; a departure of the pdf from Gaussianity at small scales, a characteristic of turbulence and nonlinear interaction [28][29].

1.4.2 The Magnetosphere

A *magnetosphere* is the region surrounding a planet in which the planet's own magnetic field dominates the dynamics of any local charged particles [30]. In free space, a planetary magnetic field resembles a dipole. When the solar wind approaches the Earth's dipole field, Alfvén's theorem prevents the incoming flow from penetrating the field. Instead, the supersonic plasma wind is rapidly slowed, or *shocked*, and forms a parabolic structure in front of the magnetosphere known as the *bow shock*, named for its resemblance to the waves formed at a ship's bow. The interaction of the solar wind creates an asymmetry in the terrestrial magnetosphere, splitting it into the *dayside* and *nightside*. A significant fraction of the kinetic energy of the solar wind is converted to thermal energy on the dayside as a result of this interaction [31]. The bow shock standoff distance, the distance from the centre of the Earth to the nose of the shock parabola, is approximately 12-14 Earth radii, and varies according to the incoming solar wind dynamic pressure, sound speed,

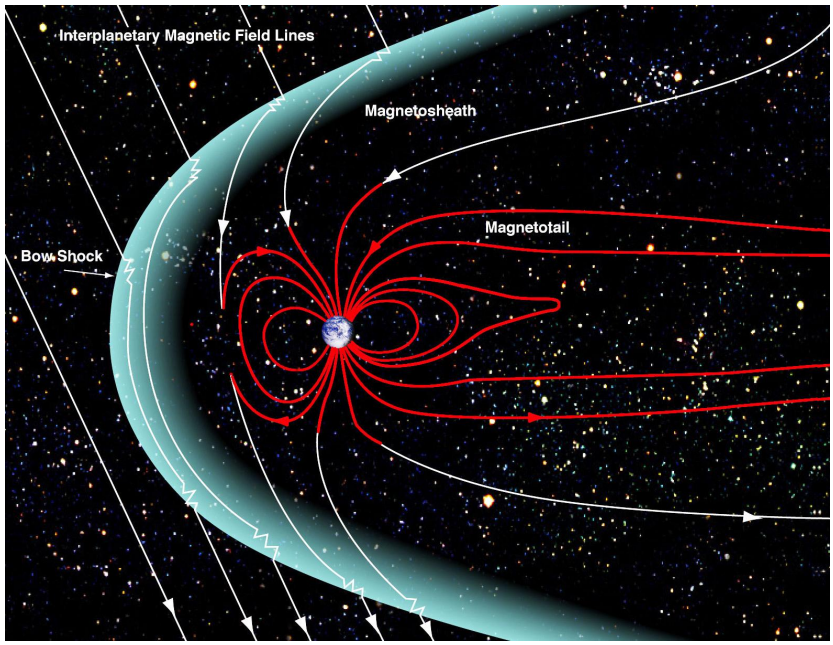

Figure 1.12: The magnetosphere. The IMF lines are not in general parallel to the solar wind flow. The inability of the IMF to penetrate Earth's dipole field produces the bow shock, and upstream of this, the foreshock. Credit: NASA/Goddard/Aaron Kaase

and magnetosonic Mach number [32]. The bow shock is separated from the magnetosphere proper by a layer of shocked plasma known as the *magnetosheath* [33]. The plasma in the magnetosheath is compressed by the bow shock and the incident solar wind, and is therefore hotter and denser than the solar wind, and the magnetic field is stronger. The magnetic field strength and density are subject to large fluctuations in this area and the directions of the magnetic field and solar wind velocity may also vary substantially [34]. The general structure of the magnetosphere is shown in figure (1.12). The plasma comprising the magnetosheath is generally more turbulent than the the plasma upstream, and can couple to the magnetospheric field, dragging the field lines in the direction of the bulk solar wind in a process called *reconnection*[35][36]. Such reconnection processes facilitate energy transfer from the dayside to the nighside magnetosphere and are an area of ongoing research [37][38][39]. The terrestrial magnetosphere is depicted in figure (1.12).

1.4.3 The Foreshock

The area that is upstream of, and magnetically connected to, the bow shock is referred to as the *foreshock*, and is shown in figure (1.13) [40]. At the bow shock, incident solar wind particle distributions are specularly reflected upstream, towards the sun [41][42]. The foreshock, at the intersection between the shocked, turbulent and nonlinear solar wind and energetic reflected particle beams, is a system that exhibits a variety of phenomena.

1.4.3.1 Topology

The topology of the foreshock is determined by the IMF, creating two distinct regions according to θ_{Bn}, the angle between the bow shock normal, n, and the direction of the IMF. The *quasi-perpendicular* shock is that part of the shock for which $\theta_{Bn} > 45°$, and the *quasi-parallel* that for which $\theta_{Bn} < 45°$. Assuming a time-stationary bow shock, we may infer that the reflected solar wind particles have a velocity component $v_{\parallel}$ parallel to the IMF field, $\vec{B}$, and experience an $\vec{E} \times \vec{B}$ drift perpendicular to $\vec{B}$ in accordance with equation (1.10) such that:

$$\vec{v}_d = \frac{\left(-\vec{v}_{sw} \times \vec{B}\right) \times \vec{B}}{B^2} \tag{1.121}$$

due to the motional electric field associated with the movement of the solar wind. Here, $\vec{v}_{sw}$ is the solar wind bulk velocity. Reflected electrons move quicker, and are thus under the influence of this drift velocity for a shorter duration [44]. The more inertial ions drift deeper into the foreshock, resulting in the formation of the reflected electron-dominated *electron foreshock* and ion-dominated *ion foreshock*. The electron foreshock is bounded by

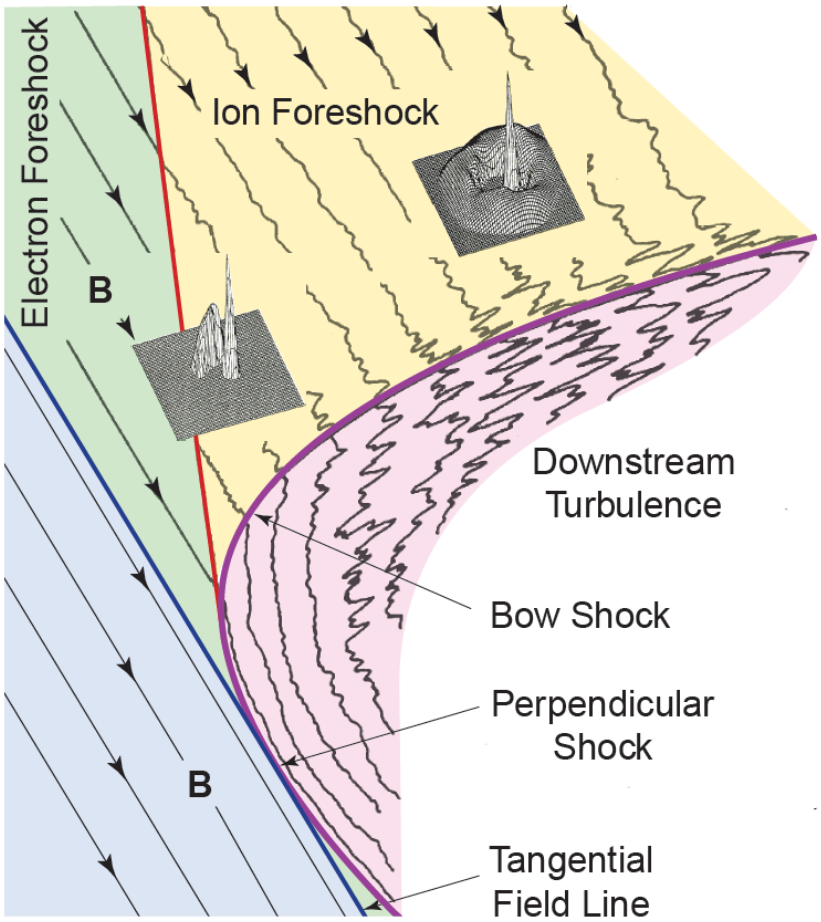

Figure 1.13: Schematic of the terrestrial foreshock. The solar wind flows from the left, and the bow shock is represented by the purple-coloured parabola. The quasi-parallel and perpendicular bow shock regions, formed by the areas where the shock-normal and IMF lines coincide, are both visible. The electron foreshock, on the nose of the bow shock, and the larger ion foreshock, are also visible. In the electron foreshock only backstreaming electrons are observed. Behind the boundary, field-aligned backstreaming ion distributions are found. The diffuse ion populations exist deeper into the ion foreshock. Two-dimensional velocity-space relief plots are included to show the position and scale of the ion diffusion. The more turbulent regions are represented by perturbed field lines. (From [43])

the field line tangent to the quasi-perpendicular shock and the ion foreshock boundary; the ion foreshock extends deeper into the quasi-parallel foreshock. The topology is shown in figure (1.13).

1.4.3.2 Shock Reflection

A portion of the particles that make up the incoming solar wind are specularly reflected at the bow shock. Typically, these reflected particles have energies 4-6 times larger than the average solar wind proton, and are accelerated by the electric field during the reflection process [45]. One proposed mechanism for this reflection is through *shock drift acceleration*. Figure (1.14) shows a still from a simulation of the geometry of an oblique shock in its rest frame. The shock surface is taken as planar and is depicted by the red line. Plasma flows in from the left to the right side of the figure. The magnetic field, shown in cyan arrows, has different magnitude in the upstream and downstream regions of the shock, and the motion of the incoming plasma creates an induced electric field in the shock rest frame, parallel to the magnetic field, depicted by the red arrows. A group of electrons (represented in yellow in figure (1.14) and ions (blue) are launched towards the shock. For the figure, the electrons have been simulated with masses 1/6th that of the ions to keep their gyroradii on a comparable scale. The stronger electric field in the shock can act to accelerate or decelerate particles dependent on their charge and direction of entry into the shock. When the particles enter the shock, the radius of their gyrorotation is constricted due to the increased magnetic field, as required by equation (1.4). For some of these particles, the constricted orbit will still be large enough to pass again into the area of increased electric field, accelerating the particle. The $\vec{E} \times \vec{B}$ drift accelerates both the electrons and ions in the same general direction (rightwards in figure (1.14), left), and so once the centre of gyration is downstream of the shock, each successive passing of a particle through the central area of increased electric field strength will further accelerate the particle [46].

Particles can experience this acceleration effect until they are downstream of the shock, or expelled from it upstream. The important parameter is the speed at which the intersection of the field line with the shock moves along the field line. For a locally planar shock, this speed is $v = v_{sw}\cos(\theta_{B,n})$ in the shock frame, where v_{sw} is the solar wind velocity and $\theta_{B,n}$ is the angle between the magnetic field line and the shock normal [49][46]. Particles with a velocity parallel to the field line that exceed this value will escape upstream. This is depicted in the right panel of figure (1.14). At Earth's bow shock, electrons can be accelerated up to a few tens of keV [50]. Shock drift acceleration requires particles to cross the shock front many times, consistent with reflected populations existing mainly at quasi-parallel shocks [51]. Only that portion of the incoming plasma that is successively accelerated to

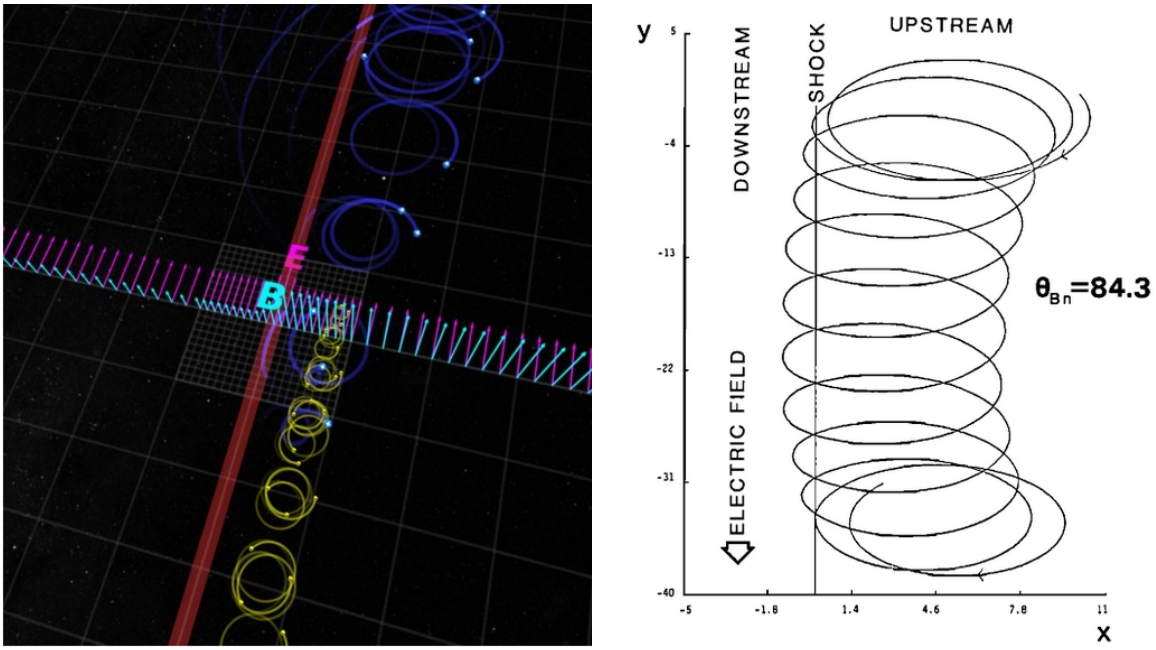

Figure 1.14: Left: Shock drift acceleration in the shock frame. The cyan and magenta lines represent the magnetic and electric field magnitudes respectively. The gyrating electron (yellow) and ion (blue) populations are shown downstream of the shock, after crossing and experiencing an $\vec{E} \times \vec{B}$ drift; the variant gyroradii across each population is due to the difference in pitch angle when crossing the shock. Right: particle trajectory showing specular reflection of a single particle, injected 5 gyroradii from the shock at a pitch angle of 31.4°. The units of the axes are dimensionless. (From left: NASA.gov, right: [47])

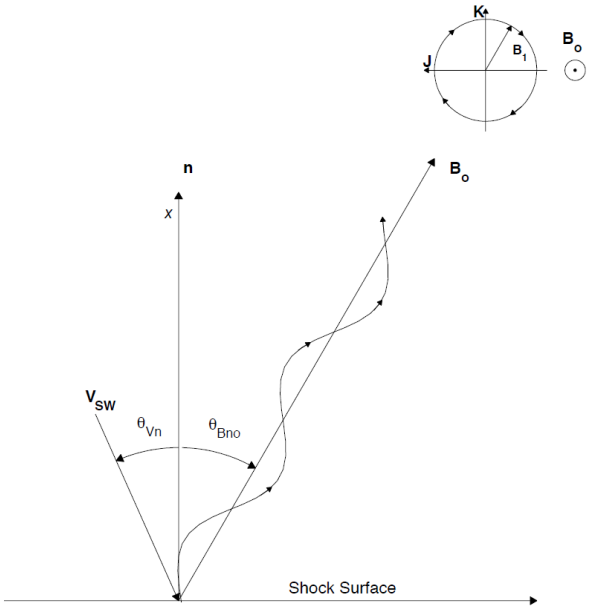

Figure 1.15: Depiction of $\theta_{B,n}$ modulation by upstream waves ([48])

parallel speeds greater than $v_{sw}\cos(\theta_{B,n})$ will be specularly reflected, which is consistent with observations of the reflected particles being less numerous than the bulk solar wind plasma [52][53]. The presence of ULF waves upstream of the shock can modulate $\theta_{B,n}$, affecting the specular reflection. This is shown in figure 1.15 [48].

1.4.3.3 Foreshock Particle Distributions

Early satellite missions to the foreshock, such as The International Sun-Earth Explorers (ISEE), found two distinct types of ion distribution in the foreshock, distinguishable by their pitch-angle distributions and energy range, relief plots of which are shown in figure (1.13). The first of these are the so-called *field-aligned beams (FABs)* or *reflected* ions [54]. These are typically observed on magnetic field lines connected to the quasi-perpendicular shock with $\theta_{B,n} = 40° - 70°$, and stream away from the shock with speeds ranging from one to several times the incident solar wind speed [55]. FABs are composed mainly of protons, are generally found within one Earth radius of the ion foreshock boundary, and show a decrease in kinetic energy with increasing depth into the foreshock [56]. FABs have core beam energies of a few keV, with more energetic nonthermal "tails" that can contain significantly more Helium ions [57][58]. The *diffuse ions* made up the second population [59]. These are of lower density than the field-aligned beams, and less spatially organised [60]. They are composed of a roughly isotropic shell-like distribution, with thermal energies up to ~200keV [61]. Diffuse populations have variable densities, ~0.01-0.8cm^{-3}, contain comparable or slightly higher fractions of alpha particles as the solar wind, and are usually observed for $\theta_{B,n} < 45°$. Most of the energy of the diffuse populations is thermal, contrasting the kinetic nature of the FABs [60]. The exact generation mechanism of these diffuse ions is unknown but they may arise from a reflection and acceleration process at the quasi-parallel shock [62], during shock reformation processes [63], or by scattering of ring-beam distributions at the shock [64]. Populations that share characteristics of both the diffuse and field-aligned populations are termed *intermediate*. These ions are similar to FABs, but have a large spread in pitch-angle and have crescent shape distributions.

The backstreaming particles of the foreshock produce a "bump on tail" velocity distribution, or a *two-stream instability*, of a form similar to figure (1.6). For a purely Maxwellian distribution, waves produced in the collisionless solar wind will undergo Landau damping and their energy will be transferred to the solar wind particles, since the differential of the velocity distribution is negative [65]. The presence of the secondary maximum in the distribution means the differential can be positive, and waves can grow in resonance with the beam. Under typical foreshock conditions, this instability produces kinetic fast magnetosonic waves, which will give a left-handed polarization in the spacecraft frame

[66]. Other modes are also common in the foreshock. Electron Langmuir waves along with their second harmonic, are found in the electron foreshock [67]. Deeper into the foreshock, these waves are shifted to frequencies above and below the electron gyrofrequency [68].

1.4.3.4 ULF Waves

Downstream of the ion foreshock boundary, there is a large array of *ulta low frequency (ULF)* waves, spanning a broadband of ~(0.005-0.1)Hz [69]. The majority of these ULF waves are either MHD modes, and of these most are transverse, or magnetosonic whistlers. Generally, the Alfvénic modes are linearly or left-hand polarized and the magnetosonic modes are linearly or right-hand polarized. These ULF modes can be further categorized by their frequencies and amplitude. Low frequency, large amplitude waves, so called *30-second waves*, coined by Fairfield [70] are some of the most well studied and salient examples of foreshock waves. These waves are associated with the intermediate ion populations, and multi-spacecraft studies have shown them to propagate upstream and experience advection towards the Earth by the solar wind [54] [71]. They have peak-peak amplitude of ~5nT, around as large as the background magnetic field strength, and are mostly transverse. Near the foreshock boundary, 30s waves are mostly monochromatic, but steepen and evolve behind the boundary [54][72]. The existence of these waves upstream of the bow shock is important, since they are responsible for modifying the solar wind and turbulent spectrum convected downstream across the magnetopause. The compressional nature of these waves cause significant density fluctuations, up to 20% of the background solar wind, modifying the dynamical pressure of the unshocked solar wind, which can affect the bow shock standoff distance [73][69]. The large amplitude 30s waves in the foreshock influence wave-generation mechanisms in the magnetosphere but are often dominated by local sources of waves. The compressional 30-second waves appear with both left and right handed polarization in the spacecraft frame, with both polarizations exhibiting similar form, frequencies and wavelengths [72]. Since the 30-second waves are known to steepen, they can be split into two further types; those waves that appear nearly sinusoidal, and the more compressional 30-second waves. The origin of the sinusoidal waves is the ion/ion resonant instability, in which right-handed polarized waves resonate with the backstreaming FABs [74]. This instability produces right-handed waves that propagate upstream, that therefore appear left-handed when advected towards the shock [75][61]. This instability is also responsible for the generation of the left-handed compressional waves [76]. The right-handed compressional waves are producible by the nonresonant firehose instability created by fast and dense backstreaming ion beams [76],

or by the left-handed Alfvén/ion resonant instability produced by extremely hot backstreaming ions [77]. ULF waves have also been the subject of simulations. Blanco-cano et al [64] performed global hybrid kinetic simulations of the solar wind coupling to various strengths of magnetic dipoles to study the effects on the foreshock morphology. In the context of ULF waves, two main types were found; sinusoidal almost-parallel propagating modes, comparable to the 30s modes of the foreshock, and highly compressive oblique fluctuations. It was found that the sinusoidal waves were generated by field-aligned backstreaming ions, but contrary to previous studies, the compressive waves near the shock were found to be generated by gyrating ion beams closer to the shock. The dipole strength of the magnetic field was shown to correlate with the dominance of either the 30s modes or the compressive fluctuations, for low dipole magnetization, noncompressive waves dominate the foreshock, while compressive waves grow just in a very small region and do not have time to evolve, so the quasi-parallel shock does not form. Conversely, when the system scale size is much larger than an ion inertial length, the compressive waves convect into the quasi-parallel region, evolving into large steepened structures that eventually form the shock transition.

So called *1Hz waves* have a higher frequency and smaller amplitude (3-4% of the background field) than 30 second waves, and are made up of backstreaming magnetosonic whistlers, with frequencies ~(20-100)ω_{ci} and wavelengths ~100km in the plasma rest frame, and are found with both left and right handed polarizations. The term 1Hz waves is something of a misnomer, as in modern usage waves of this category fall within a wide ~(0.5-4)Hz peak in the power spectrum, which translates to a broadband spectrum of (10-20)Hz in the plasma frame [78]. 1Hz waves can be observed in excess of 1 Earth radius upstream of the quasi-parallel bow shock, usually in conjunction with reflected ion beam distributions. Hoppe et al [79] used the cold plasma dispersion relation to determine that the waves have wavelengths 10-100km, and propagate mostly 30°-50° to the magnetic field. Orlowski and Russell [80] discovered that the group speed, but not the phase speed, of these 1Hz waves could exceed the solar wind bulk velocity. The waves therefore have phase fronts that are advected with the solar wind, but they may still transfer wave energy upstream [81][82]. The 1Hz modes were identified by Fairfield as being upstream-propagating whistlers [81]. The association of 1Hz waves with the FABs lead to the initial assumption that the 1Hz modes are driven by the ion/ion instability. This assumption was supported by some theories [83], but other observations argued in favour of anisotropic [84] or hot-beam electrons [85] as the cause of these modes. Hoppe found that the ion beams were not a necessary condition for the presence of 1Hz waves [86] and Orlowski [87][88] provided further evidence that the 1Hz modes are produced locally at the shock. Russell [89], concluded that the shock generation of the 1Hz waves is the most consistent

with observations, since it explains the polarization reversal, oblique propagation, and decrease in amplitude with increasing distance from the shock [78]. Feldman [90] showed a correlation between 1Hz waves and backstreaming intermediate energy electrons in the foreshock. Sentman [84] showed that the resulting instability can generate oblique whistler modes. As more supporting evidence for shock-local generation, the observed wavelengths of 1Hz modes are typical of the supercritical quasi-perpendicular shock [91]. The waves are then observed upstream of the shock due to their dispersive nature. A kinetic approach is favourable over an MHD-based interpretation of the 1Hz modes, as theoretically, ULF waves are observed in a plasma in which the thermal pressure is comparable to the magnetic pressure, and the rest-frame wave frequency can be a moderate fraction of the proton gyro-frequency [82]. 1Hz waves are observable at Venus, Mercury and Earth, with similar amplitudes but varying distributions in polarization [92][80]. At Mercury, the waves are always left-handed, at Venus they are mostly left-handed, and at Earth around half are left-handed. This is explained by the varying angle made by the shock front and the IMF, lending more evidence to generation mechanisms at the shock, and by the different strengths of the dipole fields experienced at these planets [64][93]

1.4.3.5 SLAMS

1Hz waves are often found in association with a third type of foreshock phenomena known as *shocklets* or *SLAMS;* Short, Large-Amplitude Magnetic Structures. Early observations of the foreshock [94][70] noted these large amplitude magnetic pulsations, and nonlinearly steepened magnetosonic whistler waves, terming them shocklets due to their resemblance to small shock-like structures. Shocklets and SLAMS have a magnetosonic nature but can also exhibit left-hand polarizations [95]. Shocklets are generally observed with a radiated whistler precursor mode (originally called a *discrete wave packet*), and therefore contain a low-frequency large scale compressional pulse along with a higher-frequency and smaller amplitude pulse, although not all shocklets have this precursory mode. These whistler modes are of variable wavelengths of (30-2100)km and propagation angle 20°-30° to the magnetic field [54]. SLAMS are larger, an amplitude of at least twice the background field, propagate upstream with phase velocities 1-6 times that of the Alfvén speed but still less than the solar wind velocity [96][97]. SLAMS exhibit soliton-like behaviour, with their phase speed increasing with their amplitudes, and show decreasing advection speed with decreasing distance to the shock [98][99]. Dual spacecraft observations revealed that the shock surface itself was not moving rigidly, and did not produce so called nested signatures; changes in the magnetic field strength due to boundary crossings that are detected at one satellite and not at a second satellite within the time taken for the shock to traverse

the relevant distance. Instead, SLAMS are embedded within the overall transition.

The quasi-parallel shock transition is often modelled as a patchwork of SLAMS. This model implies a spatially extended shock transition, as the SLAMS collectively cause a thermalization of the plasma [100]. It has been shown in simulations that the shape of the SLAMS structure is reproducible as a steepening of ULF modes upstream of the shock into symmetric magnetic field enhancements that then further evolve into asymmetric fluctuations [101]. For a sufficiently oblique angle between the upstream magnetic field and shock normal ($\theta_{B,n} = 30°$), magnetosonic waves are excited by the ion/ion beam instability between the background plasma and diffuse backstreaming ions over spatial scales up to 20 ion inertial lengths upstream of the shock ramp, a scale much larger than that reached by specularly reflected ions [96]. When the density gradient scale of the upstream ions is comparable to the ULF wavelength, the waves undergo strong shrinking and steepening and develop into SLAMS [102][103]. ULF waves and SLAMS can therefore be interpreted as part of the same process at different stages of development, and play a crucial role in the cyclic reformation of the shock. SLAMS that pass downstream from the shock are constantly replaced by steepening ULF modes that are advected from the upstream regions [102]. SLAMS and similarly compressive modes have been shown to be dependent on the dipole field strength, becoming more prevalent at larger magnetic fields [64].

1.4.3.6 Other Foreshock Phenomena

The interaction of compressive and transverse ULF waves leads to the formation of *foreshock cavitons*, or cavities [104][105]. These cavitons are independent structures characterised by large density depressions accompanied by low magnetic field magnitude, bounded by enhancements of both of these parameters [106]. Density cavitons also exist, but are always observed amongst a background of ULF modes, whilst foreshock cavitons are isolated structures. Cavitons are advected by the solar wind through the bow shock, where their properties may change, leading to large density pulses in the magnetosheath that can cause surface waves in the magnetosphere [107]. Cavitons present in the solar wind generate spontaneous hot flow anomalies (HFAs); transient intervals of very hot plasma flowing almost perpendicular to the magnetic field close to the bow shock [108]. HFAs typically contain low magnitude and turbulent magnetic field edged on one or both sides by compressed or mildly shocked solar wind. The velocities of HFAs are slower than the background solar wind, however their duration (~minutes) implies that they are a few Earth radii in size [109]. HFAs are caused by the interaction of the interplanetary current sheet with the bow shock [110]. Reflected particles from the bow shock experience a motional electric field from the movement of the IMF. If the discontinuity is oriented such

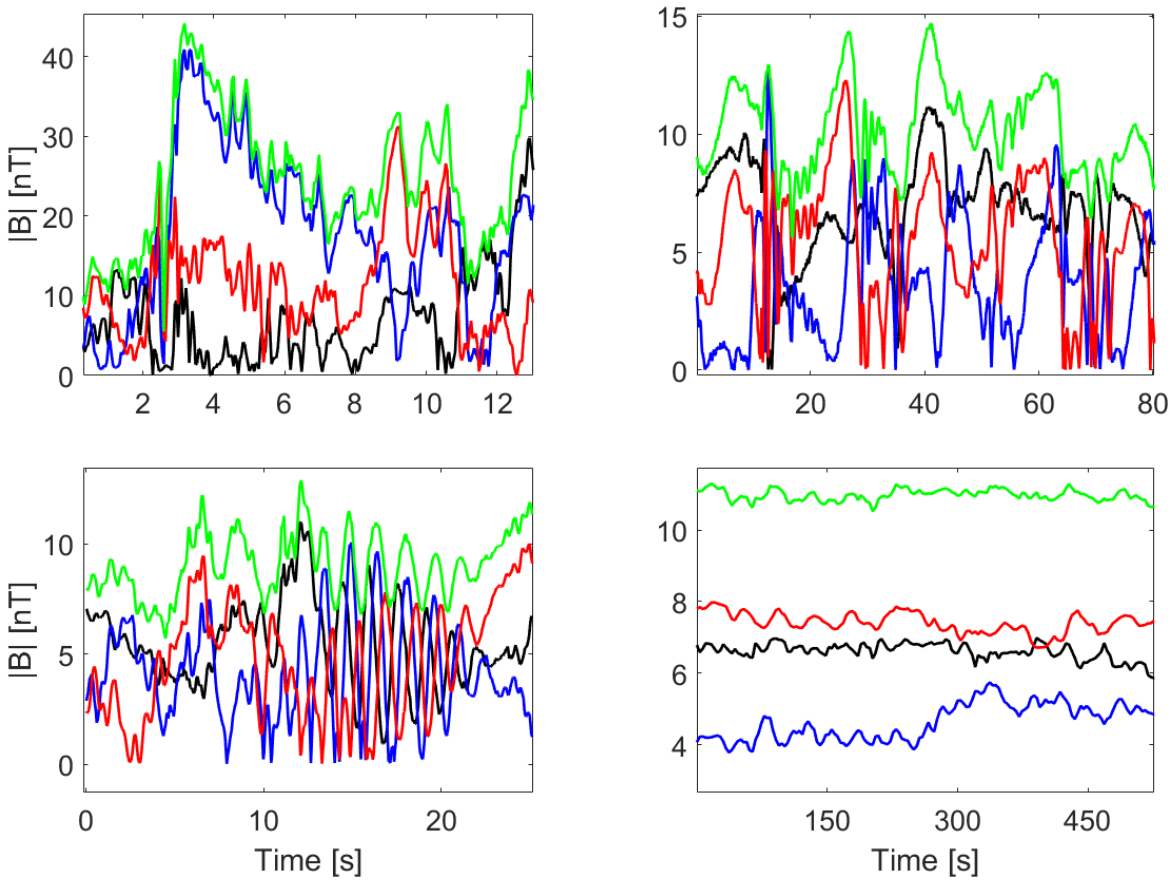

Figure 1.16: Examples of foreshock waveforms taken from C3. Top: waveforms from 20/02/2002, left: SLAMS, starting 17:36:40 ; right: shocklets with precursory whistlers, starting 16:54:20. Bottom left: 1Hz waves taken on 20/02/2002, starting 17:13:40. Bottom right: 30 second waves taken on 18/02/2002, starting 13:50:19. The black, blue and red lines are the absolute values of the x,y, and z GSE components of the magnetic field respectively. The green line is their magnitude.

that the magnetic field on at least one side of the HFA tends to focus these reflected ions towards the plane of the discontinuity, and the discontinuity travels slowly in comparison to the reflected beam velocity, then an HFA will form provided that the discontinuity is not thicker than a gyroradius of the reflected population. The discontinuity plane will then contain a significant population of reflected ions that can interact with the solar wind beam ions, generating waves and heating the two ion populations forming the HFA [40].
Another common structure observed at the edges of the foreshock is the foreshock compressional boundary (FCB). These structures separate the unperturbed solar wind or the region populated by field aligned beams from the region of the foreshock populated by compressive ULF waves and diffuse ions [111]. FCBs have been associated with foreshock cavities [104]. Omidi et. al. [112] reproduced the effects of foreshock cavities by launching two consecutive IMF rotational discontinuities between which the IMF connected to the otherwise quasi-perpendicular bow shock in such a way that the angle $\theta_{B,n} < 45°$. This leads to the development of foreshock-like regions upstream of a portion of their simulated bow shock between the two IMF discontinuities, which were convected along the shock surface. These regions were called travelling foreshocks. FCBs formed at the edge of these regions [113].

1.4.4 Geocentric Solar Ecliptic Coordinates

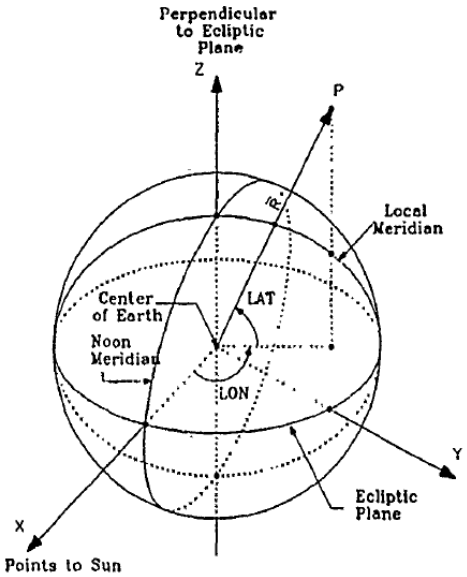

Figure 1.17: Geocentric Solar Ecliptic (GSE) coordinate system. (From [114])

Throughout this work, all quantities are expressed in the Geocentric Solar Ecliptic system, or GSE, unless stated otherwise. As shown in figure (1.17), GSE describes a right-handed orthogonal axes set based on the Sun-Earth line, where the x axis points from the centre

point of the Earth to the Sun (ie almost opposite to the general solar wind bulk flow), the z axis points perpendicular to the plane of the Earth's orbit around the sun, the Ecliptic plane, in the northward direction; the ecliptic north pole, and the y axis completes the set, pointing in the direction opposite to the Earth's instantaneous velocity around the Sun (ie; from the duskside)

1.5 The Cluster Spacecraft

Cluster II, or more commonly just *Cluster*, is a multi-satellite mission launched in 2000 to further the understanding of the magnetosphere. At the mission's launch, the three-dimensional topology of the foreshock was not wholly understood; the IMF, solar wind and shock normal are not necessarily coplanar. Two-dimensional depictions of the foreshock such as figure (1.13) are therefore simplifications. The stability and location of the foreshock and ULF mode boundaries were also not completely known. The properties of the ULF modes themselves required further study, as before Cluster observations, the instabilities proposed for the generation of the ULF waves produced growth rates that were maximized for parallel-propagation, however the observed waves were oblique.

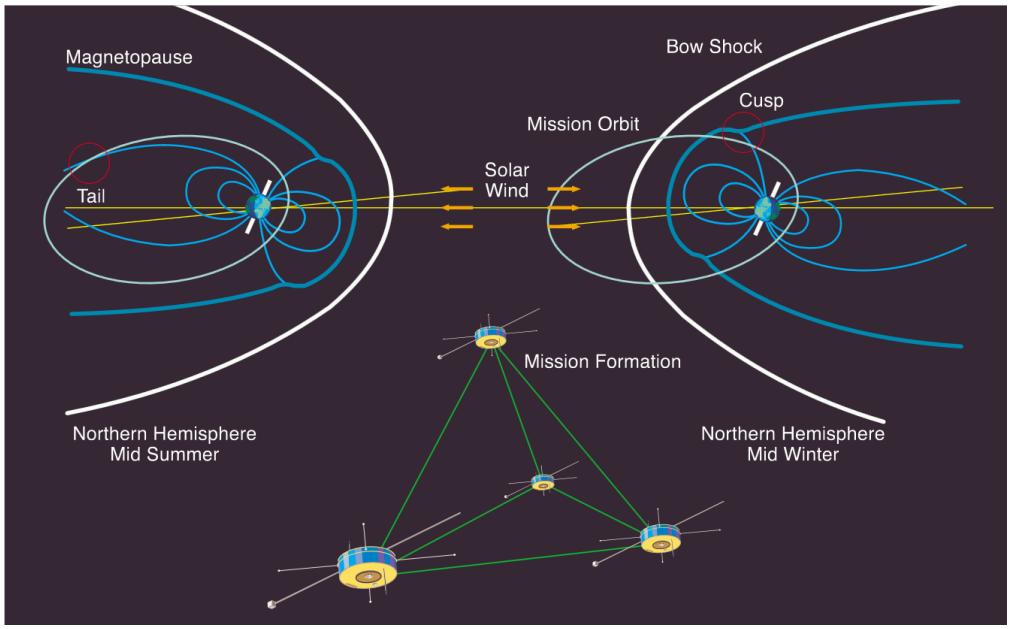

Figure 1.18: Artist interpretation of the Sun (not pictured) and Earth system with Cluster. Left and right depict Earth six months apart. Cluster's orbit (white) is inertial and so changes location with respect to Earth seasonally, the orbit also evolved over the course of the mission. Shown as well is the tetrahedral formation in which the satellites fly. (From [115])

1.5.1 Orbit

Cluster consists of 4 identical spin-stabilized satellites, commonly labelled C1, C2, C3 and C4, that fly in a variable tetrahedral configuration [116]. The distances between the satellites is variable, to allow the study of both small and large scale features, and has ranged from 4 to 10,000 km. The distances throughout the mission lifetime are shown in figure (1.20), until time of writing. Cluster follow elliptical polar orbits with a perigee of $4R_E$ and an apogee of $19R_E$ (Earth radii). The orbital plane is fixed in inertial space so it rotates with respect to the magnetosphere over the course of a year, allowing the satellites to measure different parts of the magnetosphere and solar wind environment, shown in figure (1.18). The orbits of the satellites in the mission's infancy (2001) and more recently (2009/2010) are shown in figure (1.19), where the identical shape of the orbit between the "tail" and "dayside" seasons can be seen. As shown, the orbits have evolved through the course of the mission to include a pass through the magnetospheric cusps; points of entry of the solar wind plasma into the magnetosphere; and the magnetopause; the current layer that separates the magnetosphere and the solar wind. Cluster also crosses the bow shock itself and passes into the foreshock. As the mission matured, the orbit of Cluster precessed to pass through the aural acceleration region; that region which accelerates electrons up to aurorae-generating energies; and the near-Earth magnetotail, a region of key importance in the study of magnetic substorms [117].

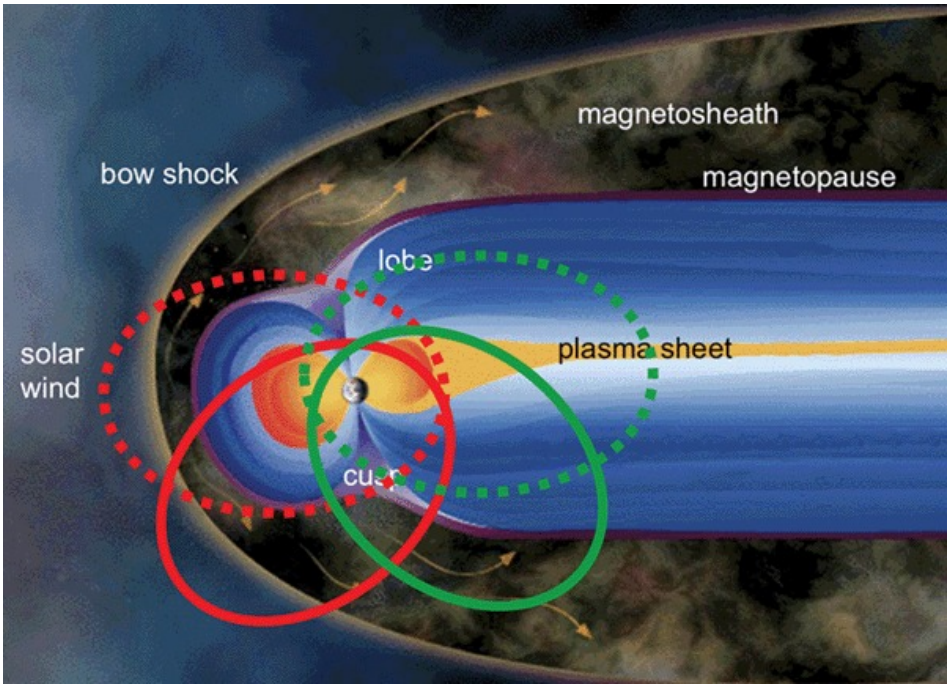

Figure 1.19: Cluster orbit evolution. The dashed orbits are Cluster's initial 2001 orbit and the solid lines are those of 2009/2010. Green and red orbits represent the magnetotail and dayside seasons, respectively. (From [118]).

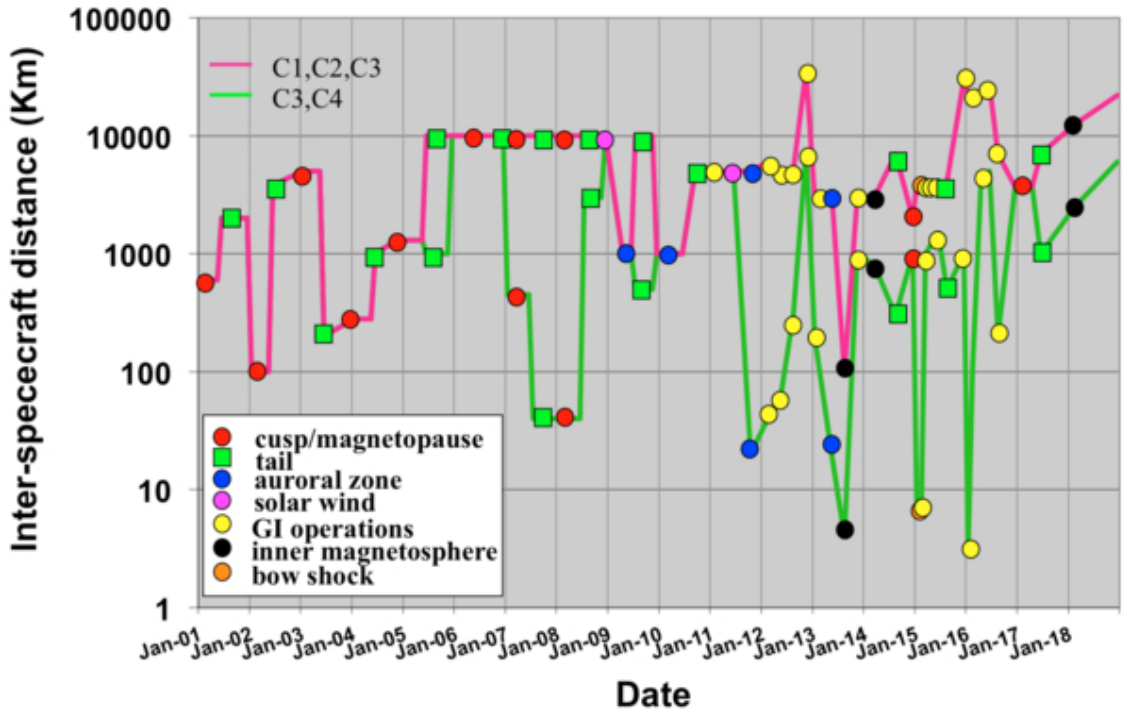

Figure 1.20: Cluster separation distances throughout the mission timeline, and location of satellites. (Credit: ESA)

1.5.2 Instrumentation

Each Cluster satellite is equipped with identical instrumentation, listed in full in table (1.3). The instruments mainly employed in this thesis are the *Fluxgate Magnetometer (FGM)* and the *Cluster Ion Spectroscopy* experiment, specifically the *Hot Ion Analyzer (CIS-HIA)*. The FGM measures the magnetic field in all three GSE directions, and consists of two triaxial magnetometers and an on-board data processing unit. One magnetometer is located at the end of one of the two 5.2m experimental booms, shown in figure (1.21). The other sensor is located 1.5m inwards from the end of the boom. This configuration minimizes the magnetic background of the spacecraft. Either sensor is capable of being used as the primary sensor, and is operable in 5 different operating ranges, shown in table (1.4). The sensor itself records data at a rate of 201.75 vectors per second, and it digitally filtered to the resolutions of table (1.4) depending on the operating and telemetry rates of the instrument when measurements are recorded.

Instrument	Measurement	Purpose
Active Spacecraft Potential Control Experiment (ASPOC)	Electrostatic Potential 0.033s or 0.5s resolution	Enables PEACE to measure cold electrons and stores Cluster command history
Cluster Ion Spectroscopy experiment (CIS)	Ion energies (0-40)keV 4s resolution	Creates 3D ion distributions in azimuthal and polar directions, calculates ion plasma parameters (temperatures, pressure, density, etc)
Digital Wave Processing (DWP)	Processes EFW, STAFF, WBD and WHISPER data	Enables more complex operational modes and facilitates synchronization.
Electron Drift Instrument (EDI)	Electron drift 4s resolution	Calculates $\vec{E}$ field, perpendicular gradient of $\vec{B}$ field and electron azimuthal angle.
Electric Field and Wave experiment (EFW)	Electric field vector 0.2s or 4s resolution	Calculates $\vec{E}$, spacecraft potential, $\vec{E} \times \vec{B}$ drift velocity, electron density and directional temperature
Fluxgate Magnetometer (FGM)	Magnetic field vector 0.044s or 4s resolution	Calculates high-res $\vec{B}$ field data from (0 ~ 30)nT.
Plasma Electron and Current Experiment (PEACE)	Electron energies (0.0007-30)keV (4-12)s resolution	Creates 3D electron distributions in azimuthal and polar directions, for low and high energy electrons.
Research with Adaptive Particle Imaging Detectors (RAPID)	Electron energies (39-406)keV and ion energies (20-450)keV 4s resolution	Creates 2D/3D electron, proton and Helium pitch-angle distributions
Spatio-Temporal Analysis of Field Fluctuation experiment (STAFF)	Magnetic field power spectral density 8Hz - 4kHz resolution	Highlights small-scale current structures and sources of waves and turbulence. Calculates high-res $\vec{B}$ field data for ~ 10nT+, and $\vec{E} \times \vec{B}$
Wide Band Data receiver (WBD)	Electric and Magnetic field waveform data 25Hz-577kHz resolution	Calculates high time-resolution calibrated waveform data, in three frequency bands, to highlight plasma waves.
Waves of High Frequency and Sounder for Probing of Density by Relaxation (WHISPER)	Electric field spectrograms (2-80)kHz resolution	Calculates high-resolution electron spectral power density, in three modes: active passive and natural

Table 1.3: Cluster instrumentation summary [116][115]

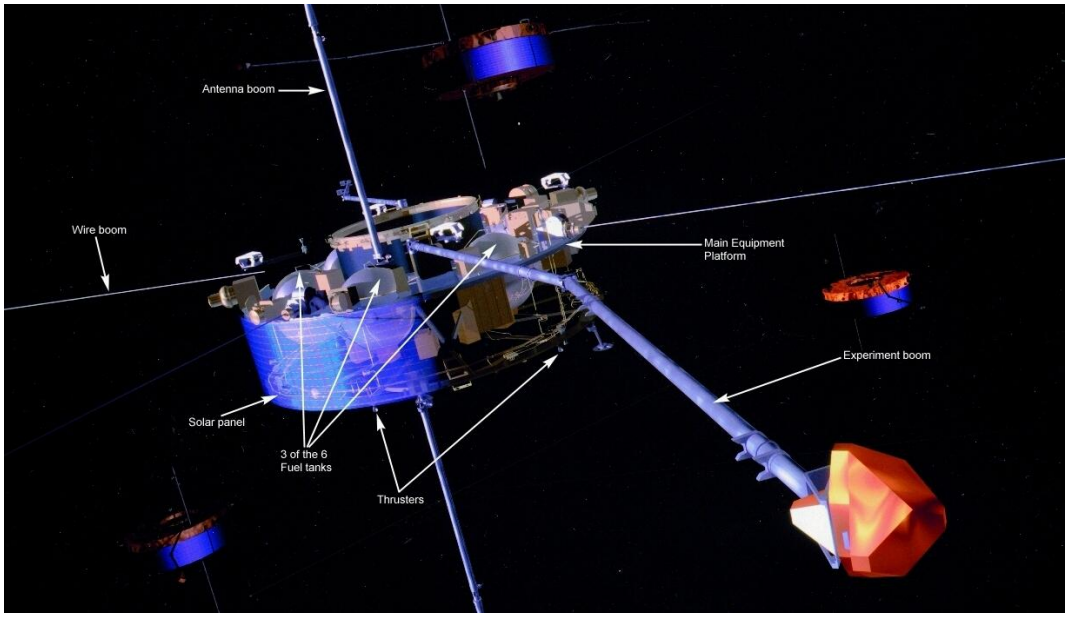

Figure 1.21: Schematic of a Cluster satellite. The experiment boom houses the FGM instrument. Credit: ESA.

The CIS experiment is a comprehensive ionic energy spectrometry package capable of obtaining full three-dimensional ion distributions at spin (4 seconds) resolution. The CIS consists of two instruments, the HIA and a time-of-flight ion Composition Distribution Function (CODIF), plus data processing systems. Both instruments use symmetric optics to give continuous uniform phase space coverage. The HIA instrument combines the selection of incoming ions according to their energy per charge through the use of 62 energy channels. Adjacent channels are then binned together to fit into allocated telemetry, so the energy resolution is smaller in practice. In order to include ion populations from the solar wind and magnetosheath, a dynamic range of 10^5 is required for the energy/charge. The HIA therefore is made of two 180° field-of-view sections, with two different sensitivities. These are the high-g and low-g sides. The low-g side allows detection of the solar wind via the use of two sets of eight detector sectors around the spin plane of the satellite. The first set of eight have a width of 5.625° and are used to capture a high angular resolution. The remaining eight sections are 11.25° in width. The high-g side consists of 16 sectors of 11.25° width. Both the high-g and low-g sides perform a full 4π steradian scan, consisting of 32 energy sweeps, every time the spacecraft spins, ie; every 4 seconds, giving a full three-dimensional distribution of ions in the energy range $5\frac{eV}{e}$-$32\frac{keV}{e}$ [116].

The instruments on CIS can operate in any of 16 modes. These modes can be loosely grouped into the solar wind tracking modes (with mode numbers 0,2,4), the solar wind study modes that focus on upstreaming ions (1,3,5), magnetospheric modes (8-11,13), magnetosheath modes (12,14), and calibration and test modes (6,7,15). These modes dic-

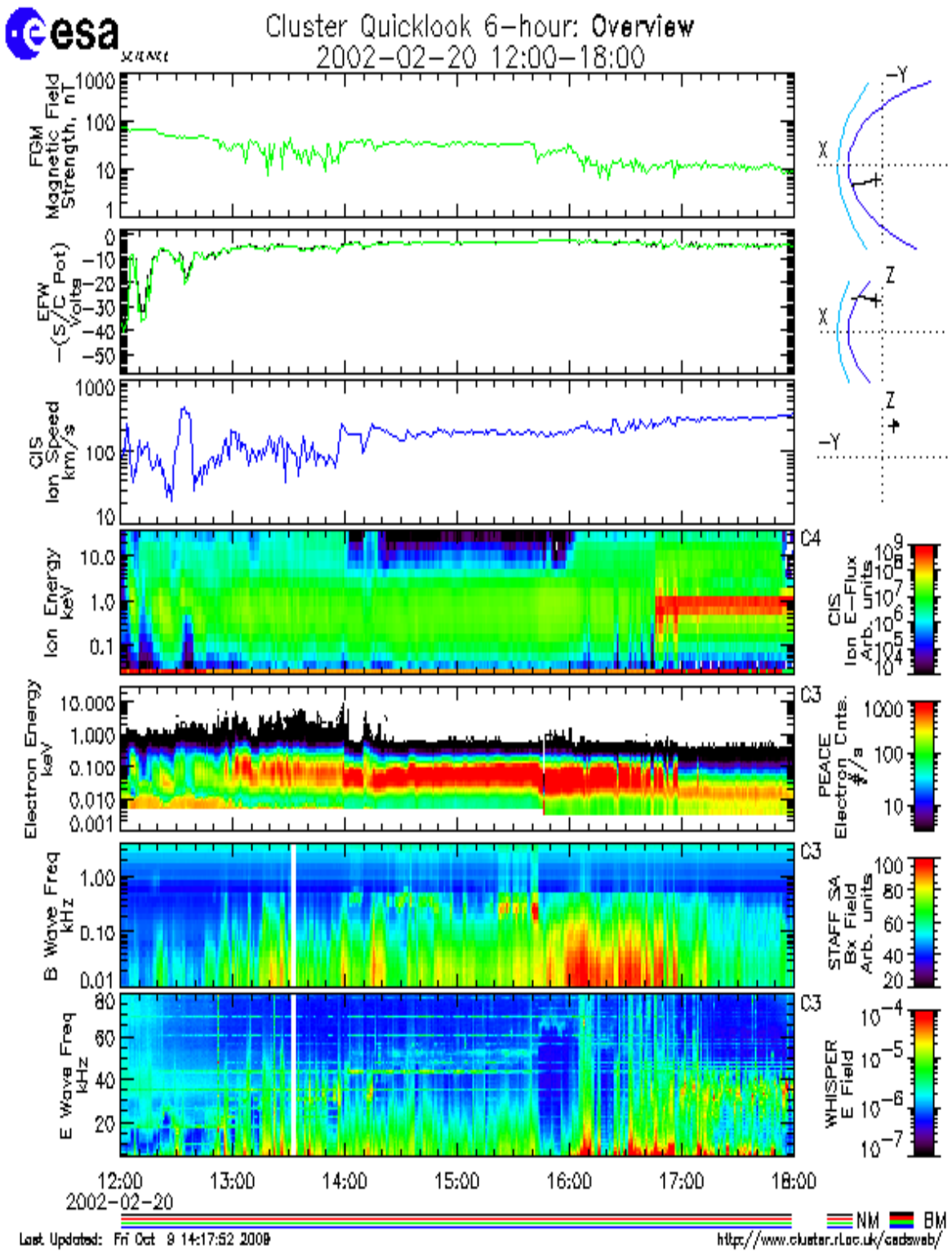

Figure 1.22: An example of the Cluster quick-look plots showing the variety of measurements taken, for 20th February 2002, 12:00-18:00. Information includes readings of the magnetic field strength, spacecraft potential, particle speeds, wave frequencies, and the spacecraft location relative to a time-averaged bow shock.

Instrument mode	Sensor vector rate (vectors/s)
A	15.519
B	18.341
C	22.416
D	67.249

Table 1.4: FGM operating ranges.

tate the energy sweeping scheme of the instrument, and the telemetry products transmitted from the satellites [116]. The solar wind tracking modes (0,2,4) detect ions only when the low-g side of the instrument is facing the 45° cone centered on the sun. Since the focus of the work of this thesis is the foreshock, which contains significant backstreaming ions, the CIS data is collected when the instruments are in the upstreaming ions modes; ie modes 1, 3 and 5. In these modes, the solar wind beam is tracked once every 16 spins. In the remaining 15 spins, a broad energy sweep is performed by the low-g side of the instrument. At the same time, the high-g side, which is positioned facing a 45° cone facing the anti-sunward direction, measures the upstreaming ions [119].

1.6 Motivation

As demonstrated in section (1.4.3.3), the foreshock is an area of enhanced wave activity and plasma processes. The vast wavefield generated in the foreshock provides a free energy source for a variety of processes that in turn may influence the topology of the foreshock or the wavefield itself. The ULF waves (~0.01-1Hz) have the highest growth rates in the foreshock and so their dynamics are of particular importance for the thesis. Generally, these waves are well understood and obey linearized dispersion relations of the type derived in sections (1.3). In the foreshock, the proton cyclotron and whistler modes, described by equations (1.91) and (1.92) respectively, are prevalent. In principle the dispersion relations for these waves are readily attainable. However, the ULF waves are the background to a large amount of nonlinear phenomena which complicate observations of the foreshock, some of which phenomena are described in section (1.4.3.3). These fluctuations are described as nonlinear because they obey equations that are not linear, ie; equations where in each term the dependent variable and its derivatives are of more than first degree. Linear analysis of foreshock processes are therefore strictly incomplete, and research into analysis techniques suitable for nonlinear fluctuations is ongoing. In the second chapter, an analysis technique that is capable of separating linear from nonlinear fluctuations is applied to build dispersion relations for linear wave modes in the foreshock. These high growth rate ULF modes are involved in the dynamics of reflected ion beams,

SLAMS and HFAs, amongst other phenomena, and are of fundamental importance to the foreshock system. This technique requires two probes for measurements, and is presented as an alternative to existing techniques such as the wave telescope, which ideally requires the use of four satellites in a tetrahedron formation. Additionally, the technique of chapter 2 partitions linear wave modes with respect to their powers, and can therefore easily be used to create dispersion relations that have multiple branches, of the type shown in figure (1.4). This is another benefit over the wave telescope technique, which generally produces large errors at higher values of the wavenumber, making the distinction between branches of the dispersion relation ambiguous.

The general wave equation (1.53) represents one dimensional undamped linear waves in an isotropic medium and is unsuitable for describing nonlinear fluctuations. Comparatively, nonlinear phenomena do not obey the superposition principle and there are no general analytical methods for obtaining their solutions. Thus, each particular nonlinear wave equation must be treated separately, and they exist in numerous forms. The question of exactly which equation most closely describes particular nonlinear fluctuations is not a trivial one. Dispersive slow and fast magnetoacoustic waves (equation 1.110) travelling obliquely down magnetic field lines, for example, have been shown to obey the Korteweg-de Vries (KdV) equation, originally derived to model water waves [120]. Alfvén and fast magnetoacoustic fluctuations that travel parallel to the magnetic field are well described by the Derivative Nonlinear Schrödinger (DNLS) equation however their unambiguous detection in the foreshock has been elusive. In chapter 3, solutions of the DNLS are compared to observations of the foreshock, showing for the first time that these fluctuations exist in the foreshock and are well modelled. These observed fluctuations are steepened fast magnetoacoustic waves (section (1.3.4.1)) and contain the SLAMS introduced in section (1.4.3.3) and shown in figure (1.16). These SLAMS are the basic components of the shock layer itself and are important to the understanding of the cyclic shock reformation process. Because these SLAMS are nonlinear in nature, the analysis techniques of chapter 2 are unsuitable for their study. Hence, the empirical mode decomposition (EMD) will be used to separate the SLAMS from their internal structure. The EMD is a technique that decomposes a set of input data into a set of modes derived empirically from the dataset itself, and is applicable to non-stationary and nonlinear data. The modes derived from the EMD process will be compared to solutions of the DNLS derived using a new canonical form of the potential function, which differs to previous forms in its dependence on the magnetic field magnitude.

The foreshock is also a region of turbulent plasma. Turbulence describes the transfer of energy between scales. Turbulent systems contain many degrees of freedom, and so clas-

sical thermodynamical models cannot be applied because the temperature, as the average amount of energy per degree of freedom, becomes inaccurate [121]. Magnetic turbulence is found in most space plasmas, including the Earth's magnetosphere, and the interaction region between the magnetosphere and the solar wind, and is in general well studied. However, analysis of phenomena specific to the foreshock in the context of plasma turbulence is scarce. It has been shown that the solar wind contains Alfvénic vortices which produce energy cascades between scales [28][122]. The cascades are usually presented in terms of Kolmogorov exponents; values that describe the energy distribution between scales, in a similar manner to figure (1.11), shown for frequencies. These exponents do not provide information on the physical processes that facilitate the energy cascade, however, and are mainly used to detect changes in energy transfer rates amongst scales. In chapter 4, foreshock data is investigated for its applicability to the wave turbulence model. This is a framework that models turbulence as the statistical mechanics of random nonlinear waves. In wave turbulence, the wave modes present in the system interact with each other to facilitate the movement of energy between frequencies, and therefore scales. This is a particularly useful model for the foreshock as the expansive wavefield offers a large amount of potential wave interaction. More importantly, in the wave turbulence model it is possible to identify the exact frequencies, and therefore physical processes, that couple together to facilitate the transfer of energy between scales. To identify these relevant modes, the bicoherence will be employed to identify interaction between the wave modes themselves. The bicoherence only provides information on the interaction of modes in frequency space, however, so to add to the analysis, the wavenumber mismatch will also be studied. This is a measure of the coplanarity of interacting modes and is used to determine the strength of the wave interaction in real space. Hence, modes with high bicoherence and low wavenumber mismatch can be confidently classed as interacting. The wavenumber mismatch also produces information on the modes themselves, since modes that propagate parallel to the magnetic field will have high mismatches with modes propagating obliquely, furthering the amount of information available on the interacting modes.

Chapter 2

Statistical Dispersion Relations of Magnetic Field Fluctuations in the Terrestrial Foreshock

2.1 Introduction

The collisionless and turbulent nature of the solar wind facilitates the redistribution of the kinetic energy of its constituent particles via a wide array of complex interactions [123]. As a result, the local particle populations may become heated, and understanding the mechanisms through which this occurs is integral to understanding the nature of momentum and energy exchange in the system. Wave generation in the foreshock is driven by the two-stream instability (section (1.3.5)) of the continuous solar wind and the counter-propagating ion beam reflected at the quasi-parallel bow shock. A beam of sufficient strength will create a two-stream instability, generating a local maximum on the velocity distribution function that can sustain wave growth with phase velocities close to the velocity that corresponds to the bump maximum [124]. The waves receive energy from the beam in doing so, and are said to be *beam resonant*. Wave generation mechanisms in the quasi-parallel foreshock are associated with particle distributions; FAB ion distributions are associated with the generation of ULF fluctuations with fast magnetosonic waves whereas the diffuse distributions are associated with compressive fluctuations [76][60]. The existence of minor ions in the solar wind, in particular Helium ions, He^{++}, may resonate with the left-hand mode found in the FABs, at frequencies $\omega_{ci}/2$, where the power is generally much greater. This interaction can provide an energy source for the magnetoacoustic cyclotron instability [125].

The dynamics of the foreshock are further complicated by the fluctuations contained in

the solar wind itself. At 1 AU, the solar wind plasma shows correlations between velocity and magnetic field fluctuations that are characteristic of transverse Alfvén modes [126]. However, the phase coherence of these modes is generally destroyed prior to their arrival to the foreshock, and only a single observation has been reported to date [127]. Small density perturbations are also detected in the solar wind; they are formed of both pressure-balanced structures in the corona and of fast magnetosonic modes [128]. The ion cyclotron waves (field-aligned Alfvén waves with a frequency near the ion gyrofrequency) of equation (1.93) have been suggested as a possible source of solar wind heating and acceleration but detection of these modes in the solar wind is ambiguous [129].

The experimental delineation of modes generated *in situ* at the foreshock, in opposition to those modes that are directly implanted into the foreshock via the solar wind, is important to the understanding of wave-particle interactions and the channels of energy transfer in the system. Previous results based in the foreshock have made use of the wave telescope, or k-filtering, technique [130][131]. This is a technique based on a generalized minimum variance analysis (section (2.3.1)) that uses multi-station measurements to determine both wavenumber vectors and their associated wave power. Narita [132] used this technique to derive dispersion relations from Cluster data and identified estimates of the dominant modes and their associated dispersion relations, in the ULF domain[132]. It has been clearly demonstrated that these modes propagate upstream, in accordance with the proposed ion beam instability generation mechanism [133]. The unstable distributions may be abundantly found throughout the quasi-parallel shock, and the growth rates of the instabilities are on the order of 100s, with propagation velocities of the associated ULF waves typically (50-100)kms^{-1}. A continuous distribution of power would therefore be expected amongst the unstable modes [76]. Additionally, non-linear processes distinct from the ion beam instability, such as the decay instability of the Alfvén waves, or the modulation instability of the fast magnetosonic mode, may also be present and redistribute power on separate channels [134].

There are two main limitations of the wave telescope technique. Firstly, the technique requires measurements from three or more probes, ideally four probes arranged in a 3-D tetrahedron, to accurately determine wave vectors [135]. Secondly, the technique is sensitive primarily to the most powerful fluctuations at each wavenumber-frequency pair [136]. The work of this chapter is concerned with quantifying how fluctuating power is distributed amongst different coexisting quasi-coherent modes in the foreshock. Using simultaneous two-point measurements, the dispersion relations for three intervals that have differing macroscopic parameters, but similar ion distributions, are derived using a technique able to resolve multiple branches of the dispersion curves. The method involves

first rotating the magnetic field vectors from GSE coordinates to a frame centred on the wave propagation using the minimum variance analysis (section (2.3.1)). The wavevectors are then found by a statistical technique that characterizes the vectors by their associated powers at given frequencies (section (2.3.2)). The powers are then collated in a histogram of wavenumber and frequency pairs and a dispersion relation is formed. Crucially, this means that the technique introduced in this chapter is able to associate absolute powers to particular wavenumber-frequency pairs, a capability lacking in previously employed techniques. Multiple ensembles of measurements are necessary for the technique to work effectively. The frequency of the power maxima are then individually expressed in the plasma rest frame through the Doppler correction.

2.2 Data

Three intervals were chosen for the datasets, referred to hereafter as I1, I2 and I3:

- I1 - February 16th 2002, 07:50-09:20
- I2 - February 20th 2002 16:56-17:56
- I3 - February 18th 2002 13:35-13:50

These intervals comprised foreshock crossings and were chosen based on the presence of clear wave modes in the frequency spectra. The separation vectors between C3 and C4 are also short in these intervals (table (2.1)) meaning shorter-wavelength or less coherent wave vectors can be better resolved, at the expense of larger wavenumber measurements. All three intervals show clear ULF wave signatures in their frequency spectra, shown in the wavelet spectra of figures (2.2)-(2.4), but I3 is dominated mainly by waves at 1Hz. Narita et al. ([132]) studied I2 using a wave-telescope technique, and found both right and left handed modes, amongst the background FAB. Some defining characteristics of the spectra are shown in table (2.1). The magnetic field data was taken from the FGM aboard Cluster (see figure (1.3)) and is of 22.4Hz resolution. Plasma parameters were calculated using the CIS-HIA with spin, 4s, resolution. The two intervals are characterised by largely different values of plasma beta; I1 has a dominant thermal pressure and I2 a dominant magnetic. Also variable is the x-component of the magnetic field, the main component of the GSE coordinate system. For I1 the magnetic field is directed towards Earth, for I2 the field is sunwards. From table (2.1), the bulk speed velocity, $<\vec{V}_{sw}>$ of $300-400\text{kms}^{-1}$ puts these intervals in the slow solar wind category. Figure (2.1) shows a summary of the magnetic field data for the two intervals. Clear quasi-monochromatic wave trains can be identified in panels (a) and (b), in which the transverse magnetic field is shown. Traces from both C3

	$<\vec{\chi}>$ (km)	$<\vec{B}>$ (nT), GSE	$<\vec{V}_{sw}>$ (km s^{-1})	β	$\vec{V}_A$ (kms^{-1})	$\Theta_{V,B}(^\circ)$	$\Theta_{\chi,V}(^\circ)$	$\Theta_{\chi,B}(^\circ)$	ω_{ci} (rad s^{-1})	r_i(km)
I1	70.5	(-6.9,0.3,1.3)	315.5	0.4	60.5	11	62	71	0.7	42.1
I2	82.3	(7.9,-3.9,4.7)	406.6	3.2	93.0	147	31	141	1.0	177.5
I3	64.1	(7.5,-4.0,7.2)	365.6	0.3	80.1	134	138	37	1.0	37.4

Table 2.1: Physical and spacecraft parameters for the investigated Cluster intervals. χ is the spacecraft separation, $<\vec{B}>$ is the average magnetic field, $<\vec{V}_{sw}>$ the average solar wind velocity, β the plasma beta, $<\vec{V}_A>$ the average Alfvén speed, $\Theta_{V,B}$, solar wind velocity and magnetic field angle, $\Theta_{\chi,V}$ separation vector and solar wind speed angle, $\Theta_{\chi,B}$ separation and magnetic field angle, ω_{ci} ion cyclotron frequency in the plasma frame, and r_i the ion gyro-radius calculated from the ion temperature. <> denote time averages over the entire intervals, defined in section (2.2)

and C4 are visible, from which we may conclude that the largest temporal lag between the satellites is never larger than a period of a wave. Panels (c) and (d) show the hodograms for the intervals, demonstrating that for a sufficiently short subinterval, a unique sense of polarization can be found in the spacecraft frame. Interval I2 shows fairly consistent left-handed polarization, whilst I1 exhibits frequenct changes between left and right handedness. The frequency spectra, panel (e), shows peaks at frequencies lower than the proton gryro-frequency (0.01-0.1Hz) and a broadband power-law behaviour at higher frequencies for both intervals. The proton gyrofrequency has been calculated at 0.11Hz for I1 and 0.16Hz for I2, but these are subject to a large Doppler shift and are closer to 3-5Hz in the spacecraft frame. The values shown in table (2.1) show the Doppler-corrected values in the plasma frame. The wavelet power spectra of figure (2.2), shows the ULF activity of I1. Interval I2 shows a comparable amount of power in the ULF modes, however most of the power is contained in a large structure at ~17:07.

Figures (2.2)-(2.4) show overviews of plasma parameters and spacecraft positioning for the intervals I1-I3 respectively. The top row of each figure shows the positions of C3 and C4 in GSE against a time-averaged bow shock model based on an empirical model [137]:

$$x = a_{mp}\left[1 + 1.1\frac{(\gamma-1)M^2+2}{(\gamma+1)(M^2-1)}\right] - \left[0.0223\left(\frac{P_{sw}}{1.8}\right)^{\frac{1}{6}}\right](y^2+z^2) \tag{2.1}$$

where x, y, z refer to the GSE coordinates, M is the fast magnetosonic Mach number, γ is the effective ratio of specific heats assumed to be $\frac{5}{3}$, P_{sw} is the solar wind dynamic pressure (in nPa) and a_{mp} is the magnetopause standoff distance taken as [138]:

$$a_{mp} = (11.4 + 0.013 < B_z >) (P_{sw})^{\frac{-1}{6.6}} \tag{2.2}$$

The values of M and P_{sw} are calculated from HIA data. The bow shock curves are calculated as a slice through the shock at the average position of the spacecraft, and so generally are not exactly the same form in both planes shown. The blue and red vectors of these plots show the magnetic field and solar wind velocity unit vectors (enlarged for visibility), time-averaged over the intervals . The second row shows the FGM, left, and HIA velocity, right, components for the full intervals. On the third row, the HIA density, left and temperature,right, measures are shown. The black line of the temperatures plot is the temperature parallel to the magnetic field, the red line is perpendicular. The fourth row displays the wavelet frequency-time power spectrum, left, and the same spectrum integrated over time, right.

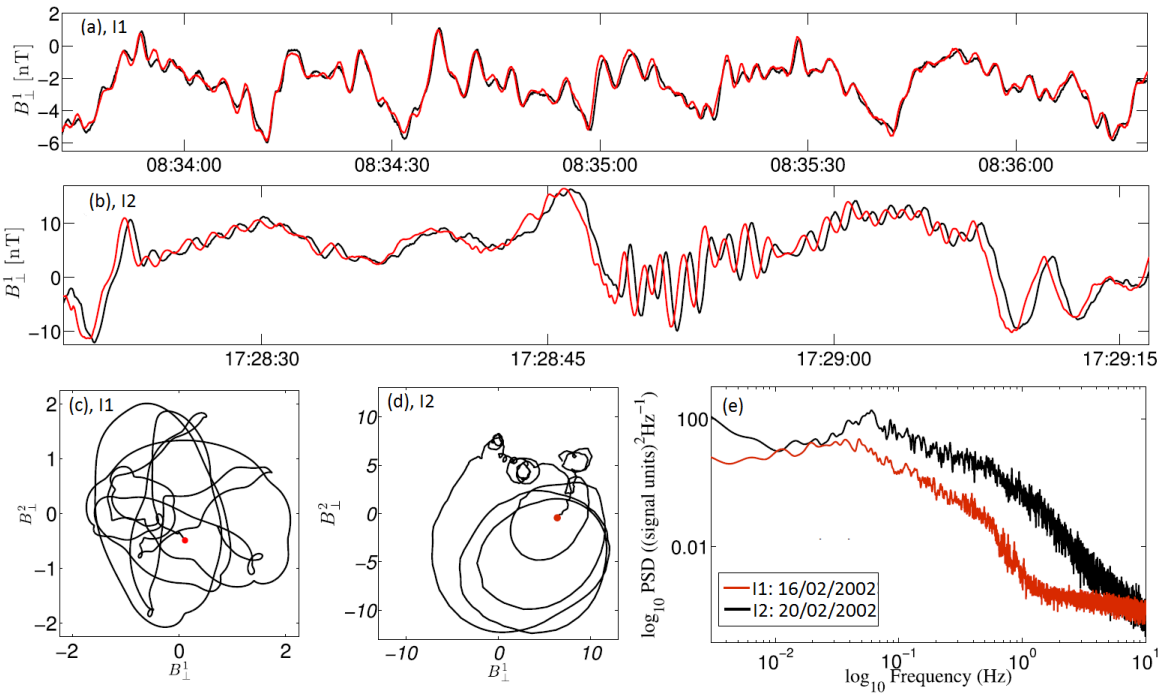

Figure 2.1: Magnetic field data summary for I1 and I2. Panel (a); transverse magnetic field component found using minimum variance analysis for I1 excerpt, for spacecraft C3 (red) and C4 (black). Panel (b) shows the equivalent data for I2 excerpt. Panels (c) and (d) show hodograms of the transverse magnetic field components for the excerpts of I1 and I2 used in panels (a) and (b), respectively. Panel (e): power spectral density for $B_{\perp,1}$ for I1 (red) and I2 (black).

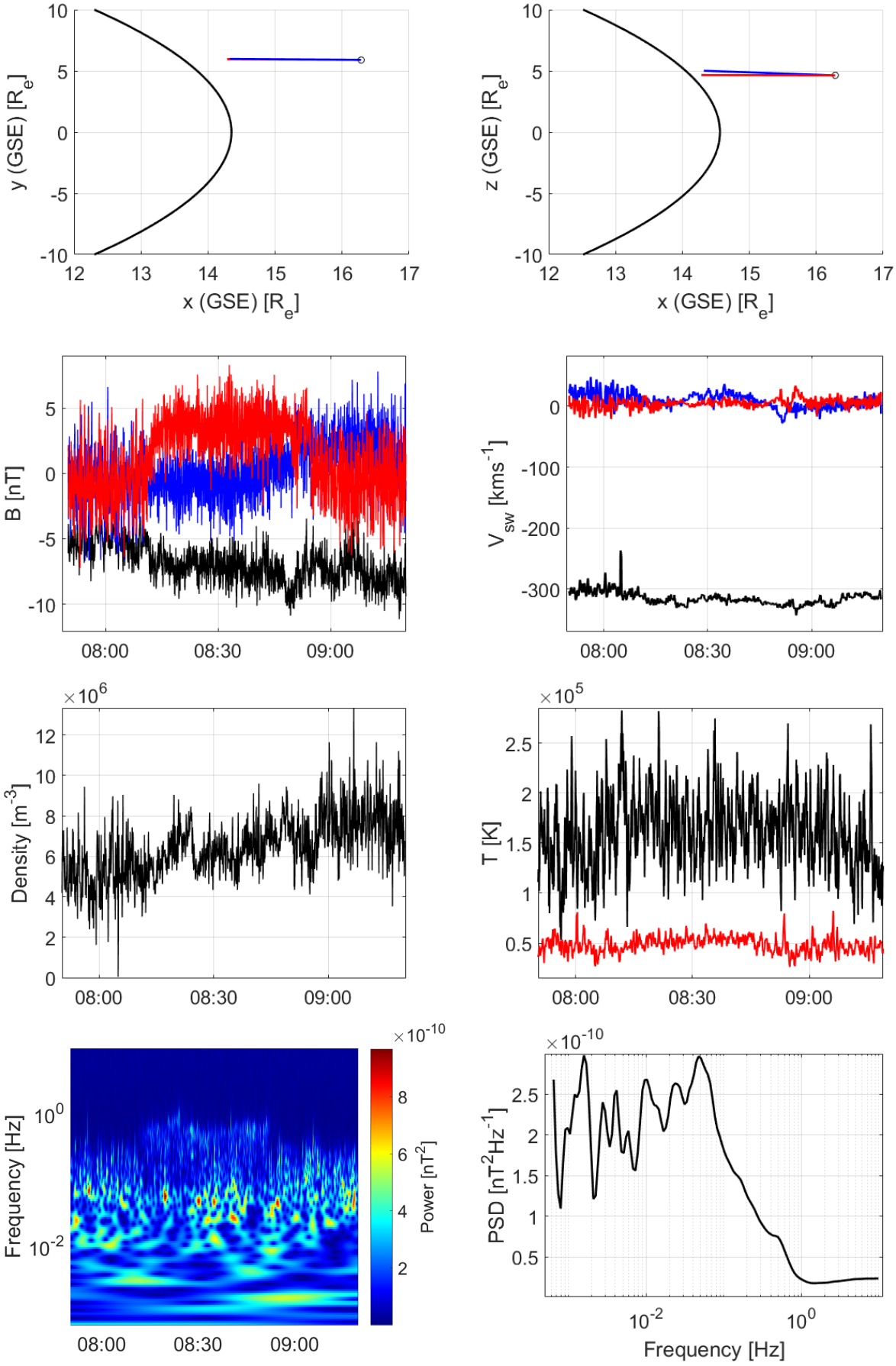

Figure 2.2: Overview plots for I1. Panels are as explained in section (2.2).

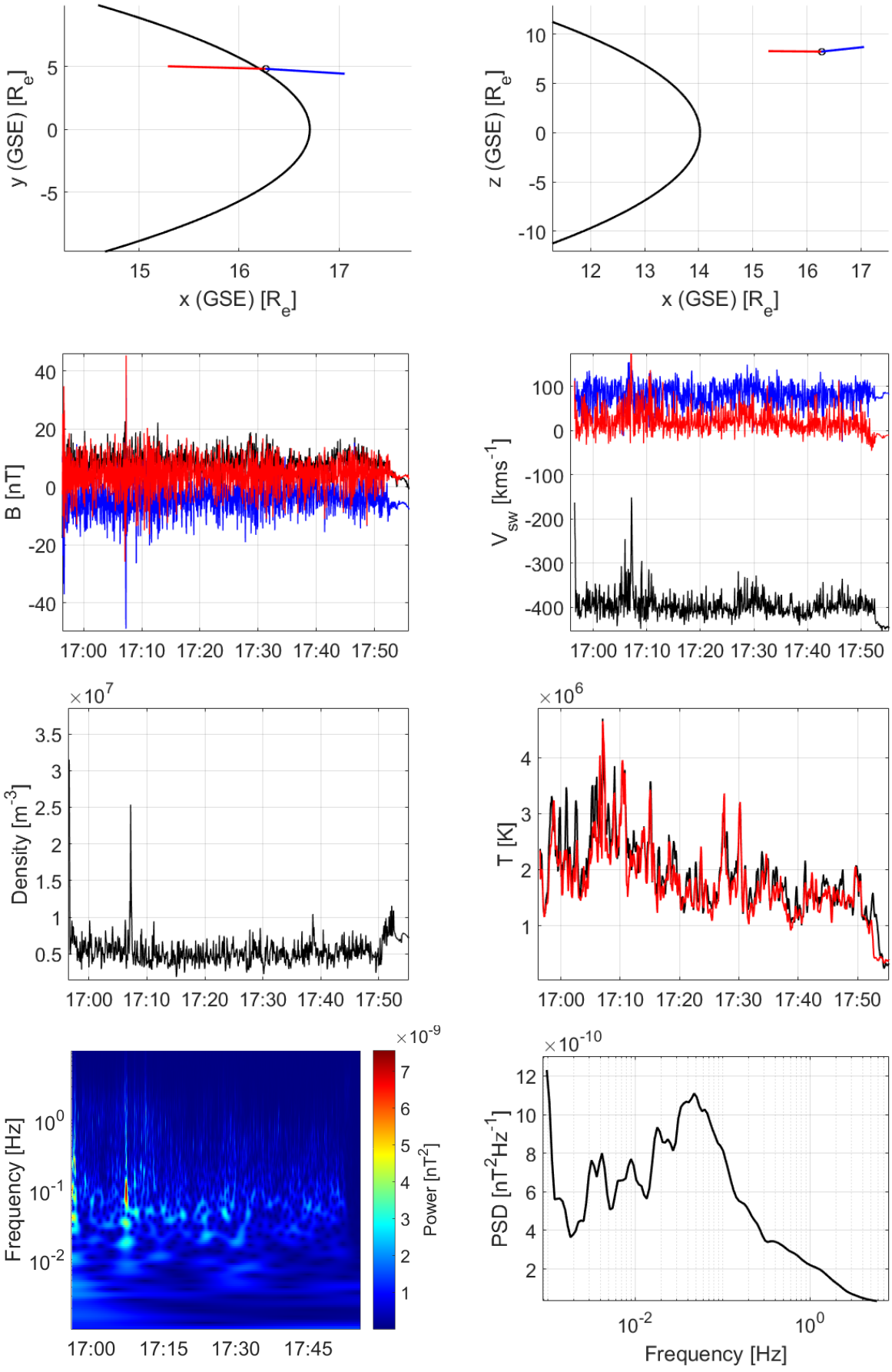

Figure 2.3: Overview plots for I2

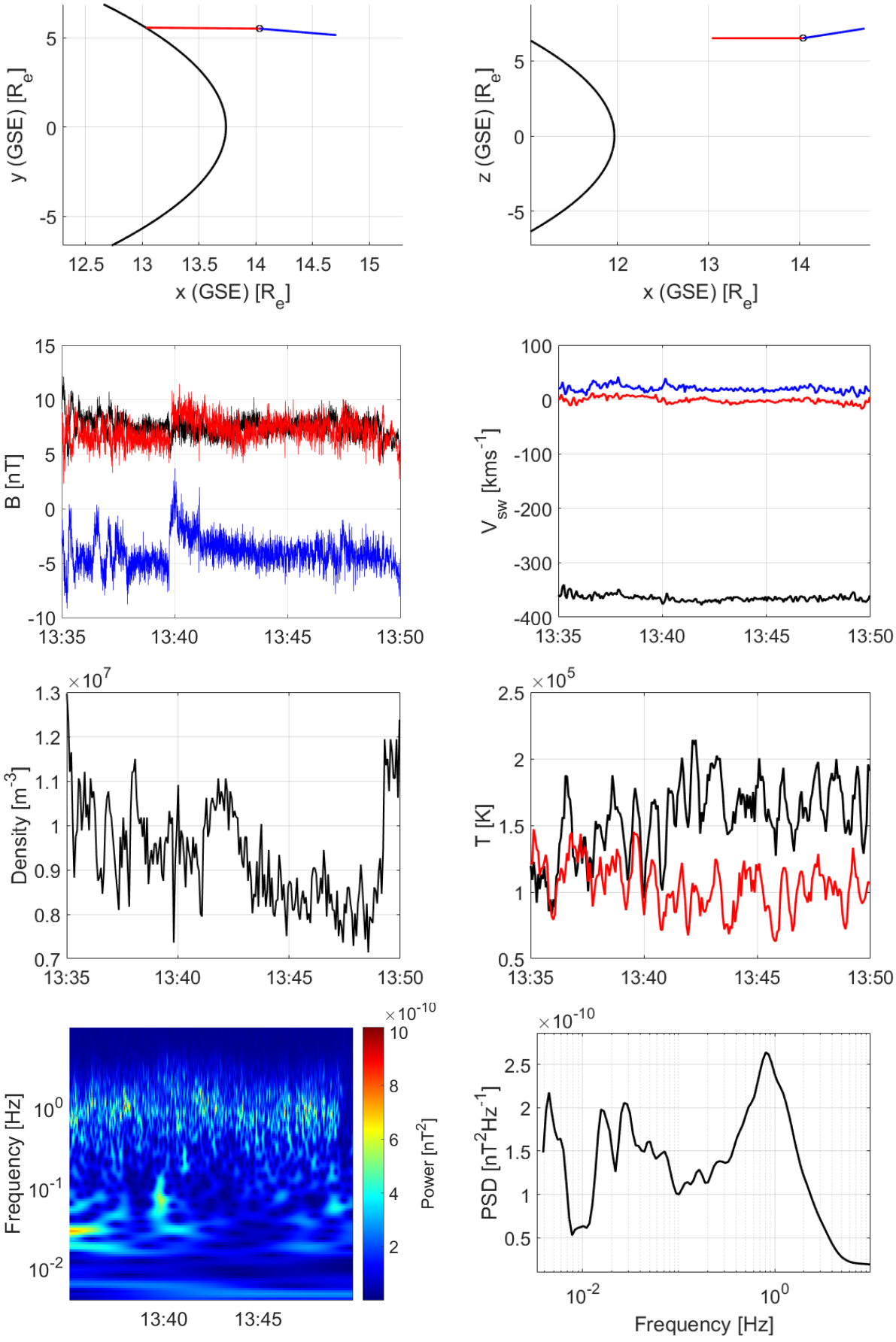

Figure 2.4: Overview plots for I3

2.3 Methodology

2.3.1 Minimum Variance Analysis

All data is taken directly from the Cluster Science Archive (CSA), and is expressed in GSE coordinates. Whilst this coordinate system is convenient, it is not physically relevant to the foreshock. The data is therefore transformed through *minimum variance analysis (MVA)*. The aim of MVA is to ascertain from single-probe data, an estimate for the direction normal to a one-dimensional, or approximately one-dimensional, current-layer, wavefront or other transition layer in a plasma. For the present study, MVA is employed to ascertain the approximate direction of wave propagation from magnetic field data. We shall define a coordinate system (x, y, z), such that the z axis points along the direction of the wavefront normal, which we shall denote by $\hat{n}$. Assuming the wavefront is completely one-dimensional, $\frac{\partial}{\partial x} = 0, \frac{\partial}{\partial y} = 0$, and the divergence of $\vec{B}$ through the front can be written [139]:

$$\vec{\nabla} \cdot \vec{B} = \frac{\partial B_z}{\partial z} = 0 \tag{2.3}$$

Hence, B_z is independent of z. We may deduce from Faraday's law, equation (1.17), that the field component B_z must also be time-independent. A spacecraft traversing this wavefront would then observe a strictly constant value of B_z. In this ideal case, only three measurements are needed to determine $\hat{n}$. These values we shall denote by $\vec{B}^{(1)}, \vec{B}^{(2)}$ and $\vec{B}^{(3)}$. Typically, $\vec{B}^{(1)}$ and $\vec{B}^{(3)}$ are measured on either side of the wavefront, and $\vec{B}^{(2)}$ is measured near the middle of it. The time and z independent B_z condition is akin to ensuring

$$\vec{B}^{(1)} \cdot \hat{n} = \vec{B}^{(1)} \cdot \hat{n} = \vec{B}^{(1)} \cdot \hat{n} \tag{2.4}$$

the vectors comprising $(\vec{B}^{(1)} - \vec{B}^{(2)})$ and $(\vec{B}^{(2)} - \vec{B}^{(3)})$ are tangential to the layer, so their cross product must be along $\hat{n}$. Hence, we can find $\hat{n}$ by:

$$\hat{n} = \pm \frac{(\vec{B}^{(1)} - \vec{B}^{(2)}) \times (\vec{B}^{(2)} - \vec{B}^{(3)})}{|(\vec{B}^{(1)} - \vec{B}^{(2)}) \times (\vec{B}^{(2)} - \vec{B}^{(3)})|} \tag{2.5}$$

The condition $\vec{B} \cdot \hat{n} = 0$, which is occasionally made in MVA, is not strictly necessary [140]. We may use the above to calculate B_n, the normal field component:

$$B_n = \vec{B} \cdot \hat{n} = \pm \frac{\vec{B}^{(1)} \cdot (\vec{B}^{(2)} \times \vec{B}^{(3)})}{|(\vec{B}^{(1)} - \vec{B}^{(2)}) \times (\vec{B}^{(2)} - \vec{B}^{(3)})|} \tag{2.6}$$

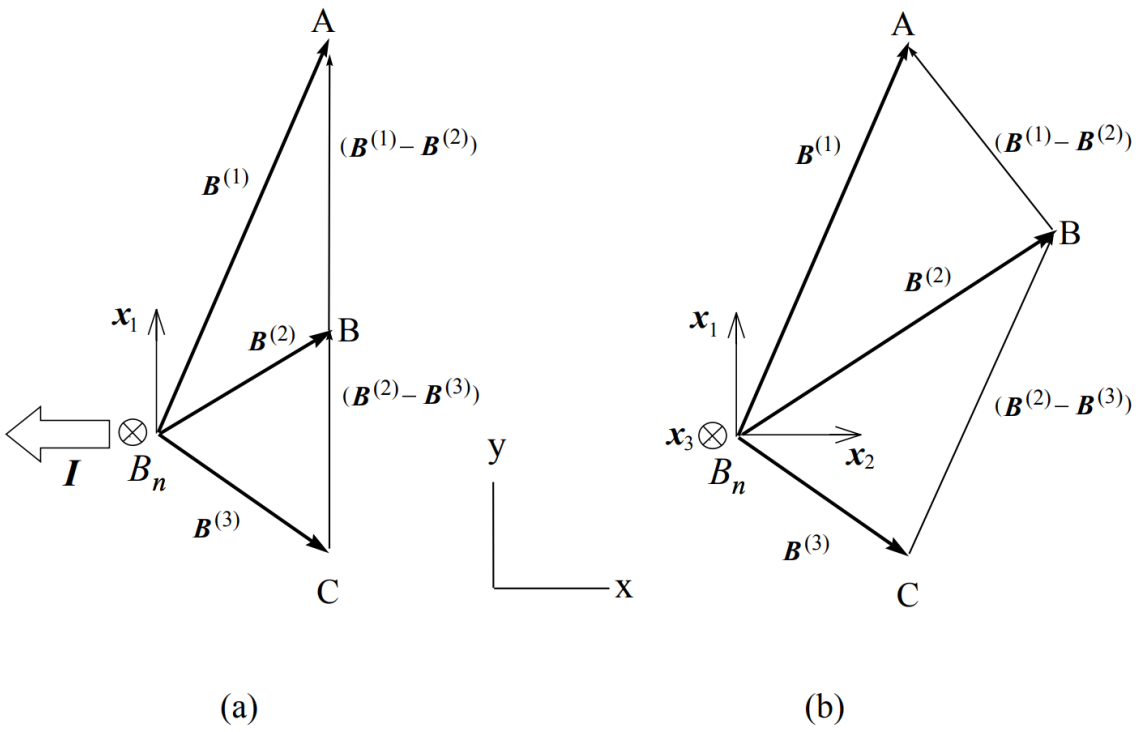

Figure 2.5: Projection of the three magnetic field vectors $\vec{B}^{(1)}, \vec{B}^{(2)}$ and $\vec{B}^{(3)}$ onto the wavefront plane. $\vec{B}^{(1)}$ is measured before the wavefront, $\vec{B}^{(2)}$ within it, and $\vec{B}^{(3)}$ after traversing it. Each vector has the same component B_n that points along the normal vector, into the paper. Difference vectors are therefore tangential. In panel (a), the difference vectors are colinear, so their cross product does not have a definite direction. In (b), the difference vectors are misaligned, and hence their cross product defines $\hat{n}$. The eigenvector triads $(\vec{x}_1, \vec{x}_2, \vec{x}_3)$, where $\vec{x}_3 = \hat{n}$, is also shown. (From [139])

Exactly three vectors are required to obtain a unique determination of $\hat{n}$ and B_n, providing that the difference vectors in the denominator of equation (2.5),$(\vec{B}^{(1)} - \vec{B}^{(2)})$ and $(\vec{B}^{(2)} - \vec{B}^{(3)})$ are not aligned. Figure (2.5) shows two configurations of $\vec{B}^{(1)}, \vec{B}^{(2)}$ and $\vec{B}^{(3)}$, as well as their separation vectors. Panel (a) shows the difference vectors aligned. In this case, the line ABC does lie in the tangent plane to the wavefront, but crucially, any vector perpendicular to ABC will satisfy equation (2.5). Hence, we must ensure the lines AB and BC are coplanar, but not aligned, to ensure that their cross-product points only along $\hat{n}$. It should also be noted here that the form of equation (2.5) prohibits the difference vectors from being too small; if they both approach zero then a reliable measure of $\hat{n}$ becomes impossible.

A real propagating wavefront is likely to have a time-dependent normal owing, for example, to dispersion effects.Therefore, multiple measurements of a propagating wavefront will give different values of the vector $\hat{n}$. The MVA technique is designed to mitigate the impact of these factors by identifying the direction in space along which the field-component

set $\left\{\vec{B}^m \cdot \hat{n}\right\}, (m = 1,2,3...M)$ has minimum variance. Hence, $\hat{n}$ is determined by:

$$\sigma^2 = \frac{1}{M}\sum_{m=1}^{M} |\left(\vec{B}^{(m)} - < \vec{B} >\right) \cdot \hat{n}|^2 \tag{2.7}$$

Where $< \vec{B} >$ is the average field:

$$\langle \vec{B} \rangle = \frac{1}{M}\sum_{m=1}^{M} \vec{B}^{(m)} \tag{2.8}$$

The minimization is performed using the method of the Langrange multiplier, subject to the normalisation constraint, $|\hat{n}|^2 = 1$. We therefore seek the solution of the set of three homogeneous linear equations [141]:

$$\frac{\partial}{\partial n_X}\left(\sigma^2 - \lambda(|\hat{n}|^2 - 1)\right) = 0 \tag{2.9}$$

$$\frac{\partial}{\partial n_Y}\left(\sigma^2 - \lambda(|\hat{n}|^2 - 1)\right) = 0 \tag{2.10}$$

$$\frac{\partial}{\partial n_Z}\left(\sigma^2 - \lambda(|\hat{n}|^2 - 1)\right) = 0 \tag{2.11}$$

Here, $\hat{n}$ is represented by its three components (n_X, n_Y, n_Z) along the three axes of the GSE coordinate system (figure (2.5). When the above differentiations have been performed, the equations produced may be written in matrix form:

$$\sum_{\nu=1}^{3} M^B_{\mu\nu} = \lambda n_\mu \tag{2.12}$$

where $\mu, \nu = 1,2,3$, denoting the GSE components and

$$M^B_{\mu\nu} \equiv \langle B_\mu B_\nu \rangle - \langle B_\mu \rangle \langle B_\nu \rangle \tag{2.13}$$

is the magnetic variance matrix. We see from equations (2.12) and (2.13) that the allowed values of λ are the eigenvalues $\lambda_1, \lambda_2, \lambda_3$ of $M^B_{\mu\nu}$. Since $M^B_{\mu\nu}$ is real, the eigenvalues are all real and the eigenvectors, defined $\vec{x}_1, \vec{x}_2$ and $\vec{x}_3$, must be orthogonal. These eigenvectors represent the directions along the maximum, intermediate and minimum variance of the field components along each vector. The λ values represent the actual variances. Hence:

$$M^B_{ii} = \langle B_i B_i \rangle - \langle B_i \rangle \langle B_i \rangle = \lambda_i \tag{2.14}$$

Thus, by constructing the matrix $M^B_{\mu\nu}$ as in equation (2.13) in terms of the GSE coordinates, and then finding the eigenvector $\vec{x}_3$, for which the variance λ_3 is minimized, we obtain an estimate for the wavefront normal vector $\hat{n}$. The value of λ_3 is the magnetic field variance itself, and can be used as a measure of the accuracy of the MVA rotation. The remaining eigenvectors, $\vec{x}_1$ and $\vec{x}_2$, represent the vectors transverse to the direction of propagation, completing a right-handed orthonormal set.

2.3.2 Beall Method

The MVA determines the direction, but not magnitude, of the wavevector. Beall [142] developed a statistical technique for determining the value and associated power of the wavenumber using two-probe data. Generally, for a zero-mean, stationary, homogeneous random field $\phi(x,t)$, a function of time and one spatial dimension, we may expand the field as a Fourier series during a time interval T and within a region of space L as:

$$\phi(x,t) = \int \frac{d\omega}{2\pi} \Phi(x,\omega) e^{-i\omega t} \tag{2.15}$$

$$\Phi(x,\omega) = \int_{T/2}^{T/2} dt\, \phi(x,t) e^{i\omega t} \tag{2.16}$$

$$\Phi(k,\omega) = \int_{L/2}^{L/2} dx\, \Phi(x,\omega) e^{-ikx} \tag{2.17}$$

Where Φ is the Fourier amplitude of ϕ. We define the spectral density as:

$$S(k,\omega) = \lim_{L,T\to\infty} \frac{1}{LT} \langle |\Phi(k,\omega)|^2 \rangle \tag{2.18}$$

which describes the distribution of power across modes. The cross-spectral density is defined:

$$\begin{aligned} H(\chi,\omega) &= \lim_{T\to\infty} \frac{1}{T} \langle \Phi^*(x,\omega)\Phi(x+\chi,\omega) \rangle \\ &= \int \frac{dk}{2\pi} S(k,\omega) e^{ik\chi} \end{aligned} \tag{2.19}$$

and is a measure of the power of the modes across both probes, equivalent to the Fourier transform of the cross-correlation. Here, χ is the distance between the probes. When

$\chi \to 0$, the cross-spectral density becomes the frequency spectral density:

$$H(0,\omega) = S(\omega) = \int dk\, S(k,\omega) \tag{2.20}$$

Let us assume that $\phi(x,\omega)$ represents a physical property subject to a deterministic linear partial differential equation in x and t. The plane wave description of equations (1.47), subject to (1.54) and (1.55) provide a decent example. In this case, the dispersion relation, $k(\omega)$, is a one-to-one function and the spectral density will take the form:

$$S(k,\omega) = S(\omega)\delta[k - k(\omega)] \tag{2.21}$$

We may calculate the dispersion relation fairly simply for this case. Firstly, we represent specific Fourier modes in polar notation;

$$\Phi(x,\omega) = a(x,\omega)e^{i\theta(x,\omega)} \tag{2.22}$$

where

$$a(x,\omega) = |\Phi(x,\omega)| \tag{2.23}$$

is the Fourier amplitude. The phase of the mode is represented by $\theta(x,\omega)$, which is calculable as:

$$\theta(x,\omega) = \tan^{-1}\left[\frac{\mathrm{Im}(\Phi(x,\omega))}{\mathrm{Re}(\Phi(x,\omega))}\right] \tag{2.24}$$

Where $\mathrm{Im}(\Phi(x,\omega))$ and $\mathrm{Re}(\Phi(x,\omega))$ represent taking the imaginary and real parts of $\Phi(x,\omega)$. The wavenumber is defined:

$$K(x,\omega) = \frac{\partial\theta(x,\omega)}{\partial x} \tag{2.25}$$

So for two fixed probes at x_1 and x_2;

$$K(x,\omega) \approx \frac{\Theta(x_2,\omega) - \Theta(x_1,\omega)}{x_2 - x_1} \tag{2.26}$$

where $x = (x_1 + x_2)/2$. Wavenumbers calculated in this fashion are restricted to the interval defined by the limits $\pm\frac{\pi}{\chi}$, to avoid indeterminancies of $\frac{2\pi n}{\chi}$. For the plane wave example,

the frequency of the propagating mode is constant in space and so $K(x,\omega) = k(\omega)$.

As has been demonstrated in section (1.3.3) and figures (1.3) and (1.4), real plasma systems exhibit wave behaviour that does not obey a one-to-one frequency-wavenumber dependence, and the power in a specific frequency band $\omega \rightarrow \omega + \Delta\omega$ may be distributed broadly in wavenumber space. This broadening is further exacerbated by the effects of turbulence and other non-linear phenomena in the ion foreshock. Beall et. al. [142] introduced the conditional wavenumber spectral density, $s(k|\omega)$:

$$s(k|\omega) = \frac{S(k,\omega)}{S(\omega)} \tag{2.27}$$

The value of $s(k|\omega)\Delta k$ is the fraction of the power at the frequency ω that is contained within fluctuations in $\phi(x,t)$ in the range of wavenumbers between k and $k+\Delta k$. The concept is analogous to that of conditional probability. If A and B are events that are equally likely to occur, then the conditional probability is defined $P(A|B) = P(A,B)/P(B)$, and represents the expected fraction of the times when B occurs that include the simultaneous occurrence of A. If we interpret the spectral density as a density of "quasiparticles" in frequency and wavenumber space, then $S(k,\omega)\Delta k\Delta\omega/\langle\phi^2\rangle$ is the probability that one of these quasiparticles, selected at random, will have a wavenumber in the range $k+\Delta k$ and a frequency within $\omega+\Delta\omega$. We can determine a relation between the cross-spectral density and the conditional wavenumber spectral density from equations (2.27) and (2.19):

$$\frac{1}{i^n H(0,\omega)}\left(\frac{\partial^n H(\chi,\omega)}{\partial\chi^n}\right) = \int dk\; k^n s(k|\omega) \tag{2.28}$$

Extending this notion of quasiparticles, we may model the fluctuations of $\phi(x,t)$ as a superposition of wave packets that satisfy [143]:

$$\left|\frac{1}{a(x,\omega)}\frac{\partial^n a(x,\omega)}{\partial x^n}\right| < \left|K^n(x,\omega)\right| \tag{2.29}$$

$$\left|\frac{1}{K(x,\omega)}\frac{\partial^n K(x,\omega)}{\partial x^n}\right| < \left|K^n(x,\omega)\right| \tag{2.30}$$

These oscillations are approximately sinusoidal in space and time, with slowly varying amplitudes and wavenumbers [144]. The power of a single realization, $|\Phi(k,\omega_0)^2|$, is then concentrated at both a given frequency, ω_0 and wavenumber, k_0, although the statistically averaged power, $<|\Phi(k,\omega_0)^2|>$ may be broadly distributed over different values of the wavenumber. We can then deduce from equation (2.19):

$$\begin{aligned}\frac{\partial^n H(\chi,\omega)}{\partial \chi^n} &= \lim_{T\to\infty}\frac{1}{T}\frac{\partial^n}{\partial \chi^n}\langle \Phi^*(x_1,\omega)\Phi(x_2,\omega)\rangle \\ &= \lim_{T\to\infty}\frac{1}{T}\langle \sum_{m=0}^{n}\binom{n}{m}\frac{\partial^{n-m}\Phi^*(x_1,\chi)}{(-2\partial x_1)^{n-m}}\ \frac{\partial^m \Phi(x_2,\omega)}{(2\partial x_2)^m}\rangle\end{aligned} \tag{2.31}$$

If we consider $a^2(x,\omega)$ and $K(x,\omega)$ to be random variables with joint probability density $f(a^2,K;\omega)$, then we may rewrite the moments above as:

$$\begin{aligned}\lim_{T\to\infty}\frac{1}{T}\langle a^2(x,\omega)K^n(x,\omega)\rangle &= \lim_{T\to\infty}\frac{1}{T}\int\int da^2\ dK\ a^2\ K^n\ f(a^2,K;\omega) \\ &= \int dK\ K^n\ S_l(K,\omega)\end{aligned} \tag{2.32}$$

Where we define the *local wavenumber and frequency spectral density* $S_l(K,\omega)$ as:

$$S_l(K,\omega) = \lim_{T\to\infty}\frac{1}{T}\int da^2\ a^2 f(a^2,K;\omega) \tag{2.33}$$

$S_l(K,\omega)$ is the wavenumber and frequency spectral density local to a probe measuring the field $\phi(x,t)$. Dividing equation (2.32) by $S(\omega)$, we have:

$$\frac{1}{H(0,\omega)}\frac{\partial^n H(\chi,\omega)}{\partial \chi^n} = \int dK\ K^n\ s_l(K|\omega) \tag{2.34}$$

Where

$$s_l(K|\omega) = \frac{S_l(K,\omega)}{S(\omega)} \tag{2.35}$$

And hence, if equations (2.29) and (2.30) hold:

$$s(k|\omega) = s_l(k,\omega) \tag{2.36}$$

and the local wavenumber and frequency spectral density is identical to the conventional wavenumber and frequency spectral density. Thus, if the system that we wish to study can be faithfully reproduced as a superposition of wavepackets, that is; if equations (2.29) and (2.30) are satisfied, then $S_l(K,\omega)$ yields an estimate of the conventional spectral density $S(k,\omega)$, which can be used to build a wavenumber-frequency plane representative of a

dispersion relation.

2.3.3 The Wavelet Transform

The power of the plasma sampled by the Cluster probes is spread unevenly amongst various types of modes and structures, and so to capture an accurate representation of any one phenomena it is necessary to take multiple data ensembles to satisfy the terms in the expectation operators of (2.19). This ensures that the method, which is designed to capture power over multiple modes, can capture the low-power ULF modes without being dominated by relatively more powerful structures. These data ensembles were firstly created by using a windowed Fourier technique. This involves splitting each interval into smaller overlapping windows and computing a separate Fourier transform for each window. This approach requires windows of sufficient length to capture ULF waves (>5 minutes) but if the data is discontinuous in any part of the window, the Fourier decomposition will be inaccurate for the entire window. The minimum window size requirement also means that only intervals which are stationary over the minimum window length can be investigated.

Consequently, we seek an alternative technique that allows for the analysis of shorter intervals but not at the expense of spectral range. One such technique is the wavelet transform. Whilst the Fourier transform reproduces an input signal using a superposition of infinite sinusoids; that is, functions localized in Fourier space; the wavelet transform decomposes a signal using damped sinusoids; functions localized in both real and Fourier space. Generally, the wavelet transform can be expressed as [145]

$$\Phi(a,\Delta x) = \frac{1}{a^{\frac{1}{2}}}\int_{-\infty}^{\infty} \phi(x)\ \psi^*\left(\frac{x-\Delta x}{a}\right)\ dx \tag{2.37}$$

where Δx represents a lag and a a scale, of the input signal, $\phi(t)$ and $\psi^*_{a,b}(x)$ is some function, called the *mother wavelet*. In the continuous wavelet transform, the transform effects a convolution of the input signal with arbitrary scales of the mother wavelet. If the input signal is of length N, then the output will have dimensions $N \times M$, where M is the number of scales chosen by the wavelet, and will represent the time-frequency domain directly. The choice of mother wavelet is the most important factor in this technique and is the primary method for changing the frequency/time sensitivity. The Morlet wavelet, for example, consisting of a damped cosine wave, allows for a sharp frequency resolution but a poorer one in time. In contrast, the derivative of Gaussian (DoG) wavelet results in a decent temporal localization but a reduced frequency resolution [146]. The wavelets used in this chapter are the generalized Morse wavelets (GMWs). These are a family of exactly analytical wavelets, and are complex-valued. The complex nature of these wavelets makes

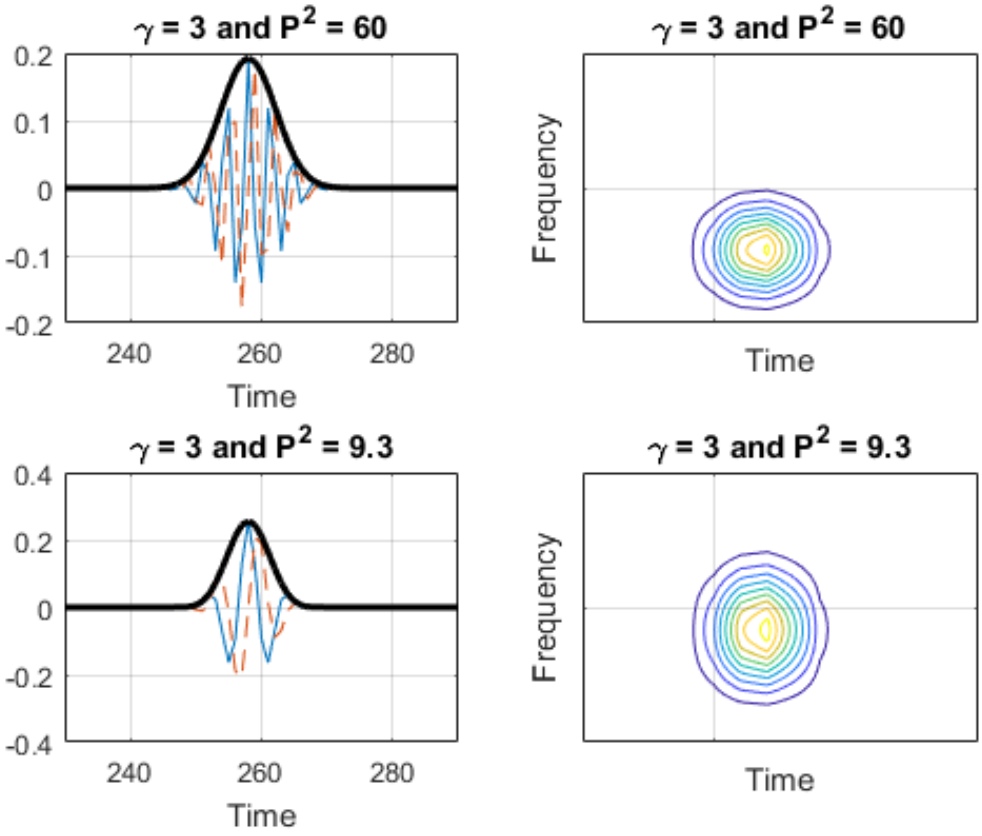

Figure 2.6: Generalized Morse wavelets (GMWs), defined by equation (2.38). The blue and red dotted lines are the real and imaginary component respectively. The spread in the frequency-time plane is shown in the diagrams on the right.

them ideal for analysing phasal relationships in time series, and therefore a good fit for the purpose of measuring the phase differences of equation (2.26) [147]. GMWs are useful for analyzing signals of time-varying amplitude and frequency, and with localized discontinuities [148]. They are therefore a useful choice for analyzing foreshock data in general. The Fourier transform of these wavelets is:

$$\Psi(\omega) = U(\omega)\ a_{\beta,\gamma}\omega^{\beta}e^{-\omega^{\gamma}} \tag{2.38}$$

where $a_{\beta,\gamma}$ is a normalization constant, γ is a variable that determines the symmetry of the wavelet, and β is the decay or compactness parameter. The frequency components that make up the wavelets are adjustable and the duration of the input signal determines how many oscillations of the peak frequency can fit into the time-domain wavelet's center window. Depictions of the GMWs for varying γ and $P = \sqrt{\beta\gamma}$ are shown in figure (2.6). For the analysis, wavelets of $\gamma = 3,\ P^2 = 60$ are used.

2.3.4 Doppler Shift

In order to identify the plasma dispersions in the plasma rest frame, the wavenumbers must be Doppler shifted to correction for the solar wind advection, subject to [149]:

$$\omega_{pl} = \omega_{sc} - k_{\chi} < V_{sw} > \cos\theta_{V,k} \tag{2.39}$$

where ω_{pl} is the frequency in the plasma rest frame, ω_{sc} the measured frequency in the spacecraft frame, $< V_{sw} >$ the time-averaged solar wind velocity magnitude for the interval and $\theta_{V,k}$ is the angle between χ and $\vec{V_{sw}}$. In practice, since a lot of the power peaks are over-resolved, it is better to selectively apply the shift to (ω, k) pairs then to the entire spectrum.

We may calculate $\theta_{V,k}$ from the results of the MVA. Since the MVA provides an estimate for the propagation of the wave relative to the magnetic field as a function of frequency, and the angle between the solar wind velocity and the magnetic field vector is calculable from Cluster data (see table (2.1), the angle between the propagation direction and the solar wind velocity is also known. Equation (2.39) can produce negative frequencies. We have chosen to abide by the convention whereby ω is always positive and a negative ω represents a wave travelling antiparallel to k, ie, if $\omega < 0$, then ω is taken as positive and the sign of the associated wave vector is reversed.

2.3.5 Process

The initial task of the methodology is to identify a pair of satellites that show similar traces of wave activity in their FGM data. The magnetic field measurements are then rotated from GSE into a coordinate system that centres on the direction of the wavevector, using the minimum variance analysis outlined in section (2.3.1), in order to separate the FGM data into components perpendicular and parallel to the average wavevector. The rotated data is then subject to a wavelet decomposition (section (2.3.3)), giving a time-frequency power spectra, of a resolution dependent on the properties of the mother wavelet used in the decomposition. The resulting spectra provides n sets of amplitudes for m frequencies, where n is equal to the number of data of the input signal to the wavelet transform, ie; the number of FGM data points of the original signal. The value of m, the total number of frequencies, is smaller and dependent on the parameter of the mother wavelet, but is usually ~50. There are therefore n ensembles of frequency amplitudes for each interval, represented by equation (2.23), which are used to calculate the local wavenumber and frequency spectra as equations (2.24) and (2.25), the powers associated with each mode with equation (2.18), and their conditional wavenumber spectral densities, equa-

tion (2.18). This produces a set of n ensembles of the wave vector, $K(\chi,\omega)$, the power associated with each mode at the j^{th} satellite, $S_j(\omega)$, and the cross-spectral density $H(\chi,\omega)$. These quantities are ensemble averaged such that:

$$\hat{H}(\chi,\omega) = \frac{1}{n}\sum_{i=1}^{n} \Phi_i^*(x_1,\omega)\Phi_i(x_2,\omega) \tag{2.40}$$

$$\hat{S}_1(\omega) = \frac{1}{n}\sum_{i=1}^{n} \Phi_i^*(x_1,\omega)\Phi_i(x_1,\omega) \tag{2.41}$$

$$\hat{S}_2(\omega) = \frac{1}{n}\sum_{i=1}^{n} \Phi_i^*(x_2,\omega)\Phi_i(x_2,\omega) \tag{2.42}$$

and the conditional spectrum estimate is:

$$\hat{s}_l(K,\omega) = \frac{\hat{S}_l(K,\omega)}{\frac{1}{2}\left(\hat{S}_1+\hat{S}_2\right)} \tag{2.43}$$

the average of the estimates at each probe. For each ensemble, values are added to the sums of (2.40)-(2.43) at discrete values of the wave vector satisfying $-\frac{\pi}{\chi} \le K(\omega) \le \frac{\pi}{\chi}$, building a histogram of the powers associated at each frequency-wavenumber pair averaged over the two probes. From this histogram, frequency-wavenumber pairs can be individually Doppler shifted to the spacecraft frame according to equation (2.39). The resulting shifted pairs can be compared to solutions of the cold plasma dispersion relation to identify the mode of the oscillation.

2.4 Results and Discussion

Figure (2.7) shows images of the cumulative power $\hat{S}$, using the Fourier-window technique. Angular frequencies have been normalized by the ion gyrofrequency, ω_{ci}, and the wavenumbers by the proton gyroradius, r_p, calculated using the proton temperatures perpendicular to the magnetic field from CIA-HIA. The frequency range of figure (2.7) is much lower than the Nyquist frequency (11.2Hz), since for I1, $\omega_{ci} \approx 0.11$Hz, and for I2, $\omega_{ci} \approx 0.16$Hz. This frequency range is chosen to show the complete domain over which correlations between ω and k are clearly visible. For frequencies greater than $5\omega_{ci}$, the turbulent dynamics dominate and the spectrum becomes random and featureless. The Fourier spectra are created with ~100 strongly overlapping (~75%) windows of 5 minutes length. The data for each realization is linearly detrended and the mean is subtracted before the Fourier components are calculated.

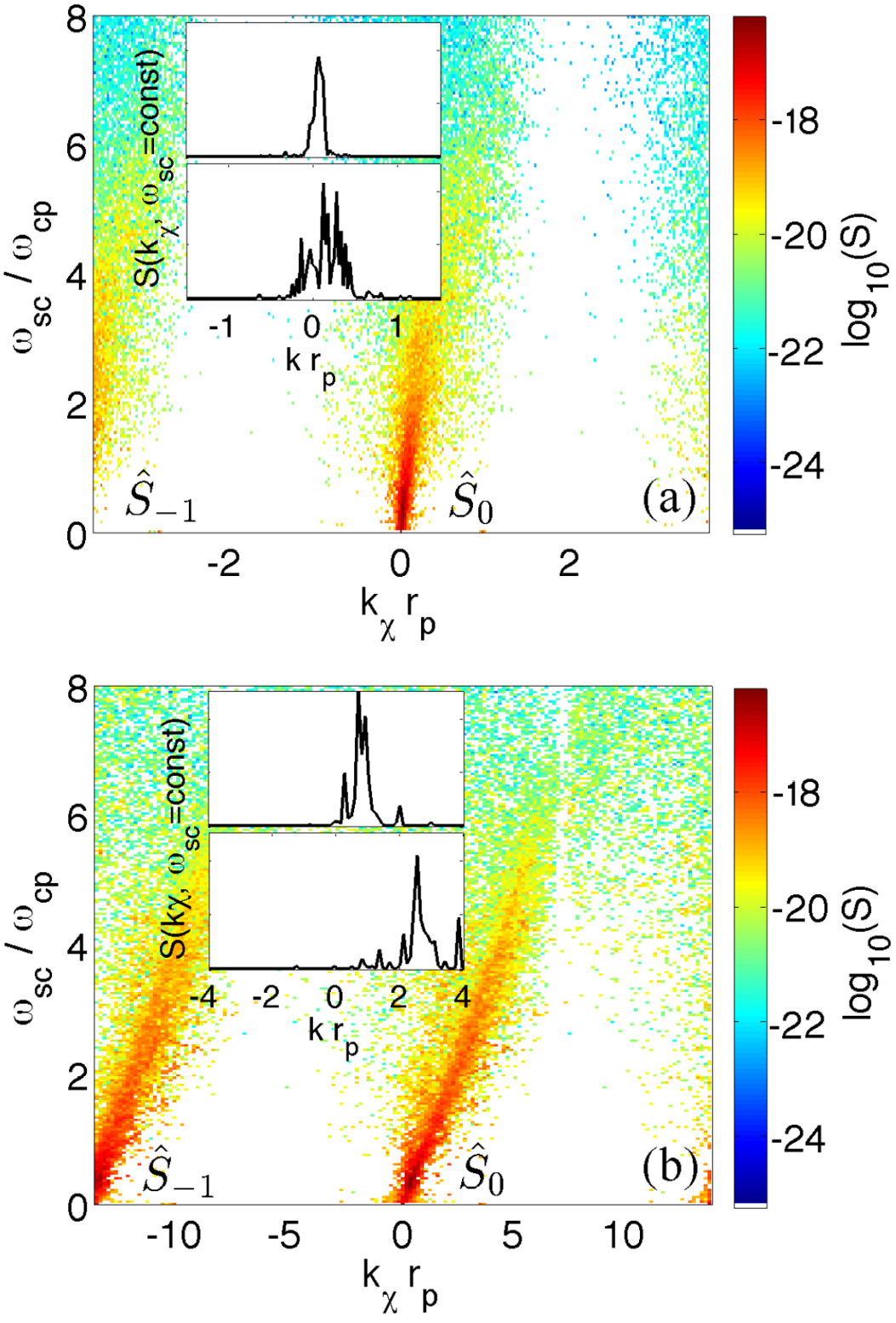

Figure 2.7: Histograms of the normalized cumulative power on the normalized frequency-wavenumber plane for interval I1, top, and I2, bottom. Symbols $\hat{S}_0$ and $\hat{S}_{-1}$ refer to wavenumbers obtained from the phase difference $\Delta\theta$ and $\Delta\theta - 2\pi$ respectively. Insets show cuts through $\hat{S}_0$ for two fixed frequencies, the top pair $\omega \approx 0.35\omega_{ci}$ and bottom pair $\omega \approx 2.25\omega_{ci}$

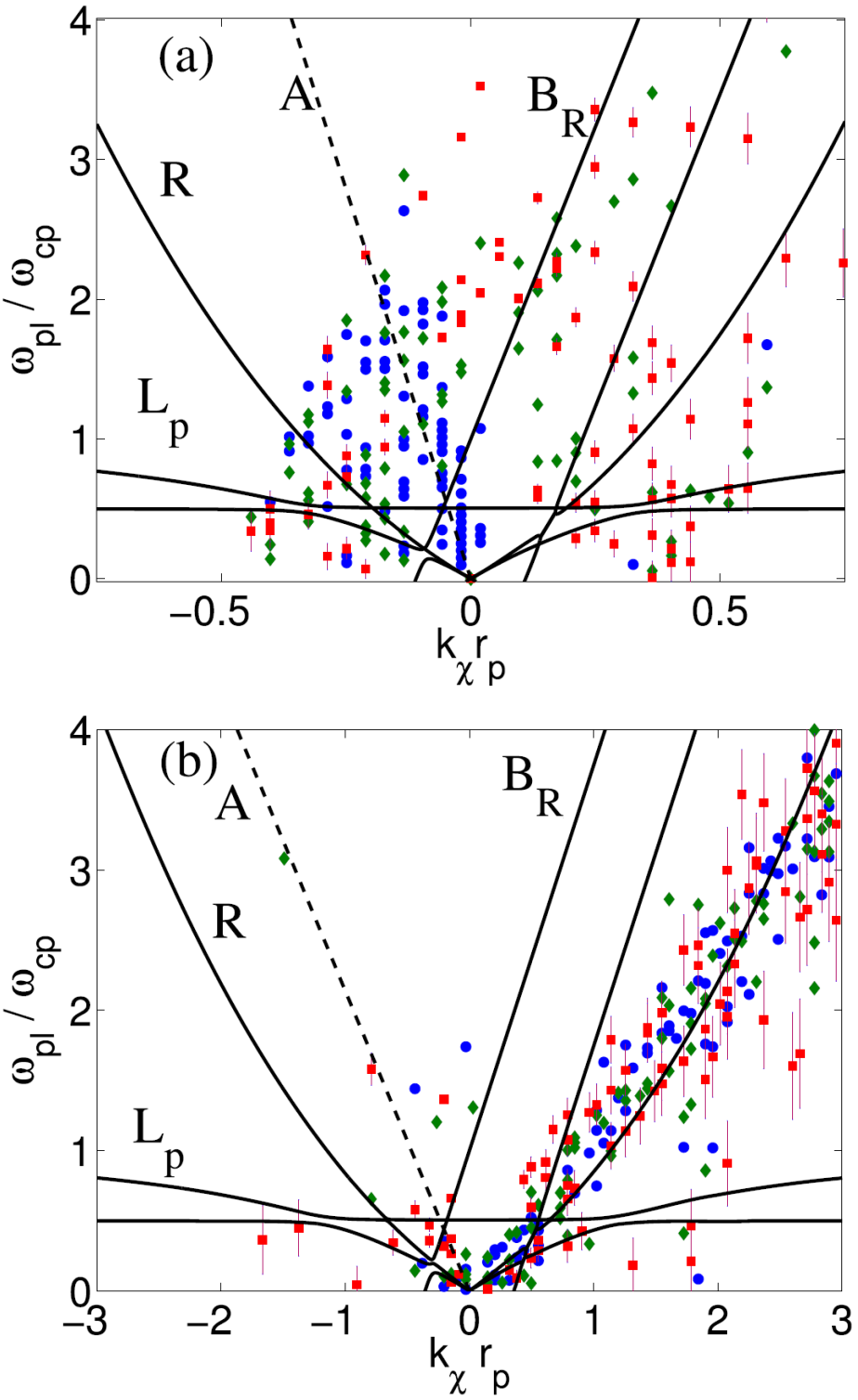

Figure 2.8: In solid points: Doppler-corrected estimates of dispersion relations obtained for interval I1 (a) and I2 (b), and in solid lines: cold plasma dispersion relations as a function of wave vector amplitude. Symbols correspond to different power maxima in $\hat{S}$; highest power: blue circles, second highest: green diamonds, third highest: red squares. Errors are calculated from the uncertainty in the Doppler shift calculation. The solid line indicators are as follows: R - fast magnetosonic mode, A - static structures in the solar wind, B_R - beam resonant modes, L_P - resonant modes.

The $2n\pi$ ambiguity of the phase is demonstrated in figure (2.7) by the repeated pattern of the dispersion relation into $\hat{S}_0$ and $\hat{S}_{-1}$. This has been obtained with an artificial extension to the wavenumbers to the range $(-2\pi/\chi,\ +2\pi/\chi)$, normalized to the proton Larmor radius. The observed wavevectors are positive, consistent with propagation from C3 to C4, and by inspection of figure (2.7), the data does not support phase shifts greater than π. The analysis is then confined to the data between $(-\pi/\chi,\ +\pi/\chi)$, which corresponds to wavelengths between $(-2.5,\ 2.5)\times 10^4$m in SI units. This range is divided into 94 equally spaced bins for I1, and 120 for I2. The choice for the number of bins is not arbitrary; if the number is too large, the peaks become over-resolved, the power of each peak is spread amongst a wide array of wavevectors, and the Doppler correction becomes inaccurate. The colour scale of figures (2.7) is $\log_{10}(\hat{S}_0)$.

Figure (2.7) shows that a clear trend between ω and k can be established with the method, and also demonstrates the extent to which the Doppler shift influences the result. The striking feature of $\hat{S}_0$is the large leaning feature that extends from $k = 0$. The two insets of figure (2.7) show cuts through $\hat{S}_0$ at $\omega \approx 0.35\omega_{ci}$, top, and $\omega \approx 2.25\omega_{ci}$, bottom. These cuts reveal the internal structure in the histogram that is hidden in the central peak; multiple peaks are determined, of varying heights, corresponding to different dispersion relations. To identify which dispersion relation these peaks belong to, the three highest peaks are selected and shifted according to equation (2.39). The minimum variance analysis is used to find the angle between the time-averaged magnetic field and the wave vector, $\theta_{B,k}$, for which we find $\theta_{B,k} \approx 55°$ for I1 and $\theta_{B,k} \approx 60°$ for I2. The minimum variance direction is similar for both intervals. The angle $\theta_{B,k}$ is stable over the intervals, varying only by ~1°. Using known values of the angles between the averaged vectors of the solar wind velocity, $<\vec{V}_{sw}>$, the magnetic field, $<\vec{B}>$ and the spacecraft separation $<\chi>$, we obtain the magnitude of the wave vector and its angle to the average solar wind velocity, $\theta_{V,k}$. This angle is $\theta_{V,k} \approx 44°$ for I1 and $\theta_{V,k} \approx 27°$ for I2. With these angles, the Doppler-corrected dispersion relation is calculated using equation (2.39), shown in figure (2.8). The results are interpreted using dispersion relations calculated for Alfvén, ion cyclotron and magnetoacoustic modes in the presence of an ion beam. Verscharen and Chandran [150] showed that the instability threshold for ULF modes in the presence of an ion beam is a function of the beam velocity, given the following four conditions:

- In order for a wave to be unstable at some value of $k_\parallel$, it cannot undergo cyclotron-resonant interactions with thermal protons at that $k_\parallel$, since such interactions would critically damp the wave.

- A wave of frequency ω_{kr} and parallel wavevector $k_\parallel$ will cause a particle of species s to diffuse in velocity space according to the resonance condition:

Name	Resonance	Threshold
Parallel magnetosonic	$n = -1$	~$1.7v_A$
Oblique magnetosonic	$n = 0$ or n=-1	$\gtrsim 1.7v_A$
Alfvén I	$n = -1$	~$1.2v_A$
Alfvén II	$n = 0$	~$0.8v_A$

Table 2.2: Summary of the unstable modes and their thresholds, expressed in multiples of the Alfvén velocity. "Threshold" refers to the beam speeds. There are two Alfvén instabilities. The resonances pertain to equation (2.44).

$$\omega_{kr} - k_{\parallel} v_{\parallel} = n\omega_{ci} \tag{2.44}$$

where n is an integer. When $n = 0$, this is equivalent to the Landau resonance condition.

- The resonant wave-particle interactions must cause the beam to lose energy, so that the wave can gain energy and grow.
- In order for a wave to be driven unstable by an $n = 1 (n = -1)$ cyclotron resonance, the wave must be left-hand (right-hand) polarized.

Subject to these constraints, the cold plasma dispersion relations are shown in figure (2.8) for a plasma consisting of massless electrons, background protons and alpha particles (He^{++}), in the presence of a proton beam. The beam propagation angle to the magnetic field is taken as 10° and the beam speed is taken as $4.25 < v_A >$ for I1 and $5 < v_A >$ for I2. Figure (2.8) portrays the different power maxima of $\hat{S}_0$ with different symbols; the filled circles, diamonds, and squares represent the greatest, second and third greatest powers for each frequency, before Doppler correction, respectively. The errors are due to the uncertainty in the Doppler shift and are calculated based on the variance of the solar wind velocity.

For interval I2, all three of the most powerful modes are predominantly of the right-hand polarized and magnetoacoustic type, propagating sunwards. There is also a large clustered population of points along the low-frequency proton beam resonant modes, marked B_R. Similarly to I1, some of the secondary and tertiary populations appear to be present near the He^{++} cyclotron branch. Additionally, some of these points have $kr_p > 1$, which may be indicative of a large perpendicular wavenumber component. This result is consistent with previous analyses of the interval [132], and supports numerical results which indicate

that the diffuse ion populations are associated with instabilities that produce both left and right handed modes that propagate sunwards. There is some residual power in the modes propagating toward the bow shock, which we associate with the solar wind. It should be noted that the power in the tertiary peak is significant, ~50% of the power of the primary peak for $\omega < 0.5\omega_{ci}$.

The two intervals exhibit clear differences in their dispersion. For interval I1, the Doppler shift changes the dispersion from $kr_p > 0$ to $kr_p < 0$, showing that the technique is sensitive to the direction of wave propagation. The most powerful fluctuations (filled circles) approximately satisfy the relation $\omega_{pl} \approx k < V_{sw} >$ (dashed line), which implies that these fluctuations propagate, in the spacecraft frame, with velocities much larger than the Alfvén speed. Such unrealistically high-speed fluctuations suggest that the majority of the fluctuations are not plane-wave like, but most likely represent field-aligned structures, advected across the spacecraft [151]. A small fraction of these most powerful fluctuations are also positioned near the fast magnetosonic and Alfvén branches of the dispersion curves for $k < 0$. These waves are therefore travelling towards the bow shock, and are most likely associated with the incoming solar wind. The second and third most powerful peaks are equally distributed between fast magnetosonic and Alfvén modes, propagating both towards and away from the bow shock, as well as the beam resonant mode. The largest value of kr_p for the sunward propagating Alfvén branch is $kr_p = 0.5$, which is larger than the numerically found value for the most unstable left and right hand polarized mode driven by a cold beam. Finally, the dispersion relations show a presence of points near the ion cyclotron branch of ionic Helium, He^{++}, for I1. The low-frequency nature of this branch, and the fact that the alpha particles make up around 5% of the solar wind's total volume, makes is difficult to draw conclusions from these data. However, if the background plasma is capable of supporting Bernstein modes, the minor ion resonance can contribute to the magnetoacoustic cyclotron instability (Dendy 1994).

Figure (2.9) shows $\hat{S}$ for I1 and I2 when the windowed Fourier technique is replaced with the continuous wavelet transform. It can be immediately seen that $\hat{S}$ shows more visible features when calculated using wavelets, especially in I2. The increased spatial resolution of the wavelet decomposition is also shown in the insets of figure (2.9). The main advantage of using wavelets is that the length of the time series that can be adequately resolved is vastly reduced. Whilst ~1 hour of data is necessary for the Fourier window technique to produce enough power variance to build the histogram, for the wavelet transform, this is vastly reduced. We can therefore use wavelets to study the time dependence of the dispersion relation itself, as depicted in figures (2.10-2.11) for I1, I2 respectively. As can be seen, the entire interval actually encompasses periods in which the majority of the power

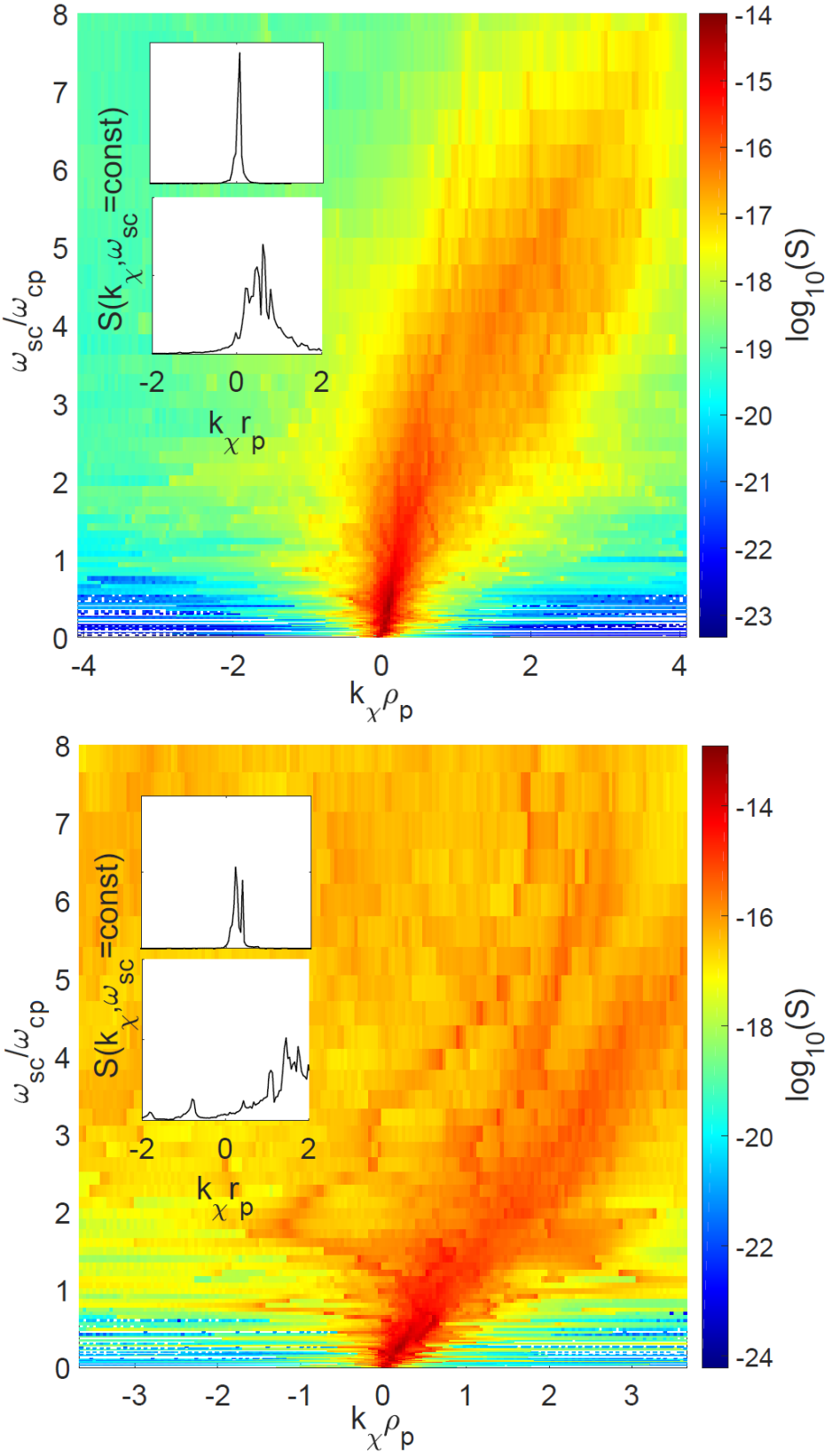

Figure 2.9: Normalized cumulative power histograms for interval I1, top, and I2, bottom, using the wavelet technique. Symbols and insets are as used in figure (2.7)

is alternately directed sunward and antisunward. However, this does not diminish the importance of taking the full interval, as it is still the case that the majority of the power is directed in one direction when averaged over the entire interval, evidenced in figures (2.9). The Doppler-corrected results of figure (2.10) show that for I1, the most potent modes are clustered around the sunward propagating magnetosonic curve, with some power near the structure line. The first subinterval shows some power near the beam resonant mode, but the overall noise of this period means these points are difficult to separate from the more powerful modes. For I1, the remaining two subintervals show more accurate results centred on both the magnetosonic mode and structure line. The second subinterval shows a visible broadening in the unshifted power, accompanied by an increase in the amount of data on the structure line, demonstrating how the nonlinear structures advected by the solar wind can obfuscate the results of the dispersion relation. Figure (2.11) shows three subintervals for I2. These intervals show clear power concentrations amongst the fast mode, the beam resonant mode, and the structure line. The fast mode is consistently the highest-power mode, followed by the beam resonant mode, and then the structure line, except in the case of the last subinterval which is dominated by structures. The tendency of the power to move from the fast and beam resonant modes towards the structure lines as the interval progresses is also marked by a visible shift in the direction of the power plots; as the structures dominate the dispersion lines, the majority of the power changes direction. In both I1 and I2, the transition to turbulence at higher frequencies is difficult to pinpoint in the Fourier technique but is made clearer with the wavelet plots.

Figure (2.12) shows the wavelet power and Doppler-corrected peaks for I3. The interval is split into two parts; the first contains ULF and 1Hz waves in comparable powers, the second is dominated by the 1Hz modes. The turbulent signature of $\hat{S}$ at comparatively low frequencies $\omega > 3\omega_{ci}$ is expressed in the Doppler-corrected plots as the majority of the power in the first segment is along the structure line, in both the positive and negative k directions, with a few points near the fast magnetosonic and Alfvén lines. The method described in section (2.3.5) is based on the linear coherence of modes over two probes and is not sensitive to non-linear processes. The turbulent spectrum at these higher frequencies therefore indicates the possible presence of nonlinear processes. The Doppler-corrected plots (right) of figure (2.12) show that the power is concentrated mainly on the structure line, however, in contrast to I1 and I2, the power is concentrated on both the positively and negatively leaning structure line. For this reason, both structure lines are shown on figure (2.12) whereas only the line that contains the relevant power concentration is shown for figures (2.10) and (2.11). The fact that I3 contains power on both the sunwards and antisunwards structure lines is interpreted as further evidence of nonlinear processes distributing the power across scales, rather than as a physical reflection of the

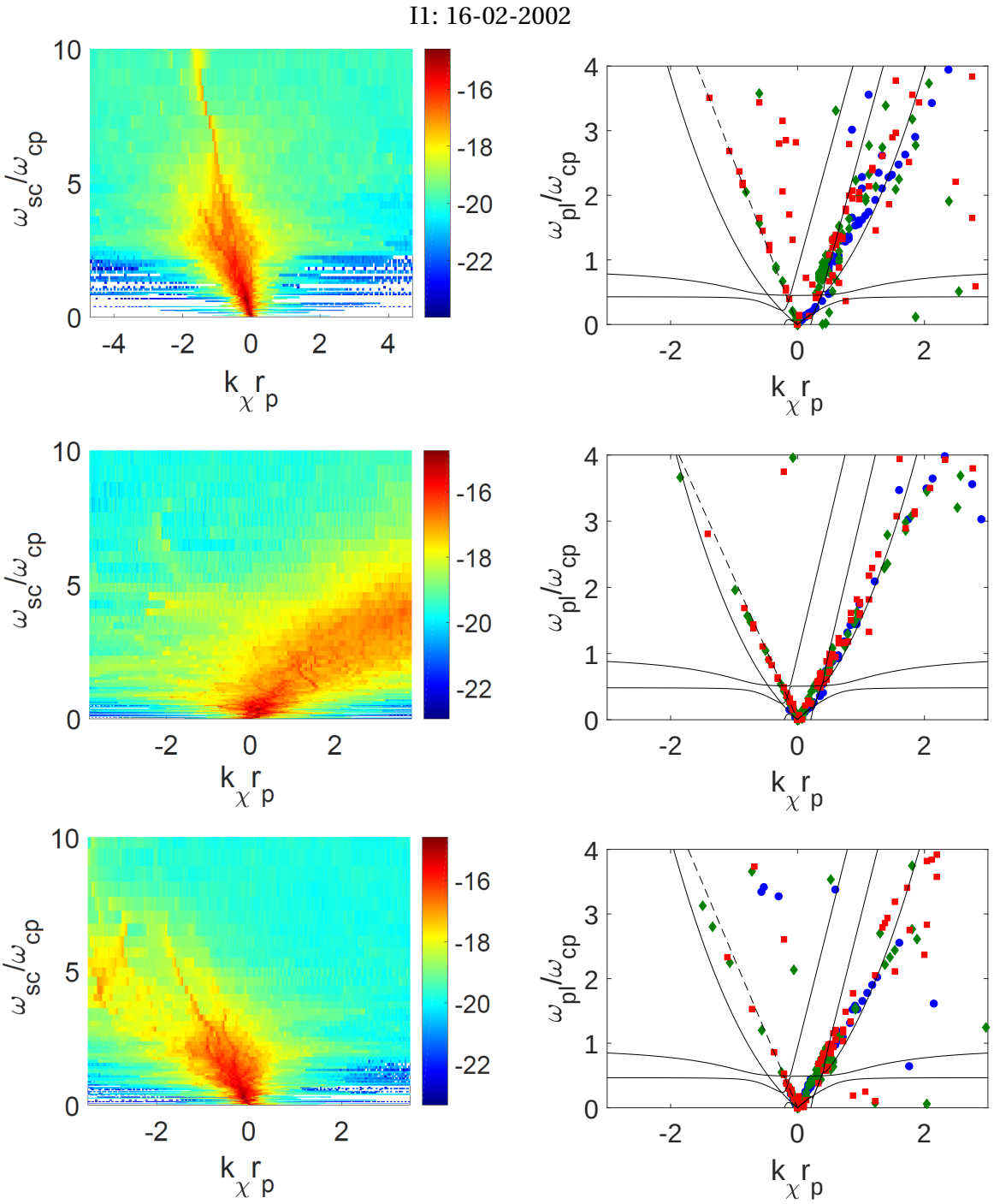

Figure 2.10: Left: $\hat{S}$ calculated using the wavelet technique, showing the time dependence of the power of I1. Top: 07:50-08:10, middle: 08:10-08:50, bottom: 08:50-09:20. The right panels show the corresponding Doppler-corrected powers for the three most powerful peaks.

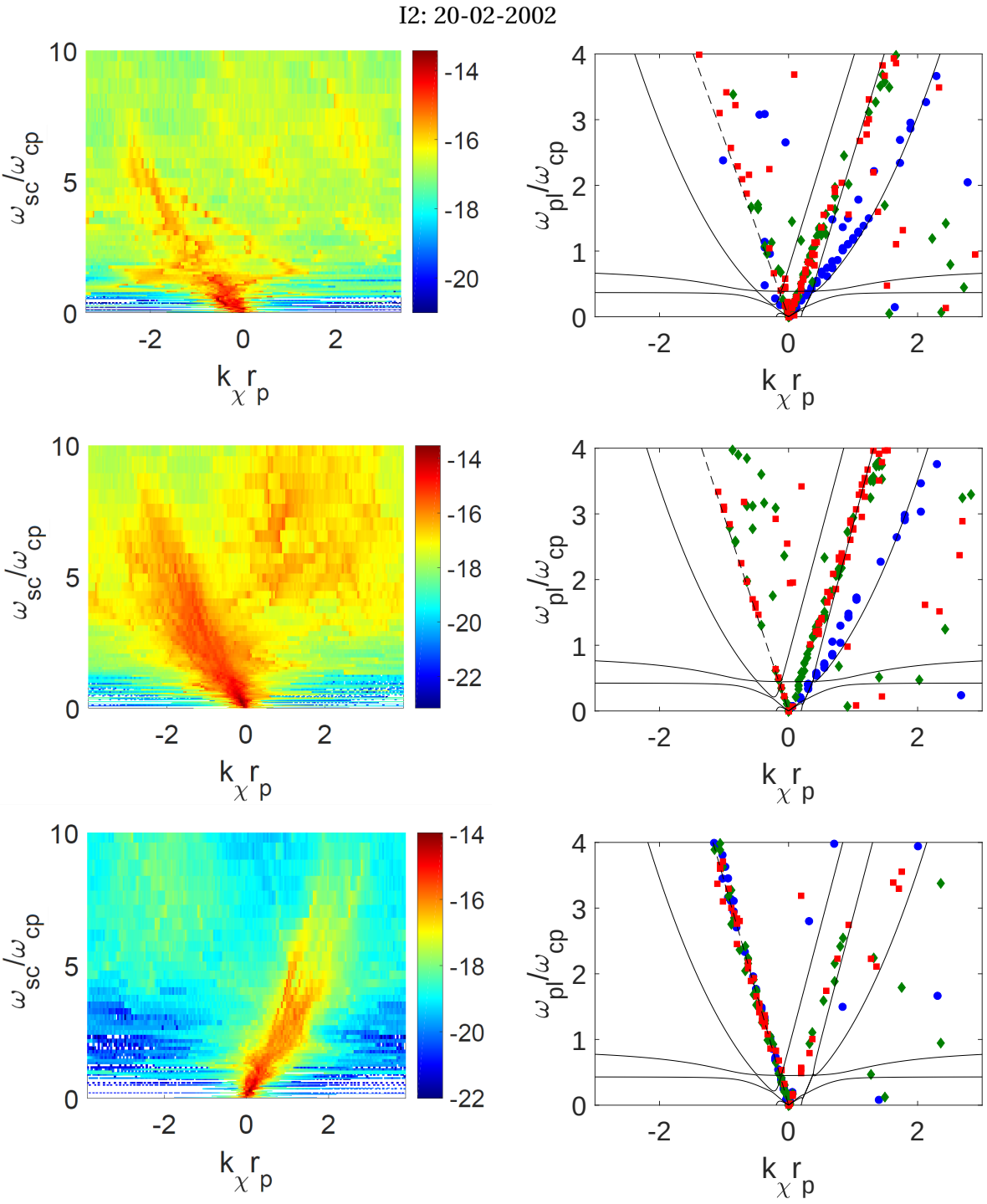

Figure 2.11: Left: $\hat{S}$ calculated using the wavelet technique, showing the time dependence of the power of I2. Top: 16:56-17:10, middle: 17:10-17:40, bottom: 17:40-17:50. The right panels show the corresponding Doppler-corrected powers for the three most powerful peaks.

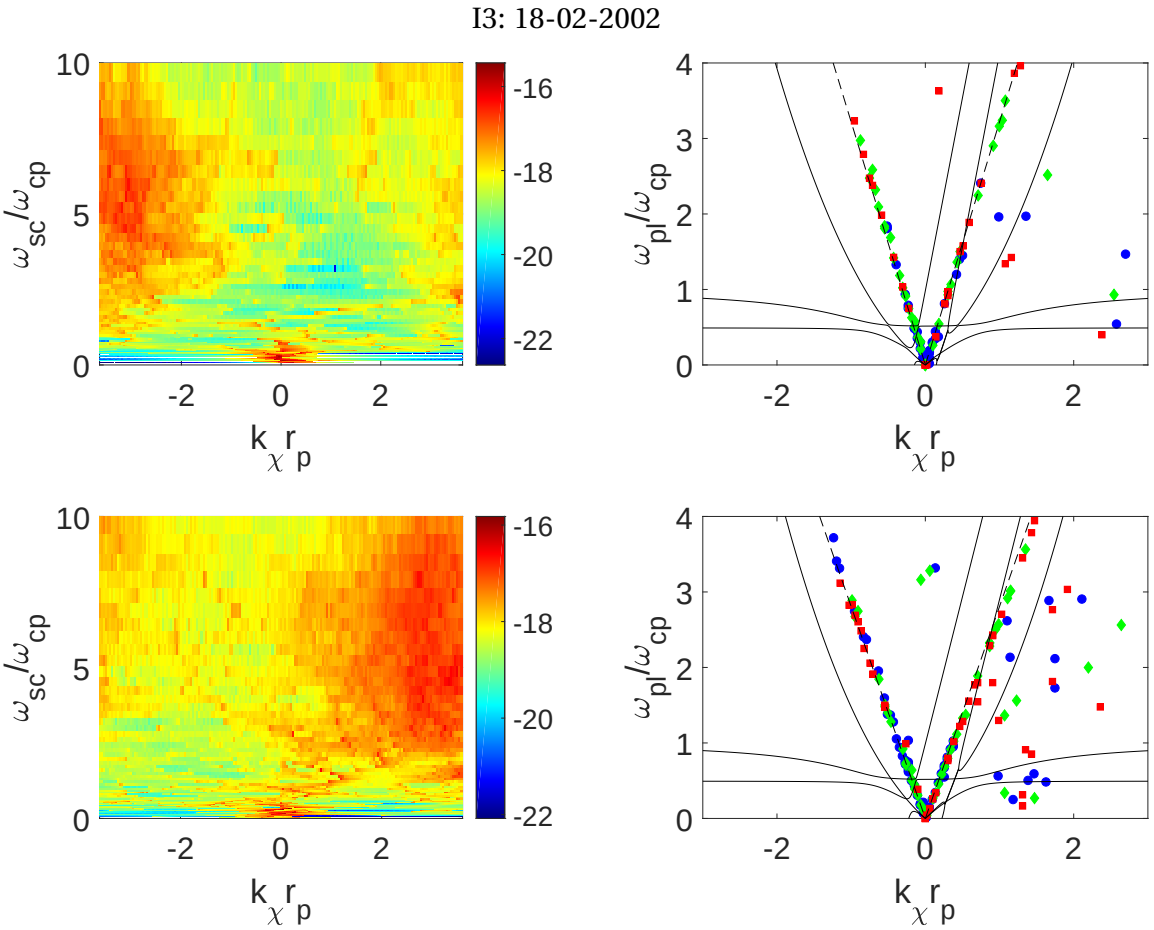

Figure 2.12: $\hat{S}$ plots using the wavelet technique for I3; 18/02/2002, top pair: 13:35-13:40, bottom pair: 13:40-13:50

structures in a manner similar to the FABs. This is evidenced further by the fact that the power is distributed fairly equally between the two lines. Were the structures reflected, the power would be expected to lie more on the line that describes the movement of the solar wind, and less so on the reflection, since only a fraction of the incoming structures would be reflected. Besides the structure lines, power in I3 is also present, in much smaller quantities, firstly along the magnetosonic line, and then on the Alfvén branches. The increased density of points around these wave lines is accompanied by an increase in the visibility of features at $\omega < 2\omega_{ci}$ on the histograms. Power is also present at the level of the He resonance. This is comparable to I1, figure (2.10), consistent with both intervals having a low value of plasma β.

There are four Cluster spacecraft, and therefore six possible pairs of satellites to use for the analysis. An example of a different pairing is given in figure (2.13), showing the Doppler-corrected peaks for the interval I1, repeated for probes C1 and C2 and split into the same intervals as figure (2.10). This pair of probes is situated such that $\theta_{VB} = 14.10°$, $\theta_{\chi V} = 115.05°$, $\theta_{\chi B} = 127.95°$. Comparing to the values for C3 and C4 given in table (2.1), we note that θ_{VB} is similar but $\theta_{\chi V}$ and $\theta_{\chi B}$ are significantly larger for the C1 and C2 pairing. It can be seen in figure (2.13) that the dispersion relations bear similarities to figure (2.10). The first subinterval shows a clustering of power close to the sunward-directed fast magnetosonic branch for the largest power peaks (blue), with the second (green) and third (red) largest peaks concentrating closer to the beam resonant mode and structure line. The second subinterval is similar to the first in that power is clustered mainly around the right-polarized sunward propagating modes but some power is also visible at the Alfvén modes. However, the overall increased noise of this plot makes it difficult to determine whether this is a significant result. The third subinterval shows the power concentrated mainly in low frequencies, with some residual power on the structure lines and fast magnetosonic branch. This can be compared to the third subinterval of figure (2.10) in which the power changed from being concentrated on the magnetosonic modes to the structure line. All three subintervals contain more noise that the data of figures (2.10) owing to the less favourable angles, $\theta_{VB}, \theta_{\chi V}$ and $\theta_{\chi B}$. When $\theta_{\chi B}$ is large it is difficult to capture the projection of wave activity travelling down the magnetic field onto the spacecraft separation vector, when $\theta_{\chi V}$ is large the Doppler-shift correction becomes much more sensitive, and when θ_{VB} is large waves are significantly advected tangentially between the spacecraft separation, destroying coherence. In all three cases, the dispersion relations of figure (2.13) become inaccurate. For this reason, the analysis for I1, I2 and I3 was undertaken for the pairs C3 and C4, as these pairs were arranged such that the angles $\theta_{VB}, \theta_{\chi V}$ and $\theta_{\chi B}$ were minimal.

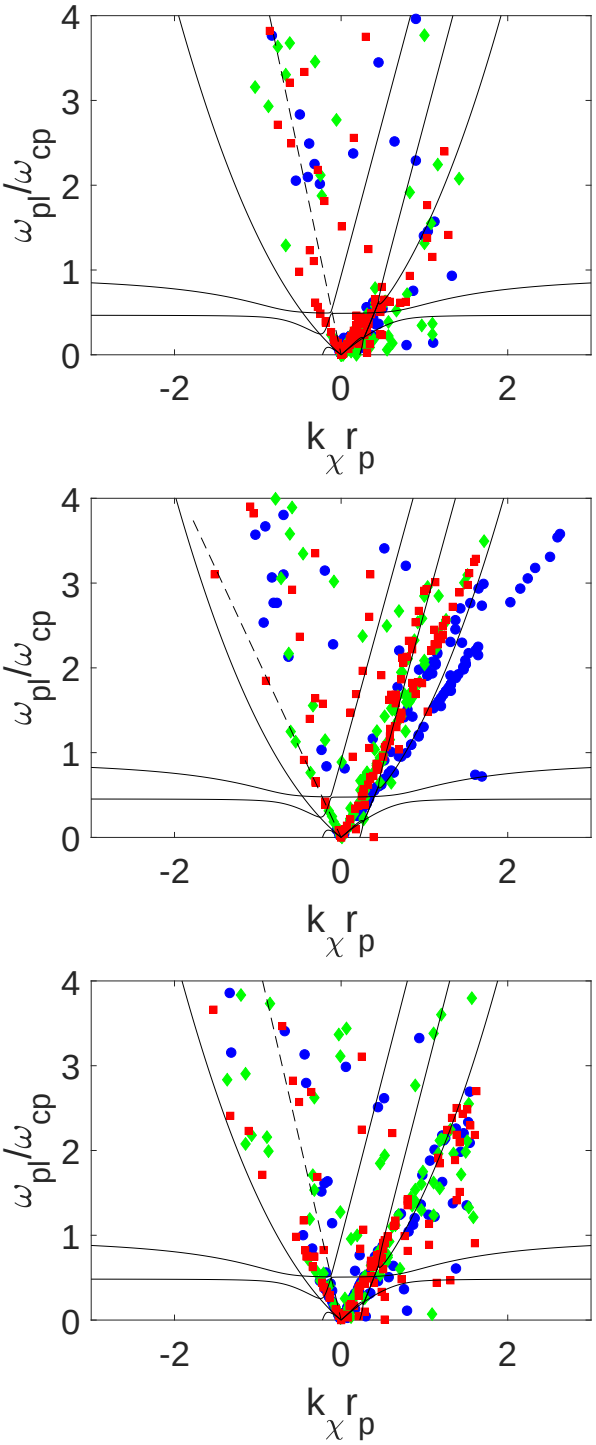

Figure 2.13: Doppler-corrected peaks for I1, repeated for satellites C1 and C2, for comparison to figure (2.10)

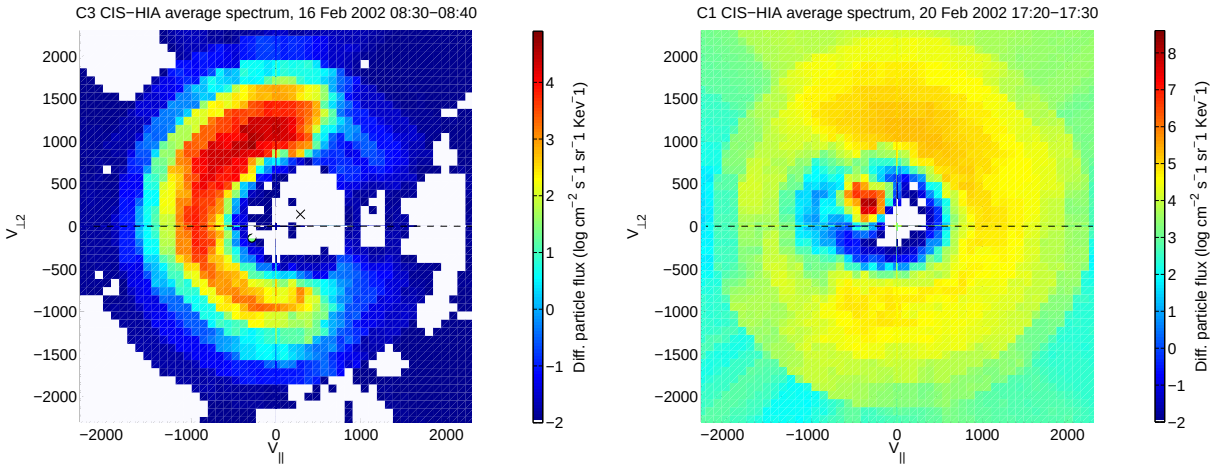

Figure 2.14: Differential particle flux in a magnetic field aligned coordinate system for I1 (left) and I2 (right). The left panel is measured when HIA is in the solar wind mode, in which the solar wind is excluded from the measurements. The location of this removed solar wind has been marked with a cross. This data is unavailable for I3

To contextualize these results, it is useful to evaluate the proton distribution functions. Figure (2.14) shows HIA ion flux pitch angle distributions, observed within a window of ~10 minutes for each interval. For I1, CIS-HIA was in the solar wind mode, excluding the solar wind flow from the distribution measurements. For I2, the magnetospheric mode was used, measuring the full angular spectrum. The distribution for I2 is therefore mainly dominated by the solar wind. It is still possible however to discern the shell-like distributions of the diffuse populations, typical of the quasi-parallel foreshock, for each interval. In both cases, the peak ion energies are a few keV, and the distributions have some angular asymmetry. Interval I1 shows a lower degree of solar wind interference with the distribution, showing the warm proton beam at an energy of around 10keV. The ion beam density is an important variable when considering the types of modes that can be destabilized and the power associated with the resulting fluctuations. The beam density is calculated by integrating phase space contributions whilst specifically excluding those due to the solar wind beam; essentially those between ±45° and ±55° around the GSE x-axis. For I1, the average beam number density is $n_B \approx 0.025\text{cm}^{-1}$, and for I2, $n_B \approx 0.23\text{cm}^{-1}$, a ratio of an order of magnitude. The solar wind density itself is calculable using upstream data from the OMNI database, for I1, this is $n_{sw} \approx 7\text{cm}^{-1}$ and for I2 the beam is twice as dense, $n_{sw} \approx 14\text{cm}^{-1}$. The ion distribution data for I3 was unavailable from the Cluster active archive.

The described analysis provides a method of identifying the dominant linear wave modes, in contrast to other previously used methods such as the wave telescope. The identification of ULF modes is of importance to the study of the foreshock as they are generated

by the two-stream instability, depicted in figure (1.7). The modes created by this instability depend on the relative velocity difference between the two streams, and knowledge of the most dominant wave modes and their velocities can therefore provide information on the exact form of the distribution function. Since the technique relies on two-probe data, the tetrahedral formation that forms the ideal topology for the wave telescope technique is not required and we are free to choose pairs of probes that have magnetic field and solar wind velocity vectors most closely aligned to the separation vector χ, or otherwise conveniently oriented. More importantly, the technique applied here allows for the categorization of frequency-wavenumber pairs by their total powers - these are the figures (2.10)-(2.12). Whilst previous techniques are able to recover plots for the dispersion relations, they only contain information on the wavenumber and frequency and not the power associated with the pair. The analysis provided in this chapter shows the relative power between the three most powerful modes for each dataset, shown in figures (2.10)-(2.12). The values of the powers of each of the modes is not presented here, but is calculated, and so in principle it is possible to study the growth in the absolute power of any of these ULF modes. This simultaneous measurement of the power, wavevector and frequency is unique to the technique outlined here, and can expand the capabilities of the method. For example, the study of datasets taken at different points of the foreshock could provide information on the power of modes across the shock. Similarly, the method can be applied to the same point of the shock at different times, to study the effect of environmental phenomena such as the sign of the z component of the IMF on mode power. In principle, the technique can be applied to study waves propagating perpendicular to the magnetic field if the separation vector is perpendicular to the direction of the magnetic field. The fast magnetosonic modes upstream of the shock can undergo steepening as they are advected downstream and evolve into non-linear waves, documented in section (1.4.3.3). Eventually these nonlinear waves evolve into SLAMS, which form the basis for the shock layer itself. The exact areas of generation of these magnetosonic modes is therefore of fundamental importance to the physics of the shock layer, and this technique provides a means of measuring the most prevalent locations of these modes. The acceleration mechanism of the shock itself was described in section (1.4.3.2). It was shown that the electric field gradient across the shock is the driving force behind the acceleration and reflection of individual particles at the shock. Wave behaviour is therefore important to this process as enhanced wave activity can form a collective perturbation that influences this gradient, modifying the acceleration [55]. Whilst the primary purpose of the technique is as a means of directly measuring and ordering the most dominant wave mode peaks, it can also be used to quantify the power of nonlinear modes and structures, as these will lie on the structure line. The generation of ULF modes at the shock is important to the reflection process itself, as wave and particle phenomena upstream from the shock arise from

kinetic effects such as reflection, shock drift acceleration, particle scattering, and Fermi acceleration, and knowledge of the wave modes at each point of the shock is useful for predicting the dynamics and physical processes available at that point. The technique investigated in this chapter provides a means of identifying modes as a function of position in the foreshock and can therefore be used to further this predictive capability.

2.5 Conclusion

Multiple dispersion relations coexisting with background solar wind turbulence have been found for two different crossings of the terrestrial foreshock. These dispersions span beyond the typically studied ULF waves in frequencies and wavenumber, with a maximum angular frequency greater than $4\omega_{ci}$. The techniques used in this chapter allow for the discernment of power distributed amongst distinct branches of the dispersion relation. The first interval, I1, is dominated by slowly evolving, field aligned structures that are advected by the solar wind. Despite this, the method is able to detect significant power in the Alfvén and fast magnetosonic modes propagating both sunwards and anti-sunwards. A highly anisotropic beam, ($T_\perp > T_\parallel$) can, through the beam instability, produce ion cyclotron waves that propagate parallel and anti-parallel to the field, but it is also possible that the anti-sunwards propagating fluctuations are these already carried by the solar wind. The counter propagating Alfvén modes of I1 may interact nonlinearly with these ion cyclotron waves. The presence of cyclotron modes of He^{++} is also noted, as well as their relation to the magnetoacoustic cyclotron instability.

The second interval, I2, is dominated almost entirely by fast magnetosonic and resonant proton beam modes, propagating away from the bow shock. This is an indication of the cold ion beam instability, in keeping with previous studies of this interval that employ the wave telescope technique [132]. A significant amount of power is also found in the Alfvén branch propagating sunwards, consistent with previous results. Less power is found in modes propagating anti-sunwards, close to both the Alfvén and fast mode branches. The right-hand polarized waves of I2 reach speeds of up to ~170kms^{-1}.

The ion distribution functions have a similar form for both intervals; an intermediate ring. However, interval I2 has a beam density ($n_B \approx 0.025\text{cm}^{-1}$) an order of magnitude greater than I1 ($n_B \approx 0.23\text{cm}^{-1}$, which explains the dominance of power in the magnetosonic modes; these modes are destabilized by the beam itself. This contrasts with the approximately equal split of power between magnetosonic and Alfvén modes in I1, when controlled for the slowly evolving structures that contain a lot of the total power. For I2, the

fluctuations appear to be an intricate admixture of beam driven modes and the Alfvénic modes embedded in the solar wind.

The substitution of the Fourier transform to the wavelet transform produced better-resolved dispersion relations, and when Doppler-corrected, showed the presence of more types of modes. The wavelet technique also requires significantly shorter time-series and is generally better suited for non-stationary data. Generally, the quasi-parallel foreshock is a region of complex plasma dynamics, in which linear plasma waves coexist with non-linear structures and waves. It has been shown that steepening of ULF waves is a process dominated by nonlinear dynamics. Individual wavepackets may evolve according to the non-linear Schrödinger equation when cubic nonlinearity processes are present, and this can lead to incorrect estimates of the phase differences, and thus the dispersion relations. These processes distribute energy not only between plasma modes, but also between the bulk plasma processes and waves. The methodology of this chapter does not account for these complications.

Chapter 3

Nonlinear Waves in the Terrestrial Quasiparallel Foreshock

3.1 Introduction

In chapter 2 it was shown that the reflected solar wind in the quasi-parallel foreshock produces a complex plasma environment that supports the generation of a variety of linear ULF modes, most commonly the fast magnetosonic. As evidenced by their Doppler-corrected dispersion relations, these field-aligned modes propagate sunwards in the plasma rest frame, with phase speeds smaller than the solar wind speed, and are thus advected back towards the bow shock. At this point in their evolution, these waves are detectable by linear techniques as was demonstrated in the previous chapter. As the modes are advected deeper into the shock by the solar wind, they move through regions of increasing diffuse ion density [60]. Giaclone et al [152] suggested that the ion density gradient changes the index of refraction of the medium, and consequently transverse modes become compressive and steepen [153][101]. As the modes are convected deeper into the foreshock, they become increasingly more oblique and compressional, and may eventually form into SLAMS.

SLAMS, introduced in section (1.4.3.3), are intrinsically left-hand elliptically polarized, and have been shown in simulations to steepen in both the downstream and upstream direction [154]. SLAMS are a nonlinear phenomenon, in that they cannot be described by linear wave equations of the form of equation (1.53). Their phase speed increases with their amplitude as they move through the foreshock, reducing their relative motion to the Earth. SLAMS are three-dimensional structures, and as they are convected by the solar wind they decelerate by merging with other similar structures, forming the shock layer itself. Since SLAMS are continuously created upstream and advected downstream, the

quasi-parallel shock is cyclically reformed of these travelling SLAMS [155][156]. As isolated SLAMS steepen and grow, fewer backstreaming particles penetrate through them but are instead returned back to the shock. The SLAMS therefore appear to "sweep-up" the ions. Consequently a trough is formed in their wake which eventually is filled in by particles from either the upstream or downstream regions [157]. Numerical studies [158] and observations [159] show that the growth rate of these SLAMS is on the order of seconds, and their spatial sizes are ~700-1000km, or ~10-15 ion inertial lengths [133]. The interaction of superthermal ions with the plasma leads to dynamics that operate on different levels of scale, distributing the overall energy accordingly [160]. These processes are described as nonlinear, in that their energetic outputs do not necessarily correspond to a proportional change of their input [161]. In the last decade, the importance of the nonlinear analysis of the Earth's quasiparallel shock has been recognized. The nonlinear decay of Langmuir waves, for example, contributes significantly to the dissipation of energy of very intense beam-generated waves in the foreshock [162].

Zhu et el [163] used multi input-single output NARMAX modelling to analyse the contributions of linear, quadratic and cubically nonlinear fluctuations to the structure of SLAMS, concluding that purely linear models are sufficient for the description of very low amplitude waves, and that the dynamics of SLAMS are dominated by third-order (cubic) nonlinear processes. A cubic nonlinearity of this nature introduces a phasal dependence of the amplitude in the observed wave packets. SLAMS have also been found to contain nonlinear solitary structures, of varying shapes, durations and scales, complicating their analysis [164]. The presence of these nonlinear waves in the quasiparallel foreshock may lead to wave collapse[165], and self focussing [166], which can generate strong electrostatic fields on kinetic scales. This field accelerates particles, modifying their distribution function[167][168]. Understanding the interactions of SLAMS and other nonlinear foreshock phenomena with the background plasma is therefore crucial to the understanding of how the Earth's shock forms under certain IMF conditions.

Finite amplitude dispersive slow and fast magnetoacoustic waves propagating at large oblique angles to the magnetic field obey the Korteweg-de Vries (KdV) equation [120]. For Alfvén and fast magnetoacoustic fluctuations propagation parallel or almost parallel to the magnetic field, the Derivative Nonlinear Schrődinger (DNLS) equation is a decent description [169][170]. Beyond MHD approximations, high-frequency nonlinear fluctuations on the whistler dispersion branch, exhibiting soliton-like features, have been identified in numerical and analytical studies [171][172].

The nonlinear nature of SLAMS is evident in the waveforms themselves; SLAMS have

forms different to those of the ULF modes detected in chapter (2). They appear as asymmetric waves, often with sharpened crests and rounded troughs. Their unique shape means that traditional Fourier-based techniques such as the fast-Fourier transform (FFT) or the wavelet decomposition provide inaccurate results [173]. Therefore, the analysis techniques of chapter 2, whilst useful for determining the types of linear modes travelling between two probes, and to a certain extent the nonlinear modes insofar as they are present on the structure lines, are insufficient to properly determine the properties of SLAMS and other nonlinear phenomena. Additionally, nonlinear features present in the datasets will be incorrectly identified as containing large amount of power when analyzed with the techniques of chapter 2, reducing the likelihood of linear mode detection. For these reasons, in this chapter the propagation characteristics and spatial structure of nonlinear fluctuations found in the quasi-parallel foreshock are directly compared to numerical solutions of the DNLS using the empirical mode decomposition (EMD) [174]. EMD is an analysis technique that projects the waveforms onto a basis set of modes that are derived directly from the waveform itself, rather than relying on some form of sinusoidal decomposition. Because nonlinear analysis is specific to particular waveforms, and cannot be generally applied to large batches of data like those of the previous chapter, the data considered for this chapter will consist of individual examples of nonlinear wave trains. These examples all have periods of several seconds and speeds consistent with the background plasma Alfvén speeds, taken by the FGM instrument aboard Cluster. The examples are compared to numerical solutions of the DNLS computed with input variables measured *in-situ* by the HIA instruments. In contrast to previous studies, the potential used for the DNLS solutions will take as a double-well shape for real values of the magnetic field, which provides two main regimes for oscillatory wave behaviour. At high amplitudes, these regimes provide nonlinear waves, and more linear small-amplitude fluctuations. The change of the magnetic field data from high to low amplitude should then be accompanied by a change in the linearity of the solutions to which the data are compared. A good agreement between the empirical data and DNLS solutions will therefore provide evidence that the new form of the potential is accurate.

3.2 Data

The datasets are taken from I2 of chapter 2, the 20th February 2002 16:56-17:52 because the dispersion relation showed the presence of fast magnetosonic modes. These are the modes that undergo nonlinear steepening and obey the DNLS. Three short subintervals are taken, defined as I1, I2 and I3:

- I1: 17:13:50-17:14:02
- I2: 17:15:20-17:15:32
- I3: 17:22:40-17:23:05

These short intervals contain ~2-5 fluctuations of nonlinear wave fluctuations. As with the previous chapter, magnetic field fluctuations are measured with the FGM, at 22.4Hz resolution. The short nature of the intervals means that the 4s CIS-HIA data is not of a high enough resolution to determine how the plasma parameters fluctuate with the magnetic structures, so time-averaged values for each interval are taken. A summary plot of the key macroscopic plasma parameters for all three intervals are shown in figures (3.1) and (3.2). This plot also shows the omnidirectional proton flux, in colour, at different energies, showing a broad high-energy ion component between $(10^3 - 10^4)$eV. During this interval, this Cluster CIS instrument was operating in the magnetospheric mode, in which the instrument samples all angular directions, and therefore includes the incoming solar wind flow; this is the dominant line at ~10^3eV.

3.3 Methodology

The FGM data is processed using the minimum variance analysis of section (2.3.1), to obtain the magnetic components transverse to the direction of propagation. The main caveat of this technique; that the difference vectors across the plane of the wavefront are not colinear; is satisfied by the fluctuations in the intervals. The nonlinear character of the waveforms are preserved through the MVA coordinate rotation. Since the data is nonlinear and nonstationary, Fourier-based spectral techniques are unsuitable. Similarly, the wavelet transform, whilst better suited for analyzing modulated signals containing local discontinuities, is also unfit for very nonlinear signals, particularly if the principal aim is to preserve the nonlinear nature of the wave trains. Both of these techniques rely on an *a priori* assignment of harmonic basis functions; for Fourier analysis, these are the cosines, and for wavelets, the choice of mother wavelet, from which to recreate the signal. For this chapter, these techniques are insufficient and so we use the *Hilbert-Huang transform* (HHT) spectral technique, which is designed for analyzing nonstationary and nonharmonic fluctuations, to separate the nonlinear waves from underlying fluctuations.

3.3.1 EMD

The HHT makes use of the *Empirical Mode Decomposition* (EMD) [175][174]. This is a technique that expands the input signal onto a set of intrinsic modes derived directly from

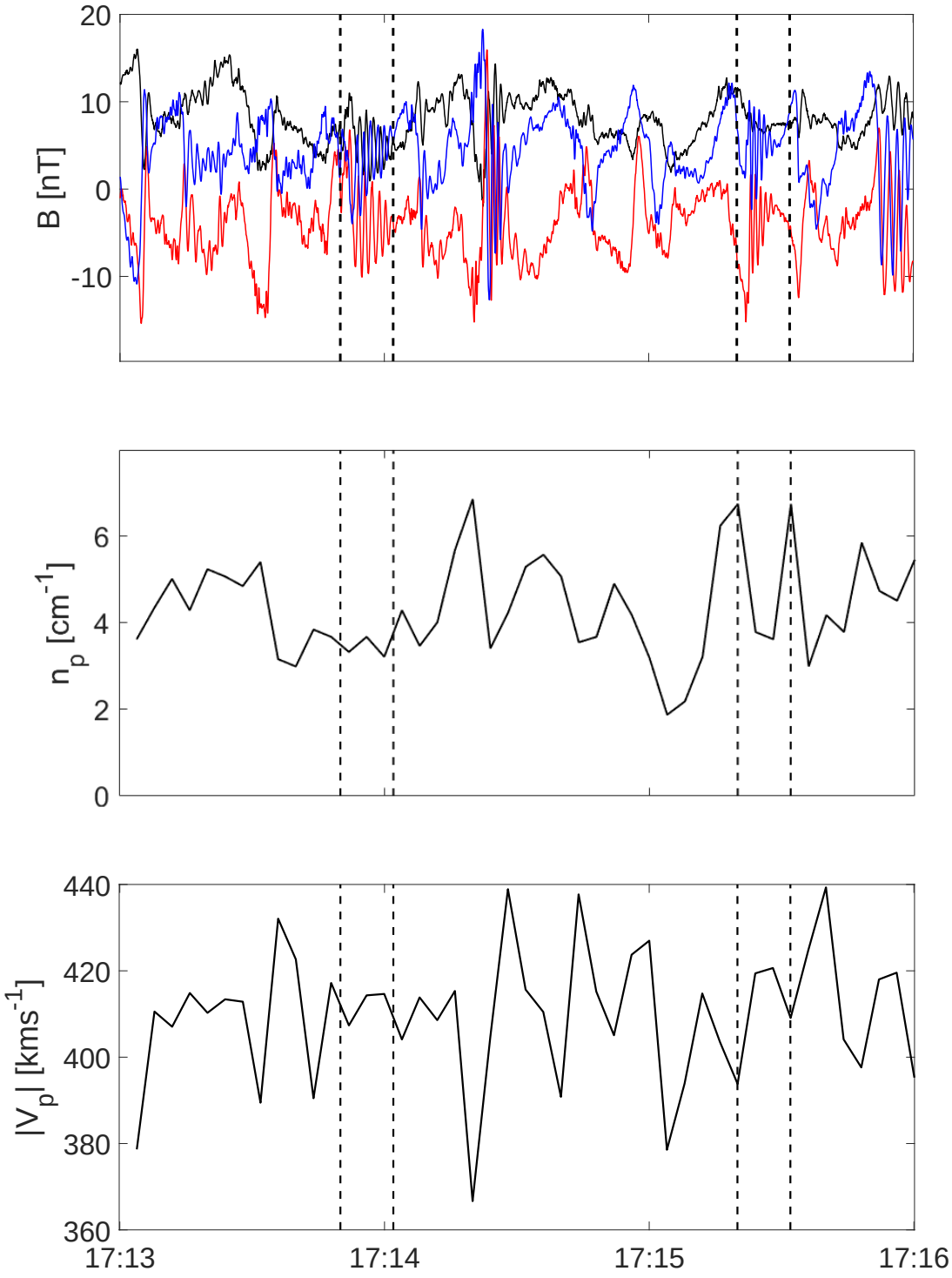

Figure 3.1: Summary of Cluster observations for a period including I1 and I2. Upper: FGM data for the x, y and z GSE components in black, blue and red respectively, showing non-linear features. Middle: proton density taken from the 4s resolution CIS-HIA instrument. Lower: magnitude of HIA solar wind velocity data. Interval I1 is between the first pair of vertical dashed lines, I2 between the second.

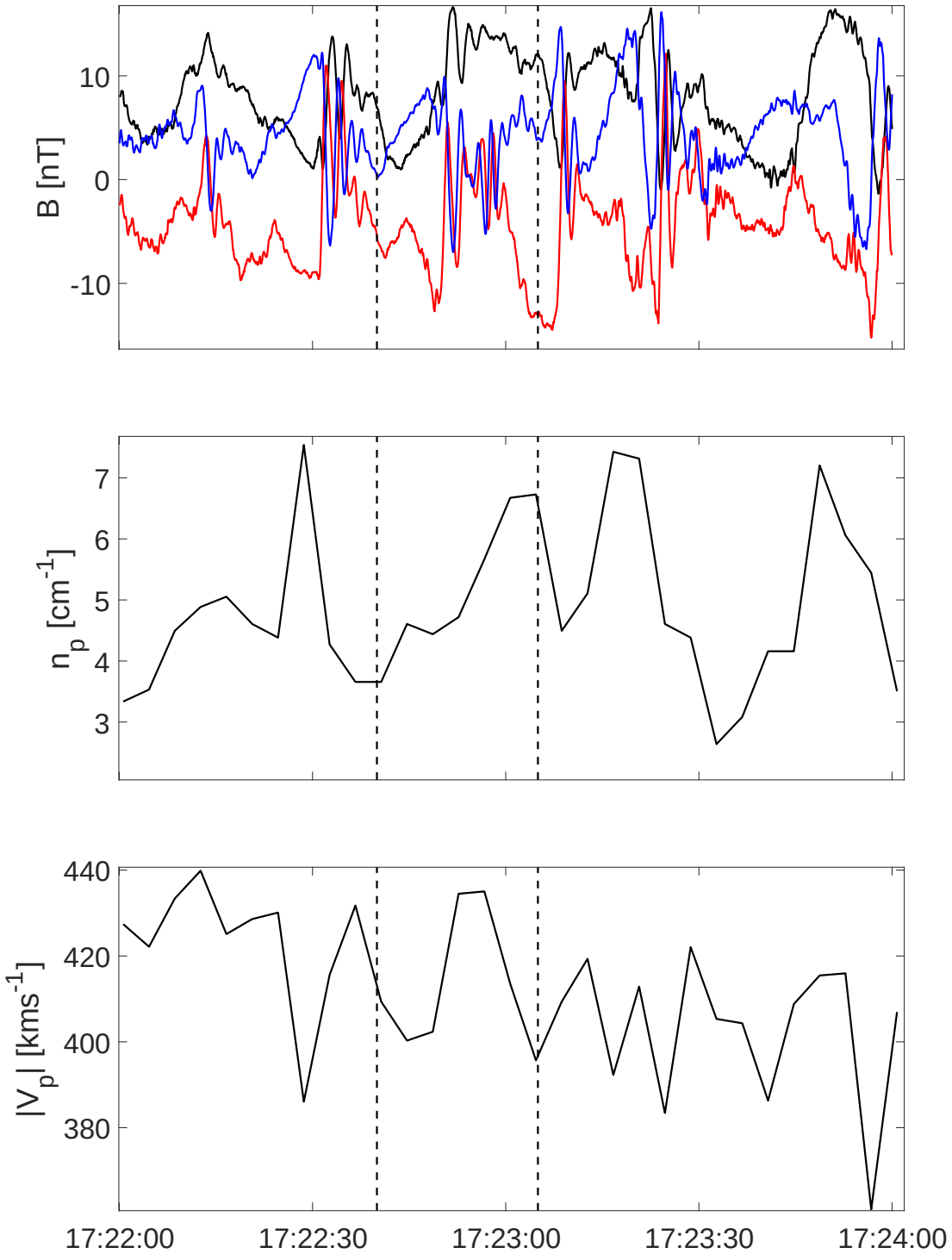

Figure 3.2: Summary of Cluster observations for a period including I3, shown between the two vertical lines. Panels are as in figure (3.1)

the data. The essence of the method is to identify the intrinsic oscillatory modes by their characteristic time scales in the data empirically, and then decompose the data accordingly. These oscillatory modes are known as the *intrinsic mode functions*, (IMFs), and sat-

isfy the following two conditions. Firstly, over the entire dataset, the number of extrema and the number of zero crossings must either equal or differ at most by one. Secondly, at any point, the mean value of the envelope described by the maximum of the signal and the minimum of the signal, is zero. The decomposition of the data into these IMFs is via the sifting process, which relies on the following conditions. One, that the signal contains at least two extrema - one maximum and one minimum; two, the characteristic time scale of these fluctuations is defined by the time lapse between the extrema. The sifting process is performed as follows: firstly, the maxima and minima of the signal are separately connected using cubic splines to form two envelopes of the data; one that contains all of the maxima and the other, the minima. These are as shown in figure (3.3). The mean of the maximum and minimum envelopes is calculated, and denoted by m_1. For an input signal $X(t)$, the difference, h_1 between the data and the mean, m_1, is given by:

$$X(t) - m_1 = h_1 \tag{3.1}$$

This envelope mean is, in general, not equal to the true local mean, especially if the data is nonlinear. The resultant, h_1, is therefore not usually an IMF. After just one iteration, the mean is still sensitive to fluctuations that ride on the envelopes. It is also sensitive to local asymmetries between waves; overshoots and undershoots are quite common even in very stationary data. The process is therefore repeated and in the second sift, the first difference h_1 is treated as the new signal:

$$h_1 - m_{11} = h_{11} \tag{3.2}$$

This process of computing the maxima and minima of the differenced time series is repeated k times until the resultant, h_{1k}, satisfies the requirements for an IMF, that is, until:

$$h_{1(k-1)} - m_{1k} = h_{1k} \tag{3.3}$$

at which point, the sifting stops and we designate:

$$c_1 = h_{1k} \tag{3.4}$$

as the first IMF component of the data. Overall, this first component c_1 should contain the finest scale, or the shortest period component, of the signal. Fluctuations at this scale c_1 are then removed from the data by:

$$X(t) - c_1 = r_1 \tag{3.5}$$

The residue, r_1, now contains all of the information of longer period components. It is then treated as the new data and subjected to the same sifting process outlined above. The procedure is repeated on all subsequent r_j, resulting in:

$$r_1 - c_2 = r_2, ..., r_{n-1} - c_n = r_n \tag{3.6}$$

This sifting process is depicted in figure (3.3). The goals of the sifting process are twofold, firstly, to eliminate riding waves on the fluctuation of interest, and secondly, to smooth uneven amplitudes. This second goal is necessary, in case neighbouring wave amplitudes have too large a disparity. However, if the sifting process is performed too much, the physically meaningful amplitude fluctuations can be destroyed, producing IMFs that are pure frequency modulated signals of constant amplitude. To combat this, the size of the standard deviation, SD, computed from two consecutive sifting results, as

$$\mathrm{SD} = \sum_{t\to\infty}^{T} \left[\frac{|(h_{1(k-1)}(t) - h_{1k}(t))|^2}{h^2_{1(k-1)}(t)} \right] \tag{3.7}$$

must be limited. For this study, the SD was limited to 0.2. For comparison, two Fourier spectra, computed by shifting 5 out of 1024 points, would have an equivalent SD of 0.2-0.3 when calculated point by point. An SD of 0.2 is therefore a very rigorous limitation for the difference between siftings.

The process of iteratively removing the residue from successive signals can be stopped either when the components, c_n, or the residue, r_n, become so small that they are less than the modes of interest, or when the residue, r_n, becomes a monotonic function from which no more IMFs can be extracted. For data with a trend, the final residue should be that trend. When the process is stopped, we obtain:

$$X(t) = \sum_{i=1}^{n} c_i + r_n \tag{3.8}$$

formally expressing the decomposition of the data into n empirical modes, and a residue, r_n, which is the mean trend.

The EMD modes are not exactly orthogonal. To prove this, we may form the square of the signal:

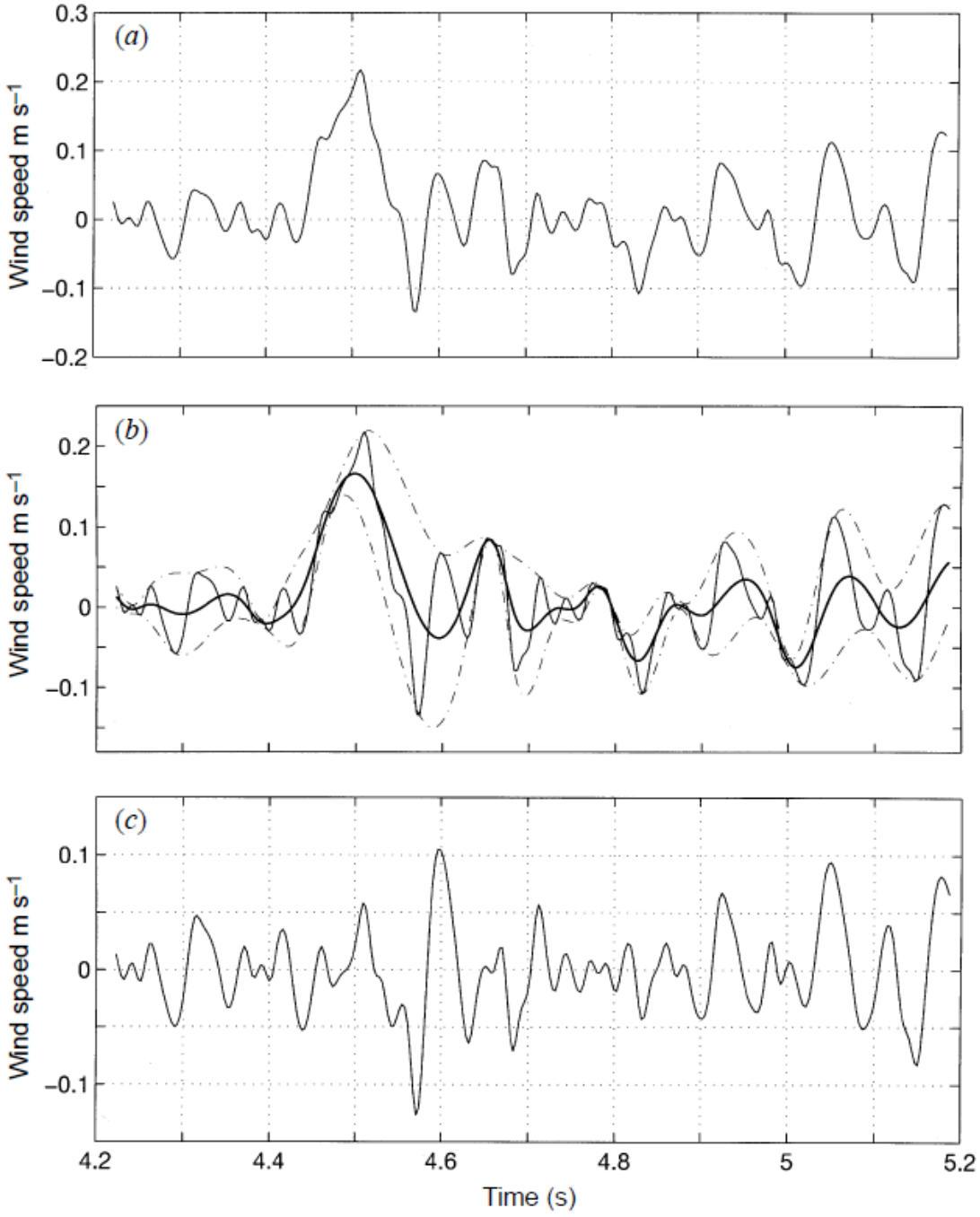

Figure 3.3: Illustration of the sifting process: (a) the original data; (b) the data in thin solid line, with the upper and lower envelopes in dot-dashed lines and the mean in thick solid line; (c) he difference between the data and m_1. This difference is not an IMF, as there are negative local maxima and positive minima indicative of riding waves.

$$X^2(t) = \sum_{j=1}^{n+1} C_j^2(t) + 2 = \sum_{j=1}^{n+1} = \sum_{k=1}^{n+1} C_j(t) C_k(t) \tag{3.9}$$

If the decomposition is orthogonal, then the cross terms should be zero. We can define an orthogonality between two components C_f and C_g with:

$$\mathrm{IO}_{fg} = \sum_{t=0} \frac{C_f C_g}{C_f^2 + C_g^2} \tag{3.10}$$

The orthogonality applies only locally, and so spectral leakage (or as it is usually referred to in EMD: mode mixing) can be time dependent. Wu and Huang [176] found mixing to be typically less than 1%, but acknowledged that the mixing is also a function of the length of the data. For very short data, such as that contained in the intervals I1-I3, mixing is increased. The phenomena is also exacerbated by intermittent data. To reduce these effects, we incorporate the *ensemble empirical mode decomposition* (EEMD) [176][177]. This is a noise-assisted data analysis method that adds white noise to the original data before the sifting process starts. The EMD modes are computed as normal until all of the IMFs are calculated. The original data is then reprocessed with a different noise profile, for a given number of noise ensembles. The true set of modes is then the ensemble average of the IMFs. Formally, for N ensembles, the true IMF is defined as:

$$C_j = \lim N \to \infty \frac{1}{N} \sum_{k=1}^{N} (C_j(t) + \alpha r_k(t)) \tag{3.11}$$

in which

$$C_j(t) + \alpha r_k(t) \tag{3.12}$$

is the k^{th} trial of the j^{th} IMF in the noise-added signal, and α is the magnitude of the added noise, which need not be small. The EEMD utilizes small-amplitude white noise, which is statistically cancelled, to dampen mode mixing between ensembles and therefore provides a more accurate and orthogonal decomposition than EMD. The EEMD provides a substantial improvement over the EMD, although it is much more computationally intensive. The EEMD is used to determine the overall trend of the datasets within the length of time of the intervals. This is essential as we wish to examine the fluctuations on scales smaller than those of SLAMS. To do this, the lower frequency modes are summed up to some cut-off to form the trend, and this trend is then subtracted from the original data. The value of this cut-off is dependent on the data, determined by eye, and variant through

the intervals. For I1 and I2, the five lowest frequency IMF modes are removed from the signal, for I3, the seven lowest form the trend.

3.3.2 DNLS

Consider a magnetized plasma with elliptically polarized Alfvén or magnetoacoustic waves propagating in the quasi-parallel z direction, causing a perturbation of the transverse field components such that $\vec{b} = b_x + i b_y$. The evolution of these polarized modes is given by the derivative nonlinear Schrődinger (DNLS) equation [178][179]

$$\frac{\partial \vec{b}}{\partial t} + \alpha \frac{\partial (\vec{b}|\vec{b}|^2)}{\partial z} - i\mu \frac{\partial^2 \vec{b}}{\partial z^2} = 0 \tag{3.13}$$

where

$$\alpha = \frac{V_A^2}{4(V_A^2 - V_s^2)} \qquad \mu = \pm \frac{1}{2} \tag{3.14}$$

Here, V_s is the plasma sound speed, defined by equation (1.84), V_A is the Alfvén speed of equation (1.97), and the sign of μ corresponds to left (-) and right (+) polarized modes. All of the temporal and spatial variables of equation (3.13) have been normalized by the ion gyrofrequency, equation (1.4) and the ion inertial length, V_A/ω_{ci}, respectively. The solution to equation (3.13), representing the transverse components, is:

$$\vec{b} = b e^{i\theta} \tag{3.15}$$

Substituting the solution into (3.13) and separating variables, we get:

$$\frac{\partial b}{\partial t} + 3\alpha b^2 \frac{\partial b}{\partial z} + \frac{\mu}{b} \frac{\partial}{\partial z} \left(b^2 \frac{\partial \theta}{\partial z} \right) = 0 \tag{3.16}$$

$$\frac{\partial \theta}{\partial t} + \alpha b^2 \frac{\partial \theta}{\partial z} + \mu \left(\frac{\partial \theta}{\partial z} \right)^2 - \frac{\mu}{b} \frac{\partial^2 b}{\partial z^2} = 0 \tag{3.17}$$

Taking the Galilean transformation

$$
\begin{aligned}
z' &= z - ut \\
t' &= t \\
\frac{\partial}{\partial z} &= \frac{\partial}{\partial z'} \\
\frac{\partial}{\partial t} &= \frac{\partial}{\partial t'} - u\frac{\partial}{\partial z'}
\end{aligned}
\tag{3.18}
$$

and substituting into equations (3.16) and (3.17)

$$
\frac{\partial b}{\partial t'} - u\frac{\partial b}{\partial z'} + 3\alpha b^2 \frac{\partial b}{\partial z'} + \frac{\mu}{b}\frac{\partial}{\partial z'}\left(b^2 \frac{\partial \theta}{\partial z'}\right) = 0 \tag{3.19}
$$

$$
\frac{\partial \theta}{\partial t'} - u\frac{\partial \theta}{\partial z'} + \alpha b^2 \frac{\partial \theta}{\partial z'} + \mu\left(\frac{\partial \theta}{\partial z'}\right)^2 - \frac{\mu}{b}\frac{\partial^2 b}{\partial z'^2} = 0 \tag{3.20}
$$

We remark that b is independent of t', and that θ is dependent on t. We may therefore deduce from (3.19) and (3.20) that:

$$
\frac{db}{dz'}\left(3\alpha b^2 - u\right) + \mu\left[2\frac{db}{dz'}\frac{\partial \theta}{\partial z'} + b\frac{\partial^2 \theta}{\partial z'^2}\right] = 0 \tag{3.21}
$$

The first half of the above expression depends only on z', so the second half ought to share this dependence. Since the first term of equation (3.21) contains u, and therefore the time dependence, θ can be expressed as a general expression dependent on t and z':

$$
\theta(z', t) = f(t) + \phi(z') \tag{3.22}
$$

where $f(t)$ and $\phi(z')$ are arbitrary functions. Substituting (3.22) into (3.20), we obtain:

$$
\frac{df}{dt} = u\frac{d\phi}{dz'} - \alpha b^2 \frac{d\phi}{dz'} - \mu\left(\frac{d\phi}{dz'}\right)^2 + \frac{\mu}{b}\frac{d^2\phi}{dz'^2} \tag{3.23}
$$

The left hand side of equation (3.23) depends only on t, and the right hand side, only on z'. They must therefore must be equal to some constant, that we shall denote with Ω

$$
f(t) = -\Omega t \tag{3.24}
$$

Substituting into (3.19):

$$\frac{db}{dz'}\left(3\alpha b^2\right)+\frac{\mu}{b}\frac{d}{dz'}\left(b^2\frac{d\phi}{dz'}\right)=0 \tag{3.25}$$

Multiplying the above by $b\,dz'$:

$$\int\left(3\alpha b^3-ub\right)db\,+\mu\int d\left(b^2\frac{d\phi}{dz'}\right)=0 \tag{3.26}$$

Performing the integration and rearranging

$$\frac{d\phi}{dz'}=\frac{1}{\mu\alpha b^2}\left[C\alpha+u\frac{\alpha b^2}{2}-3\left(\frac{\alpha b^2}{2}\right)^2\right] \tag{3.27}$$

where C is the constant of integration. We may here rewrite $s=\frac{\alpha b^2}{2}$ and $c\alpha=c$, to define $g(s)$:

$$g(s)=\frac{d\phi}{dz'}=\frac{1}{2\mu s}\left[c+us-3s^2\right] \tag{3.28}$$

Substituting (3.28) into (3.20):

$$-\Omega-u\frac{d\phi}{dz'}+\alpha b^2\frac{d\phi}{dz'}+\mu\left(\frac{d\phi}{dz'}\right)^2-\frac{\mu}{b}\frac{d^2b}{dz'^2}=0 \tag{3.29}$$

We now make use of the fact that

$$\begin{aligned}\frac{db(s)}{dz'}&=\frac{db}{ds}\frac{ds}{dz'}\\ \frac{d}{dz'}\left(\frac{db}{dz'}\right)&=\frac{d^2b}{ds^2}\left(\frac{ds}{dz'}\right)^2+\frac{db}{ds}\frac{d^2s}{dz'^2}\end{aligned} \tag{3.30}$$

and define

$$G(s)=\Omega+ug(s)-2sg(s)-\mu g(s)^2 \tag{3.31}$$

to show:

$$-G(s)+\frac{d^2b}{ds^2}\left(\frac{ds}{dz'}\right)^2+\frac{db}{ds}\frac{d^2s}{dz'^2}=0 \tag{3.32}$$

Now, let

$$F(s)=\frac{db}{ds}=(2sa)^{-\frac{1}{2}} \tag{3.33}$$

and hence:

$$F(s)\frac{d^2s}{dz'^2}+\frac{dF(s)}{ds}\left(\frac{ds}{dz'}\right)^2=G(s) \tag{3.34}$$

and

$$G(s)=\Omega\mu+V\frac{dP}{d\phi}-2s\frac{dP}{d\phi}-\left(\frac{dP}{d\phi}\right)^2 \tag{3.35}$$

Equation (3.34) is in the form of a Bernoulli differential equation [180], which can be linearized and solved through the use of an integrating factor, giving:

$$\frac{1}{2}\left(\frac{1}{\sqrt{2\alpha b}}\frac{ds}{d\phi}\right)^2+U_b=C_b \tag{3.36}$$

where the potential is written in the new canonical form:

$$U_b=\frac{1}{4\alpha}\left(s^3-2Vs^2+\left(4\Omega\mu+V^2+2C\right)s+\frac{C^2}{s}\right) \tag{3.37}$$

and C_b is a new constant of integration. If s is treated as a generalized coordinate, and ϕ as the time, of a pseudoparticle, the first and second terms on the left-hand side of equation (3.36) represent generalized kinetic and potential energies written in the canonical form. In this case, the constant, C_b, can be interpreted as the total energy of the particle, which is dependent only on the initial conditions. The form of the pseudopotential, equation (3.37), contains terms originally defined in equation (3.31) and is therefore subject to choice. Hada et al. [181] considered solutions of the DNLS for finite amplitude Alfvén waves and used a pseudopotential of the form:

$$U_H(s)=\frac{1}{2}\left[s^4-2Vs^3+\left(4\mu\Omega+V^2+2C\right)s^2-Ds+C^2\right] \tag{3.38}$$

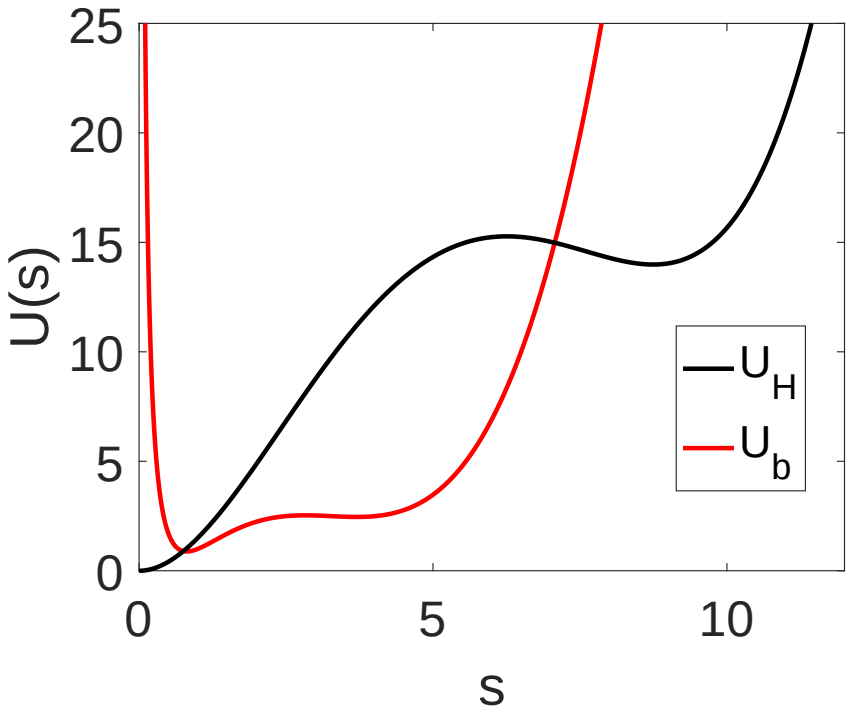

Figure 3.4: Form of the potentials of equation (3.37), black, and (3.37), red, against $s \equiv \frac{a|b|^2}{2}$. In the physically meaningful $s > 0$ range, U_b produces oscillatory solutions for arbitrary s. Both axes are arbitrary units.

where D is an integration constant. Hada et al. chose this form of the pseudopotential for its simplicity and resemblance to an anharmonic potential well. In contrast, equation (3.37) shows the choice of pseudopotential that will be used for comparison to empirical data in this chapter. Figure (3.4) shows the form of both potentials, $U(s)$, for the range $0 \leq s \equiv \frac{a|b|^2}{2} \leq 10$. The pseudopotential is shown in artbitrary units and the constants of integration of equations (3.37) and (3.38), as well as the linear coefficient of equation (3.38), D, have been chosen to keep U_H on a comparable scale to U_b. The principal difference in the form of (3.38) and the canonical form (3.37) is that as $s \to 0$, $U_H \to 0, U_b \to \infty$ and so the solutions of equation (3.13) are oscillatory for arbitrarily large amplitudes for solutions of the form U_b. The newer form U_b preserves the double-well shape of U_H but allows oscillatory solutions within either of the two wells for positive s and therefore can accommodate transitions between states described by either well. An unstable oscillatory state at the potential equal to the level of the maximum between the two minima is also possible. To compare the solutions of the DNLS with the nonlinear waveforms found in intervals I1-I3, we solve equation (3.34), the form containing U_b, numerically for different initial conditions, using plasma parameters measured directly from the interval data.

3.4 Results and Discussion

Figures (3.5-3.7) show nonlinear large amplitude quasiparallel transverse waves for each interval. Panel (a) shows the squared magnitude of the original transverse fluctuations, $B_\perp^2(t)$, in black, and the nonharmonic trend, $T(t)$, determined using the EEMD technique, in red. This trend is removed from the original signal, and the residue is normalized by the mean signal of the first and last point of the trend. The new signal is then expressed as

$$S(t) = 2\,\frac{B_\perp^2(t) - T(t)}{T(1) + T(N)} \tag{3.39}$$

where N is the number of points of the signal. $S(t)$ is plotted in panel (b) of figures (3.5-3.7). The frequency in the top right of this panel is the mean frequency of the nonlinear oscillations in the spacecraft frame, in units of the proton gyrofrequency. The start of the nonlinear waves is marked by a red dot, and the waves themselves are shown in red. The blue dot signifies the end of the nonlinear waves and the transition to small-amplitude fluctuations, which are shown in green in panel (b). The green dot shows the end of the small fluctuations. Panels (c) show hodograms of the minimum variance transverse components of the magnetic field, which are left-hand polarized in all intervals, in the spacecraft frame of reference. In the previous chapter, the dispersion relation showed that these modes propagate predominantly away from the bow shock for this crossing, and so are likely to be intrinsically right-hand polarized in the plasma frame, indicating that these fluctuations are fast magnetosonic modes. Panel (d) shows the phase plane of the signal, using the colour scheme of panel (b), and the equivalent trajectories obtained from numerical solutions, in black and blue. The trends of each interval have variabilities on the scale of tens of seconds, consistent with the period of ULF waves.

For each interval, large amplitude nonlinear waveforms, circularly polarized and spanning several cycles are identified. These waves have a characteristic shape, with rounded minima and narrowly peaked maxima. The amplitudes are 2-3 times larger than the background field and the neighbouring fluctuations, and their periods in the spacecraft frame are 0.18-0.24 times as long as the ion cyclotron motion. It is noted that the transverse field components, the ratio $\frac{\delta B_\perp}{\langle B_\perp \rangle}$ is in the range 15%-30%, for all three intervals. In all examples, the nonlinear wavetrain is followed by small amplitude nearly harmonic oscillations, depicted in green in panels (c). Noting that the advection velocity, ~400kms^{-1}, is much larger than the local Alfvén speed, the measurements indicate the spatial structure of the fluctuations and less so the temporal evolution. Using an average solar wind velocity of 420kms^{-1}, the observed periods indicate spatial gradients of around 200km, in agreement

with previous observations [182][183].

In panel (d), the phase space trajectories of the real data, shown in black, are contrasted with those of the numerical simulations, in red and green. The numerical solutions are obtained by solving equation (3.34) with the following parameters for each interval:

I1:

- Nonlinear solutions, black: C_b=18.9, V =5.1, C=3.7.
- Small amplitude solutions, blue: C_b=3.91, V=8, C=7.2.

I2:

- Nonlinear solutions, black: C_b=25.08, V =4.3, C=3.7.
- Small amplitude solutions, blue: C_b=5.31, V=8, C=7.2.

I3:

- Nonlinear solutions, black: C_b=20.25, V = 5.1, C=4.8
- Small amplitude solutions, blue: C_b=7.33, V=9, C=8.4.

The remaining variables are set as $\mu = 1/2$, $\Omega = 1$, and $\alpha = 1$. The positive value of μ is chosen to match with the intrinsic right-hand polarization detected in the dispersion relations of the previous chapter, opposite to that of the spacecraft-frame hodograms. The initial energies, C_b, are set to values that match the observations for each interval. The proton number density measurements from CIS-HIA give a value for $\beta \approx 2.5$, which would result in a negative value of α. However, the 4s resolution data are inaccurate for these intervals and are likely influenced by the dense energetic proton beam reflected from the bow shock, shown in figure (2.14). NASA OMNI data give a plasma β in the range 0.75-0.9 which is consistent with the number density of ions shown in figures (3.1) and (3.2) and the value of α used in the numerical solutions. The nonlinear and small-amplitude solutions that have the highest total energy are plotted in panel (c), in black dashed lines, for comparison to the waveforms taken from the data. In the vicinity of the nonlinear (red) data traces of panel (c), the solutions are seen to reproduce the characteristic sharpened top shape of the empirical data. In all three cases these solutions correspond to the highest-energy curve in the phase space plot, panel (d). This is the largest curve shown in black in panel (d). Close to the small-amplitude (green) data, the small-amplitude solutions are shown, and these likewise correspond to the largest small-amplitude solutions, shown in

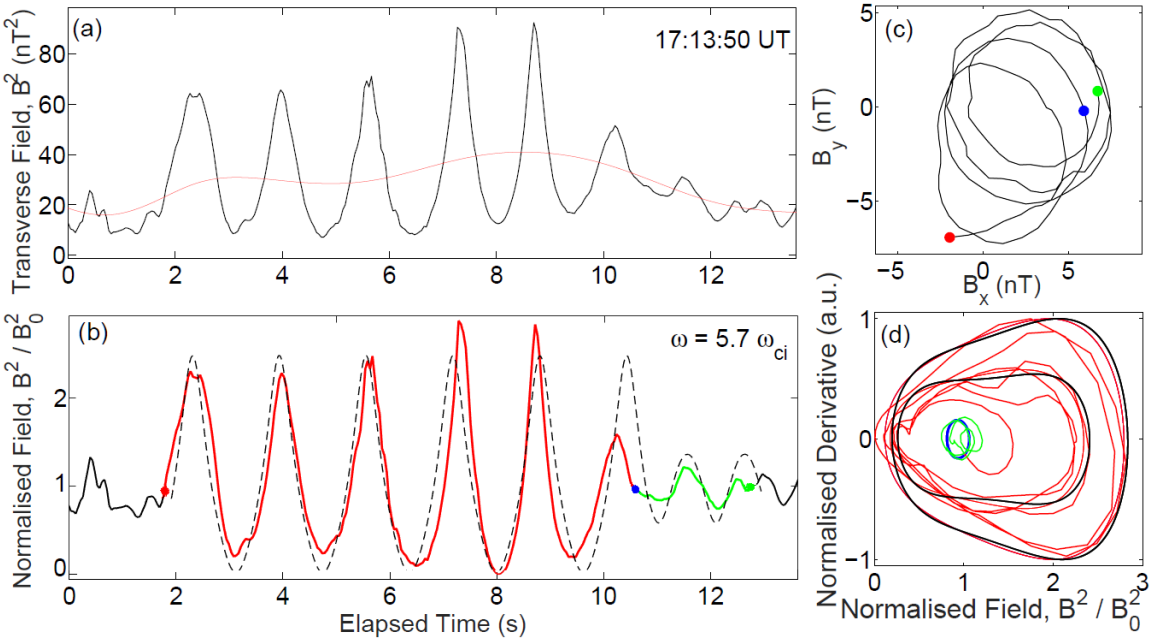

Figure 3.5: Nonlinear waveforms in the magnitude of the transverse magnetic field fluctuation for interval I1. Panel (a), Original squared magnitude of transverse fluctuations (black), and the trend (red). Panel (b): normalized and detrended signal with coloured dots marking the start of nonlinear waves (red), the transition from nonlinear waves to small-amplitude waves (blue) and the end of small amplitude waves (green). The mean frequency in the spacecraft frame is given in the top right corner of this panel. Panel (c): hodograms of the transverse components of (a). Panel (d): phase space of the signal of (b), with identical color schemes. Trajectories are calculated by solving equation (3.34).

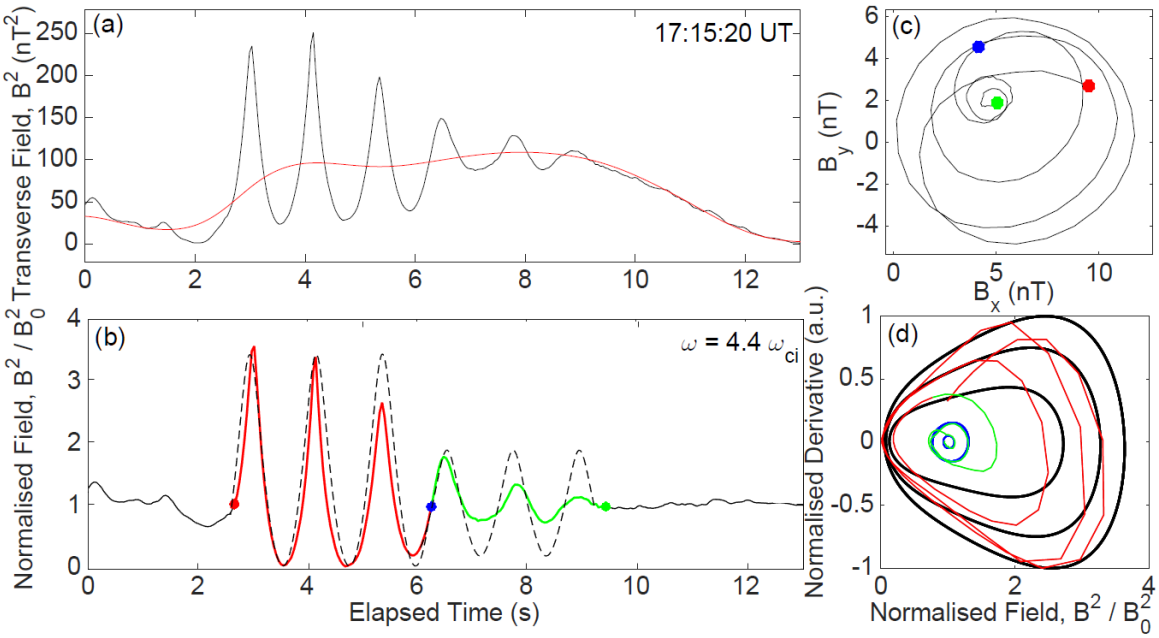

Figure 3.6: Nonlinear waveforms for interval I2. Panels are as described in figure (3.5).

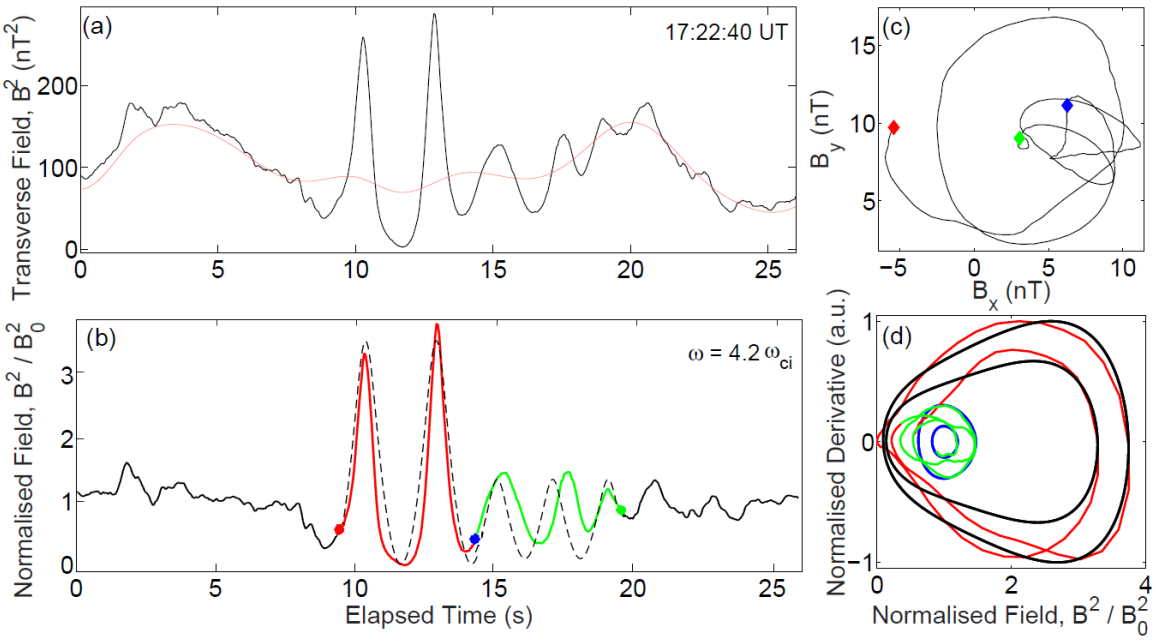

Figure 3.7: Nonlinear waveforms for interval I3. Panels are as described in figure (3.5).

blue, of panel (d) of each plot. For both the nonlinear and small-amplitude regimes, only the highest-energy solutions are shown in panel (c), as the lower-energy solutions have identical forms and similar frequencies but smaller amplitudes. The agreement between the experimental and numerical results indicate that the observed fluctuations are well described by the DNLS equation. The speed, V, used in the numerical solutions (normalized by the Alfvén speed) is modified by the solar wind speed. If we assume the waves propagate parallel to the field, the true phase speed of the wave is given by

$$V_{ph} = \vec{V} \cdot \vec{V}_A + U_{sw} \cos(\Theta_{vB}) \tag{3.40}$$

where U_{sw} is the bulk solar wind velocity and Θ_{vB} is the angle between the magnetic field and the solar wind velocity vectors. Both of these data are measurable using the CIS-HIA instrument and the phase velocities are given in table (3.1). The error on these values reflect the standard deviation of the solar wind velocity, density and magnetic field magnitude. The phase speeds are larger than the local Alfvén speed and the waves of higher amplitude propagate faster, a signature of nonlinearity. In each case the propagation direction is sunward. Within the reasonable range of physical parameters, these fluctuations are consistent with the DNLS model.

Normalized functional forms of the pseudopotential, equation (3.37), are shown in figure (3.8), corresponding to the phase space plots of panel (d) of figures (3.5-3.7). For each in-

	V_A(kms^{-1})	U_{sw}(kms^{-1})	Θ_{vB}(°)	V_{ph}(kms^{-1})
I1	86	410	141	120 ± 36
I2	110	412	140	157 ± 47
I3	110	420	156	159 ± 48

Table 3.1: Parameters used to calculate the phase velocities of the waves in each interval.

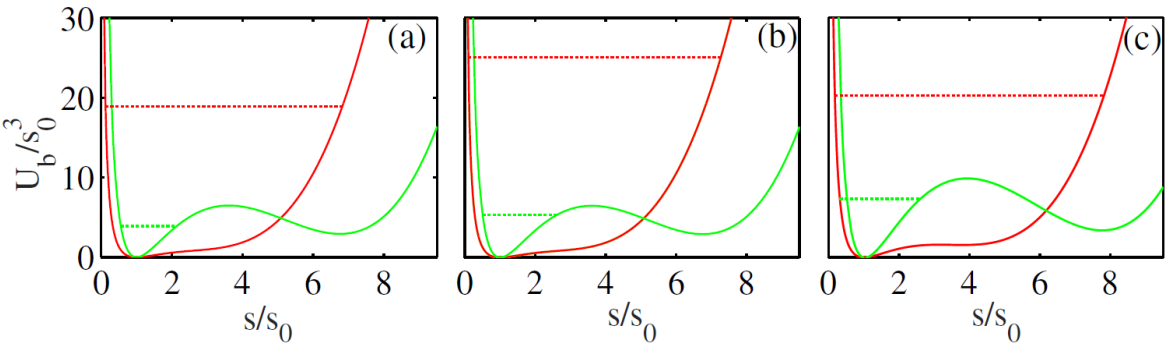

Figure 3.8: The form of the potential function U_b in canonical representation for I1 (a), I2 (b) and I3 (c). In all cases, $\mu = 1/2$, $\Omega = 1$, and $\alpha = 1$. Other parameters are as specified in the text. Red and green curves correspond to the nonlinear trajectories and the small amplitude fluctuations respectively, shown in panels (c) of figures (3.5)-(3.7).

terval, the value of U_b is calculated using the observational parameters of V, C_b and C. Red dashed lines in these plots correspond to the initial condition for the outermost black trajectory of panel (d), and green dashed lines correspond to the outermost blue trajectories of panel (d). The solid line data of panels (d) in the neighbourhood of the black numerical solutions correspond to the potential plots of a single minimum, displayed in figure (3.8) as the red solid line. Conversely, the solid green potentials correspond to the blue solutions of figures (3.5-3.7). The nonlinear potentials are likely a transient state between single and double well potentials. The energy of the nonlinear fluctuations are demonstrably larger than the local maxima or plateaus of the nonlinear potential, and so the exact form of the pseudopotential is less restrictive in this case. In contrast, the linear solutions of the phase space plots of figures (3.5-3.7) represent solutions near the local equilibrium of a double-well potential. A double-well potential solution corresponds to a limit of the large phase speeds V, with the caveat that the available energy of the system can only sustain small amplitude oscillations near one of the equilibrium points. The pseudopotential therefore reflects some of the properties of the medium in which the wave propagates, and by extension one may conjecture that the change of the potential is caused by the interaction of the nonlinear waves with the background plasma. The low temporal resolution (4s) of plasma data from Cluster precludes more detailed quantitative analysis of this phenomenon.

The analysis shown in figures (3.5)-(3.7) is for three waveforms but is generalizable to

waves that share the characteristic shape of DNLS solutions: sharpened crests and rounded troughs. Generally, SLAMS are too inconsistent to be able to uniformly apply the techniques developed in this chapter to all observable SLAMS. This inconsistency stems from the fact that SLAMS are an evolving phenomenon, and are progressively steepened as they enter the quasi-parallel shock. Their nonlinear nature may also lead to rapid amplitude growth and a departure from the DNLS solution form if a source of free energy is available. Oscillatory solutions are found to be in good agreement with the waveforms in both the large and small amplitude regimes. In the context of the new choice of potential, equation (3.31), this can be interpreted as a change in the system state from being bound by a higher potential well to a lower one, shown in figure (3.8). However, it is difficult to conclude this with certainty as the pseudopotential cannot be directly measured. The main difference in the form of the pseudopotential adopted here, U_b (equation (3.31) or (3.37)), and the form used by Hada, U_H (equation (3.38)), is that U_b is of one lower order in s than U_H, and therefore has solutions for arbitrary $s > 0$, as $U_b \to \infty$ as $s \to 0$. For the form used by Hada, as $s \to 0$, $U_H \to C^2/2$ and the dependency on s is lost. The double-well potential used here allows for periodic solutions to exist at lower values of the magnetic field magnitude than the form used by Hada, as demonstrated in the low-amplitude solutions of figures (3.5)-(3.7). These low amplitude solutions fit well to the data, providing strong evidence for the usefulness of the potential U_b.

3.5 Conclusion

Three intervals containing examples of SLAMS, or nonlinear waves, have been investigated for accuracy to numerical solutions of the derivative nonlinear Schrődnger (DNLS) equation. These waves all exhibit a characteristic shape of a sharpened crest and rounded trough, and resonate at frequencies greater than the ion gyromotion. The waves are nonlinear, and therefore the linear analysis techniques introduced in chapter 2 cannot be applied. Instead, the data is analysed using the empirical mode decomposition, a technique that reduces a waveform to a set of basis vectors derived directly from the waveform itself, without relying on an *a priori* form for the basis set. The EMD technique is implemented with the noise-assisted ensemble EMD approach, where Gaussian noise is added to the original waveform to combat mode mixing. In the DNLS, a new shape of the pseudopotential, U_b, is assumed that supports oscillatory solutions for arbitrary values of the transverse magnetic field. In contrast to previously assumed forms, this form is of a double-well shape for arbitrary values of the magnetic field, and therefore provides two regions where oscillatory nonlinear solutions are possible, as well as a transitional region between the two wells and a supernonlinear region above both wells. The experimental and numerical solutions are compared directly in phase space and it is found that the nonlinear waves

are in good agreement with the solutions formed from the new pseudopotential form. The main differences in the form of the pseudpotential assumed here, U_b, and that of previous forms is that U_b contains oscilaltory solutions for arbitrary $s > 0$, because $U_b \to \infty$ as $s \to 0$. The double-well shape is also preserved for all positive real values of the transverse magnetic field, allowing small and large amplitude solutions. Both solutions are explored and found to be in good agreement, suggesting that the double well form is valid. This shows that the cubic nonlinearities present in the DNLS, equivalent to four-wave interactions in the weak turbulence approach, are an essential component of the evolution of SLAMS, and therefore general foreshock dynamics, as SLAMS play an important role in the cyclic reformation of the shock layer. The method employed in this chapter is applied to a small sample of three individual wavetrains, but is in principle applicable to all nonlinear waveforms that exhibit the characteristic SLAMS shape, or nonlinear waves that contain cubic nonlinearities and are describable with the DNLS. It is posited that the form of the pseudopotential is dependent on the nonlinear waves themselves, as they can influence the plasma parameters from which the pseudopotential is derived. However, it is difficult to draw conclusions on the dynamics of the pseudopotential with the small sample size employed here, and the work of this chapter is presented more as a proof-of-concept of the EEMD methods and display of the general efficacy of the pseudopotential. A statistical study based on an ensemble of nonlinear waveforms similar to those shown here would prove more useful in establishing the average form of the pseudopotential. The phase speed of the nonlinear waves studied in this chapter exceed that of the local Alfvén speed by a factor of 1.4-1.5, and the speed is positively correlated with the wave amplitude. The interaction of the nonlinear waves with the background plasma is quantified by the change of the pseudopotential, a parameter dependent on core plasma parameters, which transitions from a double-well to a single-well form. The presence of a double-well potential could in principle support a super-nonlinear wave, but that falls out of the scope of the present discussion.

Chapter 4

Wave-Wave Interactions of Magnetic Field Fluctuations in the Terrestrial Foreshock

4.1 Introduction

The emphasis of the previous chapters was on the interactions between waves and the background plasma. The work of this chapter is concerned with the interactions between these waves themselves, specifically in the context of turbulence. Turbulence is a flow regime concerned with the dynamics of fluids that undergo chaotic changes in pressure and flow velocity [184]. *Wave turbulence* is a framework designed to model the turbulent effects of interacting waves, defined as the out-of-equilibrium statistical mechanics of random nonlinear waves [185]. In the colisionless plasma of the foreshock, wave turbulence provides an appropriate model of the interaction of nonlinear waves of the type studied in the previous chapter. In general, turbulence theories are used to model the transport of energy between spatial scales, either from larger to smaller scales in a direct cascade, or in the reverse direction in an inverse cascade. In wave turbulence this energy transport through scales, or alternatively through frequencies, is facilitated through direct interactions between the waves themselves. In a system that contains nonlinearities of quadratic leading order, wave-wave interactions occur and form so-called *triads;* interactions between three modes satisfying the relation $f_1 + f_2 - f_3 = 0$, where f is the mode frequency. Triads that form in this way represent the most efficient method of energy transfer through frequencies in the weak turbulence limit, where energy is transferred directly between modes described by wave equations with weak nonlinearities [186][187]. Each separate dispersion relation of these interacting waves can be modelled as $\omega \propto k^{\alpha}$ for some constant α, dependent on the exact wave mode. The value of α therefore determines the shape of the dispersion relation; for $\alpha > 1$, the shape will be convex and bowl-like, for $\alpha = 1$ the dispersion will be a straight line and for $\alpha < 1$, the curve becomes concave and

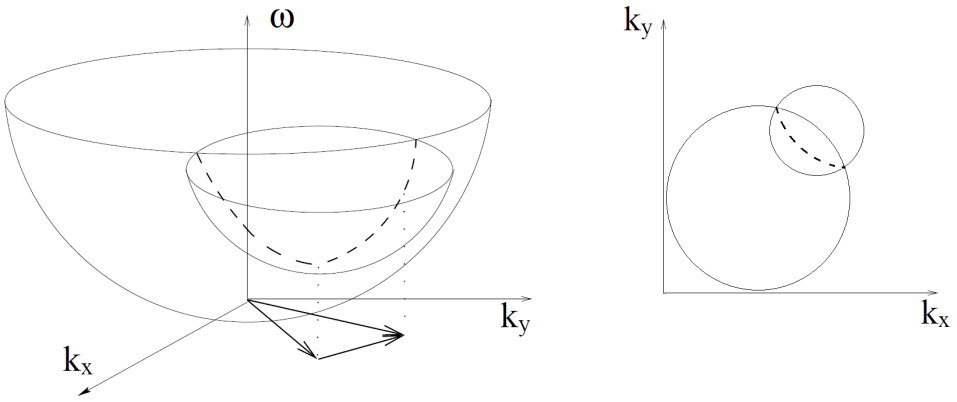

Figure 4.1: Graphical depiction of three-wave interactions in 2D k-space. Left: dispersion surfaces for two waves satisfying $\omega \propto k^{\alpha}$ with $\alpha > 1$. The dashed line is the curve describing their intersection. Right: the same diagram but viewed down the ω axis. The dispersion relation must have $\alpha \geq 1$ for the surfaces to intersect and three-wave resonance to be possible.

funnel-like. If the wave vector is further split into its component parts, for example k_x and k_y, then the curves becomes surfaces in the two-dimensional k-space. Figure (4.1) depicts two such surfaces representing dispersion relations that satisfy $\alpha > 1$. To demonstrate the orientation of the dispersion surfaces, a view of the same plot containing just the wavenumber components, that is; looking "down" the ω axis, is also shown. The intersection of these surfaces forms a curve, which is depicted by the dashed line in figure (4.1). This curve then represents the set of wavevector and frequency pairs that satisfy the resonance condition, $f_1 + f_2 - f_3 = 0$. As an example, two vectors are chosen arbitrarily from the dashed curve of intersection of figure (4.1) and their projections onto the $k_x k_y$ plane are shown in solid-line vectors. The vector sum of these projections, that is formed as the result of the two interacting waves, is also shown, completing the resonance condition. If the system is sufficiently energetic, multiple sets of triads will form, and this can lead to interaction between triads [188]. In principle, if enough free energy is available to the system, interactions between the resonant triads themselves can form; two triads can share a single common node for example. Multiple triads interacting with each other in this way will form a complicated network that describes the complete quadratic wave-wave energy transfers of the system [189]. The excitation of resonant triads is a well-understood phenomenon in fluid mechanics [190][191], and has been applied to atmospheric dynamics [192], and ocean waves [193], but observations in space plasmas are lacking. Understanding the evolution of wave-wave interactions into wave turbulence in the foreshock is integral to understanding the physical phenomena that govern energy transfer between scales.

Three-wave interactions have been identified in solar radio emissions [194] and in the

near-Earth solar wind [195]. Dudok de Wit used Volterra models to estimate quadratic energy transfer coefficients and linear growth rates from two-point measurements of the foreshock using AMPTE data [159]. Wave coupling was measured using the *bicoherence*; a higher-order statistical measure of the amplitude of triplets of phase-coherent modes. These measurements were focussed on relatively short ensembles (~3 minutes) that contained SLAMS, and concentrated on their interaction with other modes. It was shown that low-frequency (0.1Hz) SLAMS draw energy from hot ion populations before dissipating this energy as whistler waves at 1Hz, in an energetic cascade from large to smaller scales, but the dominant frequencies of energy transfer were not identified. Narita used 32 foreshock crossings of higher resolution Cluster data to investigate nonlinear behaviour and wave coupling with reference to the dispersion relations, the wavenumber spectra of the magnetic field energy, and the dimensionless cross helicity [196]. The ion/ion right hand resonant instability was identified as an important factor in the early stages of foreshock wave evolution, however the techniques used did not measure wave-wave interactions directly and subsequently the extent of wave coupling was not properly identified. Other results that make use of the bicoherence have studied frequencies outside of the ULF range, for example on the conversion of electron Langmuir waves to transverse modes [197], and therefore do not address interactions in the ULF wavefield arising from the beam instability.

In this chapter, wave-wave interactions between ULF modes up to 1Hz are investigated using techniques based on the wavelet bispectra. Emphasis is placed on the *wavenumber mismatch*, the extent to which interacting modes are spatially misaligned, and on the interaction between triads. Particular attention is paid to the direction of the energy transfer through frequencies, as facilitated by triads, in the context of wave turbulence.

4.2 Data

The interval for this chapter is the foreshock crossing dated 18-02-2002, 13:30-14:00. This interval was studied in chapter 2, and found to contain fast magnetosonic and Alfvén modes, but most of the power was contained in nonlinear advected structures, and the dispersion relations were less conclusive than the other intervals of that chapter. Plasma parameters for this interval are shown in table (4.1), and an overview plot is shown in figure (4.2). As shown in this figure, the satellites are fairly close to the time-averaged shock, but are far enough outside of it to ensure that the natural dynamics of the shock do not influence the measurements taken by the spacecraft. The FGM data, and to a lesser extent the velocity data, show obvious differences in the characteristics of the data of the

$<\vec{\chi}>$ (km)	$<\vec{B}>$ (nT), GSE	$<\vec{V}_{sw}>$ (km s^{-1})	β	$\vec{V}_A$ (kms^{-1})	$\Theta_{V,B}(^\circ)$	$\Theta_{\chi,V}(^\circ)$	$\Theta_{\chi,B}(^\circ)$	ω_{ci} (rad s^{-1})
64.1	(7.51,-4.01,7.16)	365.6	0.32	80.1	134	138	37	1.08

Table 4.1: Plasma parameters for 18/02/2002, symbols are as defined in table (2.1)

interval. Up to ~13:33, the magnetic field is dominated by large-amplitude, low-frequency intervals. Between ~13:33-13:50, the amplitude is reduced but the fluctuations are higher frequency. A close up of these higher frequency data are displayed in figure (4.3). The higher-frequency region is also accompanied by an anisotropy in temperature, with respect to the magnetic field direction, shown in figure (4.2) as the difference between the black (parallel) and red (perpendicular) data. The proton density loosely follows the trends of the FGM data but is more dramatically discontinuous at ~13:50, around the same time the higher frequency FGM data begin to taper. Because of the transitory nature of the data in this interval, the interval is split into six further subintervals, labelled A through F, which are shown on figure (4.2) as the vertical dotted lines and are:

A: 13:37:00 - 13:30:00

B: 13:30:00 - 13:33:00

C: 13:33:00 - 13:35:00

D: 13:34:30 - 13:36:00

E: 13:35:00 - 13:48:00

F: 13:49:00 - 13:57:00

There is an overlap between subintervals C and D, and D and E, to exclude the large-amplitude feature of the FGM data visible in figure (4.2). The power spectrum for the entire interval is shown in the left column of figure (4.4), taken using the wavelet transform (section (2.3.3)), top, and integrated over the interval, bottom. As shown, the interval generally has consistent power in two distinct bands of frequencies, one spanning ($10^{-2}10^{-1}$)Hz; the ULF band, and the other centred at 1Hz. During the period between 13:35-13:50 the 1Hz band dominates over the ULF modes. This partitioning of the data into two bands at these frequencies is a fairly common phenomena, demonstrated by the centre and right columns of figure (4.4) for two further intervals of the same month: 11/02/2002 and 21/02/2002. In all three inervals, the integrated power spectra (bottom) show a spike at 1Hz. The 11/02/2002 (center column) has power in the 1Hz band comparable to the ULF band over the entire interval. This is in contrast to 21/02/2002 (right

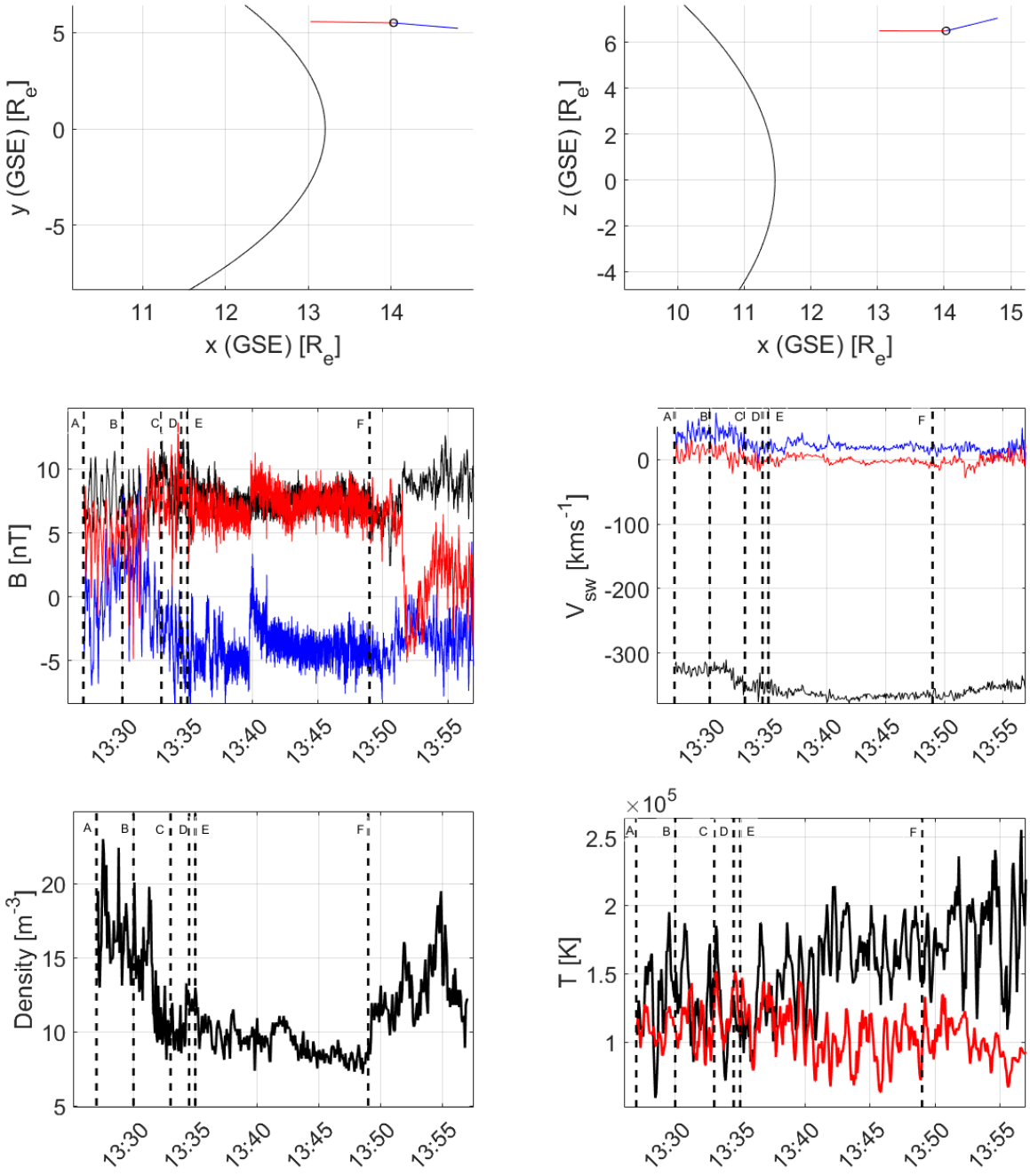

Figure 4.2: Overview plot for 18/02/2002 showing top left, right: positions of C3 probe relative to a time stationary shock. Middle left: FGM data for interval, right: HIA proton velocities in GSE. Bottom left: HIA proton density, right: HIA temperature parallel (black) and perpendicular (red) to the magnetic field. The vertical dotted lines marked A-F represent the beginnings of smaller subintervals studied later.

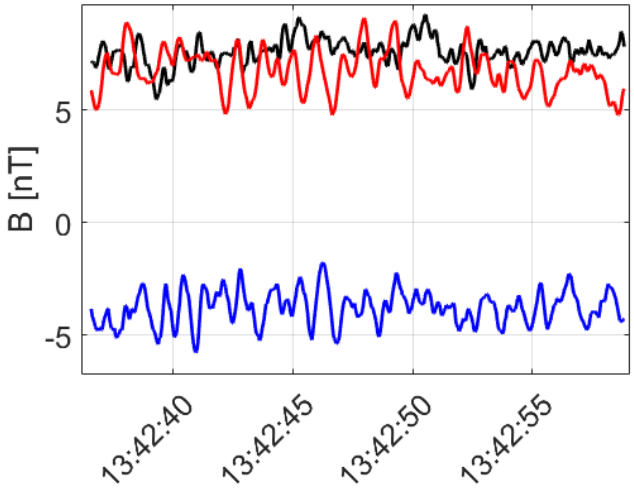

Figure 4.3: closeup of FGM data for 18/02/2002, during the period of enhanced 1Hz power.

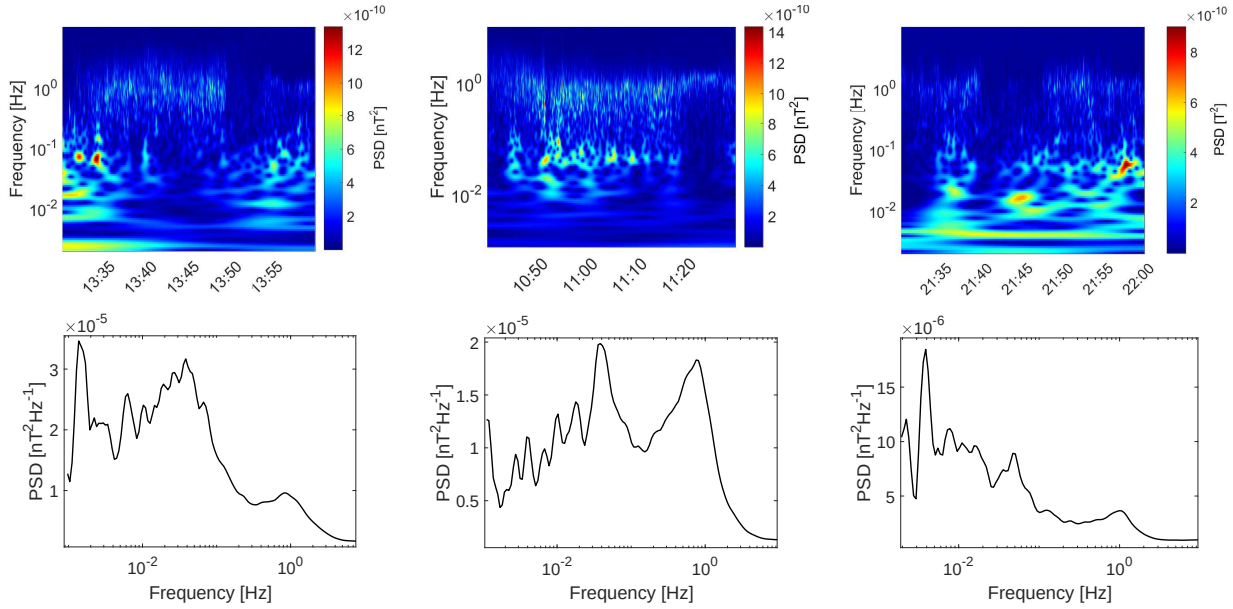

Figure 4.4: Power spectra of C3 data taken left: 18/02/2002, center: 11/02/2002, right: 21/02/2002. Top: wavelet power spectrum. Bottom: time-integrated power showing presence of dominant peaks. The power is organized into one band between 10^{-1} and 10^{-2} and another band centered on 1Hz.

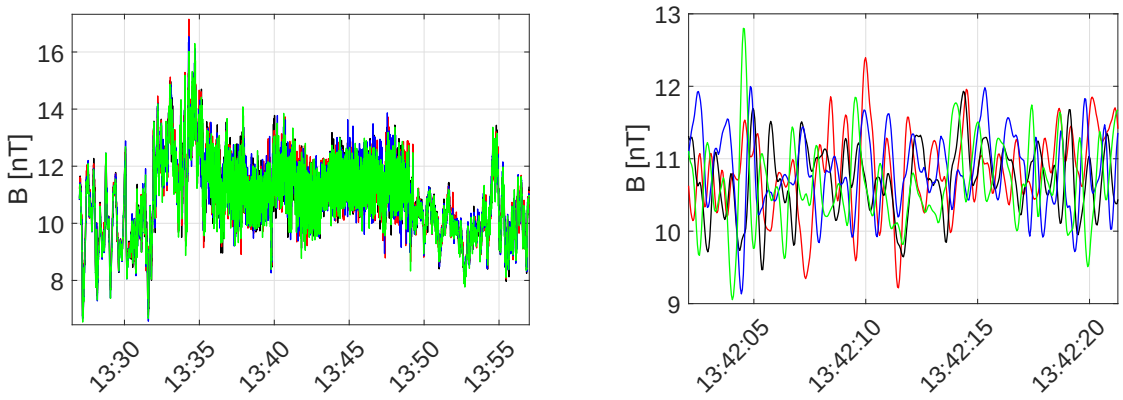

Figure 4.5: Left: FGM data for all satellites for 18/02/2002. Right: Closeup of the high-frequency dominant region. Colours represent: black; C1, red; C2, blue; C3 and green; C4.

column), in which the ULF power clearly dominates. The interval 18/02/2002 (left) contains parts in which power is equally divided between the bands, as well as parts in which either the 1Hz or ULF bands dominate. It is therefore the most informative interval and is the subject of this chapter.

The focus of the chapter is the wave-wave interactions that lead to the transfer of energy into the band of frequencies centred at 1Hz, represented by the relatively broad peaks in the integrated power spectra of figure (4.4). At the onset of the dominant 1Hz band, the subintervals are small, ~3 mins. The subinterval that contains dominant 1Hz power is longer, ~10 minutes, because this subinterval is more stable, as can be seen in figure (4.4). Also visible in this figure is the loss of power in the 1Hz band at ~13:50, and subsequent regain around 5 minutes later. Due to Cluster's crossing of the shock after the interval, it is not possible to see if the 1Hz band regains its stability after this point. The analysis, described in the next section, requires only the use of single probe data, however it is important to be sure that the results are generalizable. Figure (4.5) shows the FGM data for the entire interval for all four satellites, and a closeup of the high-frequency region. It can be seen that the general trend for the interval is followed closely for all four probes. This continues into the high frequency region where, aside from a few amplitude variations, the FGM data looks similar for each satellite. The choice of probe is therefore inconsequential and the analysis should produce similar results for whichever satellite is chosen. Since the dispersion relation for this interval was investigated in chapter 2 for C3 and C4, the C3 satellite will be used for the analysis of this chapter.

4.3 Methodology

4.3.1 Bispectral Analysis

Generally, when considering a real-valued discrete time-random process $x(t)$, we may characterize the signal in a multitude of ways, with reference to, for example, the signal's amplitude, energy, or waveform. One common method is to construct the *probability density function (PDF)* of the signal, which provides detailed information about the distribution of the amplitudes of the process and can be used to characterize the process [198]. A set of variables that describe the shape of this PDF are its *moments*. In general, these moments are calculated using the moment generating function (MGF), defined [199]:

$$M(t) =< e^{tx(t)} > \tag{4.1}$$

where <> denote the expectation operator. Applying the Taylor series expansion of the exponential:

$$\begin{aligned} M(t) &= 1 + t < x(t) > + \frac{t^2 < x(t)^2 >}{2!} + \frac{t^3 < x(t)^3 >}{3!} + ... \\ &= 1 + tm_1 + \frac{t^2 m_2^2}{2!} + \frac{t^3 m_3^3}{3!} + ... \end{aligned} \tag{4.2}$$

where m_n is the n^{th} moment of $x(t)$. The first moment is quite familiar, m_1 represents the mean of the signal. The second moment, m_2, is the variance, a measure of the spread of the signal. The third is the skewness, a measure of asymmetry in the PDF, and the fourth order moment is the kurtosis, a measure of the sharpness of the PDF [200]. In general the moments can be calculated by taking an expectation over the process multiplied by lagged values of the process:

$$\begin{aligned} m_2(\tau_1) &=< x(t)x(t+\tau_1) > \\ m_3(\tau_1,\tau_2) &=< x(t)x(t+\tau_1)x(t+\tau_2) > \\ m_4(\tau_1,\tau_3,\tau_2) &=< x(t)x(t+\tau_1)x(t+\tau_2)x(t+\tau_3) > \end{aligned} \tag{4.3}$$

The variance is then determined by $m_2(0)$, the skewness by $m_3(0,0)$, etc, and can be used to characterize the signal. A Gaussian signal, for example, is completely described by the mean and variance, and the higher order moments are all identically zero. This means

that measurement noise, which is usually assumed to be a Gaussian process, should show no trace in the higher order moments. If the process in which we are interested can be described as non-Gaussian, then the properties of this process will be readily apparent in these higher order moments.

There are also alternative measures of characterizing a signal that prove mathematically useful. One such method is using *cumulants* [201]. Similarly to how the moments can be described as the Taylor expansion of the MGF, the cumulants are described as the Taylor expansion of the *cumulant generating function (CGF)*, $K(t)$, which is defined as the natural logarithm of the MGF:

$$K(t) = \ln < e^{tx(t)} > \tag{4.4}$$

The cumulants and moments are then somewhat related, and the cumulants can be defined:

$$k_n = K^{(n)}(0) \tag{4.5}$$

as the expansion of a Maclaurin series. There are a few simplifications which persist however. For a zero-mean process ($m_1 = 0$), the second and third order cumulants are identical to the second and third order moments [202]. Practically speaking it is simple to subtract the mean from a stationary signal before performing analysis. It is also the case that a zero-mean signal has a variance, or second-order cumulant c_2, equal to the power of the signal.

In the discrete case, the power spectrum, $P(k)$, can be written either as the discrete Fourier transform (DFT) of the autocorrelation function, $R(\tau_1) = c_2(\tau_1)$, where τ_1 is a discrete lag, or as a product of two discrete Fourier transforms whose sum frequency is zero. Alternatively:

$$P(k) = F(R(\tau_1)) = F(c_2(\tau_1)) =< X(k)X^*(k) > \tag{4.6}$$

where $F(x)$ represents the DFT on x, and X is the resulting Fourier coefficient. This is the *Wiener-Khintchine* relation; it is a function of the second order cumulant and returns the usual power spectrum of the signal [202]. The sum of the power spectrum, $P(k)$ over all frequencies k is equal to the zero-lag autocorrelation function, $R(0)$. This quantity is called the variance, σ^2, of the process. We may generalize this relation to higher order cumulants;

we refer to the resulting spectra as *polyspectra*. The third and fourth order polyspectra, for example, are defined:

$$B(k,l) = F^2[c_3(\tau_1,\tau_2)] = \langle X(k)X(l)X^*(k+l)\rangle \tag{4.7}$$

$$T(k,l,m) = F^3[c_4(\tau_1,\tau_2,\tau_3)] = \langle X(k)X(l)X(m)X^*(k+l+m)\rangle \tag{4.8}$$

The first of these definitions, $B(k,l)$ is the *bispectrum*, as it is the second-degree DFT of the cumulant. The second expression is the trispectrum, as it is the third-order DFT. The bispectra and trispectra are the two most studied higher-order spectra. These expressions link the time-domain based cumulants to the frequency-based polyspectra.

The polyspectra offer analysis techniques for measuring wave-coupling in nonlinear signals. A nonlinear coupling between wave modes, which we may model as quadratic to a first approximation, of frequencies f_1 and f_2, will interact to generate a third mode with frequency f_3, such that

$$f_1 + f_2 = f_3 \tag{4.9}$$

is the frequency resonance condition for a trio of waves known as a *triad*. The mode f_3 is phase coupled to its component frequencies. If a system exhibits quadratic nonlinearities, or alternatively, if a system contains resonant triads, then these nonlinearities should be detectable with the bispectrum at the relevant frequencies. We may further normalize the bispectrum by dividing by the total power at these modes [203]:

$$b^2(f_1,f_2) = \frac{|B(f_1,f_2)|}{<|X(f_1)X(f_2)|^2><|X(f_3)|^2>} \tag{4.10}$$

Here, b represents the *bicoherence;* a measure of the bispectrum normalized to the power of the triad, such that $0 \leq b \leq 1$, which is used to quantify the amount of nonlinear coupling between modes of the triad. If b~1, the three modes are strongly phase coupled, whereas if very little phase coupling exists, b will be close to zero.

Bispectral analysis is the general method of investigation of three-wave coupling using equation (4.10) and is well suited for the study of systems containing quadratic nonlinearities and systems of advancing turbulence. For a broadband turbulent spectrum, bispectral analysis is the standard technique for quantifying the amount of mode coupling in a given signal. The summed bicoherence;

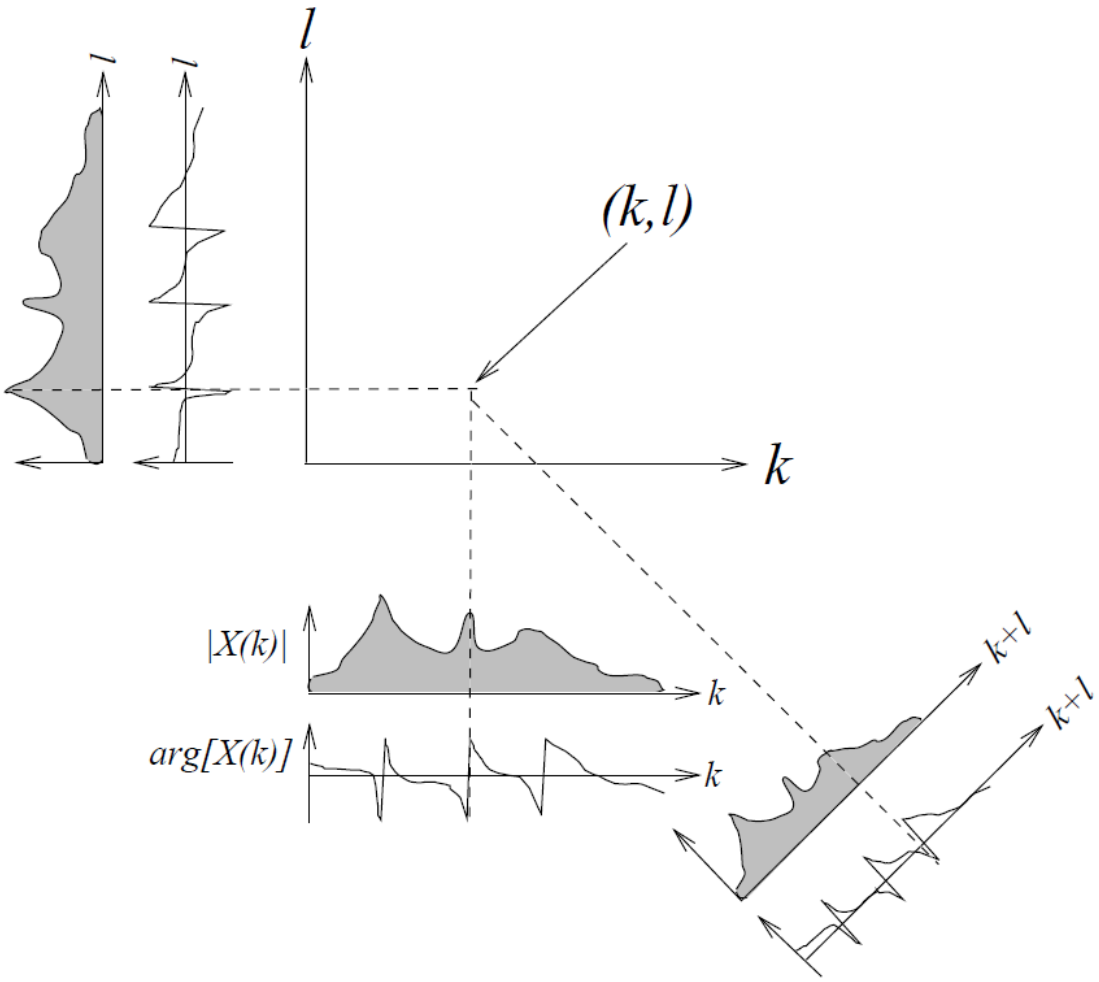

Figure 4.6: Schematic of the bispectrum, showing contributions from the magnitude and phase of the coefficients at the three frequencies l, m and $l+m$.

$$S(f) = \sum b^2(f_1, f_2) \tag{4.11}$$

represents the amount of coupling at the frequency f relative to all other frequencies [204]. In praxis, the modes, f_1, f_2, of the triads are not known *a priori*, and so the bicoherence is taken over all frequency triads that can be constructed from the decomposition that satisfy the resonance condition (4.9).

In a similar way to that in which the power spectrum has a symmetry point at the Nyquist frequency, the bicoherence has multiple symmetries in the frequency planes. There is no "preferred" order in which to take the frequency triads, as the reonance condition is commutative. For this reason, it is only necessary to calculate the bicoherence in the principal domain $0 \leq f_1 \leq f_N, f_1 \leq f_2 \leq f_N - f_1$, where f_N is the Nyquist frequency. The *principal*

domain of the bicoherence is the set of frequencies defined by $f_1 + f_2 < f_N$.

It should be noted that whilst the derivations of this section have referred to the Fourier coefficients, X, in principle these may be substituted for the coefficients of any decomposition technique that provides amplitudes that are functions of frequency. We may substitute the Fourier representation for the wavelet decomposition, for example. The wavelet decomposition (described in section (2.3.3)) does not formally devolve signals into frequencies, but rather into scales. That is, the wavelet coefficient is dependent on the scale of the mother wavelet, and not strictly the frequency. However, if the Fourier transform of the wavelet has a well-defined peak, then the scales, a, may be translated to frequencies such that $f = 1/a$. The Fourier transform of the generalized Morse wavelets is given by equation (2.38) and is sufficiently sharply-peaked for $\gamma = 3$, $P^2 \approx 60$ to allow this frequency-scale conversion.

4.3.2 Wavenumber mismatch

The resonance condition equation (4.9) is strictly incomplete as, whilst it accounts for modes that have coherent phases, it does not include any information on whether these modes are spatially able to interact [205]. To fully model resonant matching the definition of (4.9) must be extended to include wavenumber resonance:

$$\begin{aligned} f_1 + f_2 &= f_3 \\ \vec{k}_1 + \vec{k}_2 &= \vec{k}_3 \end{aligned} \tag{4.12}$$

where k represents the wavenumber of the mode. This definition of resonance is more expansive, as a selection of frequencies that satisfy the resonance condition will not necessarily result in resonant matching of the wavenumber components, and vice versa. Both conditions of (4.12) must therefore be met for resonance to exist. With single-point measurements, it is not possible to measure the wavevector k and thus the bicoherence is not a true reflection of the underlying wave-wave interaction. In order to get a more faithful representation of resonance, we may extent the concept of the bicoherence to include spatial information using two point measurements with analogy to the normal wave coherence. For two spatially separated probes, a coherent mode can be distinguished from noise by measuring the linear coherence, defined [206]:

$$\gamma^2 = \frac{< |X^*(x_1, f_1) X(x_2, f_1)|^2 >}{< |X(x_1, f_1)|^2 >< |X(x_2, f_1)|^2 >} \tag{4.13}$$

When γ^2 is close to unity, the mode f_1 can be treated as a coherent wave over the full distance of the probe separation. Conversely if γ^2 is close to zero, then the mode loses coherence over this distance, and becomes increasingly more random and uncorrelated. For single-probe data, the bicoherence (or autobicoherence) represents the extent of three mode coupling at the point at which the data is taken. In a similar fashion to the linear coherence we may define the *bispectrum coupling coherency*, (or *cross-bicoherence*) to distinguish between triads that remain coherent between spatially separated probes [205]:

$$b^2(f_1,f_2) = \frac{|<X(x_1,f_1)X(x_1,f_2)X^*(x_1,f_3)X^*(x_2,f_1)X^*(x_2,f_2)X(x_2,f_3)>|}{<|X(x_1,f_1)X(x_1,f_2)|^2><X^*(x_1f_3)^2><|X^*(x_2,f_1)X^*(x_2,f_2)|^2><X(x_2f_3)^2>} \tag{4.14}$$

Here, $x_{1,2}$ refer to the positions of the probes in real space. The numerator of the bispectrum coupling coherency is the cross-correlation of the bispectra at both positions, for a frequency triad $f_1 + f_2 = f_3$. It is a measurement of three-wave coupling between two spatial points, normalized by the total power between the modes for both positions. As the normal bispectrum reveals, based on its proximity to zero or unity, the extent to which a triad are phase-correlated, the cross-bispectrum is a normalized quantity that reveals not only that a triad exists, but that it remains resonant over the distance $x_2 - x_1$.

To measure the extent to which the wavenumbers satisfy (4.12) between the two probes, we make use of a technique that mirrors those of section (2.3.2), by making use of the phase difference of the modes between the probes. We may expand the bispectrum, (4.7), at a single point, x_1, for the triad $f_1 + f_2 = f_3$, using the polar notation, equation (2.22);

$$B(f_1,f_2) = \langle X_1 X_2 X_3^* \rangle = \langle a_1 a_2 a_3 e^{(k_3-k_2-k_1)x_1+(\phi_3-\phi_2-\phi_1)} \rangle \tag{4.15}$$

Taking the phase of the cross correlation of the bispectra at two points, will then give:

$$\begin{aligned} &ph\left(\langle X^*(x_1,f_1)X^*(x_1,f_2)X(x_1,f_3)X(x_2,f_1)X(x_2,f_2)X^*(x_2,f_3)\rangle\right) \\ &= \langle\left[(k_3-k_2-k_1)\,x_1 + \left(\phi_3-\phi_2-\phi_1\right)_1\right] - \left[(k_3-k_2-k_1)\,x_2 + \left(\phi_3-\phi_2-\phi_1\right)_2\right]\rangle \end{aligned} \tag{4.16}$$

Note that the frequency components are assumed to satisfy the resonance condition. Define:

$$\Delta\phi = \left(\phi_3-\phi_2-\phi_1\right)_2 - \left(\phi_3-\phi_2-\phi_1\right)_1 \tag{4.17}$$

$$\Delta k = (k_3 - k_2 - k_1) \tag{4.18}$$

and hence the amount of wavenumber mismatch is given by:

$$\langle \Delta k \rangle = \langle k_3 - k_2 - k_1 \rangle = \frac{\left(ph\left(\langle X^*(x_1, f_1) X^*(x_1, f_2) X(x_1, f_3) X(x_2, f_1) X(x_2, f_2) X^*(x_2, f_3) \rangle \right) + \Delta\phi \right)}{x_2 - x_1} \tag{4.19}$$

If Δk is low, then the modes satisfy the wavenumber resonance condition. This is only possible if the phase difference $\Delta\phi$, is zero between the two measurement points. This phase difference is the overall phase difference of the triad and is zero when the cross bicoherence is unity. The faithfulness of the Δk measurements are therefore predicated on a high bicoherence; a measurement of the wavenumber mismatch is meaningless if the triad is not coherent across both probes. The cross-bicoherence can be used to preclude spurious measurements of the wavenumber mismatch by thresholding the cross bicoherence at some value. The general methodology is to calculate the wavelet cross-bicoherence for FGM data, focussing on the coupling between ULF modes and the band of frequencies centred close to 1Hz. To distinguish the dominant modes of power transfer, triads are identified by wavelet power spectra integrated over short intervals. The role of the wavenumber mismatch in these coupling processes is also investigated.

4.4 Results and Discussion

To study the development of the bicoherence, the part of the interval where the 1Hz waves are dominant is split into smaller sub-5 minute segments defined in section (4.2), shown in figures (4.7)-(4.12). These plots show the wavelet power (top right), the time-integrated power (top left), the cross-bicoherence (bottom left), and the wavenumber mismatch (bottom right). The cross-bicoherence plots show the principal domain of the bicoherence and the reflection along the $f_1 = f_2$ diagonal. The most well-correlated modes are not necessarilly the modes through which most of the energy of the system moves. Therefore, to highlight the most energetic triads, the power is integrated over time and the triad corresponding to the largest two peaks, the *principal triad*, is shown in the top left of each plot. The two dashed black lines of the integrated power of (4.7)-(4.12) represent f_1 and f_2 of equation (4.9) and the red line is their sum, f_3. Hence, the vertical lines represent the triad that contains the largest share of the power. These principal triads of each subinterval are

then denoted with letters such that $A_{1,2,3}$ represents $f_{1,2,3}$ of the principal triad of the first subinterval, $B_{1,2,3}$ represents $f_{1,2,3}$ of the principal triad of the second subinterval, and so on. This terminology is used in table (4.2), which lists the frequencies of each principal triad. As shown in table (4.2), the frequency triads overlap as time progresses, creating a general trend of energy dominance into higher frequencies. The bicoherence is a useful measure of mode coupling but it cannot be used to tell the "direction" of energy transfer between modes of the triad. To this end, the wavelet power spectra (top left) are marked with the most energetic triads as horizontal lines that follow the same colour scheme as the vertical lines of the integrated power (top right). These lines are also produced in the bicoherence and wavenumber mismatch plots, in both the vertical and horizontal directions, for each subinterval.

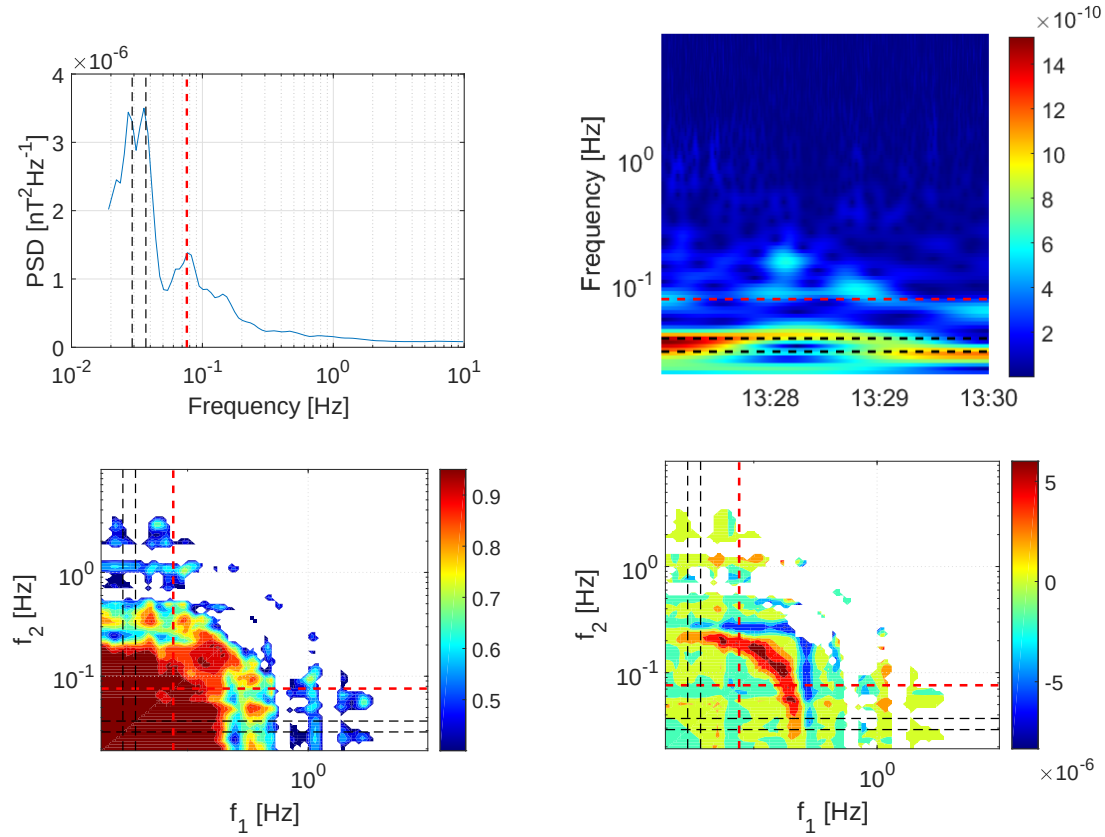

Figure 4.7: Top left: time-integrated wavelet power, top right: wavelet power spectrum, bottom left: cross-bicoherence, bottom right: wavenumber mismatch, as functions of the frequencies, for the first subinterval; A, 13:27-13:30. The dashed vertical lines of the top left panel show the principal triad; the trio of frequencies satisfying (4.9) that contain the most power. The two black lines are f_1 and f_2 and the red line is their sum, f_3. The frequencies are given in table (4.2).

Initially, in the first two subintervals, the ULF modes are very well coupled (b=0.95-1) up

to ~0.2Hz. The power is concentrated in the ULF region and very little is in the band of frequencies centred at 1Hz. The dominant modes of subinterval A, ie $A_{1,2,3}$, can be seen in the coherence plots of subinterval B, forming horizontal and vertical features at these frequencies that retain their phase coherence. In figure (4.8) it can be seen that one of these horizontal features of the cross-bicoherence lines up with the frequency B_1, indicating the coupling between the triads described by $A_{1,2,3}$ and $B_{1,2,3}$. A second feature is also visible in subinterval B which aligns with A_1, the lower frequency of subinterval A. The wavelet spectrum shows that these two modes are coexistent, and therefore the $A_{1,2,3}$ and $B_{1,2,3}$ triads couple. The wavenumber mismatch (bottom right of panel of figures (4.7)-(4.12)) in the first few subintervals is subject to the same limitations as the bicoherence; despite the fact that certain modes exhibit large values of wavenumber mismatch and are well-correlated, it is not necessarily the case that these modes are the dominant ones of the system. However, the mismatch between these lesser triads is well resolved in areas where the coherence is large, and so can be faithfully compared to the mismatch of more important triads. The dominant three-wave interaction is represented by the intersection of the first and second black lines. In subinterval A, this interaction has very little mismatch,

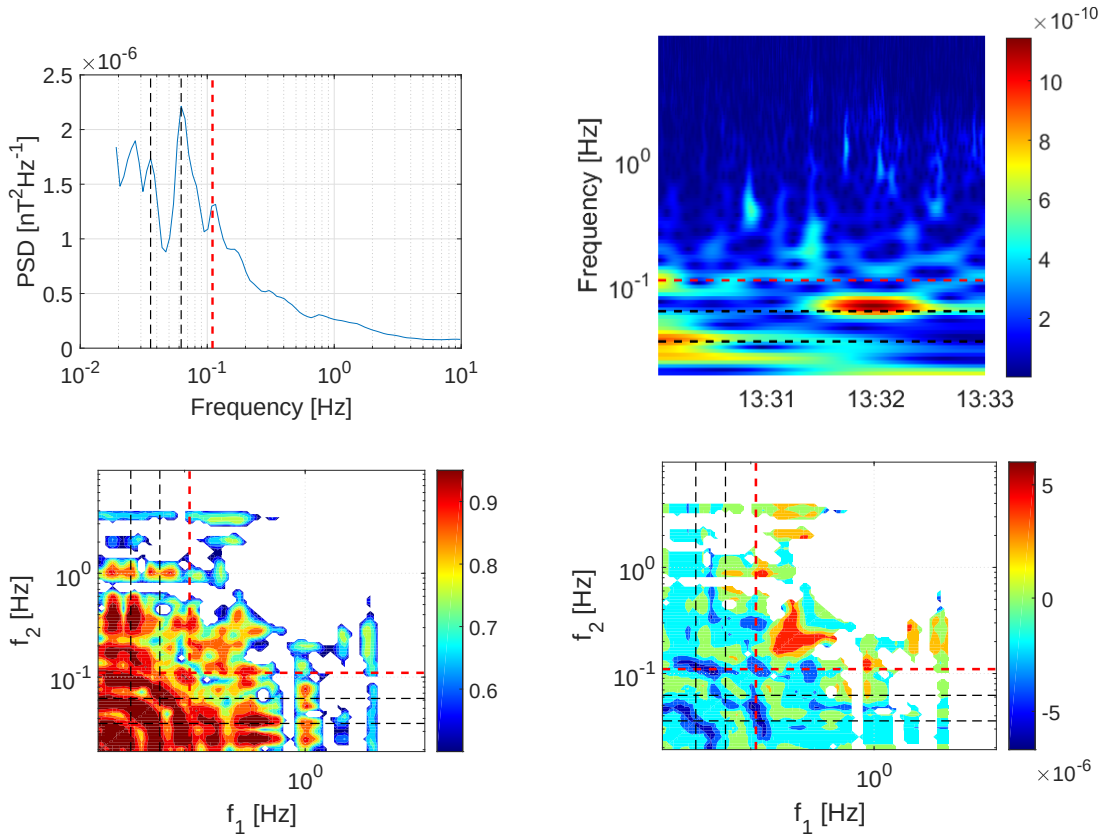

Figure 4.8: Subinterval; B, 13:30-13:33. The vertical/horizontal features at low frequencies correspond to B_1 and A_1 of table (4.2)

indicating an efficient transfer. By interval B, the mismatch of the dominant interaction has changed little, so this interaction remains efficient. The low-frequency peak A_1 still contains an appreciable amount of power at B, and this power is transferred efficiently to the principal triad of B. The interaction of B_3 with B_1, B_2, and itself, B_3, all have large mismatches, shown by the interaction of the red line of figure (4.7) with the two black, meaning that despite the fact that these three modes are well correlated, as shown in the cross-bicoherence, the resonance is weak.

By subinterval C, the broad bicoherence up to ~0.2Hz of the previous two subintervals narrows to specific frequencies of $C_{1,2,3}$, indicating the tendency of the system to favour energy transfer between those modes that are most efficient. In each case of these power spectra, the two lesser frequencies $f_{1,2}$ contain energy before the higher frequency f_3 does, and can be seen losing power with a simultaneous increase in power in f_3, demonstrated most clearly in the spectrum of the subinterval C, figure (4.9). In this example, power in C_1 continues to grow as C_2 does, and then is transferred to C_3 at a quicker rate. As power increases in C_1, the peak broadens, and then loses power rapidly at the frequency of C_1, but

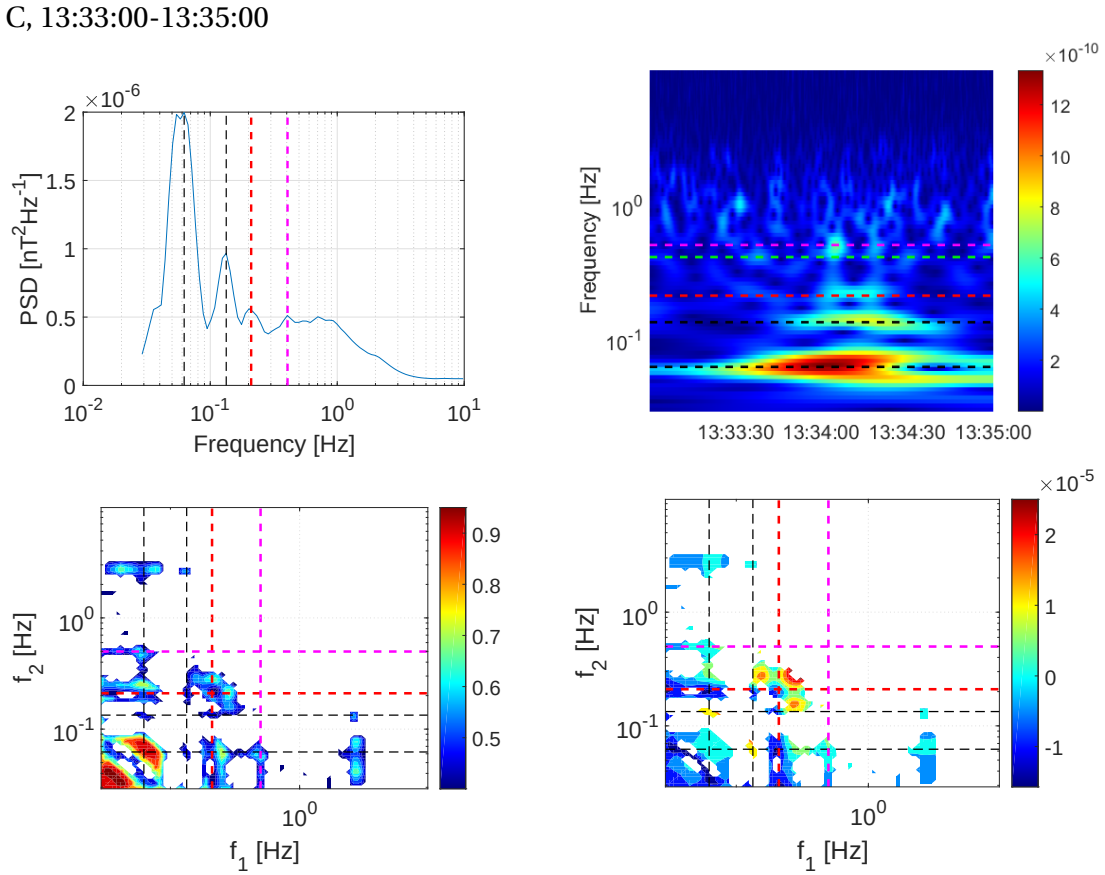

Figure 4.9: Three-wave interactions for subinterval C, 13:33-13:35. The magenta line shows a peak corresponding to a four wave interaction, $f_4 = f_3 + f_2 + f_1$.

retains power either side of this frequency, splitting into two peaks of lower power. This example also shows a four wave-interaction at the peak denoted by the magenta line. The power of this fourth peak is less than that contained in the triad, indicating the relative weakness of 4-wave compared to 3-wave coupling at this point. The horizontal teal line of the wavelet spectrum of figure(4.9) is the exact line $C_1 + C_2 + C_3$, which is slightly less than the peak at the magenta line. The difference between the teal and magenta line is equal to the difference between C_1 and the edge of the broadened peak around C_1 at the time of the emergence of the peak at C_4, suggesting that the broadening of the ULF modes contributes to the onset of four-wave coupling processes to higher frequencies. The coupling is supported by the increase in the cross-bicoherence at the intersections of the C_1 line with each of the other C_2, C_3, and C_4 lines, indicating coupling between these frequencies. The duration over which the power increases between C_1 and C_2 is shorter than the duration of power increase of C_3. This is expected; the triads at higher frequencies will interact quicker than those at lower frequencies, as the peaks of their constituent frequencies will align quicker. The principal triad for interval C has a wavenumber mismatch ~10^{-5}m, the largest of any principal three-wave interaction up to this point. All of the low frequency modes, including those of the principal triad, are also much less correlated in this subinterval. The modes that remain highly correlated, most notably the self-interaction of C_1, are the modes for which the wavenumber mismatch is close to zero. However in general, the lower frequency modes are not as subject to wavenumber mismatch as the higher frequencies, at this point.

More four-wave processes are evident in subinterval D, figure (4.10). This subinterval captures the onset of the 1Hz power dominance and occurs directly after the first four-wave processes become visible in subinterval C. The integrated spectrum of interval D shows six lines. The first three of these, the red and two black, are the usual principal triad ($f_1 + f_2 = f_3$) composed of ULF modes. The magenta line is at the frequency equal to the sum of the two black lines and the red line, indicating a four-wave interaction. This is denoted by D_4 in table (4.2). The green line, D_5, is at a frequency equal to the sum of the magenta, red, and the higher black line, and the mustard line, D_6, is equal to the sum of the green, magenta, and red line. These higher frequency coloured lines then represent the energy transfer due to a sequential four-wave coupling processes. The frequencies of these processes are listed in table (4.2). Also noteworthy in this interval, where the four-wave interactions are strongest and visibly present in the integrated power, is that the maximum wavenumber mismatch is at its highest value, and is much larger and more localized in the ULF range.

The development of three-wave to four-wave interactions is accompanied by an increase

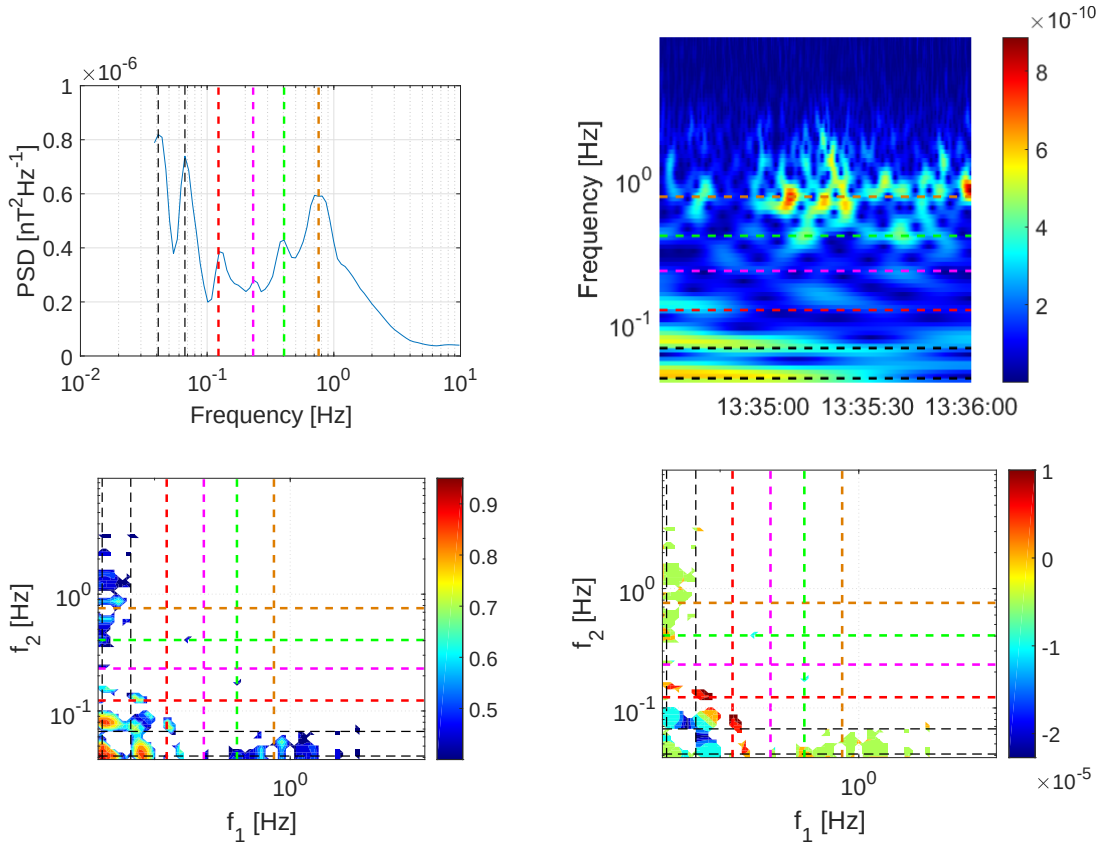

Figure 4.10: Subinterval D, 13:34:30-13:36, showing the onset of 1Hz power dominance and four-wave interactions. The red line is equal to the two previous black lines, the magenta line is equal to the sum of the red and black lines, the green line is the sum of the magenta, red, and highest black line, and the mustard line is equal to the sum of the green, magenta and red line.

in power in the band of frequencies close to 1Hz. In the integrated power spectrum of subinterval E, figure (4.11), this band is broader than the ULF peaks, but the wavelet spectrum shows that this broad peak is composed of multiple smaller peaks that exist for shorter durations than the ULF modes, with power contained in clusters that are close in frequency. This broad 1Hz peak has a width larger than 1Hz, and so therefore can theoretically couple to any of the ULF modes; largely expanding the amount of available wave-wave interactions. This is demonstrated in figure (4.11), for which two triads have been highlighted. In this subinterval, the four-wave interactions are less visible than the three-wave, as shown in the second triad. The peak of E_6, the third frequency of the second triad, lines up with the sum of E_4 and E_5 but not when E_3 is also included in the sum. However, the four wave interaction is likely still available, and contributes to the broadening of the 1Hz peak. The ULF peaks are notably broader in subinterval E than earlier, indicating the larger number of potential energy transfer channels. This is consistent with

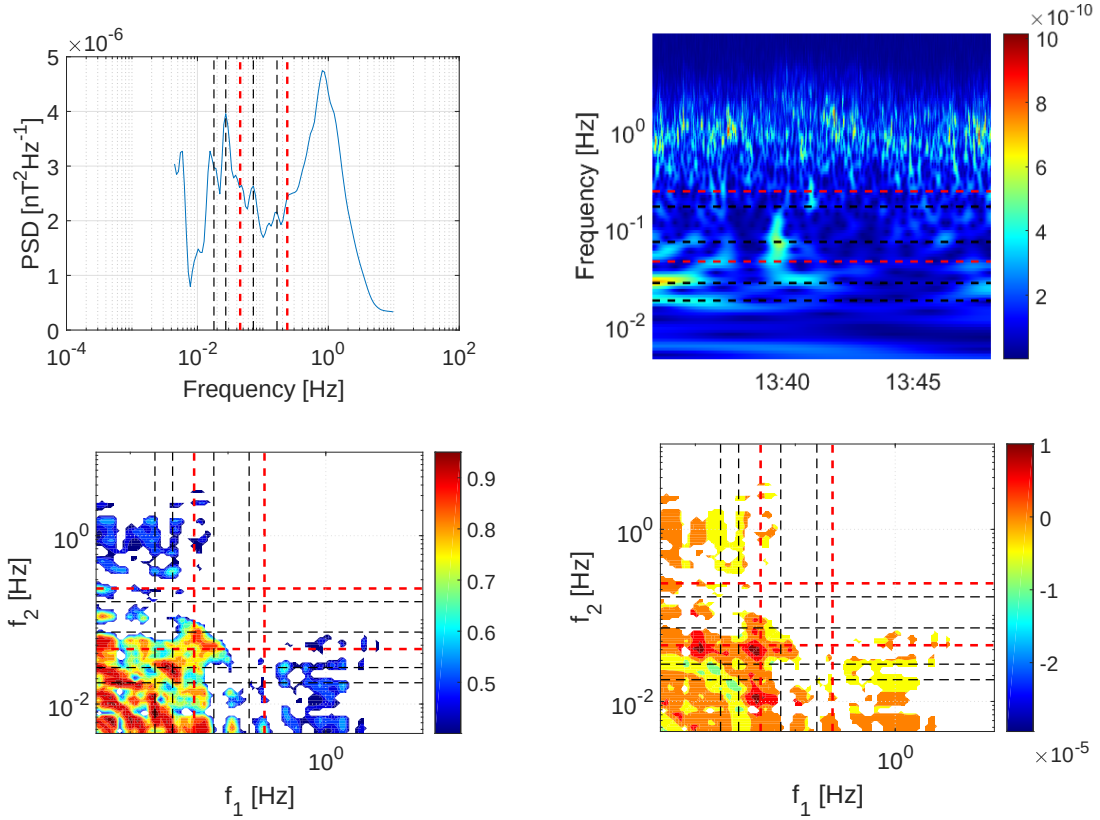

Figure 4.11: subinterval E, 13:35-13:48. This subinterval contains constant power in 1Hz and ULF modes. Two triads are shown for this energetic region. Four-wave processes are likely present and contribute to the broadening of the 1z waveband, but not dominant.

the example of subinterval C, where the four-wave coupling occurred simultaneously with the broadening of the lower frequencies. The two highlighted triads of subinterval E exist simultaneously, and share a common node, but the frequencies of these triads are smaller than the large broad peak at ~1Hz. The 1Hz peak has also broadened from the previous subinterval, D. The increase in visible triads suggests power is transferred from the lower triads, through the higher, into the 1Hz peak, at which point the energy is prohibited from transferring to frequencies higher than the 1Hz band. Instead, the power either dissipates relatively slowly back to ULF modes through one, or a series, of the multiple triads that are now available for coupling to the 1Hz band, or the power remains in the 1Hz band and is transferred to neighbouring frequencies within the band through the three-wave resonant interaction of close frequencies within the 1Hz band and the ULF modes. This is evidenced by the fact that the lower triads in the ULF modes lose most of their power after 13:43, midway through interval E, accompanied by a delayed drop in power in the 1Hz peak. The dominant energetic input for the 1Hz waves is then cut off, and the power escapes firstly to frequencies close to 1Hz, as these higher-frequency interactions are the

quickest, and then slowly to the ULF modes in an inverse cascade.

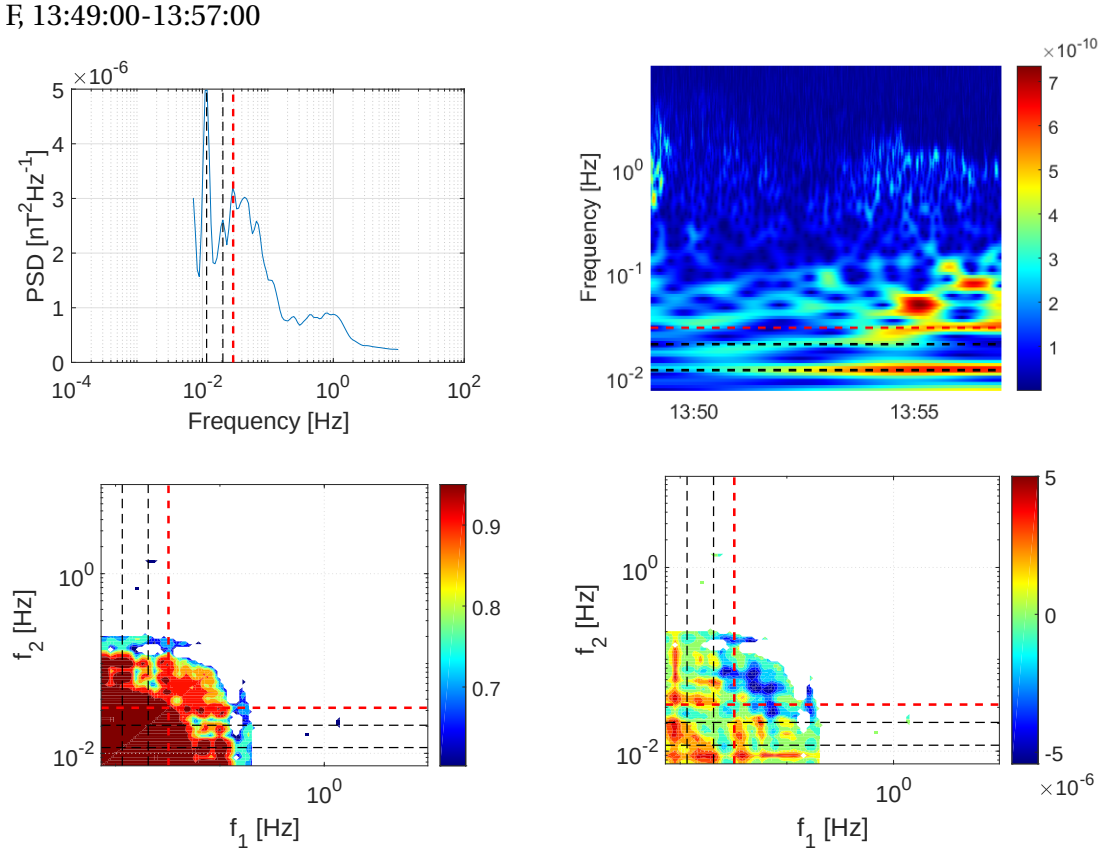

Figure 4.12: Subinterval F; 13:49-13:57, showing the removal of the 1Hz power into lower frequencies, and the interactions that drive power back into the 1Hz band.

After 13:49, little power remains in the 1Hz band after it is drained into the ULF modes. When power returns to the ULF modes in interval F, figure (4.12) the process restarts, with the lower triads containing most of the energy of the integrated power. The wavelet power spectrum shows the transfer of energy from ULF modes to the band just below, and then directly to, the 1Hz frequency band. The cross-bicoherence at this point is similar to interval A, whereby most of the low-frequency modes are very well correlated, but less so to the higher frequencies. As the intervals progress through E and F, the wavenumber mismatch returns to the lower values of A and B. The mismatch of a particular interaction is therefore well correlated with the system's tendency for energy transfer, and can reveal inefficient modes of energy transfer even amongst highly phase-correlated modes. The change of the initially well-correlated (>0.95) triads of A and B into poorly correlated (>0.4) triads is accompanied by an increase in mismatch, indicating that these modes becomes spatially misaligned and represent inefficient channels of energy transfer. In all cases, the mismatch is highest along the diagonal $f_1 = f_2$, indicating the general inefficiency of self-

	f_1[Hz]	f_2[Hz]	f_3[Hz]	f_4[Hz]	f_5[Hz]	f_6[Hz]
A	0.0291	0.0370	0.0761	-	-	-
B	0.0358	0.0623	0.1100	-	-	-
C	0.0623	0.1336	0.2100	0.4059	-	-
D	0.0411	0.0668	0.1229	0.2308	0.4049	0.7586
E	0.0179	0.0271	0.0450	0.0716	0.1644	0.236
F	0.0116	0.02055	0.0295	-	-	-

Table 4.2: The frequencies of each dashed vertical line of figures (4.7)-(4.12) for each subinterval A-F. The frequency f_3 is the sum of f_1 and f_2, the values of $f_{4,5,6}$ represent 4 wave interactions and are explained in more detail in the text.

interaction. Some modes, however, exhibit little mismatch for self-interaction and are well-correlated, transferring energy to higher frequency multiples efficiently.

The four-wave resonance of the type $f_1 + f_2 + f_3 - f_4 = 0$ is limited by the dimensionality of the system [185]. Figure (4.13) represents the dispersion relations for three waves in a 1D system, represented by $\omega \propto k^{\alpha}$. Solutions for additive four wave interactions correspond to the points of intersection of these three curves. The first of these curves is drawn according to the dispersion relation, and each subsequent curve is drawn with the same shape but with the minimum shifted along the first curve to arbitrary points on the first curve. The shifted curves, representing two of the three wave processes, will intersect only once, and there are therefore no four wave interaction processes available for the 1D case however, solutions may exist of the type $f_1 + f_2 - f_3 - f_4 = 0$. In higher dimensions, solutions for $f_1 + f_2 + f_3 - f_4 = 0$ are still possible. Figure (4.14) depicts the 2D case for $0 < \alpha < 1$. The funnels are nested so that each subsequent funnel has its vertex on the edge of the preceding funnel. In a similar argument to the 1D case, it can be seen that the funnels will not intersect and that four-wave processes are therefore not possible for this case. However, for $\alpha \geq 1$, a solution exists when one of the wavenumbers is much smaller than the other two. In this case, the solution reduces to the three-wave interaction. In the context of figures (4.7-4.12), the ULF waves can be modelled as a 1D picture as they propagate along the magnetic field line. A possible interpretation for the onset of four-wave processes satisfying the condition $f_1 + f_2 + f_3 - f_4 = 0$ is that the 1D approximation of the ULF waves break down, corresponding to a significant increase in perpendicular propagation. The system then becomes 2D, and the four wave processes are permitted.

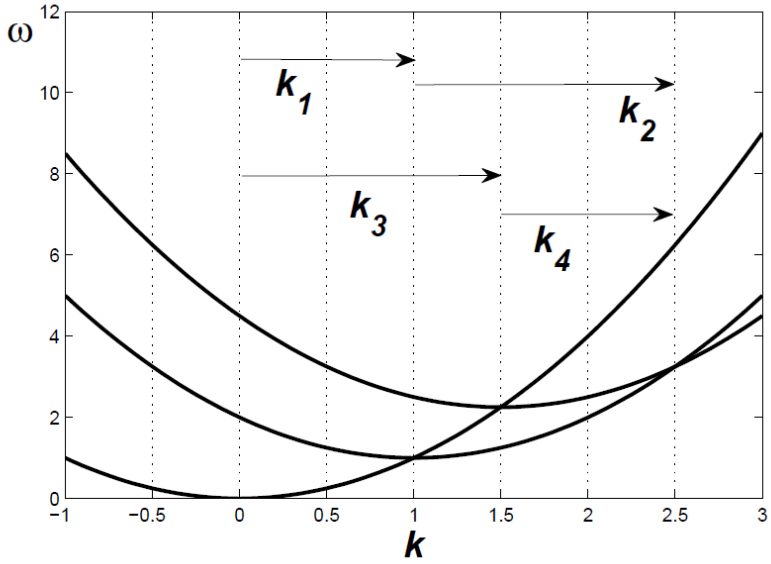

Figure 4.13: 1D solutions of four-wave interaction processes for $\alpha \geq 1$. All curves have the same shape, and the two rightmost curves are created by shifting along the curve centred at 0. The vectors $k_{1,2,3,4}$ represent the wave vectors of the waves. None of the three intersection points ($k = 1, 1.5, 2.5$ contain all three curves and so four-wave processes of the form $f_1 + f_2 + f_3 - f_4 = 0$ are not possible. [185]

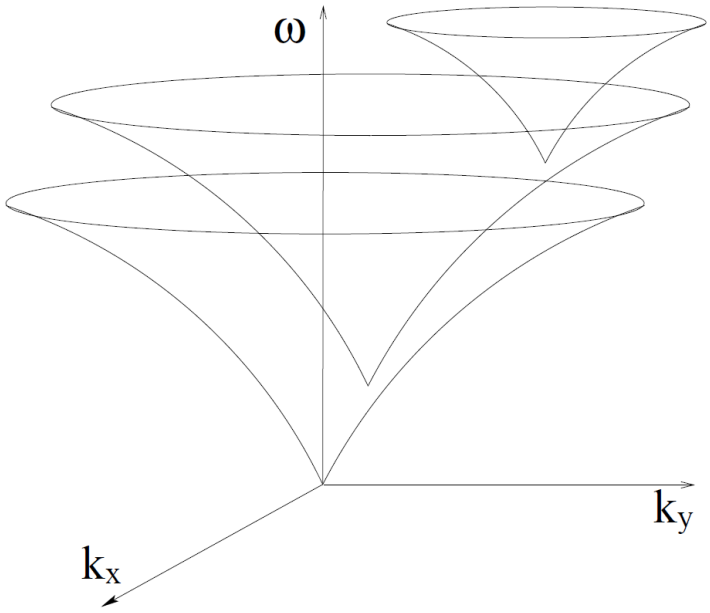

Figure 4.14: Solutions of the dispersion relation for three waves with $0 < \alpha < 1$. The three funnels do not intersect so no solutions for four-wave processes exist. At $\alpha \geq 1$, the surfaces can intersect and so solutions are available. [185]

4.5 Conclusion

The foreshock crossing on 18/02/2002 has been studied for wave-wave interactions using the cross-bispectrum, a technique that extends the notion of the bispectrum to two-point measurements, and the wavenumber mismatch, a measurement of the efficiency of wave-wave interactions. It is found that initially energy transfer occurs mostly between triplets of waves such that $f_1 + f_2 = f_3$, so-called triads. Evidence for the interaction between triads being the dominant process of energy transfer to higher frequencies is presented. The wavenumber mismatch of these triads grows as the interval progresses and eventually it becomes more efficient for the energy transfer to occur through four-wave processes. These four and three-wave processes act simultaneously to drive the energy from the slowly-interacting ULF modes to the faster band of frequencies around 1Hz. When the power to the ULF modes drops, the power of the 1Hz modes also drops after a delay. The increasing breadth of the frequencies centred at 1Hz is noted, and it is posited that this broadening is linked to the increasing power of the ULF modes. In the context of wave turbulence, the frequencies of these triads give insight into the channels of energy transfer between wave modes in the system.

It has been shown that it is the interaction between the triads themselves, rather than through singular triads, that acts to drive energy through frequencies. Two separate triads that act in such a way to produce their energy outputs at two close frequencies will tend to broaden the energy spectrum around those two output frequencies. As more triads push the energy into higher frequencies, this broadening effect is increased, which increases the total number of potential wave modes that are available to interact and thereby increases the total number of channels of energy flow of the system. Eventually a peak may become so broad that the frequencies at the lower end of the peak can interact with the frequencies at the higher end of it, transferring the energy of the peak back into lower frequency modes. In the example studies here, the peak in the power spectrum at 1Hz is approximately 1Hz wide, and therefore acts as a stopping point for the natural flow of energy into higher frequencies; the direct energy cascade. The energy transfer in the wave turbulence model can be expressed as a network of nodes representing frequencies of interacting modes, with connections between nodes dependent on the available triads (or 4-wave interactions) that are identified through the bispectral analysis. It should be possible in principle then to compare the network of energy transfer generated from data of one interval to a similar energy network created from data of a separate interval on a separate date. As long as both of these data sets are taken from foreshock plasma of somewhat similar conditions, the energy transfer network is presumed to be comparable between the sets, and its size should be dependent on the amount of free energy available to the

system. These hypotheses are not tested in this chapter but provide a direction for future work. The physical significance of the frequencies of the network is also not explored here but would likely provide insight into the underlying processes that drive the energy cascade.

The wave turbulence approach offers an alternative method of studying turbulence to the more usual techniques that involve taking differences in data over time scales, such as calculating structure functions. Such previously used techniques rely on taking the differences in magnetic field magnitude directly as a function of distance between probes. Since Cluster is a system of only four satellites, and therefore six possible differences, this approach is unsuitable. Instead, time-series data from one satellite is used, and differences are taken on temporal scales rather than spatial ones. The time lag is then converted into a distance using the average speed of the fluctuation. This speed itself is time-dependent and difficult to estimate accurately which increases the uncertainty of this approach. Large amounts of data are required for these structure-function techniques to be worthwhile, as the largest scale that can be measured is proportional to the largest time-lag difference that can be calculated. Additionally, the amount of data points that are available at large time-lags is much smaller than those available for a smaller lag, for any given datasets, because only those data points that are at the very beginning or end of the time series can be considered for large lags. Structure function methods can also require significant ensemble averaging of data to account for statistical noise, which means that the small number of large-scale lag differences are inaccurate. In the wave turbulence approach employed in this chapter, these limitations do not apply, as the interactions between waves are measured directly in frequency space. The confirmation of wave turbulence as a viable model of nonlinear plasma wave dynamics is therefore important to the future study of the foreshock.

Chapter 5

Conclusion

The aim of the thesis is to further the understanding of processes in the foreshock; the region of the Earth's magnetosphere that is upstream of, and magnetically connected to, the bow shock. This is a turbulent region that contains energetic backstreaming particles that originate from the specular reflection of the solar wind at the bow shock. The collisionless nature of the solar wind plasma means that energy transfer takes place through complex wave-particle and wave-wave interactions. The two-stream instability that forms from the reflected ion beam drives a wavefield in the frequency range ~(0.005-1)Hz, the so-called ultra-low frequency (ULF) range. These waves propagate sunwards but are advected back to the bow shock by the solar wind, reversing their polarities. In chapter 2, two-point measurements of FGM data provided by the Cluster mission were used to identify the dispersion relations of these backscattered waves for two foreshock crossings using a statistical technique based on collating wavenumber-frequency pairs into a histogram by power. Previous results had relied on the wave telescope, or k-filtering, technique; a method based on a generalized minimum variance analysis that uses three or more spacecraft in a tetrahedral configuration to determine dispersion relations. A statistical technique was employed instead that is able to resolve multiple peaks of the dispersion relation. It was found that, after applying a Doppler-correction, these measurements are sufficient to identify a multitude of modes in the plasma, including the fast magnetosonic and beam resonant modes, as well as identify and separate static structures advected by the solar wind. The direction of propagation of these modes in the plasma rest frame is also discernible from their corrected dispersion relations. This technique provides a means of reliably calculating dispersion relations that have multiple branches, since it has significantly smaller errors at higher values of the wavenumber than previous techniques, and it is therefore useful for identifying different modes. The identification of different modes at different locations in the foreshock is therefore possible with this technique, which has important consequences for the dynamics of the shock itself. Fast magnetoa-

coustic modes propagting sunwards are advected and steepen to form SLAMS which form the basis for the shock layer itself, and identifying where these modes are most prevalent is possible with this technique. Since the work presented in chapter 2, was mainly a proof-of-concept, the work could be expanded by surveying samples of foreshock data during which the Cluster satellites are in different parts of the shock, and identifying the most salient modes and their associated powers. From this, the location of separate ULF modes could be discovered with greater accuracy than through previous studies. The sensitivity of the technique to the power of the ULF modes is also useful, as the power dominance of each mode can be tracked throughout the foreshock. This would mean that the rise in power of one or a group of particular modes could be correlated with, for example, depth into the forechock. Since the inner ion foreshock is known to be strongly turbulent, such an analysis could provide information on the physical processes that correlate with or cause turbulence.

The technique of chapter 2 is unable to determine the dispersion relations for waves that exhibit nonlinear effects, however. One of the intervals studied in that chapter (20/02/2002 16:56-17:56) contains power primarily concentrated on the fast magnetosonic branch. As these modes are advected deeper into the foreshock, they encounter gradients in diffuse-ion density, and refract. This causes their transverse components to become compressive, and the waves to steepen. These nonlinear modes are theoretically describable by the derivative nonlinear Schrödinger equation (DNLS), which contains a cubic nonlinear term. In chapter 3, three single examples of these nonlinear wavetrains were compared to analytical solutions of the DNLS, with good agreement, providing strongly conclusive evidence that the cubic nonlinearity is an important factor in the evolution of large amplitude magnetic structures in the terrestrial foreshock. The approximate phase speeds of these nonlinear waves were on the order of the local Alfvén velocity. The pseudopotential used in the calculation of the DNLS solutions differed by previous forms in its dependence on the magnetic field strength, which allowed for a double-well shape at real values of the transverse field. This double-well potential can support two regimes of oscillatory solutions, since solutions can oscillate in either well. The shape of the pseudopotential also allows for osillatory solutions at arbitrarily small values of the transverse field, allowing the system to exhibit supernonlinear waves. To further test the applicability of this pseudopoential form, an ensemble of nonlinear waves similar to those studied in chapter 3 could be collected and decomposed individually using the EEMD technique of that chapter. Plotting the period against the amplitude of each resultant mode should then reveal two clusters of data, corresponding to solutions that oscillate in each of the two wells of the pseudopotential. It is expected that the data would not be split approximately evenly between the two wells, but that solutions of the well at a lower potential would be more

numerous than the higher. One limitation of such a study would be that it assumes a constant, or nearly constant, shape for the pseudopotential for each example. Since the pseuopotential is based on plasma parameters, and the nonlinear waves can influence these parameters, it seems likely that the pseudopotential itself is influenced by the nonlinear waves, and is time-dependent. However, this time-dependence is difficult to prove directly and would require further study.

Chapter 4 focussed on interactions between the wave modes themselves, specifically the coupling between ULF modes close to (0.01-0.5)Hz and the band of frequencies close to 1Hz, in the context of wave turbulence. Wave turbulence is a model of turbulence that focusses on the statistical mechanics of random nonlinear waves. In general, turbulence is a well-studied phenomenon but most investigation into the foreshock has been centred on the calculation of Kolmogorov indices; values that determine the energy distribution through scales. In the wave turbulence model, energy is channelled through the system directly via wave-wave interactions, the most efficient of which are known as triads; three-wave processes that satisfy $f_1 + f_2 = f_3$. Hence, the energy moves through frequency space via wave interactions, which determines how it is distributed through real spatial scales. Wave turbulence offers an alternative technique to the widely employed data-differencing based techniques such as the structure function, which are subject to inaccuracies due to the large amount of data required to average out statistical noise. In chapter 4, wave-wave interactions are studied directly in frequency space by the use of the cross-spectral bicoherence, a measure of the bicoherence of modes between two satellites. Since two probes are used, the wavenumber mismatch is also measurable. This is a measure of the average difference in wavenumber of two interacting modes, between two probes, and is used to quantify the extent to which modes are coplanar in real space. It was found that for the interval studied, the majority of the power was initially contained in single triads formed at the lower ULF frequencies. Over time, further triads formed at higher frequencies, containing common nodes with the triads of lower frequencies. The triads therefore interacted to facilitate the movement of energy into higher frequencies. As the total power of the system increased, three-wave processes were discovered amongst four-wave processes that accompanied the movement of power to frequencies around 1Hz. The wavenumber mismatch showed that the three-wave processes became less efficient in comparison to the four wave processes as the interval progressed. Eventually, the 1Hz band of frequencies became the dominant energetic processes. The peak at the 1Hz band of frequencies was found to be broader than the lower frequencies, at approximately 1Hz wide. This equality between the frequency of the band itself and the breadth of the peak means that there are many possible three-wave processes possible at this point, and the power drains rapidly from the band. To expand upon the work of this chapter, the physical

significance of the frequencies that correspond to the lower triads can be investigated. In principle this would require only a Doppler correction of these frequencies to the plasma rest frame, and then a calculation of their significance based on relevant plasma parameters. However, it is also feasible that the modes that interact have a physical significance even if their frequencies do not correspond to the usual expected quantities such as the gyrofrequencies. To further investigate the efficacy of the wave turbulence model, a network of the frequencies that form into triads and four-wave processes can be created. This network would contain nodes that represent the major modes of interaction, labelled as $A_{1,2,3}$ through $F_{1,2,3}$ in chapter 4, and edges linking interacting modes, ie; mainly triads. The network would then represent the channels of energy transfer in the system. This network could then be recreated with data taken from different points of the foreshock, in order to study how the conduits to energy transfer change spatially. Since wave turbulence is most applicable in colisionless plasmas, where most or all of the energy is manifest in wave activity, such networks could be created at most parts of the foreshock.

Appendix A

The choice to neglect collisions in our discussion of the general dispersion relation was made because it is the most relevant to the systems discussed in this work, but it also allows for the diagonalization of the matrix containing the equations governing our system. When collisions are ignored, we may transform table (1.2) into a symmetric fourth order matrix. To simplify the writing, we set $y = \frac{k^2c^2}{\omega^2}$ as well as:

$$p = \frac{\omega_{pe}}{\omega}, \qquad l = \frac{\omega_{ce\parallel}}{\omega}, \qquad t = \frac{\omega_{ce\perp}}{\omega} \qquad \sqrt{\epsilon_e} = \frac{c}{V_e} \tag{A.1}$$

$$P = \frac{\omega_{pi}}{\omega}, \qquad L = \frac{\omega_{ci\parallel}}{\omega}, \qquad T = \frac{\omega_{ci\perp}}{\omega} \qquad \sqrt{\epsilon_i} = \frac{c}{V_i} \tag{A.2}$$

We then perform the following transformations on table (1.2):

- Multiply rows (2) and (5) by p
- Multiply rows (3) and (6) by P
- Multiply row (8) by $p\sqrt{\epsilon_e}$
- Multiply row (9) by $P\sqrt{\epsilon_i}$
- Multiply columns (2) and (5) by $\frac{1}{p}$
- Multiply columns (3) and (6) by $\frac{1}{P}$
- Multiply column (8) by $\frac{\sqrt{\epsilon_e}}{p}$
- Multiply column (9) by $\frac{\sqrt{\epsilon_i}}{P}$

This will produce the matrix shown in table (A.1). The equation obtained by setting the determinant of this table to zero resembles an eigenvalue equation, and only four of the

diagonal terms contian the unknown variable y. We shall therefore perform a transformation of table (A.1) into an eigenvalue equation of a fourth order matrix. Firstly, simple permutations between lines and columns enable us to regroup the diagonal terms which contain y. We obtain for the determinant:

1	0	$-l$	0	0	p	0	$l\sqrt{\epsilon_e}$	0
0	1	0	L	0	P	0	0	$-T\sqrt{\epsilon_i}$
$-l$	0	1	0	0	0	p	0	0
0	L	0	1	0	0	P	0	0
0	0	0	0	1	0	0	$p\sqrt{\epsilon_e}$	$P\sqrt{\epsilon_i}$
P	P	0	0	0	$1-y$	0	0	0
0	0	p	P	0	0	$1-y$	0	0
$t\sqrt{\epsilon_e}$	0	0	0	$p\sqrt{\epsilon_e}$	0	0	$\epsilon_e - y$	0
0	$-T\sqrt{\epsilon_i}$	0	0	$P\sqrt{\epsilon_i}$	0	0	0	$\epsilon_i - y$

We may rewrite this determinant in vectorial form, making use of a nine-dimensional space of vectors $\vec{u}''$ whose coordinates are the variables shown on the first row of table (A.1), and then subdivide this space into the two subspaces:

$$\vec{u}_1\left(\frac{v_{ex}m_e\omega_{pe}}{iq_e},\quad \frac{v_{ix}m_i\omega_{pi}}{iq_i},\quad \frac{v_{ey}m_e\omega_{pe}}{q_e},\quad \frac{v_{iy}m_i\omega_{pi}}{q_i},\quad iE_z\right) \tag{A.3}$$

$$\vec{u}_2\left(E_x,\quad iE_y,\frac{v_{ez}m_e\omega_{pe}}{q_e\sqrt{\epsilon_e}},\frac{v_{iz}m_i\omega_{pi}}{q_i\sqrt{\epsilon_i}}\right) \tag{A.4}$$

The linear system that describes the determinant is then:

$$A_1\vec{u}_1 + A_2\vec{u}_2 = 0 \tag{A.5}$$

$$A_3\vec{u}_1 + A_4\vec{u}_2 = y\vec{u}_2 \tag{A.6}$$

The symbols A_1, A_2, A_3, A_4 represent the four matrices separated by lines as shown in the determinant, such that:

$$\begin{array}{c|c} A_1 & A_2 \\ \hline A_3 & A_4 \end{array}$$

E_x	$\frac{v_{ex}m_e\omega_{pe}}{iq_e}$	$\frac{v_{ix}m_i\omega_{pi}}{iq_i}$	iE_y	$\frac{v_{ey}m_e\omega_{pe}}{q_e}$	$\frac{v_{iy}m_i\omega_{pi}}{q_i}$	iE_z	$\frac{v_{ez}m_e\omega_{pe}}{q_e\sqrt{\epsilon_e}}$	$\frac{v_{iz}m_i\omega_{pi}}{q_i\sqrt{\epsilon_i}}$
$1-y$	p	P	0	0	0	0	0	0
p	1	0	0	$-l$	0	0	$t\sqrt{\epsilon_e}$	0
P	0	1	0	0	L	0	0	$-T\sqrt{\epsilon_i}$
0	0	0	$1-y$	p	P	0	0	0
0	$-l$	0	p	1	0	0	0	0
0	0	L	P	0	1	0	0	0
0	0	0	0	0	0	1	$p\sqrt{\epsilon_e}$	$P\sqrt{\epsilon_i}$
0	$t\sqrt{\epsilon_e}$	0	0	0	0	$p\sqrt{\epsilon_e}$	ϵ_e-y	0
0	0	$-T\sqrt{\epsilon_i}$	0	0	0	$P\sqrt{\epsilon_i}$	0	ϵ_i-y

Table A.1: Transformation of table (1.2) using $y=\frac{k^2c^2}{\omega^2}$. The variables are listed in the first row in an identical way to table (1.2).

Eliminating $\vec{u}_1$ from equations (A.5) and (A.6), we get:

$$\left(A_4 - A_3 A_1^{-1} A_2\right)\vec{u}_2 = y\,\vec{u}_2 \tag{A.7}$$

In $\vec{u}_2$ space, y is then the eigenvalue of the matrix $A_4 - A_3A_1^{-1}A_2$. Computing this matrix, we find that $A_3A_1^{-1}A_2$ is equal to:

$\frac{p^2}{1-l^2}+\frac{P^2}{1-L^2}$	$\frac{p^2 l}{1-l^2}-\frac{P^2 L}{1-L^2}$	$\frac{pt\sqrt{\epsilon_e}}{1-l^2}$	$\frac{PT\sqrt{\epsilon_i}}{1-L^2}$
$\frac{p^2 l}{1-l^2}-\frac{P^2 L}{1-L^2}$	$\frac{p^2}{1-l^2}+\frac{P^2}{1-L^2}$	$\frac{plt\sqrt{\epsilon_e}}{1-l^2}$	$\frac{PLT\sqrt{\epsilon_i}}{1-L^2})$
$\frac{pt\sqrt{\epsilon_e}}{1-l^2}$	$\frac{plt\sqrt{\epsilon_e}}{1-l^2}$	$\epsilon_e\left(p^2+\frac{t^2}{1-l^2}\right)$	$pP\sqrt{\epsilon_e\epsilon_i}$
$-\frac{PT\sqrt{\epsilon_i}}{1-L^2}$	$\frac{PLT\sqrt{\epsilon_i}}{1-L^2}$	$pP\sqrt{\epsilon_e\epsilon_i}$	$\epsilon_i\left(P^2+\frac{T^2}{1-L^2}\right)$

This is a symmetric matrix. Since A_4 is also symmetric, the difference $A_4 - A_3 A_1^{-1} A_2$ must be symmetric. The roots of y are therefore the eiegenvalues of the symmetric matrix in table (A.2).

$1-\frac{p^2}{1-l^2}-\frac{P^2}{1-L^2}-y$	$-\left(\frac{p^2 l}{1-l^2}-\frac{P^2 L}{1-L^2}\right)$	$-\frac{pt\sqrt{\epsilon_e}}{1-l^2}$	$\frac{PT\sqrt{\epsilon_i}}{1-L^2}$
$-\left(\frac{p^2 l}{1-l^2}-\frac{P^2 L}{1-L^2}\right)$	$1-\frac{p^2}{1-l^2}-\frac{P^2}{1-L^2}-y$	$-\frac{plt\sqrt{\epsilon_e}}{1-l^2}$	$-\frac{PLT\sqrt{\epsilon_i}}{1-L^2})$
$-\frac{pt\sqrt{\epsilon_e}}{1-l^2}$	$-\frac{plt\sqrt{\epsilon_e}}{1-l^2}$	$\epsilon_e\left(1-p^2-\frac{t^2}{1-l^2}\right)-y$	$-pP\sqrt{\epsilon_e\epsilon_i}$
$\frac{PT\sqrt{\epsilon_i}}{1-L^2}$	$-\frac{PLT\sqrt{\epsilon_i}}{1-L^2}$	$-pP\sqrt{\epsilon_e\epsilon_i}$	$\epsilon_i\left(1-P^2+\frac{T^2}{1-L^2}\right)-y$

Table A.2: Symmetrized version of table (A.1) obtained by eliminating the variables associated with the subspace $\vec{u}_1$, equivalent to $A_3 A_1^{-1} A_2$

We find the roots of y by setting the determinant of table (A.2) to zero. It a property of symmetric matrices that the roots of their equations are real. We could use the dispersion relation in the form of table (A.2) by setting $t = T = 0$, corresponding to longitudinal propagation. We see that the determinant then breaks down into a product of two second order determinants. By setting the first of these equal to zero, we recover equations (1.91) and (1.92); the dispersion relations for the ion and electron cyclotron waves. Setting the second to zero, we find equation (1.70). The matrix A_1^{-1} does have singularities at $l = 1$ and $L = 1$ however, so table (A.2) cannot be used in the neighbourhood of these singularities. In these limits we would use the general equation in table (1.2). In some certain cases, it is useful to transform table (A.2) by dividing row and column (3) by ϵ_e and row and column (4) by ϵ_i. This has the effect of eliminating ϵ_e and ϵ_i from the matrix elements and transforming the variables associated with the determinant to:

$$E_x, \quad E_y, \quad v_{ex}\left(\frac{m_e\omega_{pe}}{q_e}\right), \quad v_{ix}\left(\frac{m_i\omega_{pi}}{q_i}\right) \tag{A.8}$$

Appendix B

In order to expand the determinant of table (1.2), it is convenient to start with an expansion with respect to the powers of $\omega_{ci\perp}$ and $\omega_{ce\perp}$. Applying the computation rules for determinants, we may write the general dispersion relation in the form:

$$\Delta_T \Delta_L + B + C + D + E = 0 \tag{B.1}$$

where

$$\Delta_T = \Delta_1^2 + \frac{\omega_{ce\parallel}^2 \omega_{ci\parallel}^2}{\omega^4}(y-1)^2 - \frac{\omega_{ce\parallel}^2}{\omega^2}\left(y-1+\frac{\omega_{pi}^2}{\omega^2}\right)^2 - \frac{\omega_{ci\parallel}^2}{\omega^2}\left(y-1+\frac{\omega_{pe}^2}{\omega^2}\right)^2 + \frac{2\omega_{ci\parallel}\omega_{ce\parallel}\omega_{pe}^2\omega_{pi}^2}{\omega^6} \tag{B.2}$$

$$\Delta_L = \left(1-\frac{y}{\epsilon_e}\right)\left(1-\frac{y}{\epsilon_i}\right) - x\left(1-\frac{y}{\epsilon_s}\right) \tag{B.3}$$

$$B = \frac{\omega_{ce\perp}^2}{\omega^2}\left(\frac{y}{\epsilon_i} - 1 + \frac{\omega_{pi}^2}{\omega^2}\right)\left[\Delta_1\left(y-1+\frac{\omega_{pi}^2}{\omega^2}\right) - \frac{\omega_{ci\parallel}^2}{\omega^2}(y-1)\left(y-1+\frac{\omega_{pe}^2}{\omega^2}\right)\right] \tag{B.4}$$

$$C = \frac{\omega_{ci\perp}^2}{\omega^2}\left(\frac{y}{\epsilon_e} - 1 + \frac{\omega_{pe}^2}{\omega^2}\right)\left[\Delta_1\left(y-1+\frac{\omega_{pe}^2}{\omega^2}\right) - \frac{\omega_{ce\parallel}^2}{\omega^2}(y-1)\left(y-1+\frac{\omega_{pi}^2}{\omega^2}\right)\right] \tag{B.5}$$

$$D = \frac{2\,\omega_{ci\perp}\omega_{ce\perp}\omega_{pe}^2\omega_{pi}^2}{\omega^6}\left[-\Delta_1 + (y-1)\frac{\omega_{ci\parallel}\omega_{ce\parallel}}{\omega^2}\right] \tag{B.6}$$

$$E = \frac{\omega_{ci\perp}^2\omega_{ce\perp}^2}{\omega}(y-1)\Delta_1 \tag{B.7}$$

$$\Delta_1 = y - 1 + x \tag{B.8}$$

$$y = \frac{k^2 c^2}{\omega^2} \qquad x = \frac{\omega_{pe}^2 + \omega_{pi}^2}{\omega^2} \tag{B.9}$$

$$\epsilon_{i,e,s} = \frac{c^2}{V_{i,e,s}^2} \tag{B.10}$$

The symbol Δ_T represents the determinant of the transverse modes, defined in section (1.3.3.3), and Δ_L the determinant of the longitudinal waves, discussed in section (1.3.3.2). The variables $V_{i,e,s}$ take on their meanings defined in sections (1.3.3.2) and (1.3.3.3), ie; the thermal velocities. Equation (B.1) is entirely symmetric with respect to electrons and ions. We can now order the terms of the dispersion equation in powers of $\frac{1}{\omega^2}$, that is, as a polynomial in the variable x. The equation is of third degree in x. Computing the terms, we find the coefficients:

x^3 term =

$$\begin{aligned}
&\frac{\omega_{ci\parallel}^2 \omega_{ce\parallel}^2}{\omega^4} \frac{x}{\epsilon_s} u^3 - \left[\frac{2x}{\epsilon_s} + \frac{\omega_{ci\parallel}\omega_{ce\parallel}}{\omega^2}\left(1 - \frac{1}{\epsilon_s}\right) + \frac{\omega_{ci\perp}\omega_{ce\perp}}{\omega^2}\left(1 + \frac{1}{\epsilon_s}\right)\right] \frac{\omega_{ci\parallel}\omega_{ce\parallel}}{\omega^2} x u^2 + \frac{x^2}{\epsilon_s} \\
&+ \left[2x \frac{\omega_{ci\parallel}\omega_{ce\parallel}}{\omega^2}\left(1 - \frac{1}{\epsilon_s}\right) + x \frac{\omega_{ci\perp}\omega_{ce\perp}}{\omega^2}\left(1 + \frac{1}{\epsilon_s}\right) + \frac{\omega_{ci\parallel}\omega_{ce\parallel}\omega_{ci\perp}\omega_{ce\perp}}{\omega^4}\left(1 - \frac{1}{\epsilon_s}\right) + \frac{\omega_{ce\perp}^2 \omega_{ci\perp}^2}{\omega^4} \right] x u \\
&- x^2 \left(1 - \frac{1}{\epsilon_s}\right)\left(x + \frac{\omega_{ci\perp}\omega_{ce\perp}}{\omega^2}\right)
\end{aligned} \tag{B.11}$$

x^2 term =

$$\begin{aligned}
&\frac{1}{\epsilon_e \epsilon_i} \frac{\omega_{ci\parallel}^2 \omega_{ce\parallel}^2}{\omega^4} u^4 - \left\{ \frac{x}{\epsilon_s} \frac{\omega_{ci\parallel}^2 + \omega_{ce\parallel}^2}{\omega^2} + 2x \frac{\omega_{ci\parallel}\omega_{ce\parallel}}{\omega^2 \epsilon_e \epsilon_i} + \frac{\omega_{ci\parallel}\omega_{ce\parallel}}{\omega^2}\left[\frac{1}{\epsilon_e}\left(1 - \frac{1}{\epsilon_i}\right) + \frac{1}{\epsilon_i}\left(1 - \frac{1}{\epsilon_e}\right)\right] \right. \\
&\left. + \frac{\omega_{ci\parallel}\omega_{ce\parallel}\omega_{ci\perp}\omega_{ce\perp}}{\omega^4}\left(1 - \frac{1}{\epsilon_s}\right)\right\} u^3 + \left\{ x^2 \left(\frac{2}{\epsilon_s} + \frac{1}{\epsilon_e \epsilon_i}\right) + 2x \frac{\omega_{ci\parallel}\omega_{ce\parallel}}{\omega^2}\left[\frac{1}{\epsilon_e}\left(1 - \frac{1}{\epsilon_i}\right) + \frac{1}{\epsilon_i}\left(1 - \frac{1}{\epsilon_e}\right)\right] \right. \\
&+ x \frac{\omega_{ci\parallel}^2 + \omega_{ci\parallel}^2}{\omega^2}\left(1 - \frac{1}{\epsilon_s}\right) + \frac{\omega_{ci\perp}^2 \omega_{ci\perp}^2}{\omega^4} \times \left(1 - \frac{1}{\epsilon_e}\right)\left(1 - \frac{1}{\epsilon_i}\right) + x\left(\frac{\omega_{ce\perp}^2}{\epsilon_i \omega^2} + \frac{\omega_{ci\perp}^2}{\epsilon_e \omega^2}\right) + x \frac{\omega_{ce\perp}\omega_{ci\perp}}{\omega^2}\left(1 + \frac{1}{\epsilon_e}\right) \\
&\left. + \frac{\omega_{ci\parallel}\omega_{ce\parallel}\omega_{ci\perp}\omega_{ce\perp}}{\omega^4}\left(2 - \frac{1}{\epsilon_e} - \frac{1}{\epsilon_e}\right) + \frac{\omega_{ci\perp}^2 \omega_{ce\perp}^2}{\omega^4} u^4 \right\} u^2 - \left\{ 2x\left(1 - \frac{1}{\epsilon_s}\right) + x\left[\frac{1}{\epsilon_e}\left(1 - \frac{1}{\epsilon_i}\right) + \frac{1}{\epsilon_i}\left(1 - \frac{1}{\epsilon_e}\right)\right] \right. \\
&\left. + 2\frac{\omega_{ce\parallel}\omega_{ci\parallel}}{\omega^2}\left(1 - \frac{1}{\epsilon_e}\right)\left(1 - \frac{1}{\epsilon_i}\right) - \left(1 - \frac{\omega_{ci\perp}^2}{\epsilon_e \omega^2}\right)\left(1 - \frac{\omega_{ce\perp}^2}{\epsilon_i \omega^2}\right) + \frac{\omega_{ce\perp}\omega_{ce\perp}}{\omega^2}\left(1 - \frac{1}{\epsilon_s}\right) + \frac{\omega_{ce\perp}^2 + \omega_{ce\perp}^2}{\omega^2} \right\} x u \\
&+ x^2 \left(1 - \frac{1}{\epsilon_e}\right)\left(1 - \frac{1}{\epsilon_i}\right)
\end{aligned} \tag{B.12}$$

x term =

$$-\frac{1}{\epsilon_e\epsilon_i}\frac{\omega_{ci\parallel}^2+\omega_{ce\parallel}^2}{\omega^2}u^4+\left\{x\left(\frac{1}{\epsilon_s}+\frac{2}{\epsilon_e\epsilon_i}\right)+\frac{\omega_{ci\parallel}^2+\omega_{ci\parallel}^2}{\omega^2}\times\left[\frac{1}{\epsilon_e}\left(1-\frac{1}{\epsilon_i}\right)+\frac{1}{\epsilon_i}\left(1-\frac{1}{\epsilon_e}\right)\right]\right.$$
$$\left.+\frac{\omega_{ce\perp}^2}{\epsilon_i\omega^2}+\frac{\omega_{ci\perp}^2}{\epsilon_e\omega^2}\right\}u^3-\left\{x\left(1-\frac{1}{\epsilon_s}\right)+2x\left[\frac{1}{\epsilon_e}\left(1-\frac{1}{\epsilon_i}\right)+\frac{1}{\epsilon_i}\left(1-\frac{1}{\epsilon_e}\right)\right]+\frac{\omega_{ci\parallel}^2+\omega_{ci\parallel}^2}{\omega^2}\left(1-\frac{1}{\epsilon_e}\right)\left(1-\frac{1}{\epsilon_i}\right)\right.$$
$$\left.-\left(\frac{\omega_{ci\perp}^2}{\epsilon_e\omega^2}-\frac{\omega_{ce\perp}^2}{\epsilon_e\omega^2}\right)+\frac{\omega_{ci\perp}^2+\omega_{ce\perp}^2}{\omega^2}\right\}u^2+2x\left(1-\frac{1}{\epsilon_e}\right)\left(1-\frac{1}{\epsilon_i}\right)u \tag{B.13}$$

$$x^0 \text{ term} = \\ u^2\left(\frac{u+1}{\epsilon_e}-1\right)\left(\frac{u+1}{\epsilon_i}-1\right) \tag{B.14}$$

$$u = y-1 \tag{B.15}$$

If we plot y vs x in a dispersion curve, we note that the curve generally has three horizontal asymptotes. Physically, these asymptotes correspond to taking the low frequency limit, $\omega << \omega_{ce}$. We can obtain these asymptotes by finding the roots of the equation as $x \to \infty$. In this limit, the x^3 term dominates, and the equation becomes of third degree in u. There are therefore three horizontal asymptotes. We will set:

$$A = \frac{\omega_{pe}^2+\omega_{pi}^{\omega_{ci}}}{\omega_{ce}\omega_{ci}} \tag{B.16}$$

$$s = \frac{\omega_{ce\perp}\omega_{ci\perp}}{\omega_{ce\parallel}\omega_{ce\parallel}} = \tan^2(\theta) \tag{B.17}$$

$$A' = \frac{\omega_{pe}^2+\omega_{pi}^{\omega_{ci}}}{\omega_{ce\parallel}\omega_{ci\parallel}} = A(1+s) \tag{B.18}$$

Where θ is the angle between the magnetic field and the direction of propagation. We set the coefficient, equation (B.11), equal to zero, yielding:

$$\begin{aligned}
&\frac{u^3}{\epsilon_s} - \left[\frac{2A'}{\epsilon_s} + 1 - \frac{1}{\epsilon_s} + s\left(1 + \frac{1}{\epsilon_s}\right)\right] u^2 \\
&+ \left[\frac{A'^2}{\epsilon_s} + 2A'\left(1 - \frac{1}{\epsilon_s}\right) + A's\left(1 + \frac{1}{\epsilon_s}\right) + s\left(1 - \frac{1}{\epsilon_s}\right) + s^2\right] u \\
&- A'(A' + s)\left(1 - \frac{1}{\epsilon_s}\right) = 0
\end{aligned} \tag{B.19}$$

This equation is solved by rewriting it in powers of s:

$$\begin{aligned}
&us^2 - (a - A')\left[u\left(1 + \frac{1}{\epsilon_s}\right) - \left(1 - \frac{1}{\epsilon_s}\right)\right] \\
&+ (u - A')^2\left[\frac{u}{\epsilon_s} - \left(1 - \frac{1}{\epsilon_s}\right)\right] = 0
\end{aligned} \tag{B.20}$$

The solutions are:

$$s = u - A' \tag{B.21}$$

$$s = \frac{1}{u}(u - A')\left[\frac{u}{\epsilon_s} - \left(1 - \frac{1}{\epsilon_s}\right)\right] \tag{B.22}$$

Solving these equations for u, we find the three roots of equation (B.20), with $y = \frac{k^2c^2}{\omega^2}$:

$$y_2 = \epsilon_a(1 + s) \tag{B.23}$$

$$y_{1,3} = \frac{1}{2}\left[(\epsilon_a + \epsilon_s - 1)(1 + s) + 1 \pm \left\{(\epsilon_a + \epsilon_s - 1)^2 - 4(\epsilon_a - 1)(\epsilon_s - 1)(1 + s)\right\}^{\frac{1}{2}}\right] \tag{B.24}$$

Where the + sign corresponds to y_1 and the − to y_3.

List of Figures

Bibliography

[1] V Adrian Parsegian. *Van der Waals forces: a handbook for biologists, chemists, engineers, and physicists*. Cambridge University Press, 2005.

[2] Richard P Feynman, Robert B Leighton, and Matthew Sands. *The Feynman Lectures on Physics, Desktop Edition Volume I*, volume 1. Basic books, 2013.

[3] Jeffrey P Freidberg. Ideal magnetohydrodynamics. 1987.

[4] Thomas James Morrow Boyd and Jeffrey John Sanderson. Plasma dynamics. *Plasma dynamics, by TJM Boyd and JJ Sanderson. London, Nelson, 1969. Series: Applications of mathematics series ISBN: 177616113*, 1969.

[5] José A Bittencourt. *Fundamentals of plasma physics*. Springer Science & Business Media, 2013.

[6] Albert A Galeev. Basic plasma physics i. *Plasma Physics*, 1, 1983.

[7] Emanuele Ronchi, Sean Conroy, E Andersson Sundén, Göran Ericsson, M Gatu Johnson, Carl Hellesen, Henrik Sjöstrand, Matthias Weiszflog, JET-EFDA Contributors, et al. A parametric model for fusion neutron emissivity tomography for the kn3 neutron camera at jet. *Nuclear Fusion*, 50(3):035008, 2010.

[8] Richard Fitzpatrick. *Maxwell's Equations and the Principles of Electromagnetism*. Jones & Bartlett Publishers, 2008.

[9] Stewart Harris. *An introduction to the theory of the Boltzmann equation*. Courier Corporation, 2004.

[10] Leif Arkeryd. On the boltzmann equation part ii: The full initial value problem. *Archive for Rational Mechanics and Analysis*, 45(1):17–34, 1972.

[11] Jean François Denisse and Jean Loup Delcroix. *Plasma waves*. Number 17 in Interscience Tracts on Physics and Astronomy. Interscience Publishers, 1963.

[12] Anatoly Aleksandrovich Vlasov. The vibrational properties of an electron gas. *Physics-Uspekhi*, 10(6):721–733, 1968.

[13] Herbert Goldstein, Charles Poole, and John Safko. Classical mechanics, 2002.

[14] B Srinivasan and U Shumlak. Analytical and computational study of the ideal full two-fluid plasma model and asymptotic approximations for hall-magnetohydrodynamics. *Physics of Plasmas*, 18(9):092113, 2011.

[15] Wolfgang Baumjohann and Rudolf A Treumann. *Basic space plasma physics*. World Scientific, 1997.

[16] Abraham Bers. Space-time evolution of plasma instabilities-absolute and convective. In *Basic plasma physics. 1*. 1983.

[17] S Peter Gary. Electromagnetic ion/ion instabilities and their consequences in space plasmas-a review. *Space Science Reviews*, 56:373–415, 1991.

[18] Edward J Smith, Bruce T Tsurutani, and Ronald L Rosenberg. Observations of the interplanetary sector structure up to heliographic latitudes of 16: Pioneer 11. *Journal of Geophysical Research: Space Physics*, 83(A2):717–724, 1978.

[19] Fouad Sahraoui, ML Goldstein, Patrick Robert, and Yu V Khotyaintsev. Evidence of a cascade and dissipation of solar-wind turbulence at the electron gyroscale. *Physical review letters*, 102(23):231102, 2009.

[20] C-Y Tu and Eckart Marsch. Mhd structures, waves and turbulence in the solar wind: Observations and theories. *Space Science Reviews*, 73(1-2):1–210, 1995.

[21] Steven R Cranmer. Why is the fast solar wind fast and the slow solar wind slow? a survey of geometrical models. *arXiv preprint astro-ph/0506508*, 2005.

[22] Joseph V Hollweg and Philip A Isenberg. Generation of the fast solar wind: A review with emphasis on the resonant cyclotron interaction. *Journal of Geophysical Research: Space Physics*, 107(A7), 2002.

[23] John T Gosling, JR Asbridge, SJ Bame, and WC Feldman. Solar wind stream interfaces. *Journal of Geophysical Research: Space Physics*, 83(A4):1401–1412, 1978.

[24] SD Bale, M Pulupa, C Salem, CHK Chen, and E Quataert. Electron heat conduction in the solar wind: transition from spitzer-härm to the collisionless limit. *The Astrophysical Journal Letters*, 769(2):L22, 2013.

[25] A Balogh, Chris M Carr, MH Acuna, MW Dunlop, TJ Beek, P Brown, K-H Fornacon, E Georgescu, Karl-Heinz Glassmeier, J Harris, et al. The cluster magnetic field investigation: overview of in-flight performance and initial results. In *Annales Geophysicae*, volume 19, pages 1207–1217, 2001.

[26] GA Zherebtsov and VM Tomozov. Solar physics. *Solar Physics Book*, 79, 1988.

[27] WH Matthaeus, S Dasso, JM Weygand, LJ Milano, CW Smith, and MG Kivelson. Spatial correlation of solar-wind turbulence from two-point measurements. *Physical review letters*, 95(23):231101, 2005.

[28] O Alexandrova, V Carbone, P Veltri, and L Sorriso-Valvo. Small-scale energy cascade of the solar wind turbulence. *The Astrophysical Journal*, 674(2):1153, 2008.

[29] Luca Sorriso-Valvo, Vincenzo Carbone, Pierluigi Veltri, Giuseppe Consolini, and Roberto Bruno. Intermittency in the solar wind turbulence through probability distribution functions of fluctuations. *Geophysical Research Letters*, 26(13):1801–1804, 1999.

[30] Larry R Lyons and Donald J Williams. *Quantitative aspects of magnetospheric physics*, volume 23. Springer Science & Business Media, 2013.

[31] Rudolf A Treumann and Wolfgang Baumjohann. *Advanced space plasma physics*, volume 30. Imperial College Press London, 1997.

[32] Donald H Fairfield. Average and unusual locations of the earth's magnetopause and bow shock. *Journal of Geophysical Research*, 76(28):6700–6716, 1971.

[33] H Matsumoto and Y Omura. Computer space plasma physics. *Terra Sci., Tokyo*, 1993.

[34] Timothy E Eastman, EW Hones, SJ Bame, and JR Asbridge. The magnetospheric boundary layer: Site of plasma, momentum and energy transfer from the magnetosheath into the magnetosphere. *Geophysical research letters*, 3(11):685–688, 1976.

[35] Gerhard Haerendel, G Paschmann, N Sckopke, Ho Rosenbauer, and PC Hedgecock. The frontside boundary layer of the magnetosphere and the problem of reconnection. *Journal of Geophysical Research: Space Physics*, 83(A7):3195–3216, 1978.

[36] TD Phan, JT Gosling, G Paschmann, C Pasma, JF Drake, M Øieroset, D Larson, RP Lin, and MS Davis. The dependence of magnetic reconnection on plasma β and magnetic shear: Evidence from solar wind observations. *The Astrophysical Journal Letters*, 719(2):L199, 2010.

[37] BUÖ Sonnerup, G Paschmann, I Papamastorakis, N Sckopke, G Haerendel, SJ Bame, JR Asbridge, JT Gosling, and CT Russell. Evidence for magnetic field reconnection at the earth's magnetopause. *Journal of Geophysical Research: Space Physics*, 86(A12):10049–10067, 1981.

[38] FD Wilder, RE Ergun, DL Newman, KA Goodrich, KJ Trattner, MV Goldman, S Eriksson, AN Jaynes, T Leonard, DM Malaspina, et al. The non-linear behaviour of whistler waves at the reconnecting dayside magnetopause as observed by the magnetospheric multiscale mission–a case study. *Journal of Geophysical Research: Space Physics*, 2017.

[39] VM Souza, WD Gonzalez, DG Sibeck, D Koga, BM Walsh, and O Mendes. Comparative study of three reconnection x line models at the earth's dayside magnetopause using in situ observations. *Journal of Geophysical Research: Space Physics*, 122(4):4228–4250, 2017.

[40] J. P. Eastwood, E. A. Lucek, C. Mazelle, K. Meziane, Y. Narita, J. Pickett, and R. A. Treumann. The foreshock. *Space Science Reviews*, 118(1):41–94, Jun 2005.

[41] JR Asbridge, SJ Bame, and IB Strong. Outward flow of protons from the earth's bow shock. *Journal of Geophysical Research*, 73(17):5777–5782, 1968.

[42] RP Lin, C-I Meng, and KA Anderson. 30-to 100-kev protons upstream from the earth's bow shock. *Journal of Geophysical Research*, 79(4):489–498, 1974.

[43] Rudolf A Treumann and Manfred Scholer. The magnetosphere as a plasma laboratory. *The Century of space science*, page 1495, 2001.

[44] RJ Fitzenreiter. The electron foreshock. *Advances in Space Research*, 15(8):9–27, 1995.

[45] BUn Sonnerup. Acceleration of particles reflected at a shock front. *Journal of Geophysical Research*, 74(5):1301–1304, 1969.

[46] D Burgess. On the effect of a tangential discontinuity on ions specularly reflected at an oblique shock. *Journal of Geophysical Research: Space Physics*, 94(A1):472–478, 1989.

[47] Thomas P Armstrong, Mark E Pesses, and Robert B Decker. Shock drift acceleration. *Collisionless shocks in the Heliosphere: Reviews of current research*, pages 271–285, 1985.

[48] K Meziane, C Mazelle, M Wilber, D Lequéau, JP Eastwood, H Reme, I Dandouras, JA Sauvaud, JM Bosqued, GK Parks, et al. Bow shock specularly reflected ions in the presence of low-frequency electromagnetic waves: a case study. In *Annales Geophysicae*, volume 22, pages 2325–2335, 2004.

[49] Bruce T Tsurutani. *Collisionless shocks in the heliosphere: Reviews of current research*. American Geophysical Union, 1985.

[50] Lynn Bruce Wilson III, David G Sibeck, Drew L Turner, Adnane Osmane, Damiano Caprioli, and Vassilis Angelopoulos. Relativistic electrons produced by foreshock disturbances observed upstream of earth's bow shock. *Physical review letters*, 117(21):215101, 2016.

[51] Edward L Lever, Kevin B Quest, and Vitali D Shapiro. Shock surfing vs. shock drift acceleration. *Geophysical research letters*, 28(7):1367–1370, 2001.

[52] N Sckopke, G Paschmann, SJ Bame, JT Gosling, and CT Russell. Evolution of ion distributions across the nearly perpendicular bow shock: Specularly and non-specularly reflected-gyrating ions. *Journal of Geophysical Research: Space Physics*, 88(A8):6121–6136, 1983.

[53] WA Livesey, CT Russell, and CF Kennel. A comparison of specularly reflected gyrating ion orbits with observed shock foot thicknesses. *Journal of Geophysical Research: Space Physics*, 89(A8):6824–6828, 1984.

[54] MM Hoppe, CT Russell, LA Frank, TE Eastman, and EW Greenstadt. Upstream hydromagnetic waves and their association with backstreaming ion populations: Isee 1 and 2 observations. *Journal of Geophysical Research: Space Physics*, 86(A6):4471–4492, 1981.

[55] C Bonifazi and G Moreno. Reflected and diffuse ions backstreaming from the earth's bow shock 2. origin. *Journal of Geophysical Research: Space Physics*, 86(A6):4405–4413, 1981.

[56] Arjun Raj, Tai Phan, Robert P Lin, and V Angelopoulos. Wind survey of high-speed bulk flows and field-aligned beams in the near-earth plasma sheet. *Journal of Geophysical Research: Space Physics*, 107(A12), 2002.

[57] K Meziane, AM Hamza, M Wilber, C Mazelle, and MA Lee. Anomalous foreshock field-aligned beams observed by cluster. In *Annales Geophysicae*, volume 29, page 1967. Copernicus GmbH, 2011.

[58] DO Gomez, N Andrés, C Bertucci, and MK Dougherty. Saturn's ulf foreshock boundary: Cassini observations. In *AGU Fall Meeting Abstracts*, 2011.

[59] JT Gosling, JR Asbridge, SJ Bame, G Paschmann, and N Sckopke. Observations of two distinct populations of bow shock ions in the upstream solar wind. *Geophysical Research Letters*, 5(11):957–960, 1978.

[60] G Paschmann, N Sckopke, I Papamastorakis, JR Asbridge, SJ Bame, and JT Gosling. Characteristics of reflected and diffuse ions upstream from the earth's bow shock. *Journal of Geophysical Research: Space Physics*, 86(A6):4355–4364, 1981.

[61] T Hada, CF Kennel, and T Terasawa. Excitation of compressional waves and the formation of shocklets in the earth's foreshock. *Journal of Geophysical Research: Space Physics*, 92(A5):4423–4435, 1987.

[62] D Burgess, E Möbius, and M Scholer. Ion acceleration at the earth's bow shock. *Space science reviews*, 173(1-4):5–47, 2012.

[63] Yanqing Su, Quanming Lu, Can Huang, Mingyu Wu, Xinliang Gao, and Shui Wang. Particle acceleration and generation of diffuse superthermal ions at a quasi-parallel collisionless shock: Hybrid simulations. *Journal of Geophysical Research: Space Physics*, 117(A8), 2012.

[64] X Blanco-Cano, N Omidi, and CT Russell. Macrostructure of collisionless bow shocks: 2. ulf waves in the foreshock and magnetosheath. *Journal of Geophysical Research: Space Physics*, 111(A10), 2006.

[65] Akira Hasegawa. *Plasma instabilities and nonlinear effects*, volume 8. Springer Science & Business Media, 2012.

[66] SP Gary. Theory of space plasma microinstabilities, cambridge univ. *Pres, New York*, 1993.

[67] SD Bale, D Burgess, PJ Kellogg, K Goetz, and SJ Monson. On the amplitude of intense langmuir waves in the terrestrial electron foreshock. *Journal of Geophysical Research: Space Physics*, 102(A6):11281–11286, 1997.

[68] J Etcheto and M Faucheux. Detailed study of electron plasma waves upstream of the earth's bow shock. *Journal of Geophysical Research: Space Physics*, 89(A8):6631–6653, 1984.

[69] G Le and CT Russell. The morphology of ulf waves in the earth's foreshock. *Solar wind sources of magnetospheric ultra-low-frequency waves*, pages 87–98, 1994.

[70] Donald H Fairfield. Bow shock associated waves observed in the far upstream interplanetary medium. *Journal of Geophysical Research*, 74(14):3541–3553, 1969.

[71] CT Russell and MM Hoppe. Upstream waves and particles. *Space Science Reviews*, 34(2):155–172, 1983.

[72] G Le and CT Russell. A study of ulf wave foreshock morphology—i: Ulf foreshock boundary. *Planetary and space science*, 40(9):1203–1213, 1992.

[73] MH Farris and CT Russell. Determining the standoff distance of the bow shock: Mach number dependence and use of models. *Journal of Geophysical Research: Space Physics*, 99(A9):17681–17689, 1994.

[74] Aaron Barnes. Theory of generation of bow-shock-associated hydromagnetic waves in the upstream interplanetary medium. 1970.

[75] S Peter Gary. The electromagnetic ion beam instability and energy loss of fast alpha particles. *Nuclear Fusion*, 18(3):327, 1978.

[76] DD Sentman, JP Edmiston, and LA Frank. Instabilities of low frequency, parallel propagating electromagnetic waves in the earth's foreshock region. *Journal of Geophysical Research: Space Physics*, 86(A9):7487–7497, 1981.

[77] S Peter Gary, Charles W Smith, Martin A Lee, Melvyn L Goldstein, and David W Forslund. Electromagnetic ion beam instabilities. *The Physics of Fluids*, 27(7):1852–1862, 1984.

[78] B Grison, F Sahraoui, B Lavraud, T Chust, N Cornilleau-Wehrlin, H Reme, A Balogh, and M André. Wave particle interactions in the high-altitude polar cusp: a cluster case study. In *Annales Geophysicae*, volume 23, pages 3699–3713, 2005.

[79] MM Hoppe and C Tt Russell. Plasma rest frame frequencies and polarizations of the low-frequency upstream waves: Isee 1 and 2 observations. *Journal of Geophysical Research: Space Physics*, 88(A3):2021–2027, 1983.

[80] DS Orlowski and CT Russell. Ulf waves upstream of the venus bow shock: Properties of one-hertz waves. *Journal of Geophysical Research: Space Physics*, 96(A7):11271–11282, 1991.

[81] Donald H Fairfield. Whistler waves observed upstream from collisionless shocks. *Journal of Geophysical Research*, 79(10):1368–1378, 1974.

[82] EW Greenstadt, G Le, and RJ Strangeway. Ulf waves in the foreshock. *Advances in Space Research*, 15(8-9):71–84, 1995.

[83] ME McKean, N Omidi, and D Krauss-Varban. Wave and ion evolution downstream of quasi-perpendicular bow shocks. *Journal of Geophysical Research: Space Physics*, 100(A3):3427–3437, 1995.

[84] DD Sentman, MF Thomsen, S Peter Gary, WC Feldman, and MM Hoppe. The oblique whistler instability in the earth's foreshock. *Journal of Geophysical Research: Space Physics*, 88(A3):2048–2056, 1983.

[85] Hung K Wong and Charles W Smith. Electron beam excitation of upstream waves in the whistler mode frequency range. *Journal of Geophysical Research: Space Physics*, 99(A7):13373–13387, 1994.

[86] MM Hoppe, CT Russell, TE Eastman, and LA Frank. Characteristics of the ulf waves associated with upstream ion beams. *Journal of Geophysical Research: Space Physics*, 87(A2):643–650, 1982.

[87] DS Orlowski and CT Russell. Comparison of properties of upstream whistlers at different planets. *Advances in Space Research*, 16(4):137–141, 1995.

[88] DS Orlowski, CT Russell, D Krauss-Varban, N Omidi, and MF Thomsen. Damping and spectral formation of upstream whistlers. *Journal of Geophysical Research: Space Physics*, 100(A9):17117–17128, 1995.

[89] CT Russell. Upstream whistler-mode waves at planetary bow shocks: A brief review. *Journal of Atmospheric and Solar-Terrestrial Physics*, 69(14):1739–1746, 2007.

[90] WC Feldman, RC Anderson, SJ Bame, SP Gary, JT Gosling, DJ McComas, MF Thomsen, G Paschmann, and MM Hoppe. Electron velocity distributions near the earth's bow shock. *Journal of Geophysical Research: Space Physics*, 88(A1):96–110, 1983.

[91] D Winske and KB Quest. Magnetic field and density fluctuations at perpendicular supercritical collisionless shocks. *Journal of Geophysical Research: Space Physics*, 93(A9):9681–9693, 1988.

[92] DS Orlowski, GK Crawford, and CR Russell. Upstream waves at mercury, venus and earth: Comparison of the properties of one hertz waves. *Geophysical Research Letters*, 17(13):2293–2296, 1990.

[93] Donald H Fairfield and Kenneth Wayne Behannon. Bow shock and magnetosheath waves at mercury. *Journal of Geophysical Research*, 81(22):3897–3906, 1976.

[94] EW Greenstadt, I Mi Green, GT Inouye, AJ Hundhausen, SJ Bame, and IB Strong. Correlated magnetic field and plasma observations of the earth's bow shock. *Journal of Geophysical Research*, 73(1):51–60, 1968.

[95] P Hellinger and A Mangeney. Electromagnetic ion beam instabilities: Oblique pulsations. *Journal of Geophysical Research: Space Physics*, 104(A3):4669–4680, 1999.

[96] Manfred Scholer, Harald Kucharek, and Iku Shinohara. Short large-amplitude magnetic structures and whistler wave precursors in a full-particle quasi-parallel shock simulation. *Journal of Geophysical Research: Space Physics*, 108(A7), 2003.

[97] G Mann, H Lühr, and W Baumjohann. Statistical analysis of short large-amplitude magnetic field structures in the vicinity of the quasi-parallel bow shock. *Journal of Geophysical Research: Space Physics*, 99(A7):13315–13323, 1994.

[98] Xochitl Blanco-Cano. Bow shocks in the solar wind: Lessons towards understanding interplanetary shocks. In *AIP Conference Proceedings*, volume 1216, pages 459–465. AIP, 2010.

[99] Yufei Hao, Xinliang Gao, Quanming Lu, Can Huang, Rongsheng Wang, and Shui Wang. Reformation of rippled quasi-parallel shocks: 2-d hybrid simulations. *Journal of Geophysical Research: Space Physics*, 2017.

[100] D Burgess. Foreshock-shock interaction at collisionless quasi-parallel shocks. *Advances in Space Research*, 15(8-9):159–169, 1995.

[101] K Tsubouchi and Bertrand Lembège. Full particle simulations of short large-amplitude magnetic structures (slams) in quasi-parallel shocks. *Journal of Geophysical Research: Space Physics*, 109(A2), 2004.

[102] D Burgess, EA Lucek, M Scholer, SD Bale, MA Balikhin, A Balogh, TS Horbury, VV Krasnoselskikh, H Kucharek, Bertrand Lembège, et al. Quasi-parallel shock structure and processes. *Space science reviews*, 118(1-4):205–222, 2005.

[103] Bertrand Lefebvre, Yoshitaka Seki, Steven J Schwartz, Christian Mazelle, and Elizabeth A Lucek. Reformation of an oblique shock observed by cluster. *Journal of Geophysical Research: Space Physics*, 114(A11), 2009.

[104] Steven J Schwartz, David Sibeck, Mark Wilber, Karim Meziane, and Timothy S Horbury. Kinetic aspects of foreshock cavities. *Geophysical research letters*, 33(12), 2006.

[105] L Billingham, SJ Schwartz, and DG Sibeck. The statistics of foreshock cavities: results of a cluster survey. In *Annales geophysicae: atmospheres, hydrospheres and space sciences*, volume 26, page 3653, 2008.

[106] Laurence Billingham, Steven J Schwartz, and Mark Wilber. Foreshock cavities and internal foreshock boundaries. *Planetary and Space Science*, 59(7):456–467, 2011.

[107] X Blanco-Cano, P Kajdič, N Omidi, and CT Russell. Foreshock cavitons for different interplanetary magnetic field geometries: Simulations and observations. *Journal of Geophysical Research: Space Physics*, 116(A9), 2011.

[108] Steven J Schwartz, Götz Paschmann, Norbert Sckopke, Thomas M Bauer, Malcolm Dunlop, Andrew N Fazakerley, and Michelle F Thomsen. Conditions for the formation of hot flow anomalies at earth's bow shock. *Journal of Geophysical Research: Space Physics*, 105(A6):12639–12650, 2000.

[109] SJ Schwartz. Hot flow anomalies near the earth's bow shock. *Advances in space research*, 15(8-9):107–116, 1995.

[110] N Omidi and DG Sibeck. Formation of hot flow anomalies and solitary shocks. *Journal of Geophysical Research: Space Physics*, 112(A1), 2007.

[111] N Omidi, DG Sibeck, and X Blanco-Cano. Foreshock compressional boundary. *Journal of Geophysical Research: Space Physics*, 114(A8), 2009.

[112] N Omidi, D Sibeck, X Blanco-Cano, D Rojas-Castillo, D Turner, H Zhang, and P Kajdič. Dynamics of the foreshock compressional boundary and its connection to foreshock cavities. *Journal of Geophysical Research: Space Physics*, 118(2):823–831, 2013.

[113] P Kajdič, Xochitl Blanco-Cano, Nojan Omidi, Diana Rojas-Castillo, David G Sibeck, and Laurence Billingham. Traveling foreshocks and transient foreshock phenomena. *Journal of Geophysical Research: Space Physics*, 122(9):9148–9168, 2017.

[114] KH Bhavnani and RP Vancour. Coordinate systems for space and geophysical applications. *Scientific Report No. 9 RADEX, Inc., Bedford, MA.*, 9, 1991.

[115] C Ph Escoubet. Cluster-ii: scientific objectives and data dissemination. *ESA bulletin*, pages 54–60, 2000.

[116] Patrick W Daly et al. Users guide to the cluster science data system. Technical report, DSMPA-TN-0015, April 19, 2002. ftp://ftp. estec. esa. nl/pub/csds/task for/users guide/csds guide. html, 2002.

[117] CP Escoubet, M Fehringer, and M Goldstein. Introduction the cluster mission. In *Annales Geophysicae*, volume 19, pages 1197–1200, 2001.

[118] Andrew P Walsh, C Forsyth, AN Fazakerley, CHK Chen, EA Lucek, JA Davies, CH Perry, SN Walker, and MA Balikhin. 10 years of the cluster mission. *Astronomy & Geophysics*, 51(5):5–33, 2010.

[119] I Dandouras and A Barthe. User guide to the cis measurements in the cluster active archive (caa). *CIS Team*, 3, 2012.

[120] Tsunehiko Kakutani and Hiroaki Ono. Weak non-linear hydromagnetic waves in a cold collision-free plasma. *Journal of the physical society of Japan*, 26(5):1305–1318, 1969.

[121] PA Robinson and DL Newman. Strong plasma turbulence in the earth's electron foreshock. *Journal of Geophysical Research: Space Physics*, 96(A10):17733–17749, 1991.

[122] Olga Alexandrova, Joachim Saur, Catherine Lacombe, Andre Mangeney, Jeremy Mitchell, Steve J Schwartz, and Patrick Robert. Universality of solar-wind turbulent spectrum from mhd to electron scales. *Physical review letters*, 103(16):165003, 2009.

[123] AR Bell. The acceleration of cosmic rays in shock fronts–i. *Monthly Notices of the Royal Astronomical Society*, 182(2):147–156, 1978.

[124] Anatoli Borisovich Mikhalovski. *Theory of Plasma Instabilities: Instabilities of a homogeneous plasma*, volume 1. Consultants bureau, 1974.

[125] RO Dendy, CN Lashmore-Davies, Kenneth George McClements, and GA Cottrell. The excitation of obliquely propagating fast alfvén waves at fusion ion cyclotron harmonics. *Physics of plasmas*, 1(6):1918–1928, 1994.

[126] Roberto Bruno and Vincenzo Carbone. The solar wind as a turbulence laboratory. *Living Reviews in Solar Physics*, 10(1):2, 2013.

[127] Xin Wang, Jiansen He, Chuanyi Tu, Eckart Marsch, Lei Zhang, and Jih-Kwin Chao. Large-amplitude alfven wave in interplanetary space: the wind spacecraft observations. *The Astrophysical Journal*, 746(2):147, 2012.

[128] C-Y Tu and E Marsch. On the nature of compressive fluctuations in the solar wind. *Journal of Geophysical Research: Space Physics*, 99(A11):21481–21509, 1994.

[129] Justin C Kasper, Bennett A Maruca, Michael L Stevens, and Arnaud Zaslavsky. Sensitive test for ion-cyclotron resonant heating in the solar wind. *Physical review letters*, 110(9):091102, 2013.

[130] Jean Louis Pinçon and François Lefeuvre. Local characterization of homogeneous turbulence in a space plasma from simultaneous measurements of field components at several points in space. *Journal of Geophysical Research: Space Physics*, 96(A2):1789–1802, 1991.

[131] F Sahraoui, Jean-Louis Pinçon, G Belmont, L Rezeau, N Cornilleau-Wehrlin, P Robert, L Mellul, JM Bosqued, A Balogh, P Canu, et al. Ulf wave identification in the magnetosheath: The k-filtering technique applied to cluster ii data. *Journal of Geophysical Research: Space Physics*, 108(A9), 2003.

[132] Y Narita, K-H Glassmeier, S Schäfer, U Motschmann, K Sauer, I Dandouras, K-H Fornaçon, E Georgescu, and H Reme. Dispersion analysis of ulf waves in the foreshock using cluster data and the wave telescope technique. *Geophysical research letters*, 30(13), 2003.

[133] EA Lucek, TS Horbury, A Balogh, I Dandouras, and H Reme. Cluster observations of structures at quasi-parallel bow shocks. In *Annales Geophysicae*, volume 22, pages 2309–2313, 2004.

[134] Joseph V Hollweg. Beat, modulational, and decay instabilities of a circularly polarized alfven wave. *Journal of Geophysical Research: Space Physics*, 99(A12):23431–23447, 1994.

[135] SY Huang, M Zhou, Fouad Sahraoui, XH Deng, Y Pang, ZG Yuan, Q Wei, JF Wang, and XM Zhou. Wave properties in the magnetic reconnection diffusion region with high β: Application of the k-filtering method to cluster multispacecraft data. *Journal of Geophysical Research: Space Physics*, 115(A12), 2010.

[136] F Sahraoui, ML Goldstein, Gérard Belmont, P Canu, and Laurence Rezeau. Three dimensional anisotropic k-spectra of turbulence at sub-proton scales in the solar wind. *Physical Review Letters*, (105):131101, 2010.

[137] Y Narita, Karl-Heinz Glassmeier, S Schäfer, U Motschmann, M Fränz, I Dandouras, K-H Fornaçon, E Georgescu, A Korth, H Reme, et al. Alfvén waves in the foreshock propagating upstream in the plasma rest frame: statistics from cluster observations. In *Annales Geophysicae*, volume 22, pages 2315–2323, 2004.

[138] J-H Shue, JK Chao, HC Fu, CT Russell, P Song, KK Khurana, and HJ Singer. A new functional form to study the solar wind control of the magnetopause size and shape. *Journal of Geophysical Research: Space Physics*, 102(A5):9497–9511, 1997.

[139] BENGT UO Sonnerup and Maureen Scheible. Minimum and maximum variance analysis. *Analysis methods for multi-spacecraft data*, pages 185–220, 1998.

[140] AV Khrabrov and BU Sonnerup. Error estimates for minimum variance analysis. *Journal of Geophysical Research: Space Physics*, 103(A4):6641–6651, 1998.

[141] H Kawano and T Higuchi. A generalization of the minimum variance analysis method. In *Annales Geophysicae*, volume 14, pages 1019–1024. Springer, 1997.

[142] JM Beall, YC Kim, and EJ Powers. Estimation of wavenumber and frequency spectra using fixed probe pairs. *Journal of Applied Physics*, 53(6):3933–3940, 1982.

[143] T Dudok de Wit, VV Krasnosel'skikh, SD Bale, MW Dunlop, H Lühr, SJ Schwartz, and LJC Woolliscroft. Determination of dispersion relations in quasi-stationary plasma turbulence using dual satellite data. *Geophysical research letters*, 22(19):2653–2656, 1995.

[144] Boris Borisovich Kadomtsev. Plasma turbulence. *New York: Academic Press, 1965*, 1965.

[145] Adhemar Bultheel et al. Learning to swim in a sea of wavelets. *Bulletin of the Belgian Mathematical society-simon stevin*, 2(1):1–45, 1995.

[146] S Grace Chang, Bin Yu, and Martin Vetterli. Adaptive wavelet thresholding for image denoising and compression. *IEEE transactions on image processing*, 9(9):1532–1546, 2000.

[147] Sofia C Olhede and Andrew T Walden. Generalized morse wavelets. *IEEE Transactions on Signal Processing*, 50(11):2661–2670, 2002.

[148] Jonathan M Lilly and Sofia C Olhede. Higher-order properties of analytic wavelets. *IEEE Transactions on Signal Processing*, 57(1):146–160, 2009.

[149] Stephen A Fuselier, Donald A Gurnett, and RJ Fitzenreiter. The downshift of electron plasma oscillations in the electron foreshock region. *Journal of Geophysical Research: Space Physics*, 90(A5):3935–3946, 1985.

[150] Daniel Verscharen and Benjamin DG Chandran. The dispersion relations and instability thresholds of oblique plasma modes in the presence of an ion beam. *The Astrophysical Journal*, 764(1):88, 2013.

[151] O Alexandrova, A Mangeney, M Maksimovic, N Cornilleau-Wehrlin, J-M Bosqued, and Mats André. Alfvén vortex filaments observed in magnetosheath downstream of a quasi-perpendicular bow shock. *Journal of Geophysical Research: Space Physics*, 111(A12), 2006.

[152] Joe Giacalone, Steven J Schwartz, and David Burgess. Observations of suprathermal ions in association with slams. *Geophysical research letters*, 20(2):149–152, 1993.

[153] LB Wilson, CA Cattell, PJ Kellogg, K Goetz, K Kersten, JC Kasper, A Szabo, and K Meziane. Low-frequency whistler waves and shocklets observed at quasi-perpendicular interplanetary shocks. *Journal of Geophysical Research: Space Physics*, 114(A10), 2009.

[154] N Dubouloz and M Scholer. Two-dimensional simulations of magnetic pulsations upstream of the earth's bow shock. *Journal of Geophysical Research: Space Physics*, 100(A6):9461–9474, 1995.

[155] EA Lucek, TS Horbury, I Dandouras, and H Rème. Cluster observations of the earth's quasi-parallel bow shock. *Journal of Geophysical Research: Space Physics*, 113(A7), 2008.

[156] D Burgess. Cyclic behavior at quasi-parallel collisionless shocks. *Geophysical research letters*, 16(5):345–348, 1989.

[157] Rico Behlke, Mats André, Stephan C Buchert, Andris Vaivads, Anders I Eriksson, Elizabeth A Lucek, and Andre Balogh. Multi-point electric field measurements of short large-amplitude magnetic structures (slams) at the earth's quasi-parallel bow shock. *Geophysical research letters*, 30(4), 2003.

[158] J Giacalone, SJ Schwartz, and D Burgess. Artificial spacecraft in hybrid simulations of the quasi-parallel earth's bow shock: analysis of time series versus spatial profiles and a separation strategy for cluster. In *Annales Geophysicae*, volume 12, pages 591–601. Springer, 1994.

[159] T Dudok Wit, VV Krasnosel'Skikh, M Dunlop, and H Lühr. Identifying nonlinear wave interactions in plasmas using two-point measurements: A case study of short large amplitude magnetic structures (slams). *Journal of Geophysical Research: Space Physics*, 104(A8):17079–17090, 1999.

[160] CF Kennel, JP Edmiston, and T Hada. *A quarter century of collisionless shock research*. Wiley Online Library, 1984.

[161] John Michael Tutill Thompson and H Bruce Stewart. *Nonlinear dynamics and chaos*. John Wiley & Sons, 2002.

[162] J Soucek, V Krasnoselskikh, T Dudok de Wit, J Pickett, and C Kletzing. Nonlinear decay of foreshock langmuir waves in the presence of plasma inhomogeneities: Theory and cluster observations. *Journal of Geophysical Research: Space Physics*, 110(A8), 2005.

[163] D Zhu, MA Balikhin, M Gedalin, H Alleyne, SA Billings, Y Hobara, V Krasnosel'Skikh, MW Dunlop, and M Ruderman. Nonlinear dynamics of foreshock structures: Application of nonlinear autoregressive moving average with exogenous inputs model to cluster data. *Journal of Geophysical Research: Space Physics*, 113(A4), 2008.

[164] Rico Behlke, Mats André, Stuart D Bale, Jolene S Pickett, Cynthia A Cattell, Elizabeth A Lucek, and Andre Balogh. Solitary structures associated with short large-amplitude magnetic structures (slams) upstream of the earth's quasi-parallel bow shock. *Geophysical research letters*, 31(16), 2004.

[165] Vladimir E Zakharov. Collapse of langmuir waves. *Sov. Phys. JETP*, 35(5):908–914, 1972.

[166] Akira Hasegawa. Stimulated modulational instabilities of plasma waves. *Physical Review A*, 1(6):1746, 1970.

[167] SD Bale, PJ Kellogg, DE Larsen, RP Lin, K Goetz, and RP Lepping. Bipolar electrostatic structures in the shock transition region: Evidence of electron phase space holes. *Geophysical research letters*, 25(15):2929–2932, 1998.

[168] Daniel B Graham, Yu V Khotyaintsev, Andris Vaivads, and Mats André. Electrostatic solitary waves with distinct speeds associated with asymmetric reconnection. *Geophysical Research Letters*, 42(2):215–224, 2015.

[169] André Rogister. Parallel propagation of nonlinear low-frequency waves in high-β plasma. *The Physics of Fluids*, 14(12):2733–2739, 1971.

[170] VB Baranov and MS Ruderman. Waves in a plasma with hall dispersion. *Fluid Dynamics*, 9(3):421–425, 1974.

[171] E Dubinin, K Sauer, and JF McKenzie. Nonlinear stationary whistler waves and whistler solitons (oscillitons). exact solutions. *Journal of plasma physics*, 69(4):305–330, 2003.

[172] Konrad Sauer, E Dubinin, and JF McKenzie. Wave emission by whistler oscillitons: Application to "coherent lion roars". *Geophysical research letters*, 29(24), 2002.

[173] Lawrence R Rabiner and Bernard Gold. Theory and application of digital signal processing. *Englewood Cliffs, NJ, Prentice-Hall, Inc., 1975. 777 p.*, 1975.

[174] Gabriel Rilling, Patrick Flandrin, Paulo Goncalves, et al. On empirical mode decomposition and its algorithms. In *IEEE-EURASIP workshop on nonlinear signal and image processing*, volume 3, pages 8–11. NSIP-03, Grado (I), 2003.

[175] Norden E Huang, Zheng Shen, Steven R Long, Manli C Wu, Hsing H Shih, Quanan Zheng, Nai-Chyuan Yen, Chi Chao Tung, and Henry H Liu. The empirical mode decomposition and the hilbert spectrum for nonlinear and non-stationary time series analysis. In *Proceedings of the Royal Society of London A: mathematical, physical and engineering sciences*, volume 454, pages 903–995. The Royal Society, 1998.

[176] Zhaohua Wu and Norden E Huang. Ensemble empirical mode decomposition: a noise-assisted data analysis method. *Advances in adaptive data analysis*, 1(01):1–41, 2009.

[177] Maria E Torres, Marcelo A Colominas, Gastón Schlotthauer, and Patrick Flandrin. A complete ensemble empirical mode decomposition with adaptive noise. In *Acoustics, speech and signal processing (ICASSP), 2011 IEEE international conference on*, pages 4144–4147. IEEE, 2011.

[178] David J Kaup and Alan C Newell. An exact solution for a derivative nonlinear schrödinger equation. *Journal of Mathematical Physics*, 19(4):798–801, 1978.

[179] Akira Nakamura and Hsing-Hen Chen. Multi-soliton solutions of a derivative nonlinear schrödinger equation. *Journal of the Physical Society of Japan*, 49(2):813–816, 1980.

[180] Philip J Davis and Philip Rabinowitz. *Methods of numerical integration*. Courier Corporation, 2007.

[181] T Hada, CF Kennel, and B Buti. Stationary nonlinear alfvén waves and solitons. *Journal of Geophysical Research: Space Physics*, 94(A1):65–77, 1989.

[182] LB Wilson, A Koval, DG Sibeck, A Szabo, CA Cattell, JC Kasper, BA Maruca, M Pulupa, CS Salem, and M Wilber. Shocklets, slams, and field-aligned ion beams in the terrestrial foreshock. *Journal of Geophysical Research: Space Physics*, 118(3):957–966, 2013.

[183] GA Collinson, LB Wilson, DG Sibeck, N Shane, TL Zhang, TE Moore, Andrew J Coates, and S Barabash. Short large-amplitude magnetic structures (slams) at venus. *Journal of Geophysical Research: Space Physics*, 117(A10), 2012.

[184] GK Batchelor. An introduction to fluid mechanics (cambridge mathematical library), 2000.

[185] Sergey Nazarenko. *Wave turbulence*, volume 825. Springer Science & Business Media, 2011.

[186] Miguel Escobedo and Juan Velázquez. *On the theory of weak turbulence for the nonlinear Schrödinger equation*, volume 238. American Mathematical Society, 2015.

[187] Vladimir E Zakharov, Victor S L'vov, and Gregory Falkovich. *Kolmogorov spectra of turbulence I: Wave turbulence*. Springer Science & Business Media, 2012.

[188] Elena Kartashova. *Nonlinear resonance analysis: theory, computation, applications*. Cambridge University Press, 2010.

[189] T Ho Dupree. Nonlinear theory of drift-wave turbulence and enhanced diffusion. *The Physics of Fluids*, 10(5):1049–1055, 1967.

[190] Seelye Martin, William Simmons, and Carl Wunsch. The excitation of resonant triads by single internal waves. *Journal of Fluid Mechanics*, 53(1):17–44, 1972.

[191] Mark J Ablowitz and Richard Haberman. Resonantly coupled nonlinear evolution equations. *Journal of Mathematical Physics*, 16(11):2301–2305, 1975.

[192] Elena Kartashova and Victor S L'vov. Model of intraseasonal oscillations in earth's atmosphere. *Physical review letters*, 98(19):198501, 2007.

[193] C Henry McComas and Francis P Bretherton. Resonant interaction of oceanic internal waves. *Journal of Geophysical Research*, 82(9):1397–1412, 1977.

[194] P Henri, C Briand, A Mangeney, SD Bale, F Califano, K Goetz, and M Kaiser. Evidence for wave coupling in type iii emissions. *Journal of Geophysical Research: Space Physics*, 114(A3), 2009.

[195] T Dudok de Wit and VV Krasnosel'Skikh. Wavelet bicoherence analysis of strong plasma turbulence at the earth's quasiparallel bow shock. *Physics of Plasmas*, 2(11):4307–4311, 1995.

[196] Y Narita, K-H Glassmeier, M Fränz, Y Nariyuki, and T Hada. Observations of linear and nonlinear processes in the foreshock wave evolution. 2007.

[197] SD Bale, D Burgess, PJ Kellogg, K Goetz, RL Howard, and SJ Monson. Phase coupling in langmuir wave packets: Possible evidence of three-wave interactions in the upstream solar wind. *Geophysical research letters*, 23(1):109–112, 1996.

[198] Emanuel Parzen. On estimation of a probability density function and mode. *The annals of mathematical statistics*, 33(3):1065–1076, 1962.

[199] Samir S Soliman and S-Z Hsue. Signal classification using statistical moments. *IEEE Transactions on Communications*, 40(5):908–916, 1992.

[200] David R Brillinger. An introduction to polyspectra. *The Annals of mathematical statistics*, pages 1351–1374, 1965.

[201] David R Brillinger. Some basic aspects and uses of higher-order spectra. *Signal Processing*, 36(3):239–249, 1994.

[202] Athina Petropulu. Higher-order spectral analysis. *Digital Signal Processing Handbook, VK Madisetti and DB Williams, editors, Chapman & Hall/CRCnetBASE*, 1999.

[203] Maurice Bertram Priestley. Non-linear and non-stationary time series analysis. 1988.

[204] GZ dos Santos Lima, ZO Guimarães-Filho, AM Batista, IL Caldas, SR Lopes, RL Viana, IC Nascimento, and Yu K Kuznetsov. Bicoherence in electrostatic turbulence driven by high magnetohydrodynamic activity in tokamak chauffage alfvén brésilien. *Physics of Plasmas*, 16(4):042508, 2009.

[205] MR Hajj, JB Davila, RW Miksad, and EJ Powers. A technique to measure wavenumber mismatch between quadratically interacting modes. *Experiments in fluids*, 18(4):217–224, 1995.

[206] James Douglas Hamilton. *Time series analysis*, volume 2. Princeton university press Princeton, 1994.